



universität  
wien

# DISSERTATION

Titel der Dissertation

On the microscopic dynamics of particle systems  
in and out of thermal equilibrium

angestrebter akademischer Grad

Doktor der Naturwissenschaften (Dr. rer. nat.)

Verfasser:	Hadrien Bosetti
Matrikel-Nummer:	0327195
Dissertationsgebiet( lt. Studienblatt):	Physik
Betreuer:	Prof. Dr. Harald A. Posch

Wien, im Juli 2011

Acknowledgements:

*First of all I want to thank my supervisor Harald Posch who gave me the opportunity to write this PhD thesis, for introducing me into the world of Lyapunov instabilities, for his patience with my manuscript drafts, and his excellent advice.*

*I am also grateful to Christoph Dellago who gave me a place to complete the writing of this work, and I am heartily thankful to all members of his group for the very amicable and friendly welcome.*

*Lastly, I would like to explain my gratitude to my family, my friends, my partner Lisa Fenk, as well as her family, for their encouragement and ongoing support.*

*My work has been supported by two FWF-projects (P 15348 and P 18798-N20).*

Hadrien Bosetti  
Computational Physics Group  
Faculty of Physics  
University of Vienna  
Boltzmanngasse 5, A-1090 Wien, Austria

# Contents

<b>Abstract</b>	<b>v</b>
<b>Zusammenfassung</b>	<b>vii</b>
<b>Notation and Acronyms</b>	<b>ix</b>
<b>Introduction</b>	<b>1</b>
References . . . . .	9
<b>I Transport phenomena and Lyapunov instability</b>	<b>13</b>
<b>1 The van Beijeren thermostat and a simple application</b>	<b>15</b>
1.1 Introduction . . . . .	15
1.2 The van Beijeren thermostat . . . . .	17
1.2.1 Collision map and kinetic theory . . . . .	18
1.2.2 Phase-space dynamics and tangent bundle . . . . .	21
1.3 Planar gas of hard disks . . . . .	22
1.4 Temperature and density profiles . . . . .	25
1.5 Heat conduction . . . . .	27
1.6 Summary . . . . .	29
References . . . . .	29
<b>2 Thermostated modified Lorentz Gas</b>	<b>31</b>
2.1 Introduction . . . . .	31
2.2 Model . . . . .	33
2.3 Local equilibrium and normal transport . . . . .	35

2.4	Lyapunov instability . . . . .	39
2.4.1	Behavior of specific Lyapunov exponents . . . . .	42
2.4.2	Vanishing Lyapunov exponents and conjugate pairing relation . . . . .	44
2.5	Chaos and transport . . . . .	46
2.6	Localization for large systems in microcanonical equilibrium . . . . .	48
2.7	Conclusion . . . . .	50
2.8	Appendix: Wanderer-scatterer collisions for the 3D model . . . . .	52
2.8.1	Phase space dynamics . . . . .	52
2.8.2	Tangent space dynamics . . . . .	53
	References . . . . .	55
<b>II</b>	<b>Tangent bundle dynamics and its consequences</b>	<b>59</b>
<b>3</b>	<b>Covariant Lyapunov vectors for rigid disk systems</b>	<b>61</b>
3.1	Introduction . . . . .	62
3.2	Phase-space and tangent-space dynamics . . . . .	63
3.3	Numerical considerations . . . . .	65
3.4	A simple example: the Hénon map . . . . .	67
3.5	Systems of hard disks . . . . .	67
3.5.1	Covariant versus Gram-Schmidt vectors . . . . .	69
3.5.2	Localization . . . . .	70
3.5.3	Tangent space projections . . . . .	73
3.5.4	Central manifold and vanishing exponents . . . . .	73
3.5.5	Lyapunov modes . . . . .	76
3.5.6	Transversality . . . . .	82
3.6	Conclusion . . . . .	88
3.7	Acknowledgements . . . . .	89
3.8	Appendix . . . . .	90
3.8.1	Zero Modes dynamics . . . . .	90
3.8.2	Reconstruction of the LP-modes from the experimental GS and covariant vectors (see Table 3.3) . . . . .	93
	References . . . . .	102

<b>4 Covariant Lyapunov vectors for the field-free Lorentz gas</b>	<b>105</b>
4.1 Introduction . . . . .	105
4.2 Phase-space and tangent-space dynamics . . . . .	107
4.3 Gram-Schmidt vectors and covariant vectors . . . . .	109
4.4 Projections onto coordinate and momentum subspaces . . . . .	111
4.5 Hyperbolicity . . . . .	112
4.6 Poincaré map representation of covariant vectors . . . . .	112
4.7 Appendix . . . . .	115
References . . . . .	116
<b>5 Time-reversal symmetry for simple models in/out of thermal equilibrium</b>	<b>119</b>
5.1 Introduction . . . . .	120
5.2 Covariant Lyapunov vectors and local Lyapunov exponents . . . . .	120
5.3 Differential approach to local Lyapunov exponents . . . . .	126
5.4 Numerical considerations . . . . .	126
5.5 Doubly-thermostated oscillator . . . . .	128
5.5.1 Description of the model . . . . .	128
5.5.2 Global properties . . . . .	129
5.5.3 Local Lyapunov exponents . . . . .	131
5.5.4 Hyperbolicity . . . . .	133
5.5.5 Singularities of the local Lyapunov exponents . . . . .	134
5.6 Local Lyapunov exponents for symplectic systems . . . . .	136
5.7 Concluding remarks . . . . .	140
5.8 Acknowledgements . . . . .	141
References . . . . .	141
<b>6 Symmetry properties of Lyapunov vectors and local exponents</b>	<b>145</b>
References . . . . .	147
<b>7 Domination and convergence of Lyapunov spectra for smooth-hard-disk systems</b>	<b>149</b>
References . . . . .	155

<b>8 How rotation breaks the Hamiltonian character of rough-hard-disk systems</b>	<b>157</b>
8.1 Introduction . . . . .	157
8.2 Tangent-bundle dynamics . . . . .	158
8.3 Systems of hard disks . . . . .	159
8.3.1 The rough-hard-disk system (RHDS) . . . . .	160
8.3.2 Matrix formulation of the dynamics for RHDS . . . . .	162
8.4 Covariant versus Gram-Schmidt vectors . . . . .	166
8.4.1 Angles between the position and momentum parts of perturbation vectors . . . . .	168
8.4.2 Localization of perturbation vectors . . . . .	170
8.4.3 Tangent space projections . . . . .	172
8.5 Null subspace and vanishing exponents for RHDS . . . . .	174
8.6 Transversality versus order violation in the local Lyapunov spectrum . .	181
8.7 The RHDS is not symplectic . . . . .	184
8.8 Appendix: Matrix formulation of the dynamics for SHDS . . . . .	189
References . . . . .	189
 <b>Outlook</b>	 <b>193</b>
 <b>Remarks on the thesis, by supervisor Harald A. Posch</b>	 <b>195</b>
 <b>Curriculum Vitae</b>	 <b>197</b>

# Abstract

The microscopic time evolution of a classical many-particle system is described by a trajectory in a high-dimensional state (phase) space, which is spanned by the position and momentum components of all particles. Due to the convex surface of atoms or molecules, this phase-space trajectory is highly Lyapunov unstable, which means that a tiny (infinitesimal) perturbation grows or shrinks exponentially with time. This instability is characterized by a set of exponential rate constants, the Lyapunov exponents. They are computed by following the time evolution of an associated bundle of perturbation vectors in tangent space. The number of these vectors is equal to the dimension  $D$  of the phase space. In the classical algorithm these vectors are artificially forced to stay orthonormal with a Gram-Schmidt procedure, and the Lyapunov exponents are deduced from the time evolution of all  $d$ -dimensional volume elements ( $d \leq D$ ). The local (in phase space) Lyapunov exponents depend on the instantaneous directions of these orthonormal vectors and do not reflect the time-reversal invariance property of the original system.

In a recent publication (F. Ginelli *et al.*, Phys. Rev. Lett. 99, 130601 (2007)) another set of vectors, the so-called covariant vectors, was considered, which is not orthonormal and follows the natural bundle dynamics in tangent space. At any instant of time these vectors provide a spanning set for the tangent space, and from the rate of change of their norms the Lyapunov exponents follow directly. The algorithm is more complex, since it still requires the computation of the Gram-Schmidt vectors in the forward direction of time, followed by an iteration in the backward direction to obtain the covariant vectors.

To establish and maintain a system in a non-equilibrium stationary state, computer thermostats are required. They are used to control the local temperature and/or to extract the irreversibly generated heat due to the work done on the system by the “driving”. Here, we test novel thermostated boundaries suggested by van Beijeren (Chapter 1), which consist of a non-trivial time-reversible map relating the incoming velocity vector of a particle colliding with the thermostat wall with the outgoing velocity of the same particle. This map obeys detailed balance and is shown to generate velocity distributions in front of the thermostating wall which are very close

to the Maxwell-Boltzmann distributions for the specified temperatures. Interestingly, almost no temperature jumps occur at the boundary. This method is used to study heat conduction for a two-dimensional hard-disk gas (Chapter 1), and for a modified periodic Lorentz gas (Chapter 2), for which the scatterer particles may rotate and are “rough” to allow energy exchange between the translational degrees of freedom of a gas of point particles and the rotational degrees of freedom of the disk scatterers. Since the “driving” and thermosetting is a non-stochastic and dynamical process, it allows the computation of the full Lyapunov spectrum for stationary non-equilibrium conditions.

The overwhelming part of this dissertation (Chapters 3 to 8) is devoted to the study of the covariant Lyapunov vectors and associated local exponents. It includes the first application of this algorithm to many-particle systems. The method is first applied to a gas of rigid hard disks (Chapter 3), where the emphasis is on the localized and delocalized Lyapunov modes appearing for large and small exponents, respectively. The hyperbolic properties are also studied. Similar investigations are carried out for the classical Lorentz gas (Chapter 4). Next, the symmetry properties of the Gram-Schmidt vectors and of the covariant vectors are studied in detail for a simple one-dimensional heat conducting oscillator in a temperature field varying in space (Chapter 5 and 6). We find that the local Lyapunov exponents vary smoothly in directions parallel to the phase flow, but display a fractal behavior for directions transversal to the flow. We demonstrate also that the covariant vectors nicely reflect the time reversal symmetry of the original motion equations, whereas the Gram-Schmidt vectors do not.

Finally, we study in more detail the convergence of the Lyapunov spectrum and the entanglement of local Lyapunov exponents averaged over a finite time interval (Chapter 7). Focussing on a system of rough-hard-disk particles, we demonstrate that the conservation of energy and of phase volume does not prevent this system to loose its symplectic nature due to the rotation of the particles (Chapter 8).



# Zusammenfassung

Die mikroskopische Zeitentwicklung in einem klassischen Vielteilchen-System wird durch eine Trajektorie in einem hochdimensionalen, von den Impuls und Ortskomponenten aller Partikel aufgespannten, Zustands- oder Phasenraum beschrieben. Aufgrund der konvexen Oberfläche von Atomen und Molekülen weist die Trajektorie im Phasenraum eine hohe Lyapunov-Instabilität auf. Das bedeutet, dass kleine (infinitesimale) Störungen mit der Zeit exponentiell wachsen oder schrumpfen. Diese Instabilität ist durch exponentielle Änderungsraten, die Lyapunov-Exponenten, charakterisiert. Sie werden berechnet, indem man dem Zeitverlauf von assoziierten Bündeln von Störungsvektoren im Tangentialraum folgt, wobei die Anzahl der Vektoren der Dimension  $D$  des Phasenraums entspricht. Im klassischen Algorithmus wird die Orthonormalität der Vektoren durch das Gram-Schmidtsche Orthogonalisierungsverfahren künstlich erzwungen, und die Lyapunov-Exponenten ergeben sich aus der Zeitentwicklung aller  $d$ -dimensionalen Volumenelemente ( $d \leq D$ ). Die im Phasenraum lokalen Lyapunov-Exponenten hängen von den momentanen Richtungen der orthonormalen Vektoren ab und spiegeln nicht die Zeitumkehrinvarianz des ursprünglichen Systems wider.

Eine neuere Arbeit (F. Ginelli *et al.*, Phys. Rev. Lett. 99, 130601 (2007)) betrachtet zum ersten Mal so genannte kovariante Vektoren, die nicht orthonormal sind und die der natürlichen Dynamik des Bündels im Tangentialraum folgen. Diese Vektoren spannen zu jedem Zeitpunkt den Tangentialraum auf, und die Lyapunov-Exponenten folgen direkt aus der Änderungsrate ihrer Normen. Dieser Algorithmus ist komplexer, da die Gram-Schmidt Vektoren weiterhin in Vorwärtsrichtung berechnet werden, und danach, in einer Iteration in Rückwärtsrichtung, die kovarianten Vektoren bestimmt werden.

Zur Computersimulation von dynamischen Systemen im stationären Nichtgleichgewicht benötigt man virtuelle Thermostaten. Thermostaten werden verwendet um die lokale Temperatur zu kontrollieren und/oder um die Wärme abzuführen, die durch den Antrieb des Systems irreversibel erzeugt wird. Im ersten Teil dieser Dissertation testen wir eine neue thermostatisierende Randbedingungen, die von van Beijeren vorgeschlagen wurde. Sie bestehen aus nicht trivialen, zeitem-

kehrinvarianten Abbildungen, die dem Geschwindigkeitsvektor eines Teilchens unmittelbar vor einer Kollision mit der Thermostatwand einen Geschwindigkeitsvektor nach der Kollision zuordnen und gewisse Gleichgewichtsbedingungen erfüllen. Die Abbildung gehorcht einem genau definierten Gleichgewicht, und es wurde gezeigt, dass die von ihr erzeugten Geschwindigkeitsverteilungen in der Nähe der Thermostatenwand annähernd den Maxwell-Boltzmann-Verteilungen für die definierten Temperaturen entsprechen. Interessanterweise treten kaum Temperatursprünge an der Grenzfläche auf. Die Methode wurde zur Berechnung der Wärmeleitung eines zweidimensionalen Gases harter Scheiben angewandt (Kapitel 1). Ähnliche Simulationen wurden auch für ein modifiziertes Lorentz-Gas angestellt (Kapitel 2), bei dem zentrale Streukörper mit rauher Oberfläche Rotationsenergie mit der Translationsenergie eines Punktgases austauschen. Da dies keinen stochastischen sondern einen dynamischen Prozess darstellt, ermöglicht er die Berechnung vollständiger Lyapunov-Spektren auch für stationäre Nichtgleichgewichtszustände.

Das Schwergewicht dieser Dissertation (Kapitel 3-8) liegt auf der Berechnung lokaler Lyapunov-Exponenten und deren kovarianten Lyapunov-Vektoren. Erstmals wird dieses Verfahren auf Vielteilchensysteme angewendet. Die Methode wurde zuerst für ein Gas aus harten Scheiben angewandt (Kapitel 3), wobei lokalisierte und delokalisierte Lyapunov-Moden untersucht werden, die für kleine beziehungsweise große Exponenten auftreten. Die hyperbolischen Eigenschaften werden ebenfalls betrachtet. Ähnliche Untersuchungen werden auch für das klassische Lorentz-Gas angestellt (Kapitel 4). Die Symmetrieeigenschaften von Gram-Schmidt und kovarianten Lyapunov-Vektoren werden am Beispiel eines eindimensionalen, wärmeleitenden Oszillators, der an ein räumlich variierendes Temperaturfeld gekoppelt ist, studiert (Kapitel 5 und 6). Während die lokalen kovarianten Exponenten in Richtung des Phasenflusses glatte Funktionen sind, finden wir transversal zum Fluss ein fraktales Verhalten. Wir zeigen auch, dass die kovarianten Vektoren die Zeitumkehrsymmetrie der ursprünglichen Bewegungsgleichungen widerspiegeln, während dies für die Gram-Schmidt Vektoren nicht der Fall ist.

Weiters untersuchen wir die Konvergenzeigenschaften von Lyapunov-Spektren und die Verschränkung lokaler, über ein endliches Zeitintervall gemittelter Lyapunov-Exponenten (Kapitel 7). Anhand eines Systems von rauhen harten Scheiben wird gezeigt, dass der symplektische Charakter des Systems verloren geht, wenn es zu einem Energieaustausch zwischen translatorischen und rotatorischen Freiheitsgraden kommt (Kapitel 8).

# Notation and Acronyms

## Vector and space notation

In the two- or three-dimensional physical space

- Vectors are denoted with small letters with an arrow, e.g.  $\vec{q}$  for the positions and  $\vec{p}$  for the momenta of the particles.
- Their associated perturbations are labeled by adding the prefix  $\delta$ , i.e.  $\delta\vec{q}$  and  $\delta\vec{p}$ .

In the phase space (of dimension  $D$ ):

- The phase point is identified by  $\mathbf{\Gamma}$ .
- The associated perturbed states are denoted  $\{\delta\mathbf{\Gamma}_i\}_{i=1}^D$ .

In the tangent space:

- The subspaces are denoted by bold capital letters,  $\mathbf{U}$  for the Gram-Schmidt subspaces and  $\mathbf{E}$  for the covariant subspaces.
- The spanning vectors are identified by  $\mathbf{g}$  for the Gram-Schmidt vectors, and  $\mathbf{v}$  for the covariant vectors.

## List of acronyms

GS	Gram-Schmidt
SHDS	Smooth hard disk system
RHDS	Rough hard disk system



# Introduction

One of the great success stories of modern science has been the development of kinetic theory by Clausius, Maxwell, Boltzmann [1], and others. It provides the basis of our understanding of macroscopic matter in terms of the microscopic dynamics of atoms and molecules. It is based on classical mechanics, but Boltzmann soon realized the necessity to incorporate the concept of probability [2]. He was also the first to introduce the concept of the microcanonical and canonical ensembles [3], which is sometimes incorrectly accredited to Gibbs [4]. It makes use of the principle of equal a priory probability for all accessible states in the phase space. This principle is intimately connected with the assumption of ergodicity for many body systems, which states that the phase-space trajectory of a system visits the neighborhood of any point in the accessible phase space within a finite time. This assumption has been very difficult to prove even for the most simple systems such as a gas of hard disks [5]. For this particular model, the mathematical prove believed to hold without reproach has been accomplished only very recently [5, 6]. Although originally developed only for rarefied gases, the kinetic theory was soon extended to dense systems and mixtures by Chapman and Enskog [7].

In thermodynamic equilibrium the probability distribution in phase space for many body systems is a smooth, differentiable function. The Maxwell-Boltzmann distribution may serve as an example in the single-particle phase space of a gas. If a system is driven out of equilibrium into a stationary non-equilibrium state, this smoothness is not generally preserved. If the state is made stationary with the help of dynamical time-reversible thermostats, the probability distribution collapses onto a fractal attractor [8, 9, 10], which in some cases has been identified with the Sinai-Ruelle-Bowen measure studied by mathematical physicists [11]. The existence of this fractal probability distribution was facilitated by two instances:

- i) The use of large-scale numerical computation. The numerical solution of the motion equations allows for a natural and powerful extension of the ideas of Boltzmann to complicated many body systems, which otherwise would not be accessible by analytical theory. It is, of course, futile to speculate, whether non-equilibrium statistical mechanics would have

developed even faster, if Boltzmann had been in a position to use a modern computer [12].

- ii) The application of dynamical systems theory, which not only studies the trajectory of a system in the phase space but also asks for the instability of this trajectory with respect to tiny perturbations [13, 14, 15]. If the trajectory is unstable, the system is said to be chaotic. Chaotic dynamical systems are characterized by an exponential growth of small perturbations of the initial conditions.

We consider a linearly independent set of perturbation vectors  $\{\delta\mathbf{\Gamma}_i(0); i = 1, \dots, D\}$  at an initial time ( $t = 0$ ) in phase space, which are commonly referred to as “Lyapunov vectors” (e.g. [16, 17, 18]). The number of vectors equals the dimension  $D$  of the phase space. The Lyapunov vector set, which points in all directions, corresponds to a perturbation vector set following the (phase-space) bundle trajectory. The snapshot space (affiliated to a phase point) spanned by this vector set is called the “tangent space”, and its continuous dynamical evolution is referred to as “tangent bundle”. The (long-time) evolution of the vector set allows to estimate the chaos of the system by the evaluation of the so-called (global) Lyapunov exponents  $\lambda_i$  :

$$\lambda_i = \lim_{t \rightarrow \infty} \frac{1}{t} \ln \frac{\|\delta\mathbf{\Gamma}_i(t)\|}{\|\delta\mathbf{\Gamma}_i(0)\|} .$$

The global Lyapunov exponents correspond to the time-averaged rates of exponential divergence ( $\lambda_i > 0$ ) and convergence ( $\lambda_i < 0$ ) of neighboring phase-space trajectories with respect to the reference trajectory. For conservative systems, the sum  $\sum_{i=1}^D \lambda_i$  is equal to zero, which indicates that any infinitesimal phase space volume is conserved by the dynamics. For dissipative systems the sum is negative. Several experimental studies for many-particle systems [19, 20, 21, 22, 23] as well as theoretical work [24] strongly suggest that the Lyapunov spectrum for particle systems with a repulsive pair potential converges to a finite limiting spectrum in the thermodynamic limit. Besides, the local evolution of the perturbation vectors reveals other very important properties of the systems, as will be discussed in the following.

This thesis is concerned with the Lyapunov instability of many body systems, which include hard disk fluids in two dimensions and various versions of planar Lorentz gases. It basically consists of two parts. In Part I, which may be summarized as “Transport phenomena and Lyapunov instability” and which incorporates Chapters 1 and 2, we provide the groundwork for the following chapters. Here we introduce the basic tools such as a dynamical thermostat suited for the study of heat conduction in non-equilibrium stationary state. The main part of thesis includes the Chapters 3 to 8 and may be summarized under the heading “Tangent bundle dynamics and its consequences”. The thesis is concluded with a short Outlook.

## Part I : Transport phenomena and Lyapunov instability

Non-equilibrium systems are dissipative. If a stationary system far from equilibrium is considered, where stationarity is acquired with a dynamical thermostat, a contraction of the phase-space density onto a multifractal attractor takes place. This fact explains why such systems are macroscopically irreversible as specified by the Second Law of thermodynamics, despite the time-reversible nature of the equations of motion [8, 21]. Generally, the transport coefficient of a driven thermostated non-equilibrium system may be expressed in terms of the sum of all Lyapunov exponents. For a certain subclass of systems, it is in principle possible to determine transport coefficients with the knowledge of one single conjugate pair of exponents – the most positive and the most negative [25].

In Chapter 2, we consider a modified Lorentz gas, which consists of a set of point-particles of mass  $m$  moving around hard-disk scatterers of diameter  $\sigma$  in a two-dimensional space. Energy exchange between disks and particles is allowed, but no point-particle collisions take place (similar to a photon gas in a crystal). The center of the scatterers are fixed on a triangular lattice, but each disk rotates with an angular velocity  $\omega_i$  and has a moment of inertia  $I$ . The particle-disk reflections are governed by “rough collisions”. The energy exchange between the point particles occurs via collisions with the rotating disk scatterers, which act as local energy storage devices. It is common to use a finite horizon to avoid the flight of particles through the box without undergoing collisions.

The Lorentz gas is confined to a box with periodic boundaries parallel to the horizontal direction. To the left and right, two thermostats delimit the box (see Fig. 1), one at temperature  $T_1$ , the other at temperature  $T_2 \neq T_1$ . The zig-zag form of the thermostat walls excludes the possibility of particles crossing the box in the vertical direction without collision. The velocity distribution of the particles reflected by the thermostats follows the Boltzmann distribution. Deterministic thermostats instead of stochastic ones are used for the computation of the Lyapunov spectrum. The system is driven away from equilibrium by setting the left and right temperature to different values. As a consequence, heat flows from the warm to the cold reservoir, which defines the heat current and the heat conductivity. The heat flow is “normal” [26, 27] in the sense that it is finite in the thermodynamic limit, although the temperature profile is not linear. We established the relation between the Lyapunov spectrum and the heat flux for various temperature gradients. The corresponding shape of the Lyapunov spectrum depends on  $T_2 - T_1$ , on the moment of inertia  $I$  of the scatterers, and on the number of point particles.

The deterministic thermostat we use for the reservoirs is the topic of Chapter 1, where it is tested for a simple two-dimensional smooth-hard-disk gas. For this purpose, thermodynamically

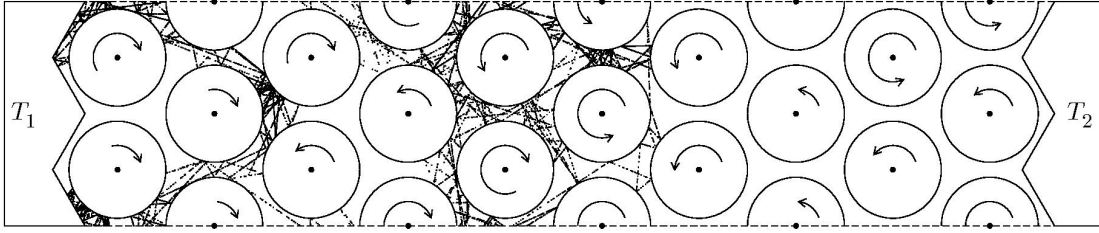


**Figure 1 :** A typical arrangement of disks (diameter  $\sigma = 1$ ) on a triangular array is shown. For the temperatures of the thermostats we have  $T_1 < T_2$ . The lines visualize the trajectory of a single particle of the gas consisting of 25 particles. The arrows on the disks are proportional to the initial disk velocity.

relevant quantities (e.g. the velocity distribution at the surface of the thermostats, the temperature profile, the density profile, the heat flux and the heat conductivity) and chaos quantifiers (based on the Lyapunov spectra) are calculated. The heat conductivity, which is the only transport coefficient relevant in this case, is determined experimentally using Fourier's law of heat conduction and is compared to the theoretical value obtained from the Enskog theory [28, 29]. Good agreement between the experimental and the theoretical values is found for the present model.

## Part II : Tangent bundle dynamics and its consequences

The study of Lyapunov exponents provides a new theoretical tool for the understanding of dynamical properties of a system in and out of thermodynamic equilibrium:

- i) In **equilibrium systems** the Lyapunov vectors associated with the large exponents are localized in physical space [30, 31], whereas the vectors belonging to the smallest positive exponents are coherently spread out in space and display wave-like structures, which are referred to as “Lyapunov modes” (e.g. [32, 33, 34, 35]). Lyapunov modes have been characterized in detail by Eckmann *et al.* [36]. They are found in hard-disk and hard-sphere systems in two and three dimensions, but also in systems with smooth particle interactions. However, as shown in the last chapter of this thesis, the existence of modes is restricted to Hamiltonian systems. For example, the present Lorentz gas (Fig. 1) is not a Hamiltonian system and no Lyapunov modes exist even in equilibrium.
- ii) In stationary **non-equilibrium systems**, the Lyapunov spectrum is asymmetric,

$$\sum_{i=1}^D \lambda_i < 0 ,$$

and provides a good estimate for the dimension of the multifractal attractor.



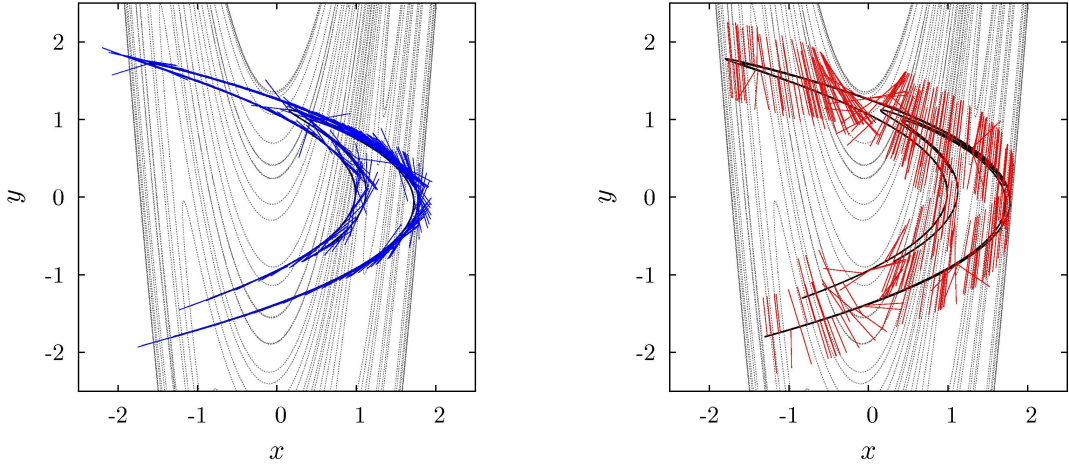


**Figure 2 :** For any phase-space point  $\Gamma$  (at any time  $\tau_n$ ) the covariant Lyapunov vectors (blue lines) parallel to the unstable manifold and the covariant Lyapunov vectors (red lines) parallel to the stable manifold are shown.

The Lyapunov vectors in the tangent space have the tendency to reorient over time towards the most unstable direction of the phase space. In order to avoid this characteristic in a numerical algorithm, it is common to use the Gram-Schmidt re-orthonormalization procedure at periodic time intervals, as was proposed by Benettin *et al.* [37, 38] and Shimada and Nagashima [39]. The Lyapunov vectors obtained with this approach, which are referred to as “Gram-Schmidt Lyapunov vectors”, are pairwise orthogonal but in general not covariant: their direction is not only determined by the microscopic dynamics of the linearized motion equations, but also by the periodic re-orthonormalization. As a consequence, the Gram-Schmidt vectors do not display time-reversibility, whereas the “covariant Lyapunov vectors” do. A vector set is covariant if, at a given phase-space point, it can be mapped by the linearized dynamics into the vector set associated with the phase-space point the system occupies at a later instant of time [36]. In simple terms, the covariant Lyapunov vectors correspond to the intrinsic local expanding/contracting directions in phase space strictly associated with the respective Lyapunov exponents. We can thus study the transversality (intersection of manifolds) and/or the degree of hyperbolicity (which determines whether stable and unstable manifolds are everywhere transversal or not) [40] in chaotic systems.

Based on the general theory of dynamical systems established by Ruelle [15], a general method for the construction of the covariant Lyapunov vectors has been introduced by Ginelli *et al.* [41]. This algorithm is based on storing the Gram-Schmidt vector set in the forward direction of the simulation, and using this information to find the covariant vectors in a time-reversed phase of the simulation. The stable subspace in the forward direction corresponds to the unstable subspace in the backward direction.

To demonstrate this method with a simple example, we show in Fig. 2 the famous Hénon attractor [42] as an example for a dissipative system. It is a two-dimensional map, and the attractor is given by the black full line. The attractor itself is identical to its unstable manifold in the phase space, whereas the stable directions are (approximately) indicated by the black dotted lines (stable manifold). If the two covariant Lyapunov vectors are computed for this model, one of them is aligned with the attractor (left panel), the other with the stable manifold (right panel).

In the work leading to this thesis, we provided the first computation of covariant Lyapunov vectors for various many-body systems. The Lyapunov spectrum (calculated with this new vector set) is identical with that obtained by the classical method, but the Lyapunov vector projections onto various subspaces now display the expected symmetries not present in the Gram-Schmidt approach.

In Chapter 3, the algorithm was first applied to a smooth-hard-disk system. We are especially interested in a comparison of the different properties associated with the Gram-Schmidt Lyapunov vectors and the covariant Lyapunov vectors, namely, the Lyapunov modes, the “localization width” [43], and the orientation in tangent space of the stable and the unstable directions [44]. Furthermore for the same kind of model, in Chapter 7 we investigated the convergence of the Lyapunov spectrum, considering computations at different time scales. In particular, we observe a strong dependence of the transversality property between covariant Lyapunov vectors (i.e. angles between covariant vectors) on the position of their associated exponents in the Lyapunov spectrum.

In Chapter 4 we study the covariant vectors for the simple Lorentz gas [45]. This model is simpler than the modified version introduced in Chapter 2 insofar as the scatterer disks do not rotate on their location in the lattice, and only a single point particle is followed in time and is elastically scattered off the disks. Periodic boundary conditions are applied. It is interesting to note that Fourier’s law of heat conduction for the simple periodic Lorentz gas was found to hold by D. Alonso *et al.* [46]. This, however, was contested by A. Dhar and D. Dhar [47], who assert that the standard Lorentz gas does not develop local thermal equilibrium (even in the limit of large system size) due to the existence of an infinity of local conservation laws. As a consequence, Fourier’s law would not exist. We did not study this particular point in further detail. Such simple billiards have been the subject of many studies in chaos theory (e.g. the Sinai billiard [48]). Dellago *et al.* were the first to study the Lyapunov exponents for this model [49]. We investigated the orientation of the covariant vectors and found a characteristic symmetry for some projections of these vectors as well as a strong hyperbolicity (i.e. the stable and the unstable directions are everywhere transversal to each other) in accordance with theoretical

considerations [5].

The covariant Lyapunov vectors are a new tool of dynamical system theory, which offers further insight concerning the intricate structure of the phase space of equilibrium systems. Its application to non-equilibrium systems is the topic of Chapters 5 and 6, where we investigate the time-reversibility of the covariant Lyapunov vectors for simple particle models in and out of thermal equilibrium, with particular attention given to the local Lyapunov exponents.

Finally, Chap. 8 is devoted to the rough-hard-disk gas [50], where we prove that the rotations break the Hamiltonian character of this model.

## How collisions affect the tangent bundle

Lyapunov exponents were originally defined only for linear systems [51]. In nonlinear systems they are introduced via a linearization about the bundle trajectory. Benettin *et al.* [37, 38] derived an algorithm for computing the full Lyapunov spectra for smooth dynamical systems, which became the standard approach. These authors follow the time evolution of the reference trajectory and of a complete set of perturbation vectors by solving the corresponding linearized equations of motion. Dellago *et al.* [21] introduced a generalization for rigid-body systems, where the time-continuous streaming is interrupted by particle collisions. Here, we review this approach since it forms the basis of our numerical work with hard particle systems in the following chapters.

For a system with instantaneous collisions, the initial phase point  $\mathbf{\Gamma}(0)$  is transformed to a final phase point  $\mathbf{\Gamma}(\tau)$ , at a later time  $\tau$ , via successive periods of time-continuous streaming (free flight in the simplest case) interrupted by instantaneous collision events. The latter consist of an instantaneous collision map  $\mathcal{M}$  connecting the phase point immediately before the collision to that immediately after the collision. The streaming consists of a smooth flow determined by the equation of motion

$$\dot{\mathbf{\Gamma}} = \mathcal{F}(\mathbf{\Gamma}) . \quad (1)$$

An infinitesimal perturbation vector  $\delta\mathbf{\Gamma}$  connects the reference trajectory in the phase space,  $\mathbf{\Gamma}$ , to a slightly shifted satellite trajectory,

$$^{(S)}\mathbf{\Gamma} = \mathbf{\Gamma} + \delta\mathbf{\Gamma} . \quad (2)$$

Between two successive collisions, the time evolution of the perturbation vector is obtained by

linearizing Eq. (1),

$$\delta\dot{\mathbf{\Gamma}} = \mathcal{D}_{\mathbf{\Gamma}} \delta\mathbf{\Gamma} + \mathcal{O}(\delta\mathbf{\Gamma})^2, \quad (3)$$

where  $\mathcal{D}_{\mathbf{\Gamma}} \equiv \partial\mathcal{F}/\partial\mathbf{\Gamma}$  is the Jacobi matrix for the smooth flow.

Let us consider the instantaneous time  $\tau_c$ , at which a collision takes place for the reference trajectory. For the satellite trajectory, the associated collision takes place at the instant  $\tau_c + \delta\tau_c$ , which may be earlier or later ( $\delta\tau_c \geq 0$  or  $\delta\tau_c \leq 0$ ),

$$\mathbf{\Gamma}'_{\tau_c} = \mathcal{M}(\mathbf{\Gamma}_{\tau_c}), \quad (4)$$

$${}^{(S)}\mathbf{\Gamma}'_{\tau_c + \delta\tau_c} = \mathcal{M}\left({}^{(S)}\mathbf{\Gamma}_{\tau_c + \delta\tau_c}\right). \quad (5)$$

In the following, the unprimed quantities ( $\mathbf{\Gamma}$  and  $\delta\mathbf{\Gamma}$ ) refer to the states immediately before the collision event, whereas the primed quantities refer to the states immediately after. Since  $\delta\tau_c$  is proportional to components of  $\delta\mathbf{\Gamma}$ , a first-order time approximation is tantamount to a first-order perturbation-vector approximation: the terms  $(\delta\tau_c)^2$ ,  $(\delta\mathbf{\Gamma})^2$ , and  $(\delta\mathbf{\Gamma} \delta\tau_c)$  (as well as the higher order terms) are discarded.

Connecting Eqs. (2) and (5) yields

$$\mathbf{\Gamma}'_{\tau_c + \delta\tau_c} + \delta\mathbf{\Gamma}'_{\tau_c + \delta\tau_c} = \mathcal{M}(\mathbf{\Gamma}_{\tau_c + \delta\tau_c} + \delta\mathbf{\Gamma}_{\tau_c + \delta\tau_c}). \quad (6)$$

For the phase point, the time linearization of Eq. (1) directly suggests that

$$\mathbf{\Gamma}_{\tau_c + \delta\tau_c} = \mathbf{\Gamma}_{\tau_c} + \mathcal{F}(\mathbf{\Gamma}_{\tau_c}) \delta\tau_c + \mathcal{O}(\delta\tau_c)^2 \quad \text{and} \quad \mathbf{\Gamma}'_{\tau_c + \delta\tau_c} = \mathbf{\Gamma}'_{\tau_c} + \mathcal{F}(\mathbf{\Gamma}'_{\tau_c}) \delta\tau_c + \mathcal{O}(\delta\tau_c)^2. \quad (7)$$

For the perturbation vector  $\delta\mathbf{\Gamma}$ , the time linearization of Eq. (3) yields

$$\delta\mathbf{\Gamma}_{\tau_c + \delta\tau_c} = \delta\mathbf{\Gamma}_{\tau_c} + (\mathcal{D}_{\mathbf{\Gamma}_{\tau_c}} \delta\mathbf{\Gamma}_{\tau_c}) \delta\tau_c + \mathcal{O}(\delta\tau_c)^2 + \mathcal{O}(\delta\mathbf{\Gamma}_{\tau_c})^2. \quad (8)$$

Considering an arbitrary infinitesimal perturbation vector  $\delta\mathbf{\Gamma}$  corresponding to the phase point  $\mathbf{\Gamma}$ , the linearization of the transformation map  $\mathcal{M}$  is expressed as

$$\mathcal{M}(\mathbf{\Gamma} + \delta\mathbf{\Gamma}) = \mathcal{M}(\mathbf{\Gamma}) + \mathcal{L}_{\mathbf{\Gamma}} \delta\mathbf{\Gamma} + \mathcal{O}(\delta\mathbf{\Gamma})^2, \quad (9)$$

where  $\mathcal{L}_{\mathbf{\Gamma}} \equiv \partial\mathcal{M}/\partial\mathbf{\Gamma}$  is the Jacobi matrix for the collision map. According to Eq. (6) and the

linear time approximations (7) and (8), one has

$$\begin{aligned} \mathbf{\Gamma}'_{\tau_c} + \mathcal{F}(\mathbf{\Gamma}'_{\tau_c}) \delta\tau_c + \delta\mathbf{\Gamma}'_{\tau_c+\delta\tau_c} = & \mathcal{M}\left(\mathbf{\Gamma}_{\tau_c} + \delta\mathbf{\Gamma}_{\tau_c} + \mathcal{F}(\mathbf{\Gamma}_{\tau_c}) \delta\tau_c + \mathcal{D}_{\mathbf{\Gamma}_{\tau_c}} \delta\mathbf{\Gamma}_{\tau_c} \delta\tau_c\right) \\ & + \mathcal{O}(\delta\tau_c)^2 + \mathcal{O}(\delta\mathbf{\Gamma}_{\tau_c})^2 . \end{aligned} \quad (10)$$

Using Eqs. (4) and (9) in Eq. (10), we can finally write the first-order approximation of the perturbation vector immediately after a collision event,  $\delta\mathbf{\Gamma}'_{\tau_c+\delta\tau_c}$ , as a function of  $\mathbf{\Gamma}_{\tau_c}$ ,  $\delta\mathbf{\Gamma}_{\tau_c}$ , and  $\delta\tau_c$ :

$$\begin{aligned} \delta\mathbf{\Gamma}'_{\tau_c+\delta\tau_c} = & \mathcal{L}_{\mathbf{\Gamma}_{\tau_c}} \delta\mathbf{\Gamma}_{\tau_c} + [\mathcal{L}_{\mathbf{\Gamma}_{\tau_c}} \mathcal{F}(\mathbf{\Gamma}_{\tau_c}) - \mathcal{F} \circ \mathcal{M}(\mathbf{\Gamma}_{\tau_c})] \delta\tau_c \\ & + \mathcal{O}(\delta\tau_c)^2 + \mathcal{O}(\delta\mathbf{\Gamma}_{\tau_c})^2 + \mathcal{O}(\delta\mathbf{\Gamma}_{\tau_c} \delta\tau_c) . \end{aligned} \quad (11)$$

In general, the state vector  $\mathbf{\Gamma} = \{\vec{q}_i, \vec{p}_i\}_{i=1}^N$  contains spatial and momentum components  $\{\vec{q}_i\}_{i=1}^N$  and  $\{\vec{p}_i\}_{i=1}^N$ , respectively, and so does the perturbation vector  $\delta\mathbf{\Gamma} = \{\delta\vec{q}_i, \delta\vec{p}_i\}_{i=1}^N$ . If a collision between the particles  $k$  and  $\ell$  takes place, then the infinitesimal time delay  $\delta\tau_c$  is given by

$$\delta\tau_c = - \frac{(\delta\vec{q}_k - \delta\vec{q}_\ell) \cdot \vec{n}}{\left(\frac{\vec{p}_k}{m_k} - \frac{\vec{p}_\ell}{m_\ell}\right) \cdot \vec{n}} ,$$

where  $\vec{n}$  is a unit vector normal to the collision surface at the collision point, and  $m_i$  is the mass of the  $i$ -th particle. The transformation (11) is completely general [21] and forms the basis for the algorithms used in this thesis.

## References

- [1] L. Boltzmann, “Vorlesungen ueber Gastheorie” (J.A. Barth, Leipzig, 1896 (Part I) and 1898 (Part II)); “Lectures on Gas Theory”, translated by G. Brush, U. of California press (1964).
- [2] L. Boltzmann, Sitzungsberichte der k. Akad. der Wiss., Wien, **vol. 75**, 62 (1877).
- [3] L. Boltzmann, *Journal fuer die reine und angewandte Mathematik* (Crelles Journal), **vol. 98**, 68 (1884); also in Wiener Berichte **89**, 714 (1884).
- [4] J.W. Gibbs, *Elementary Principles in Statistical Mechanics* (Yale University Press, New Haven, 1902).
- [5] D. Szász (editor), *Hard Ball Systems and the Lorentz Gas*, Encyclopedia of Mathematical Sciences **vol. 101** (Springer-Verlag, Berlin, 2000).

- [6] D. Szasz, private communication.
- [7] S. Chapman and T.G. Cowling, *The Mathematical Theory of Non-Uniform Gases* (Cambridge University Press, New York, 3rd ed., 1990).
- [8] B.L. Holian, Wm.G. Hoover, and H.A. Posch, Phys. Rev. Lett. **59**, 10 (1987).
- [9] H.A. Posch and Wm.G. Hoover, Phys. Rev. A **38**, 473 (1988).
- [10] Wm.G. Hoover, *Time reversibility, computer simulation, and chaos* (World Scientific, Singapore, 1999).
- [11] D. Ruelle, J. Stat. Phys. **95**, 393 (1999).
- [12] Ch. Dellago and H.A. Posch, "Realizing Boltzmann's dream: computer simulations in modern statistical mechanics", in *Boltzmann's Legacy*, edited by G. Gallavotti, W.L. Reiter, and J. Yngvason, European Math. Society Publishing House (2008); ISBN 978-3-03719-057-9.
- [13] N.S. Krylov, in *Works in the Foundation of Statistical Mechanics*, edited by A.S. Wightman and P.A. Anderson (Princeton University Press, Princeton, 1979) p.239; Appendix by Y.G. Sinai.
- [14] V.I. Oseledec, Trudy Moskov. Mat. Obsc. **19**, 179 (1968). English transl. Trans. Moscow Math. Soc. **19**, 197 (1968).
- [15] D. Ruelle, Publ. Math. de l'IHÉS **50**, 27 (1979).
- [16] E. Ott, *Chaos in Dynamical Systems* (Cambridge University Press, New York, 3rd ed., 1993).
- [17] K.T. Alligood, T.D. Sauer, and J.A. Yorke, *Chaos: an introduction to dynamical systems* (Springer-Verlag, New York, 1996).
- [18] B. Legras and R. Vautard, Proceedings of the Seminar on Predictability, ECWF Seminar **vol. 1**, edited by T. Palmer (EC MWF Reading, UK, 1996) p 1.
- [19] R. Livi, A. Politi, and S. Ruffo, J. Phys. A **19**, 2033 (1986).
- [20] Wm.G. Hoover and H.A. Posch Phys. Rev. E **51**, 273 (1995).
- [21] Ch. Dellago, H.A. Posch, and Wm.G. Hoover, Phys. Rev. E **53**, 1485 (1996).
- [22] Ch. Dellago and H.A. Posch, Physica A **240**, 68 (1997).
- [23] Lj. Milanović, H.A. Posch, and Wm.G. Hoover, Molec. Phys. **95**, 281 (1998).

- [24] Y.G. Sinai, International Journal of Bifurcation and Chaos **6**, 1137 (1996).
- [25] D.J. Evans, E.G.D. Cohen, and G.P. Morriss, Phys. Rev. A **42** 5990 (1990).
- [26] C. Mejía-Monasterio, H. Larralde, and F. Leyvraz, Phys. Rev. Lett. **86**, 5417 (2001).
- [27] H. Larralde, F. Leyvraz, and C. Mejía-Monasterio, J. Stat. Phys. **113**, 197 (2003).
- [28] D. Gass, J. Chem. Phys. **54**, 1898 (1971).
- [29] D. Risso and P. Cordero, J. Stat. Phys. **82**, 1453 (1995).
- [30] Ch. Forster, R. Hirschl, H.A. Posch, and Wm.G. Hoover, Physica D **187**, 294 (2004).
- [31] Lj. Milanovic and H.A. Posch, J. Mol. Liquids **96 - 97**, 221 (2002).
- [32] H.A. Posch and R. Hirschl, in *Hard Ball Systems and the Lorentz Gas*, Encyclopedia of Mathematical Sciences **vol. 101**, edited by D. Szász (Springer-Verlag, Berlin, 2000) p. 269.
- [33] J.P. Eckmann and O. Gat, J. Stat. Phys. **98**, 775 (2000).
- [34] S. McNamara and M. Mareschal, Phys. Rev. E **64**, 051103 (2001).
- [35] T. Taniguchi and G.P. Morriss, Phys. Rev. E **65**, 056202 (2002).
- [36] J.P. Eckmann, Ch. Forster, H.A. Posch, and E. Zabey, J. Stat. Phys. **118**, 813 (2005).
- [37] G. Benettin, L. Galgani, A. Giorgilli, and J.M. Strelcyn, *Part I: Theory*, Meccanica **15**, 9 (1980).
- [38] G. Benettin, L. Galgani, A. Giorgilli, and J.M. Strelcyn, *Part II: Numerical application*, Meccanica **15**, 9 (1980).
- [39] I. Shimada and T. Nagashima, Prog. Theor. Phys. **61**, 1605 (1979).
- [40] G. Gallavotti and E.G.D. Cohen, Phys. Rev. Lett. **74**, 2694 (1995).
- [41] F. Ginelli, P. Poggi, A. Turchi, H. Chat, R. Livi, and A. Politi, Phys. Rev. Lett. **99**, 130601 (2007).
- [42] M. Hénon, Comm. Math. Phys. **50**, 69 (1976).
- [43] T. Taniguchi and G.P. Morriss, Phys. Rev. E **68**, 046203 (2003).
- [44] J. Bochi and M. Viana, Ann. I. H. Poincaré **19**, 1 (2002).
- [45] K. Pearson, *The Life, Letters and Labours of Francis Galton* **vol. 3** (Cambridge University Press, 1930).

- [46] D. Alonso, R. Artuso, G. Casati, and I. Guarneri, Phys. Rev. Lett. **82**, 1859 (1999).
- [47] A. Dhar and D. Dhar, Phys. Rev. Lett. **82**, 480 (1999).
- [48] Y.G. Sinai, Russian Math. Surveys **25**, 137 (1970).
- [49] Ch. Dellago and H.A. Posch, Phys. Rev. E **52**, 2401 (1995).
- [50] J.A. van Meel and H.A. Posch, Phys. Rev. E **80**, 016206 (2009).
- [51] A. Lyapunov, Annales de la faculté des sciences de Toulouse **vol. 9** (1907) p. 203.



## Part I

# Transport phenomena and Lyapunov instability

### Contents

1	The van Beijeren thermostat and a simple application	15
2	Thermostated modified Lorentz Gas	31



# CHAPTER 1

## The van Beijeren thermostat and a simple application to a planar smooth-hard-disk system

### Contents

---

1.1	Introduction . . . . .	15
1.2	The van Beijeren thermostat . . . . .	17
1.3	Planar gas of hard disks . . . . .	22
1.4	Temperature and density profiles . . . . .	25
1.5	Heat conduction . . . . .	27
1.6	Summary . . . . .	29
	References . . . . .	29

---

### 1.1 Introduction

Let us consider two initial ( $t = 0$ ) phase points infinitesimally close to each other. For chaotic systems these two points can either (exponentially) converge or diverge during the time evolution (for  $t > 0$ ). According to the Oseledec theorem [1], this unpredictable behavior of the systems for long times is revealed by the so-called Lyapunov exponents  $\{\lambda_i; i = 1, \dots, D\}$ . Here  $D$  is the phase-space dimension. The ordered set of Lyapunov exponents,  $\lambda_1 \geq \dots \geq \lambda_D$ , is referred to as Lyapunov spectrum, which gives rise, in particular, to a hierarchical arrangement of the phase-space directions. For equilibrium systems, an arbitrary  $D$ -dimensional small region surrounding the phase point does not change its volume during the dynamics, even though it will undergo deformations. For stationary non-equilibrium systems thermostated with a dynamical thermo-

stat, however, the phase volume decreases. In this case, the sum of all Lyapunov exponents is negative and the phase space distribution collapses onto a multifractal strange attractor [2]. Its fractal dimension can be calculated according to Kaplan and Yorke [3, 4] as

$$D_{KY} = d + \frac{\sum_{i=1}^d \lambda_i}{|\lambda_{d+1}|} ,$$

where  $d$  is the largest integer satisfying  $\sum_{i=1}^d \lambda_i \geq 0$ .  $D_{KY}$  provides a good estimate of the information dimension  $D_1$  of the multifractal attractors.

We are interested to drive gaseous systems away from equilibrium by setting two opposite thermostat walls to different temperatures  $T_1$  and  $T_2$ . As a consequence, the phase volume of such systems decreases due to the collisions of the particles with the thermostats. One might think of using a stochastic thermostat for that purpose. However, for such a thermostat one cannot unambiguously construct the time evolution (deformation) of a phase-volume element  $\delta\mathcal{V}$  due to a particle-thermostat wall collision. During such a collision the exchanged heat  $\Delta Q$  is related to the change of an infinitesimal phase volume element  $\delta\mathcal{V}$  by:

$$\delta\mathcal{V}' = \delta\mathcal{V} \exp\left(\frac{\Delta Q}{k_B T}\right) ,$$

where the prime superscript refers to the time immediately after the instantaneous collision, and the absence of the superscript refers to the time immediately before. Here,  $k_B$  is the Boltzmann's constant and  $T$  is the thermostat temperature. In one dimensional systems, this equation suffices to construct the Lyapunov vectors immediately after the collision without additional assumptions [5]. In two or three physical dimensions, this is not possible.

Hoover and Evans were the first to make use of deterministic thermostats in molecular dynamics simulations, by introducing a damping term in the equations of motion, which is automatically adjusted to keep the kinetic energy [6] or the internal energy [7] exactly constant. This scheme is based on Gauss' principle of least constraint and is referred to as Gauss' isokinetic or isoenergetic thermostat. For equilibrium systems, it generates trajectories consistent with an ensemble intermediate between the microcanonical (for the kinetic energy) and canonical (for the potential energy) ensemble, respectively. However, the thermostat receiving the largest attention is the Nosé-Hoover thermostat [8, 9]. This class of deterministic thermostats preserves the Hamiltonian structure of the system in a suitably enlarged phase space [10]. In equilibrium it is capable to generate trajectories consistent with a canonical ensemble [11].

Our aim is to conceive deterministic thermostat walls, that generate a non-trivial map relating the pre-collision momentum of a particle to its post-collision momentum in a deterministic time-

reversible way. They should act through the collisions at the boundary and should not affect the equations of motion of the particles once they leave the vicinity of the thermostat wall. Furthermore, the detailed balance condition should be obeyed.

One of the first thermostats of this type was introduced by Chernov and Lebowitz [2, 12], and was applied to study planar Couette flow of hard disks. Energy-preserving reflection rules of a particle reflected by the thermostat wall, which simultaneously drive the system out of equilibrium into a stationary non-equilibrium state, allow the computation of the full Lyapunov spectrum of such systems [13]. Interestingly, the conjugate pairing rule is not obeyed here due to the inhomogeneous nature of the thermostat.

Here, we implement another algorithm that is based on the Boltzmann equation and which was invented by van Beijeren [14]. The thermostat consists of a map converting pre-collisional momenta,  $\vec{p}$ , into post-collisional momenta,  $\vec{p}'$ , with detailed balance conditions fulfilled. In Sec. 1.2, the implementation of this deterministic thermostat is explicitly shown for the phase-space dynamics as well as for the tangent bundle. The two momenta cannot always be related by an elementary analytical function. In such a case,  $\vec{p}'$  is numerically obtained by solving a transcendental equation with an efficient Newton-Raphson method. For very small/large particle speeds allowed by the Maxwell-Boltzmann distribution a simplified treatment is used. In such a case the thermostat action is computed from an empirical analytical function.

The thermostat is introduced in Sec. 1.2, where the relation between the incoming and outgoing momenta is determined. In Sec. 1.3 two such thermostats with different temperature  $T_1$  and  $T_2$  are applied to a planar gas of smooth hard disks, and the heat flux and other chaos relevant quantities (based on the Lyapunov spectra) are computed. The temperature and density profiles are the topic of Sect 1.4. In Sec. 1.5, the heat conductivity, which is the only transport coefficient relevant in this case, is determined experimentally, using Fourier's law of heat conduction. It is compared to the theoretical value obtained from the Enskog theory [15, 12]. Good agreement is found for the present model. For a short remark concerning the existence of the heat conductivity for this model we refer to the Outlook at the end of this thesis.

## 1.2 The van Beijeren thermostat

The kinetic theory of gases, which attempts to explain the macroscopic behavior of a gas by considering the motion of molecules, frequently uses the distribution function  $f(\vec{q}, \vec{v}, t)$  in the single-particle phase space. It allows, in particular, to give a microscopic interpretation of thermodynamic quantities. The distribution function gives the probability of a particle to be in an

infinitesimal volume element about the position  $\vec{q}$  and with a velocity included in the range  $[\vec{v}, \vec{v} + d\vec{v}]$ .

### 1.2.1 Collision map and kinetic theory

The van Beijeren thermostat [14] is a non-trivial time-reversible map of the incoming velocity  $\vec{v}$  of a particle, hitting the thermostat wall, onto an outgoing velocity  $\vec{v}'$ , where it is assumed that at the thermostat boundary  $\vec{v}$  and  $\vec{v}'$  are distributed according to the equilibrium Maxwell-Boltzmann distribution for the thermostat temperature  $T$ .

i) Let us consider the simplest case first, where only the velocity component normal to the thermostat surface is thermostated, whereas the parallel component (in  $\mathbb{R}^2$  or  $\mathbb{R}^3$ ) is not affected. If  $\vec{n}$  denotes a normal unit vector at the collision point  $\vec{q}_{\text{w}}$  on the surface, the incoming and the outgoing normal velocities are given by  $v_n = \vec{v} \cdot \vec{n}$  and  $v'_n = \vec{v}' \cdot \vec{n}$ , respectively, where  $v_n < 0$  and  $v'_n > 0$ . At the surface, the probability distribution in the one-particle phase space obeys the kinetic equation

$$\frac{\partial f}{\partial t} \propto -v_n \delta(\vec{q} - \vec{q}_{\text{w}}) f(v_n) dv_n - v'_n \delta(\vec{q} - \vec{q}_{\text{w}}) f(v'_n) dv'_n , \quad (1.1)$$

where the first term on the right-hand side is the loss term (negative, due to the probability flow into the thermostat), and the second term is the gain term (positive, due to the probability flow back into the system). In the stationary state, the detailed balance equation becomes

$$-v'_n f(v'_n) dv'_n = v_n f(v_n) dv_n > 0 .$$

Insertion of the equilibrium distribution and using the notation

$$X = \sqrt{\frac{m}{2k_B T}} v_n , \quad X' = \sqrt{\frac{m}{2k_B T}} v'_n ,$$

gives

$$X' e^{-X'^2} dX' = -X e^{-X^2} dX ,$$

which may be readily integrated to give

$$e^{-X'^2} = C - e^{-X^2} .$$

The integration constant  $C = 1$  is fixed by requiring, that the map  $v'_n = g(v_n)$  maps the positive real line onto itself, such that  $v_n = 0$  is mapped into  $v'_n \rightarrow \infty$  and  $v_n \rightarrow \infty$  is mapped into

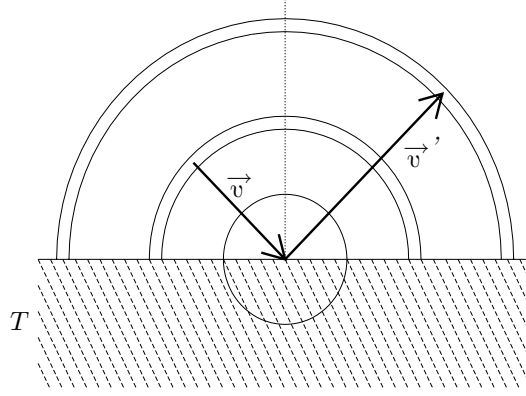


**Figure 1.1 :** Deterministic transformation of the disk's velocity at the collision with the thermostat wall (which is at a temperature  $T$ ). Here,  $\|\vec{v}\|$  and  $\|\vec{v}'\|$ , the absolute values of the velocities immediately before and after the collision, respect the Maxwell-Boltzmann distribution.

$v'_n = 0$ . The thermostat map thus becomes

$$X' = \sqrt{-\ln(1 - e^{-X^2})} .$$

This map is monotonous,  $dv'_n/dv_n < 0$ , and reversible,  $g(v'_n) = g(g(v_n)) = v_n$ .

ii) Of more interest for this thesis is the case in  $\mathbb{R}^2$  of disks colliding with a thermostat wall, such that the outgoing velocity direction is the same as for an elastic collision, but the speed is changed according to  $v' = g(v)$ . As before,  $v = \|\vec{v}\|$  and  $v' = \|\vec{v}'\|$  are the absolute values of the incoming and outgoing velocities, respectively. The kinetic equation analogous to Eq. (1.1) becomes

$$\frac{\partial f}{\partial t} \propto -v \delta(\vec{q} - \vec{q}_w) f(v) dv - v' \delta(\vec{q} - \vec{q}_w) f(v') dv'$$

(see Fig. 1.1). The Maxwell-Boltzmann distribution for  $v$  now becomes

$$f(v) = \frac{m}{k_B T} v e^{-mv^2/2k_B T} ,$$

and similarly for  $v'$ . Using the abbreviations

$$X = \sqrt{\frac{m}{2k_B T}} v , \quad X' = \sqrt{\frac{m}{2k_B T}} v' ,$$

the detailed balance condition now becomes

$$X'^2 dX' e^{-X'^2} = -X^2 dX e^{-X^2} ,$$

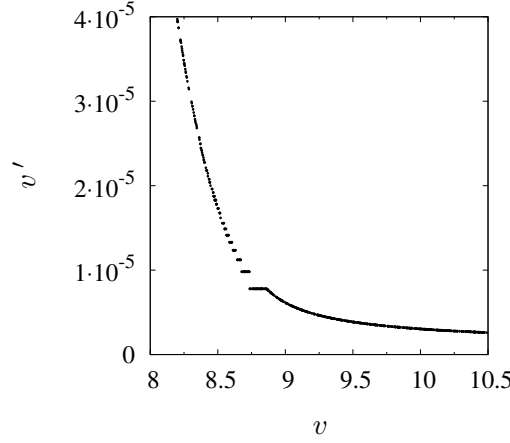


**Figure 1.2 :**  $v'$  versus  $v$  for small values of  $v'$ . One observes the empirical extension for  $v > d_2 \approx 8.86$  (see note \*).

which is integrated to give

$$X' e^{-X'^2} - \frac{\sqrt{\pi}}{2} \operatorname{erf}(X') = C - X e^{-X^2} + \frac{\sqrt{\pi}}{2} \operatorname{erf}(X) . \quad (1.2)$$

As before, the integration constant,  $C = \sqrt{\pi}/2$ , is determined by requiring the map  $v' = g(v)$  to map 0 into  $\infty$  and *vice versa* (Fig. 1.2 shows the form of  $v' = g(v)$  for small values of  $v'$ ). For given  $X$ , there is no analytic expression for  $X'$ . However, Eq. (1.2), can be easily solved by fast iteration routines \*. The thermostat action thus consists in multiplying the elastically reflected particle velocity by a factor  $v'/v = g(v)/v$ . Furthermore, from Eq. (1.2) we have

$$\frac{dv'}{dv} = -\frac{v^2}{v'^2} e^{-m(v^2 - v'^2)/2k_B T} < 0 . \quad (1.3)$$

This procedure is used below.

---

\***Remark concerning the case in  $\mathbb{R}^2$ :** We use the Newton-Raphson method [16] to solve Eq. (1.2) numerically for the outgoing speed  $v'$ , as long as the incoming speed  $v$  is within the interval  $[d_1, d_2]$ :

$$\begin{aligned} d_1 &= \sqrt{\frac{k_B T}{m}} \quad 7.786074 \cdot 10^{-6} , \\ d_2 &= \sqrt{\frac{k_B T}{m}} \quad 8.861285 . \end{aligned}$$

Outside of this interval we use the following empirical function (Fig. 1.2)

$$\begin{aligned} v' &= \frac{d_1}{v - d_2 + 1} & \text{if } v > d_2 , \\ v' &= \frac{d_1}{v} + d_2 - 1 & \text{if } v < d_1 , \end{aligned}$$

which provides a smooth extrapolation to very small/large speeds. Fig. 1.2 shows a plot of the outgoing  $v'$  as a function of the incoming  $v$  for a gas of density  $\rho = 0.6$  composed of  $N = 40$  hard disks moving in a box with an aspect ratio  $A = 0.4$ . The thermostat temperature  $T = 1$ .



iii) For completeness, we also mention the case in  $\mathbb{R}^3$  of a sphere colliding with a thermostat plane. With the same notation as before, the Maxwell-Boltzmann distribution in three dimensions is

$$f(v) = \left( \frac{m}{k_B T} \right)^{\frac{3}{2}} v^2 e^{-mv^2/2k_B T} ,$$

and the detailed balance condition becomes

$$X'^3 dX' e^{-X'^2} = -X^3 dX e^{-X^2} .$$

Integration gives

$$(1 + X'^2) e^{-X'^2} = C - (1 + X^2) e^{-X^2} ,$$

where the integration constant  $C = 1$  follows as before.

### 1.2.2 Phase-space dynamics and tangent bundle

Now we turn to the thermostat action on the trajectory in the phase space as well as on the tangent bundle. The state of the system is given by the coordinates and momenta of all the particles,

$$\mathbf{\Gamma} = \{\vec{q}_n, \vec{p}_n; n = 1, \dots, N\}.$$

Similarly, any perturbation vector  $\delta\mathbf{\Gamma}$  consists of the respective coordinate and momentum perturbations,

$$\delta\mathbf{\Gamma} = \{\delta\vec{q}_n, \delta\vec{p}_n; n = 1, \dots, N\}. \quad (1.4)$$

Let us consider the collision event of an arbitrary particle  $k$  with a thermostat wall. Only the components  $\vec{q}_k$  and  $\vec{p}_k$  of the state vector and of the perturbation vector – pertaining to the particle  $k$  – undergo changes during the collision event. According to Sec. 1.2, one has

$$\vec{q}'_k = \vec{q}_k , \quad (1.5)$$

$$\vec{p}'_k = \frac{g(\|\vec{p}_k\|)}{\|\vec{p}_k\|} (\vec{p}_k - 2(\vec{p}_k \cdot \vec{n})\vec{n}) , \quad (1.6)$$

where  $\vec{n}$  is the unit vector perpendicular to the thermostat wall at the collision point and  $g(\|\vec{p}_k\|) / \|\vec{p}_k\|$  is the thermostat factor introduced in the previous section. As usual, the mass  $m$  is unity in our reduced units. Linearizing Eqs. (1.5) and (1.6) (following Dellago *et al.* [17] as mentioned in the Introduction, see p. 7) we find for the components of the perturbation vector

after the thermostat-wall collision

$$\begin{aligned}\delta\vec{q}'_k &= \delta\vec{q}_k - (\vec{p}'_k - \vec{p}_k)\delta\tau_c, \\ \delta\vec{p}'_k &= \left(\frac{\partial\vec{p}'_k}{\partial\vec{p}_k}\right)\delta\vec{p}_k,\end{aligned}$$

where

$$\delta\tau_c = -\frac{(\delta\vec{q}_k \cdot \vec{n})}{(\vec{p}_k/m \cdot \vec{n})}$$

is the (positive or negative) delay time between the reference trajectory and the (infinitesimally) perturbed trajectory of the collision. From now on we omit the particle index  $k$  to simplify the notation. The  $2 \times 2$  Jacobian matrix  $(\partial\vec{p}'/\partial\vec{p})$  is found from Eq. (1.6),

$$\frac{\partial\vec{p}'}{\partial\vec{p}} = \begin{pmatrix} -\frac{p'}{p} - \frac{p_x^2}{p} \frac{\partial}{\partial p} \left(\frac{p'}{p}\right) & -\frac{p_x p_y}{p} \frac{\partial}{\partial p} \left(\frac{p'}{p}\right) \\ \frac{p_x p_y}{p} \frac{\partial}{\partial p} \left(\frac{p'}{p}\right) & \frac{p'}{p} + \frac{p_y^2}{p} \frac{\partial}{\partial p} \left(\frac{p'}{p}\right) \end{pmatrix},$$

where, as before,  $p$  and  $p'$  are the absolute particle momenta before and after the wall collision. According to Eq. (1.3), one has

$$\frac{\partial}{\partial p} \left(\frac{p'}{p}\right) = -\frac{p'}{p^2} - \frac{p}{p'^2} \exp\left(-\frac{p^2 - p'^2}{2mk_B T}\right).$$

Considering the thermostat-particle collision maps, as well as the inter-particle collision maps and the free-flight maps (between the successive collisions), which all affect the time evolution of the perturbation-vector set  $\{\delta\mathbf{\Gamma}_i, i = 1, \dots, D\}$ , the full Lyapunov spectrum can be computed.

### 1.3 Planar gas of hard disks

To test the behavior of the two-dimensional deterministic van Beijeren thermostat, we use a simple two-dimensional gas. It consists of  $N$  (smooth) hard disks, where the inter-particle collisions are considered elastic (without roughness). The gas is confined to a rectangular box of dimension  $(L_x, L_y)$ . The vertical box boundaries are two thermostats at two different temperatures,  $T_1$  on the left-hand side, and  $T_2 = T_1 + \Delta T$  on the right-hand side. Periodic boundary conditions are used in the  $y$ -direction. By definition, the thermostat on the right hand side has the higher temperature. We stipulate that a disk hits a thermostat when its centre does. We consider reduced units for which the particle diameter  $\sigma$  and the particle mass  $m$  are unity.

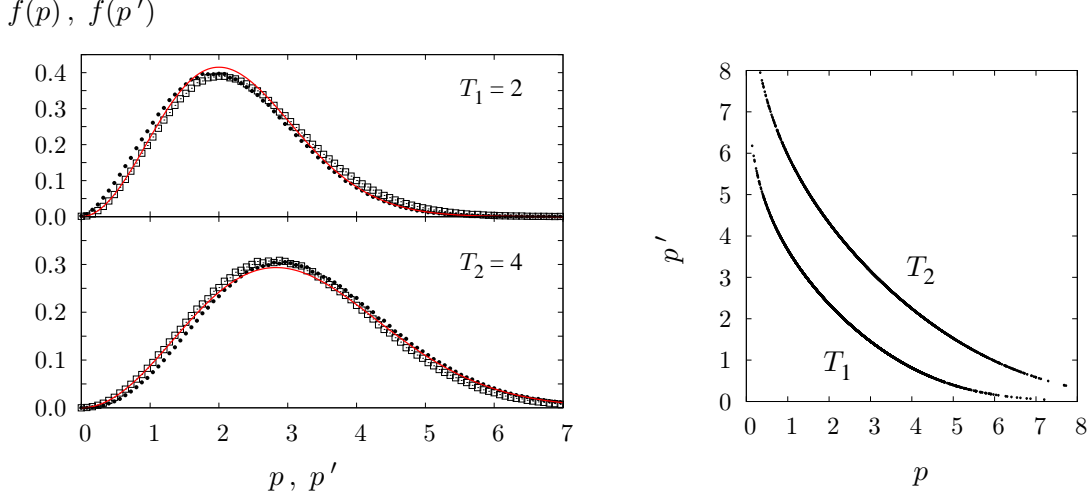


**Figure 1.3 :** We consider a system of  $N = 80$  disks moving in a rectangular box with an aspect ratio  $A = 0.2$ , and a number density  $\rho = 0.4$ . Left panel: momentum distribution  $f(p)$  for both thermostat walls (whose respective temperatures are  $T_1 = 2$  and  $T_2 = 4$ ). The empty squares correspond to the incoming particles and the full circles to the outgoing ones. The red solid lines give the theoretical two-dimensional Maxwell-Boltzmann distribution. Right panel: plot of the map  $p' = g(p)$  of the outgoing particle for the two thermostats.

Lyapunov exponents are given in units of  $\sqrt{\langle K \rangle / (Nm\sigma^2)}$ . Here,  $\langle K \rangle$  is the time-averaged kinetic energy. Our standard system consists of  $N = 80$  particles enclosed in a box, with an aspect-ratio of  $A \equiv L_y/L_x = 0.2$ , for which we consider three different possible area densities  $\rho \equiv (N\pi\sigma^2)/(4V) = \{0.1, 0.4, 0.7\}$ , where  $V \equiv L_x L_y$  is the volume of the simulation box. Note that  $\rho$  differs from the number density by a factor of  $\pi\sigma^2/4$ .

The left panel of Fig. 1.3 shows the incoming and the outgoing Maxwell-Boltzmann momentum distributions of the particles, which collide with the hot and the cold thermostat for a system with a density  $\rho = 0.4$  and with the nominal thermostat temperatures  $T_1 = 2$  and  $T_2 = 4$ . They are close to the theoretical two-dimensional Maxwell-Boltzmann distributions (smooth lines in red). Moreover, as could be expected, the mean value of the post-collision distribution is slightly shifted towards smaller (higher) speeds compared to the pre-collision distribution for the cold (hot) thermostat.

In the right panel, the outgoing momentum  $p'$  is plotted as a function of the incoming momentum  $p$ . This graph illustrates the bijective and symmetric behavior with respect to the first bisectrix of the map  $p' = g(p)$ .

Next, we compute the heat flux  $J$  generated by  $\Delta T > 0$ .  $J$  is determined from the energy per unit time transferred from the hot thermostat into the gas, as well as, from the heat per unit time extracted by the cold thermostat. Due to stationarity, the heat flux does not depend on the position in the box, which was verified experimentally. Fig. 1.4 shows the heat flux  $J$  as a function of the temperature difference  $\Delta T$ , for the three different densities  $\rho = \{0.1, 0.4, 0.7\}$ .

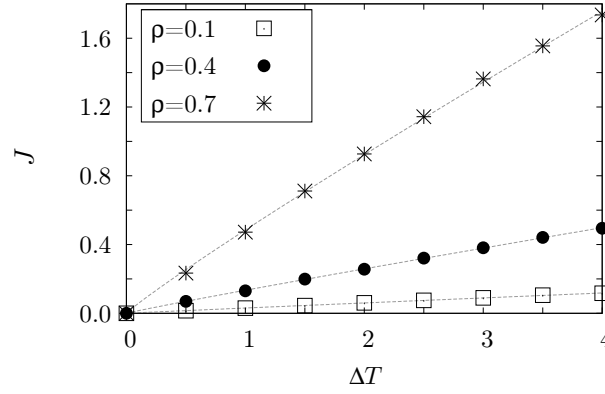


**Figure 1.4 :** Heat flux  $J$  as a function of the temperature differences  $\Delta T$  of the two thermostats for various densities  $\rho$ .

The function  $J(\Delta T)$  shows almost a straight line (with only a slight concavity) with a slope that strongly depends on the gas density and grows with it.

The Lyapunov spectra for non-equilibrium systems differ only slightly from the equilibrium spectra of the same model. As an example we show in the left panel of Fig. 1.5 three spectra for three densities:  $\rho = \{0.1, 0.4, 0.7\}$ , with the boundary temperatures  $T_1 = 1$  and  $T_2 = 5$ . The sums of the exponents are negative, although this cannot be easily observed in the figure shown. With the Kaplan-Yorke formula the information dimension  $D_1$  of the underlying strange attractor in phase space may be computed. The dimensionality reduction,  $\Delta D = D - D_1$ , as a function of the heat flux, is shown in the right panel of Fig. 1.5. For small fluxes a parabolic behavior is obtained as expected.

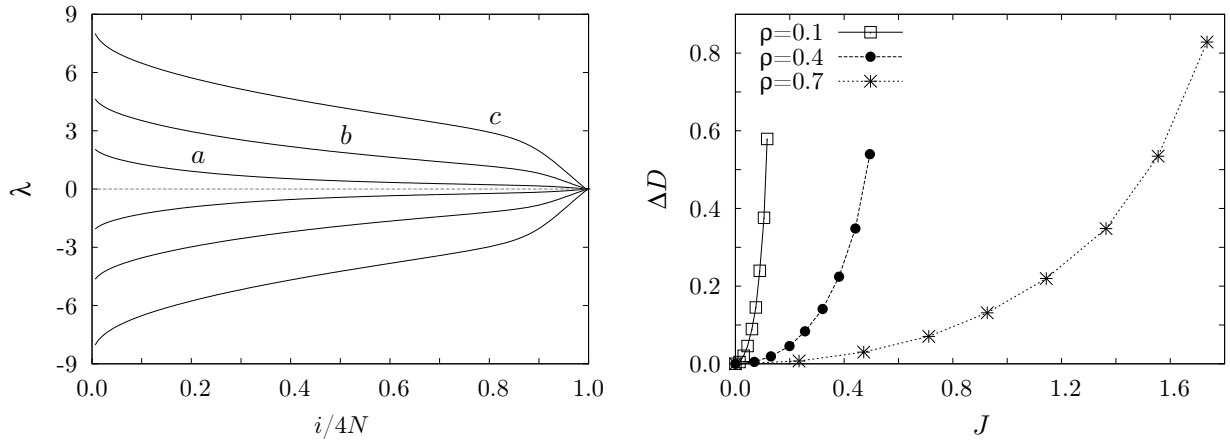


**Figure 1.5 :** Left panel: Lyapunov spectra for boundary temperatures  $T_1 = 1$  and  $T_2 = 5$ , and the densities (a)  $\rho = 0.1$ , (b)  $\rho = 0.4$  and (c)  $\rho = 0.7$ . The sum over all exponents is negative. Right panel: Dimensionality reduction  $\Delta D$  for three different densities as a function of the heat flux  $J$ .

In Table 1.1, typical results for the Lyapunov spectra are shown. The maximum Lyapunov exponent,  $\lambda_1$ , and the sum of all exponents,  $\sum_{i=1}^{4N} \lambda_i$ , are listed as a function of the density and

of the temperature difference  $\Delta T = T_2 - T_1$ . For each density, the maximum Lyapunov exponent  $\lambda_1$  has almost the same value for all temperature differences, only a slight reduction is observed when  $\Delta T$  is increased. For  $\Delta T > 0$ , the sum of all Lyapunov exponents is negative due to the particle collisions with the thermostats, and thus a multifractal attractor in the phase space is expected to exist.

**Table 1.1 :** For three different densities  $\rho$ , the maximum Lyapunov exponent  $\lambda_1$  and the sum over all exponents  $\sum_{i=1}^{4N} \lambda_i$  are listed as function of the temperature differences  $\Delta T$ , for non-equilibrium gas of  $N = 80$  hard disks moving in a box with an aspect ratio  $A = 0.2$ . The nominal mean temperature of the thermostat  $(T_1 + T_2)/2$  is taken equal to 3 (in units of  $K / Nk_B$ ).

$\Delta T$	$\rho = 0.1$		$\rho = 0.4$		$\rho = 0.7$	
	$\lambda_1$	$\sum_i \lambda_i$	$\lambda_1$	$\sum_i \lambda_i$	$\lambda_1$	$\sum_i \lambda_i$
1	2.161	-0.045	4.910	-0.094	8.557	-0.258
2	2.141	-0.192	4.863	-0.407	8.462	-1.111
3	2.104	-0.505	4.773	-1.071	8.287	-2.888
4	2.047	-1.190	4.635	-2.505	8.004	-6.654

## 1.4 Temperature and density profiles

To compute the temperature profile (i.e. the local temperatures), we have to determine the local densities and energies. We partition the channel into disjoint slices of width  $\Delta x$ . Each slice is delimited by the boundaries  $x - \Delta x/2$  and  $x + \Delta x/2$ , and its local particle number is computed as the time average

$$n(x) = \frac{1}{T} \int_0^T dt \int_0^{L_x} dx \sum_{k=1}^N \chi_{\Delta x}(x_k(t) - x) ,$$

where  $x_k(t)$  is the  $x$ -position of the particle  $k$  at the time  $t$ . The indicator function  $\chi_{\Delta x}(x_k(t) - x)$  is equal to unity, if the particle  $k$  is in the slice around  $x$ , and zero otherwise. Analogously, the local energy included in the interval  $[x - \Delta x/2, x + \Delta x/2]$  is computed as the time average

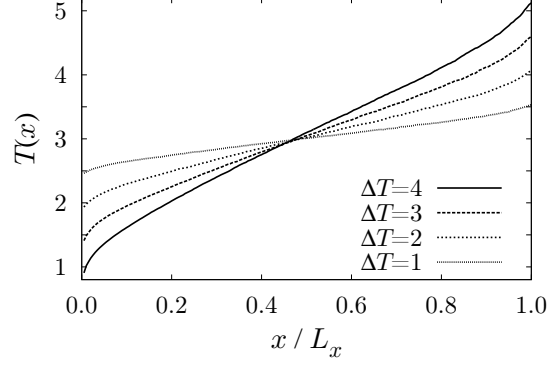
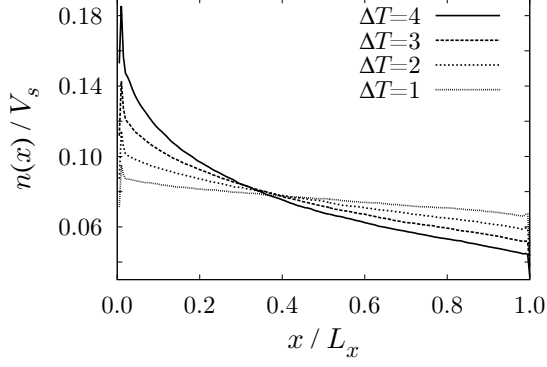
$$E(x) = \frac{1}{T} \int_0^T dt \int_0^{L_x} dx \sum_{k=1}^N \frac{\|\vec{p}_k(x_k, t)\|^2}{2m} \chi_{\Delta x}(x_k(t) - x) ,$$

where  $p_k(x_k, t)$  is the momentum of the  $k$ -th particle at time  $t$  and position  $x_k$ . The local temperature is then given by

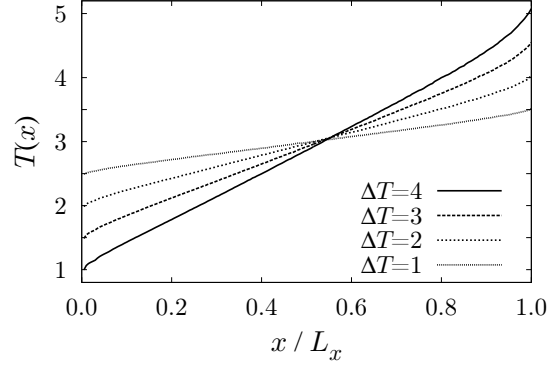
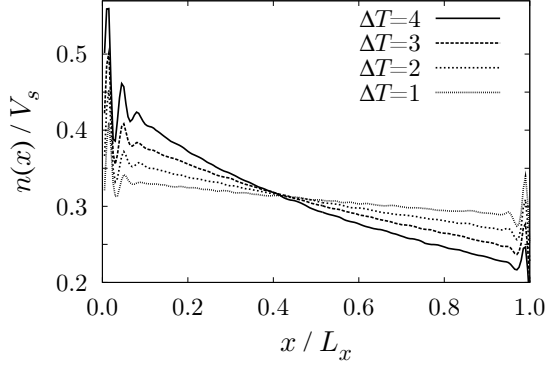
$$T(x) = \frac{E(x)}{n(x)} .$$

Fig. 1.6 gives the profiles obtained for the densities  $\rho = \{0.1, 0.4, 0.7\}$  in a simulation, where  $\Delta T \in \{1, 2, 3, 4\}$  and  $(T_1 + T_2)/2$  fixed to 3. The particle-number density profile (left panels)

$\rho = 0.1$



$\rho = 0.4$



$\rho = 0.7$

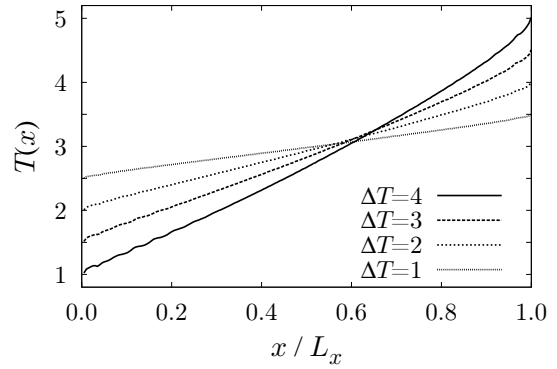
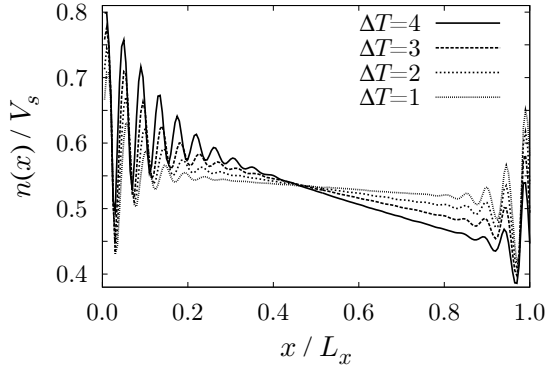


**Figure 1.6 :** Left panels: density profile  $n(x)/V_s$ . Right panels: temperature profile  $T(x)$ . The profiles are shown for systems of  $N = 80$  particles at various temperature differences between the two thermostats  $\Delta T = T_2 - T_1 = \{1, 2, 3, 4\}$ . The medial temperature is  $T^* = (T_1 + T_2)/2 = 3$ . We consider three (area) densities  $\rho = \{0.1, 0.4, 0.7\}$  for a box with an aspect ratio of  $A = 0.2$ . The total number density,  $N/V$ , is related to the area density by  $\rho = \pi N / 4V$  (since  $\sigma = 1$ ).

is defined as  $n(x)/V_s$ , where  $V_s = L_y \Delta x$  is the area of a slice. The width of the slice is small,  $\Delta x = L_x/200$ , such that the densities become insensitive to  $\Delta x$ .

Near the thermostat walls the number density oscillates (panels on the left-hand side) indicating a layered arrangement of the particles. This is particularly strong near the cold wall. A similar behavior is observed for the energy density  $E(x) / L_y \Delta x$  (not shown). The local temperature, however, is totally free of these oscillations (panels on the right-hand side) as required. Note that the local temperature is the ratio of the energy and number densities. Outside of the layered regions the density profile converges towards a straight line for growing density  $\rho$ . Furthermore, all local density profiles intersect more or less at a single point. Also the temperature profiles depicted in the right-hand panels of Fig. 1.6 seem to intersect at a single point.

Since the thermostat wall constitutes a deterministic constraint, no temperature jumps are observed: the temperatures inside the fluid in the vicinity of the thermostat walls smoothly approach the imposed boundary temperatures. In contrast, for stochastic thermostats [18, 19] a temperature discontinuity (the “boundary resistance”) near the cold (hot) thermostat wall is observed. The boundary resistance is referred to as “Kapitza resistance”, and is explained by the “phonon mismatch” between the solid and the fluid. It was experimentally observed for helium-solid interfaces [20] and was afterwards used to describe any thermal boundary resistance [21]. It is expressed in terms of the collision rate (i.e. the mean free path) and of the small temperature difference between the measured and imposed temperatures [21, 12]. Here, the advantage of using a deterministic thermostat obeying detailed balance becomes apparent.

## 1.5 Heat conduction

When the system is not in equilibrium, the distribution function satisfies the Boltzmann integro-differential equation. Usually, one is interested in the properties of gases for conditions only slightly away from equilibrium. Then, the Boltzmann equation can be solved by means of a perturbation method developed by Enskog [22]. The resulting solutions are used to obtain expressions for the transport coefficients such as the heat conductivity. First, we define the experimental effective conductivity  $\kappa_F$  according to Fourier’s law, and compare this result to the “effective conductivity”  $\kappa_E$  according to Enskog’s theory.

As is evident from the temperature profiles on the right-hand side of Fig. 1.6, the slope of the profiles varies considerably with  $x$ . This is a strong indication that we are far from the linear

regime. A naïve application of Fourier's law,

$$\kappa_F = - \frac{J L_x}{\Delta T} ,$$

only gives an effective conductivity  $\kappa_F$ , which constitutes an average over the conductivities over all thermodynamic states present in the simulation cell.

To see this we assume local thermodynamics equilibrium and compute the local conductivity  $\kappa(x)$  by Enskog's theory [15],

$$\kappa(x) = 1.029 \frac{2\kappa_B}{D\chi(\rho_A)} \left( \frac{\kappa_B T}{m\pi} \right) \left[ 1 + \frac{3}{2} (2\rho_A \chi(\rho_A)) + 0.8718 (2\rho_A \chi(\rho_A))^2 \right] , \quad (1.7)$$

where  $\rho_A(x) = \pi\sigma^2 n(x) / 4V_s$  is the local area density,  $T(x)$  is the local temperature, and  $\chi$  is the pair correlation function at contact [23]:

$$\chi(\rho_A) = \frac{1 - (7/16)\rho_A}{(1 - \rho_A)^2} .$$

For each thin slice of width  $\Delta x$ , Fourier's law requires

$$\frac{\delta T(x)}{\Delta x} = - \frac{J}{\kappa(x)} ,$$

where  $J$  is the heat flux, which does not depend on  $x$ ,  $\delta T(x)$  is the temperature difference for the slice located at  $x$ . Integration over the length of the cell provides an expression for the effective heat conductivity from the Enskog theory,

$$\kappa_E = L_x \left( \int_0^{L_x} \frac{1}{\kappa(x)} dx \right)^{-1} .$$

Taking  $T(x)$  and  $\rho_A(x)$  from the experimental profiles of Fig. 1.6, the effective Enskog conductivity  $\kappa_E$  may be obtained.

A comparison with the simulation data is provided in Fig. 1.7 for three different global densities  $\rho$ . The agreement for the intermediate density  $\rho = 0.4$  is excellent. The comparatively large differences for low density gases is not completely understood. The same computations were repeated for a system of  $N = 400$  particles and an aspect ratio of  $A = 1$  (not shown). We obtained almost the same results, which shows that the local equilibrium is not significantly affected by the rather small aspect ratio  $A \equiv L_y/L_x = 0.2$  of our first series of simulations.



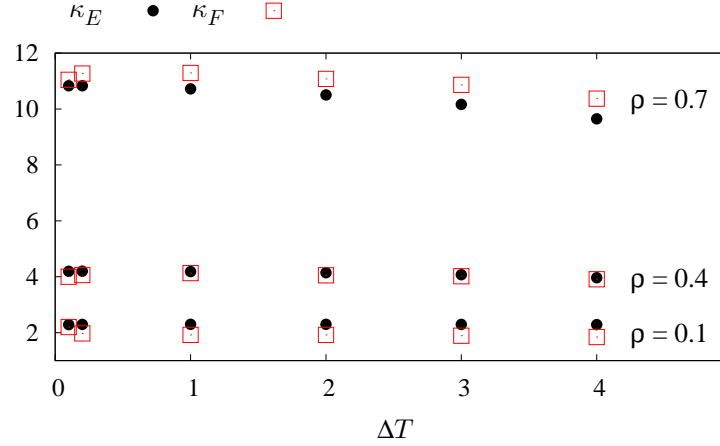


**Figure 1.7 :** Conductivities  $\kappa_F$  and  $\kappa_E$  (in units:  $k_B(K/m\sigma^2)^{1/2}$ ) versus the temperature difference,  $\Delta T$ , between the two thermostats, where the medial temperature  $T^* = 3$ .

## 1.6 Summary

In this section we studied the performance of the van Beijeren thermostat and tested its applicability for subsequent simulations of heat conduction. The thermostat is time reversible and deterministic, and provides a good coupling of the gas with the heat bath without any temperature jumps at the thermostat wall. It is interesting to note that temperature jumps were experimentally found by E. Warburg in the 1870s and were experimentally and theoretical explained by M. von Smoluchowski [24, 25]. Our simulations of the heat conductivity of a hard-disk gas under fairly large driving agrees rather well with the prediction of the Enskog theory for hard disks.

## References

- [1] V.I. Oseledec, Trudy Moskov. Mat. Obsc. **19**, 179 (1968). English transl. Trans. Moscow Math. Soc. **19**, 197 (1968).
- [2] N.I. Chernov and J.L. Lebowitz, Phys. Rev. Lett. **75**, 2831 (1995).
- [3] E. Ott, *Chaos in Dynamical Systems* (Cambridge University Press, New York, 3rd ed., 1993).
- [4] J.L. Kaplan and J.A. Yorke, in *Functional differential Equations and Approximation of Fixed Points*, Lecture Notes in Mathematics **vol. 730**, edited by H.O. Walther and H.O. Peitzen (Springer-Verlag, Berlin, 1979) p. 204.
- [5] H.A. Posch and Wm.G. Hoover, Phys. Rev. E **58**, 4344 (1998).

- [6] D.J. Evans, J. Chem. Phys. **78**, 3297 (1983).
- [7] Wm.G. Hoover, Anthony J.C. Ladd, and Bill Moran, Phys. Rev. Lett. **48**, 1818 (1982).
- [8] Sh. Nosé, J. Chem. Phys. **81**, 511 (1984).
- [9] Wm.G. Hoover, Phys. Rev. A **31**, 1695 (1985).
- [10] Wm.G. Hoover, K. Aoki, C.G. Hoover, and S.V. De Groot, Physica D **187**, 253 (2004).
- [11] B.L. Holian, A.F. Voter, and R. Ravelo, Phys. Rev. E **52**, 2338 (1995).
- [12] D. Risso and P. Cordero, J. Stat. Phys. **82** 1453 (1996).
- [13] Ch. Dellago and H.A. Posch, J. Stat. Phys. **88**, 825 (1997).
- [14] H. van Beijeren, private communication.
- [15] D.M. Gass, J. Chem. Phys. **54**, 1898 (1971).
- [16] W.H. Press, S.A. Teukolsky, T. Vetterling, and B.P. Flannery, *Numerical Recipes in Fortran 77: The Art of Scientific Computing* (Cambridge University Press, 2nd ed., 1999).
- [17] Ch. Dellago, H.A. Posch, and Wm.G. Hoover, Phys. Rev. E **53**, 1485 (1996).
- [18] R. Tehver, F. Toigo, J. Koplik, and J.R. Banavar, Phys. Rev. E **57**, R17 (1998).
- [19] S.Lepri, R.Livi, and A. Politi, Phys. Rep. **377**, 1 (2003).
- [20] P.L. Kapitza, J. Phys. USSR **4** **181** (1941); reproduced in: The Collected Papers of EL. Kapitza **vol. 2**, edited by D. ter Haar (Macmillan, New York, 1964) p. 581.
- [21] M.E. Lumpkin, W.M. Saslow, and W.M. Visscher, Phys. Rev. B **17**, 4295 (1978).
- [22] S. Chapman and T.G. Cowling, *The Mathematical Theory of Non-Uniform Gases* (Cambridge University Press, New York, 3rd ed., 1990).
- [23] J.A. Barker and D. Henderson, Rev. Mod. Phys. **48**, 587 (1976).
- [24] M. von Smoluchowski, Sitzber. Akad. Wiss. Wien **107**, 304-329 (1898).
- [25] M. von Smoluchowski, Sitzber. Akad. Wiss. Wien **101**, 5-23 (1898).

# CHAPTER 2

## Thermostated modified Lorentz Gas

### Contents

2.1	Introduction . . . . .	31
2.2	Model . . . . .	33
2.3	Local equilibrium and normal transport . . . . .	35
2.4	Lyapunov instability . . . . .	39
2.5	Chaos and transport . . . . .	46
2.6	Localization for large systems in microcanonical equilibrium . . . . .	48
2.7	Conclusion . . . . .	50
2.8	Appendix: Wanderer-scatterer collisions for the 3D model . . . . .	52
	References . . . . .	55

### 2.1 Introduction

A first important step in the analysis of how phenomenological transport equations can be understood in terms of the microscopic dynamics of a system, is the connection of transport phenomena with the chaotic properties. Fourier's law [1] is an example of a phenomenologically simple process, that is still not entirely understood on a microscopic scale. Various models have been studied in detail to unravel the connection between the (time-reversible) microscopic dynamics and the macroscopic irreversible behavior. The simple Lorentz gas is a deterministic billiard, which consists of point-particles moving freely among, and colliding with, motionless circular obstacles. The field-driven dynamically thermostated Lorentz gas has been the object of several studies for the investigation of transport phenomena [2, 3, 4, 5]. Other thermostated versions (imposing stochastic boundary conditions at opposite sides of the box containing the system) have also been used to study heat conduction: Lebowitz and Spohn [6, 7] have shown

that the Fourier's law is well satisfied in this system in the Boltzmann-Grad limit (for which the average density of randomly distributed scatterers goes to infinity and their radius to zero). Since no energy exchange takes place between the point particles, the local thermal equilibrium is not satisfied and the physical significance of temperature is difficult to interpret. Finally, the Lorentz gas was modified [8, 9] to introduce roughness to disks, which are allowed to rotate at their fixed position. Thus, the point-particles can indirectly exchange energy in this case and may establish local thermal equilibrium.

Such systems are macroscopically irreversible, as specified by the Second Law of thermodynamics, even if the equations of motion are time-reversible [10, 11]. Generally, the transport coefficient of a thermostated non-equilibrium system may be expressed in terms of the sum of all Lyapunov exponents in this case [12, 13, 14].

The main emphasis of this chapter is not the study of this particular model but the test of novel thermostating boundary conditions due to van Beijeren [15], which were introduced in Chap. 1. Such a thermostating boundary consists of a non-trivial dynamical and time-reversible map for the velocity of the point particles hitting the boundary. This map obeys detailed balance. Because of the dynamical nature of the boundary, we may compute the full spectrum of the Lyapunov exponents. Thus, we may establish a link between the chaotic properties and heat conduction in this case. The time evolution of the tangent bundle furnishes further information on the phase space structure, which is not accessible by the sole analysis of the phase space dynamics. For example, the non-Hamiltonian character of the system may be checked by the calculation of local (time-dependent) Lyapunov exponents (see Chap. 8).

The chapter is organized as follows: In Sec. 2.2 the thermostated modified Lorentz gas is introduced. We summarize in Sec. 2.3 the results concerning thermodynamics quantities, where we make use of the deterministic boundary conditions due to van Beijeren (see Chap. 1 and Ref. [15]). These results are consistent with early studies obtained for stochastic boundary thermostats [9]. We show that the assumption of local equilibrium is valid and that the heat transport is normal. An exhaustive study of the Lyapunov spectra is the topic of Sec. 2.4. Some results connecting chaos and transport phenomena are listed in Sec. 2.5. Sec. 2.6 is devoted to the understanding of the manner in which the translational and rotational parts are related. In Sec. 2.7 we conclude that the equations governing the collision do not derive from a symplectic process. For completeness, we give in the Appendix (Sec. 2.8) the collision map for the three-dimensional version of this model governing the collision of a point particle with a rough hard sphere. We also derive the linearized map for the dynamics in the tangent space for this case.

## 2.2 Model

In the simplest version, the planar periodic Lorentz gas consists of an infinite array of fixed disks (the “scatterers”) arranged on a triangular lattice. In the accessible volume between the disks, point particles (the “wanderer”) with unit mass move freely with constant speed. They collide elastically with the scatterers, but do not interact with each other. We consider only the case of a finite horizon, where the disk radii are large enough to prevent any wanderer particle from escaping to infinity without collisions with the scatterer disks.

Variants of the model use a random arrangement of disks (“random Lorentz gas”) with or without disk overlap, e.g. [6, 16, 17]. Here, we do not consider this case.

The model is driven into a non-equilibrium stationary state by the use of thermostated walls at two opposite sides of the simulation box. We study the modified Lorentz gas model introduced by Mejía-Monasterio *et al.* [8, 9], which consists of  $N_1$  wandering point-particles of mass  $m$  and momentum  $\vec{p}$ , and of  $N_2$  hard rough disks of diameter  $\sigma$  on a triangular lattice (see Fig. 2.1), which may rotate around the (fixed) lattice points with angular velocity  $\omega$ , and which have a moment of inertia  $I$ . Energy exchange between scatterers and wanderers is allowed, but no inter-wanderer collisions take place (the model is similar to a photon gas in a crystal). When a wanderer particle  $k$  hits a scatterer  $\ell$ , energy is exchanged by a “rough” hard collision such that the total energy and the total angular momentum (with respect to the center of the scatterer) are conserved. If the outgoing transversal momentum  $\vec{p}_k'$  of the point particle  $k$  and the angular velocity  $\omega_\ell'$  of the disk  $\ell$ , immediately after the collision, are expressed in terms of the incoming quantities [8] (see also the Appendix, Sec. 2.8), one finds for the collision rules

$$p_k^{n'} = -p_k^n, \quad (2.1)$$

$$p_k^{t'} = p_k^t - \frac{2\eta}{1+\eta}(p_k^t - mR\omega_\ell), \quad (2.2)$$

$$mR\omega_\ell' = mR\omega_\ell + \frac{2}{1+\eta}(p_k^t - mR\omega_\ell). \quad (2.3)$$

The superscripts  $n$  and  $t$  correspond, respectively, to the normal and tangential components of the particle momentum with respect to the surface of the disk  $\ell$  at the collision point. Here,  $R = \sigma/2$  is the scatterer radius.  $I$  is the moment of inertia of the scatterer disks. The dimensionless parameter  $\eta = 4I/m\sigma^2$  controls the coupling between translational and rotational degrees of freedom. Its range is included in  $]0, \infty[$ . Both extreme values stand for peculiar situations:

- If  $\eta \rightarrow 0$ , the translational and rotational degrees of freedom decouple and the rough hard disk model is reduced to a smooth hard disk model, if all  $\omega_s$  are discarded.

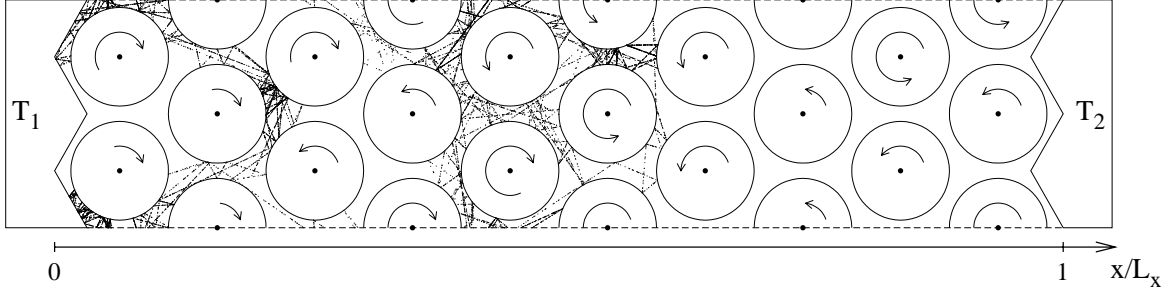


**Figure 2.1 :** Geometry of the modified Lorentz gas. The temperatures of the thermostats are  $T_1$  and  $T_2$ . The lines visualize the trajectory of one single wanderer. The length of each arrow on a disk is proportional to the initial disk angular velocity.

- If  $\eta \rightarrow \infty$ , the angular velocities of the disks never change during the simulation and the energies of the disks are not affected by the collisions.

Both limiting cases are not considered here. For  $\eta = 1$ , the tangential component of the wanderer velocity,  $p_k^t/m$ , and the rotational surface velocity,  $\frac{\sigma}{2}\omega_\ell$ , of the disk are simply interchanged. In the following, we consider various coupling parameters between  $\eta = 0.1$  and  $\eta = 20$ .

We drive this system away from equilibrium by applying two deterministic van Beijeren thermostats on opposite walls separated in  $x$ -direction, which are at different temperatures:  $T_1$  and  $T_2 = T_1 + \Delta T$  (where  $\Delta T > 0$ ). Conventionally, the thermostat on the right-hand side always is at the higher temperature. In the  $y$ -direction periodic boundary conditions are used. Unlike in Ref. [8, 9], we consider only heat flow and no simultaneous mass transport. Our main emphasis is on the properties of the tangent space.

Initially, the wanderers are positioned on a lattice shifted by  $\sigma$  in the  $x$ -direction relative to the one used for the scatterers. The initial angular and translation velocities are randomly chosen according to a linear temperature profile.

Fig. 2.1 shows the geometry of the modified Lorentz gas. The zig-zag thermostat walls are arranged such that a periodic boundary condition also in the  $x$ -direction may be implemented without difficulty. This arrangement of the thermostat walls slightly, but significantly, blurs the definition of the local fields such as the local density or temperature.

The zig-zag form of the thermostat walls and the finite horizon (due to the size and arrangement of the scatterers) exclude the possibility of particles crossing through the box in the  $y$ -direction without a collision. The triangular lattice on which the disks are positioned is such that the criterion for the critical horizon is met. It is enough to consider only two rows of scatterers to prevent the possibility that a wanderer consecutively collides with the same scatterer (Fig. 2.1). For most

of this study we restrict to this case. Only in Sec. 2.6 much wider systems are considered.

In spite of the system's complexity, the total energy  $K$  still has a simple form and is given directly by the translational and rotational kinetic energies,

$$K = \underbrace{\frac{m}{2} \sum_{k=1}^{N_1} (\vec{p}_k)^2}_{K_1} + \underbrace{\frac{I}{2} \sum_{\ell=1}^{N_2} (\omega_\ell)^2}_{K_2} . \quad (2.4)$$

We have verified in our simulations that the translational and rotational kinetic temperatures agree reasonably well:

$$\langle K_1 \rangle / N_1 \approx 2 \langle K_2 \rangle / N_2 .$$

For equilibrium systems, for which  $\Delta T = 0$ , this becomes an identity and equal to the thermostat temperature  $T_1 = T_2$ .

In the remainder of this chapter we choose to set the medial temperature  $T^* \equiv (T_1 + T_2)/2 = 3$ . For our numerical work we use reduced units, for which the scatterer diameter  $\sigma$ , the mass of the wanderer  $m$ , and the Boltzmann constant  $k_B$  are taken equal to unity. The only free parameters are the length of the box  $L$ , the number  $N_1$  of the wanderers, the nominal temperature difference  $\Delta T$  between the two thermostats and the moment of inertia  $I$  (respective the coupling parameter  $\eta = 4I$ ). The nodes of the triangular lattice are separated by  $\sqrt{4/3}\sigma$ , which corresponds to the critical scatterer geometry separating the finite horizon case from the infinite horizon case. The length of the box in  $x$ -direction is specified by  $L = N_x \sigma$ , where  $N_x$  is the number of columns of scatterers parallel to the  $y$ -direction.  $L = 10$  in Fig. 2.1.

## 2.3 Local equilibrium and normal transport

In this section we study how a system reaches the stationary non-equilibrium state for a given coupling parameter  $\eta$  and a fixed temperature difference  $\Delta T$  between the two thermostats. Most results have already been established in previous work introducing this problem [9]. The novel aspect is the use of a deterministic thermostat. We verify that the system indeed reaches local equilibrium and that the heat transport is normal.

First, we show in Fig. 2.2 the distribution functions of the transversal momentum,  $f_1(p)$  of the wanderers, and of the rotational velocity,  $f_2(\omega)$  of the scatterers, for a system in equilibrium (the two thermostats are set to the temperature  $T_1 = T_2 = T^* = 3$ ). These results agree very well with the theoretical two- and one-dimensional Maxwell distributions, which allows us to relate the time-averaged energy of the particles, or of the disks, to the imposed temperature  $T^*$

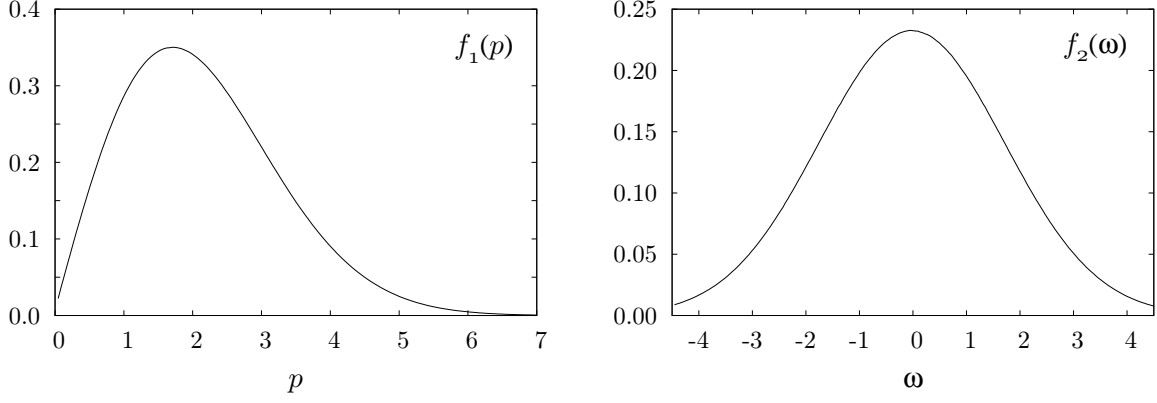


**Figure 2.2 :** Translational velocity distribution  $f_1(v)$  of the wanderer particles and disks angular velocity  $f_2(\omega)$  of the disk scatterers for an equilibrium system of 40 disks of diameter  $\sigma = 1$  and 50 particles in a box of length  $L = 20$ . The temperature imposed by the thermostats is  $T_1 = T_2 = T^* = 3$ .

of the system.

The local temperature and the local density are revealed by the corresponding profiles. We partition the box in disjoint slices of width  $\Delta x$ . Each slice is delimited by the boundaries  $x - \Delta x/2$  and  $x + \Delta x/2$ , and its local particle number is computed as the time average

$$n(x) = \frac{1}{T} \int_0^T dt \int_0^{L_x} dx \sum_{k=1}^N \chi_{\Delta x}(x_k(t) - x) ,$$

where  $x_k(t)$  is the  $x$ -position of the wanderer  $k$  at the time  $t$ , and  $\chi_{\Delta x}(x_k(t) - x)$  is the indicator function (which allows us to select the wanderers pertaining to the slice  $[x - \Delta x/2, x + \Delta x/2]$ ). Analogously, the local energy included in the region  $[x - \Delta x/2, x + \Delta x/2]$  is computed as the time average

$$E(x) = \frac{1}{T} \int_0^T dt \int_0^{L_x} dx \sum_{k=1}^N \frac{\|\vec{p}_k(x_k, t)\|^2}{2m} \chi_{\Delta x}(x_k(t) - x) ,$$

where  $p_k(x_k, t)$  is the momentum of the  $k$ -th wanderer at time  $t$  at the position  $x_k$ . Consequently, the temperature profile of the wanderers is defined as

$$T(x) = \frac{E(x)}{n(x)} ,$$

whereas the temperature profile of the scatterers is directly related to their time-averaged rotational energy. The wanderer density is given by

$$\rho(x) = \frac{n(x)}{V_a(x)} ,$$

where  $V_a(x)$  is the accessible volume in a slice at a position  $x$ , which corresponds to the volume



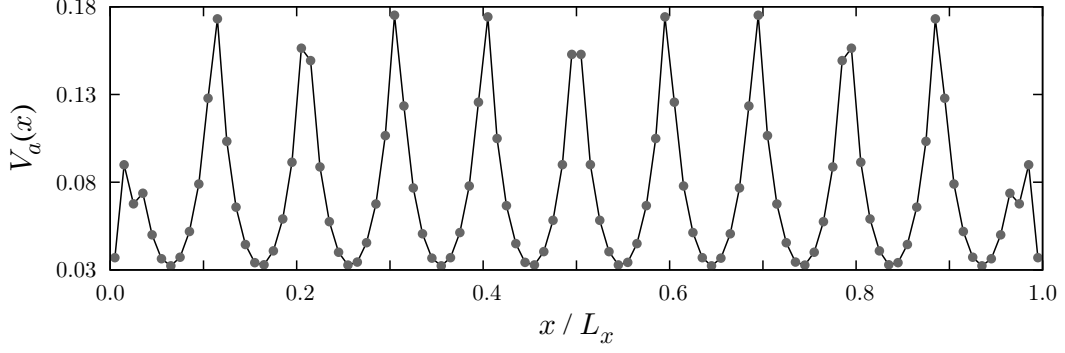


**Figure 2.3 :** The accessible volume  $V_a(x)$  in narrow slices as a function of the  $x$ -position in the box. This function depends on the width of the box (in  $y$ -direction) and, of course, on the width  $\Delta x$  of the slices. We can see the boundary effects due to the geometry of the left and right box boundary.

of the slice minus the sections of disks in this slice, also taking into account the zig-zag geometry of the thermostats on both sides. The profile of the accessible volume is plotted in Fig. 2.3.

We now consider the temperature and density profiles of the wanderers. The profiles are shown in Figs. 2.4 and 2.6 for various  $\Delta T$  with  $\eta = 1$ , and in Figs. 2.5 and 2.7 for various  $\eta$  with  $\Delta T = 4$ .  $\eta$  is the coupling parameter between translational and rotational degrees of freedom. We observe that the temperature profiles are almost linear and that the slight concavity (or convexity) of the profile depends on  $\eta$ . The wavelike structure of the gradient is correlated with the position of the disks. The density profiles show how the wanderers accumulate in the vicinity of the cold thermostat. The density profiles for large  $\eta$  tend to a plateau extending almost over the whole length of the box.

It has already been observed that, considering a fixed temperature difference between the two thermostats, for one-dimensional systems, the flow of heat is inversely proportional to system size, whereas in two dimensions the heat flow stays constant, and in three dimensions it increases [12]. That is intimately related to the Fourier's law. The Lorentz gas studied here behaves like a one-dimensional model. This is due to the narrow box in  $y$ -direction, which is kept constant when the system size is increased. Increasing the size, our model approaches local equilibrium and the dissipation decreases [12]. Consequently, the reduction in phase-space dimensionality is largest for small systems, hence, it is interesting to consider also small systems to investigate heat transport phenomena.

In non-equilibrium physics, the heat conduction is usually well described by Fourier's law. The heat flux  $J$  is related to the temperature gradient as follows

$$J = -\kappa \frac{\Delta T}{L} ,$$

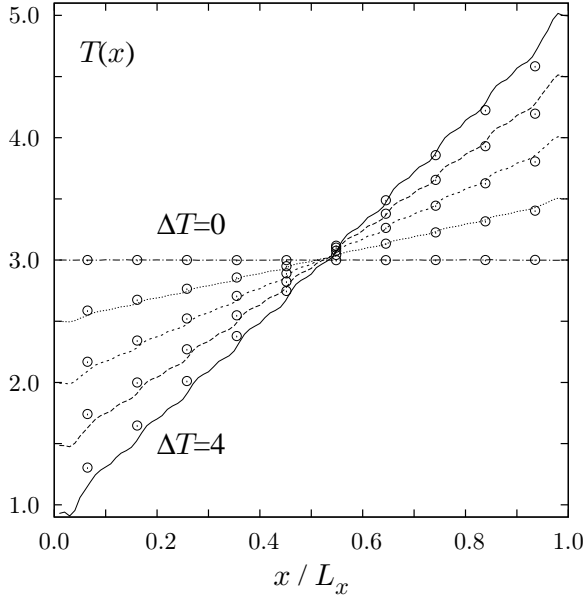


**Figure 2.4 :** The lines represent the temperature profile of the wanderers, and the circles represent the temperature of the scatterers taken at their  $x$ -position, considering various temperature differences:  $\Delta T \in \{0, 1, 2, 3, 4\}$ , where  $T^* = 3$  and  $\eta = 1$ .

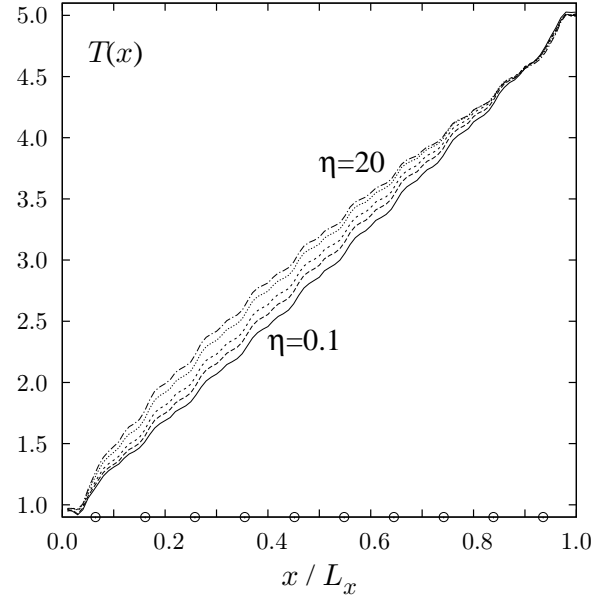


**Figure 2.5 :** Temperature profile of the wanderers when the scatterers rotate with various moments of inertia:  $\eta \in \{0.1, 2, 4, 10, 20\}$ , where  $\Delta T = 4$  and  $T^* = 3$ . (The circles on the abscissa represent the position of the scatterers.)

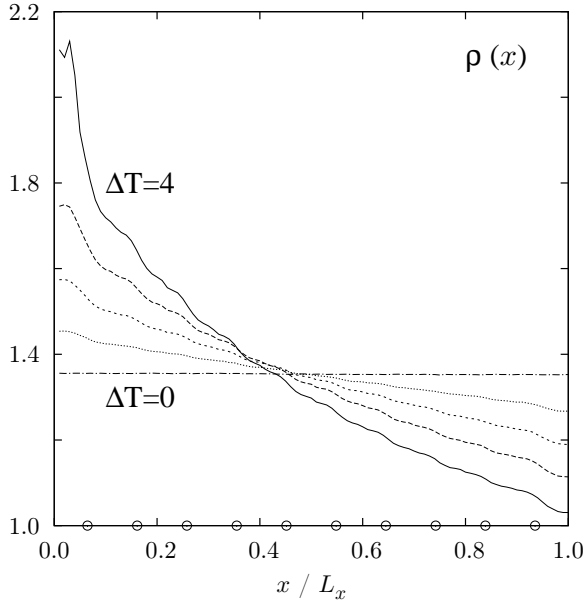


**Figure 2.6 :** Density profiles of the wanderers for various temperature differences:  $\Delta T \in \{0, 1, 2, 3, 4\}$ , where the nominal medial temperature  $T^* = 3$ , and the parameter  $\eta = 1$ . (The circles on the abscissa represent the position of the scatterers.)

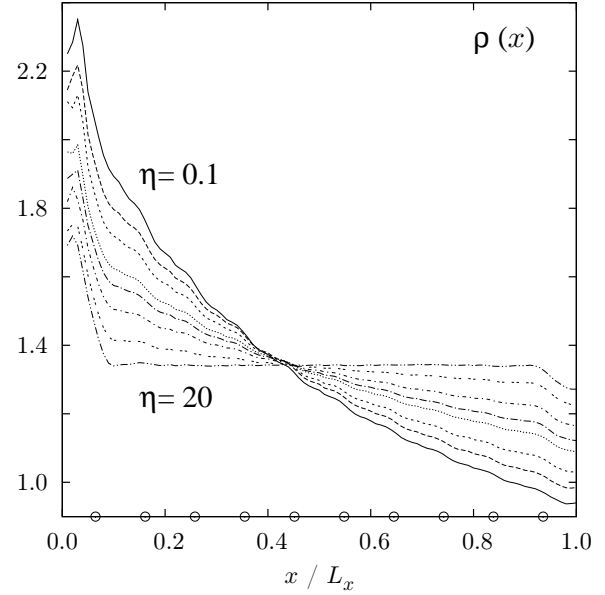


**Figure 2.7 :** Density profiles of the wanderers when the scatterers rotate with various moments of inertia:  $\eta \in \{0.1, 0.5, 1, 2, 3, 5, 10, 20\}$ , where  $\Delta T = 4$  and the nominal medial temperature  $T^* = 3$ . (The circles on the abscissa represent the position of the scatterers.)

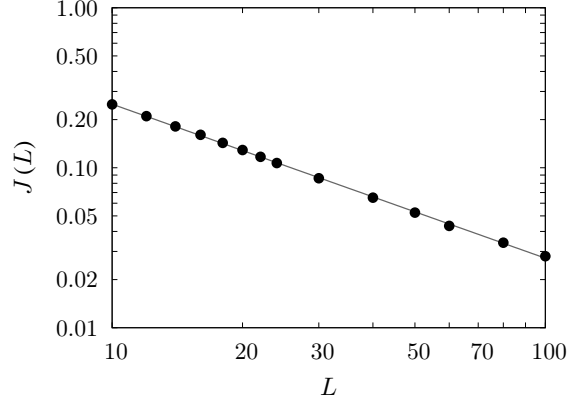


**Figure 2.8 :** Size dependence of the heat flux for a fixed temperature difference  $\Delta T = 4$  with  $T^* = 3$ , for a system of  $N_2 = 2L$  disks of diameter  $\sigma = 1$  and  $N_1 = 5/2L$  particles in a box of length  $L$ . Using logarithmic scales on both axis, we can assume the following dependence:  $J(L) = \varsigma L^{-\nu}$ .  $\varsigma$  and  $\nu$  were calculated by means of a linear regression:  $\nu = 0.9639 \pm 0.0044$ .

where  $\kappa$  is the thermal conductivity. We see in Fig. 2.8 that  $J$  and  $L$  are related by the following formula:

$$\log J(L) = -\nu \log(L - 10) + \log J(10) .$$

In our model simulation we find a value of  $\nu \approx 0.96$ , close to  $\nu = 1$  as predicted by linear hydrodynamics. Mejía-Monasterio *et al.* [8] found exactly the same value as we did for simulations in a narrow channel box with 2 disks in the vertical direction. We have thus verified that the linear hydrodynamic laws are respected in our model, and so we pass on to the study of the chaotic properties.

## 2.4 Lyapunov instability

The computation of the Lyapunov instability reveals and characterizes the chaotic behavior of our system. The assumption of the existence of local equilibrium, which is an essential point for the analysis of transport phenomena, is reasonable because of the chaotic character of our model.

For the computation of the  $(4N_1 + N_2)$  Lyapunov exponents, Benettin *et al.* [18, 19] and Shimada *et al.* [20] proposed an algorithm that is applicable to smooth bundles. Concomitantly to the phase-space dynamics, the time evolution of a complete set of  $(4N_1 + N_2)$  orthonormal (perturbation) Lyapunov vectors is followed with motion equations obtained by linearizing the phase-space equations of motion. Periodically, a Gram-Schmidt re-orthonormalization procedure is used in order to avoid the tendency of the Lyapunov vectors to collapse toward the unstable direction of the phase space. We adapt the classical algorithm for our system taking into ac-

count the wanderer-scatterer and wanderer-thermostat collisions, as was proposed by Dellago *et al.* [11]. The transformation map, which governs the collision in the phase space, are also linearized in order to find the associated transformation map of the tangent bundle. The outgoing Lyapunov vectors depend on the incoming Lyapunov vectors as well as on the incoming and outgoing state vectors. It is not possible to use a stochastic thermostat, such as in [8, 9]. All results are obtained by using the deterministic van Beijeren thermostat, which was introduced and tested in the previous chapter (Chap. 1). This thermostat is deterministic and generates Maxwell-Boltzmann distributions for the reflected velocity of the wanderer, and gives rise to well defined Lyapunov spectra.

Although we use here a two-dimensional modified version of the Lorentz gas (on the  $xy$ -plane), the transformation map of wanderer-scatterer collisions (in the phase space as well as in the tangent space) is first computed for the three-dimensional model. The details of this derivation are given in the Appendix (Sec. 2.8): the phase-space transformations consist of Eqs. (2.9) - (2.11), and the tangent-space transformations consist of Eqs. (2.15) - (2.17). All equations remain valid in the two-dimensional case, with all position vectors  $\{\vec{q}_n\}_{n=1}^{N_1}$  and transversal momentum vectors  $\{\vec{p}_n\}_{n=1}^{N_1}$  of the wanderers being considered in the  $xy$ -plane, and all angular velocity vectors  $\{\vec{\omega}_s\}_{s=1}^{N_2}$  being perpendicular to this plane. Thus, only a single component,  $\{\omega_s\}_{s=1}^{N_2}$ , of the latter remains for each disk. All superfluous components (the orientation angles of scatterers) are discarded (see also [21]).

The state of the system is given by the positions and the momenta of all point-particles, as well as by the angular velocities of all disk scatterers,

$$\mathbf{\Gamma} = \{\vec{q}_n, \vec{p}_n, \omega_s; \quad n = 1, \dots, N_1; \quad s = 1, \dots, N_2\} \ .$$

Similarly, an arbitrary (perturbation) Lyapunov vector is given by all associated perturbation components,

$$\delta\mathbf{\Gamma} = \{\delta\vec{q}_n, \delta\vec{p}_n, \delta\omega_s; \quad n = 1, \dots, N_1; \quad s = 1, \dots, N_2\} \ .$$

The time-averaged exponential growth (or decay) of the whole Lyapunov vectors gives rise to a full set of ordered Lyapunov exponents,  $\lambda_1 \geq \dots \geq \lambda_D$ , where  $D = 4N_1 + N_2$  corresponds to the phase-space dimension. The positive exponents of the Lyapunov spectrum constitute the unstable branch, whereas the negative exponents constitute the stable branch. Fig. 2.9 shows the Lyapunov spectra for a system of  $N_1 = 10$  wanderers and  $N_2 = 40$  disk scatterers, where the length of the box  $L = 20$  and the temperature difference  $\Delta T = 0$ . Since for the case  $\Delta T = 0$  the spectra yield always conjugate pairing exponents (i.e.  $\lambda_i + \lambda_{D+1-i}$ ,  $\forall i \in \{1, \dots, D\}$ ), we show only the positive, unstable, branch of the spectra. One observes a strong influence of the coupling

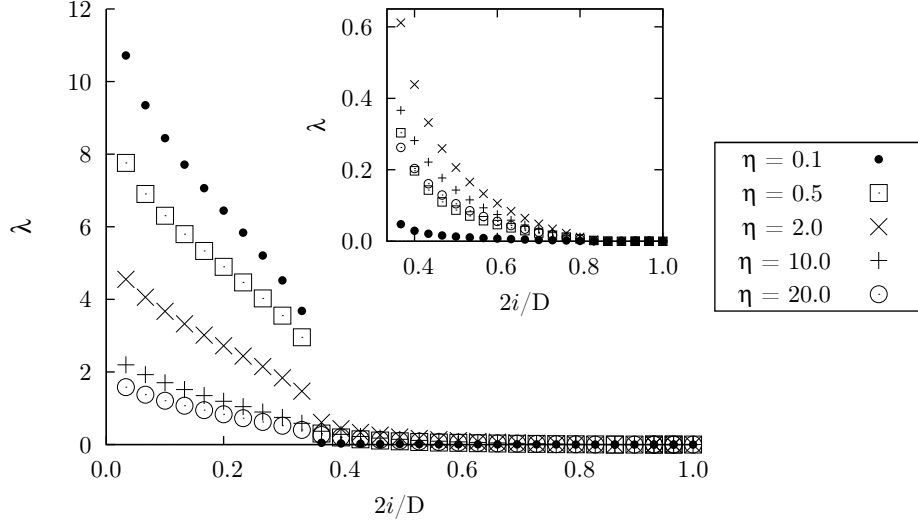


**Figure 2.9 :** Lyapunov spectrum in equilibrium ( $\Delta T = 0$ ) for the modified Lorentz system ( $N_1 = 10$  wanderers and  $N_2 = 40$  disk scatterers, where the length of the box  $L = 20$ ). Reduced Lyapunov indices  $2i/D$  are used on the abscissa, where  $D = 4N_1 + N_2$  is the phase-space dimension.  $\eta$  is the reduced moment of inertia of the scatterers.

parameter  $\eta$  on the spectra, and this indicates that the scatterers and wanderers have *a priori* certain assigned roles in the Lyapunov spectrum. In particular, the  $N_1$  first exponents seem to be most strongly influenced by the wanderers. One notes a fast drop between the two exponents  $\lambda_{N_1}$  and  $\lambda_{N_1+1}$ .

The vanishing exponents are a consequence of the fundamental continuous symmetries that leave the Lagrangian and, hence, the motion equations invariant. According to Nöther's theorem, each continuous symmetry corresponds to a constant of the motion [22]. Each continuous symmetry is associated with two vanishing Lyapunov exponents. However, it is still possible to obtain an odd number of vanishing Lyapunov exponents, because this number depends on the number  $N_1$  of the wanderers. This reveals a peculiarity of the system, which is due to the fact that the wanderers do not interact directly with each other (and similarly, the scatterers do not interact directly with each other). The modified Lorentz gas operates like a hybrid system: even though one obtains a smooth decreasing Lyapunov spectrum involving all wanderers and all scatterers, which brings out a certain coupling between all protagonists, it behaves more like two slightly interacting subsystems. We are not able to give the fundamental reason why the number of vanishing exponents depends on the number of wanderers. It will be useful to investigate more specifically how the null subspace, associated with these Lyapunov exponents, is spanned by the “covariant vectors” (Part II and Ref. [23, 24, 25]).

To specify the null subspace, we may say that for an even number of wanderers and an even number of scatterers the vanishing exponents belong to Lyapunov indices included in  $[(3N_1 + N_2)/2 + 1, (5N_1 + N_2)/2]$ .

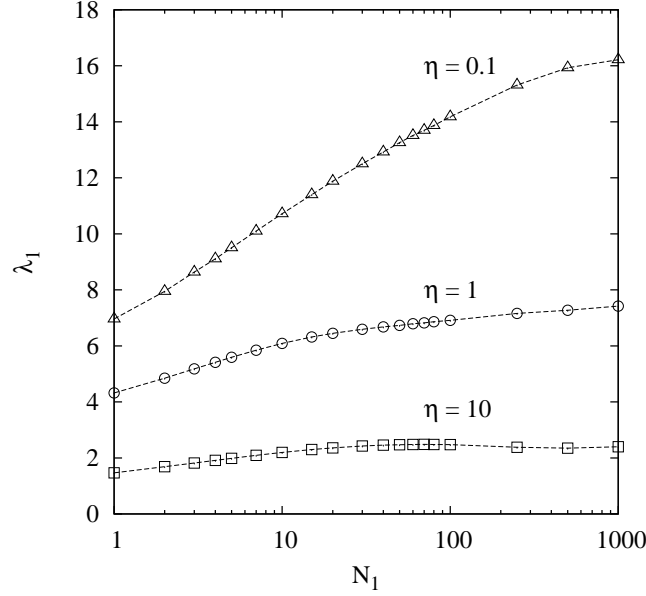


**Figure 2.10 :** Maximum Lyapunov exponent  $\lambda_1$  as a function of the number of wanderers  $N_1$  for the modified Lorentz gas at equilibrium, where the length of the box  $L = 10$  (the number of scatterers  $N_2 = 20$ ). The coupling parameter  $\eta \in \{0.1, 1, 10\}$ . The number of wanderers is shown on a logarithmic scale.

### 2.4.1 Behavior of specific Lyapunov exponents

To investigate how the disks and the wanderers affect the spectrum, we first consider some specific Lyapunov exponents  $\{\lambda_1, \lambda_{N_1}, \lambda_{N_1+1}, \lambda_{(3N_1+N_2)/2}\}$ , which may be taken to characterize the whole Lyapunov spectrum. We analyze the behavior of these exponents in relation to the coupling parameter and the temperature difference between the two thermostats. We use a system with  $N_2 = 20$  disk scatterers in a box of length  $L = 10$ , and with  $N_1 = 10$  point-particles.

The maximum Lyapunov exponent  $\lambda_1$  serves as an indicator for the strength of dynamical chaos, and the Kolmogorov-Sinai entropy  $h_{KS}$  determines the time for the phase-space mixing [26]. Phase points that are initially confined to a small segment of phase space will spread and, after a sufficiently long time, occupy homogeneously the whole energy hypersurface. The mixing time is defined as  $D/h_{KS}$  [27, 28]. The entire set of positive Lyapunov exponents completely characterizes the asymptotic unstable expansion rate present in the dynamical system. According to Pesin's entropy formula [29],  $h_{KS}$  is equal to the sum of the positive exponents. For the modified Lorentz gas, we verified that the Kolmogorov-Sinai entropy per wanderer,  $h_{KS}/N_1$ , remains constant for different values of  $N_1$  and for fixed  $N_2$  (not shown). It is interesting to show how the maximum expansion is influenced by  $N_1$ . In Fig. 2.10, we plot  $\lambda_1$  as a function of  $N_1$  for the modified Lorentz gas in equilibrium, where the length of the box is fixed to  $L = 10$ .

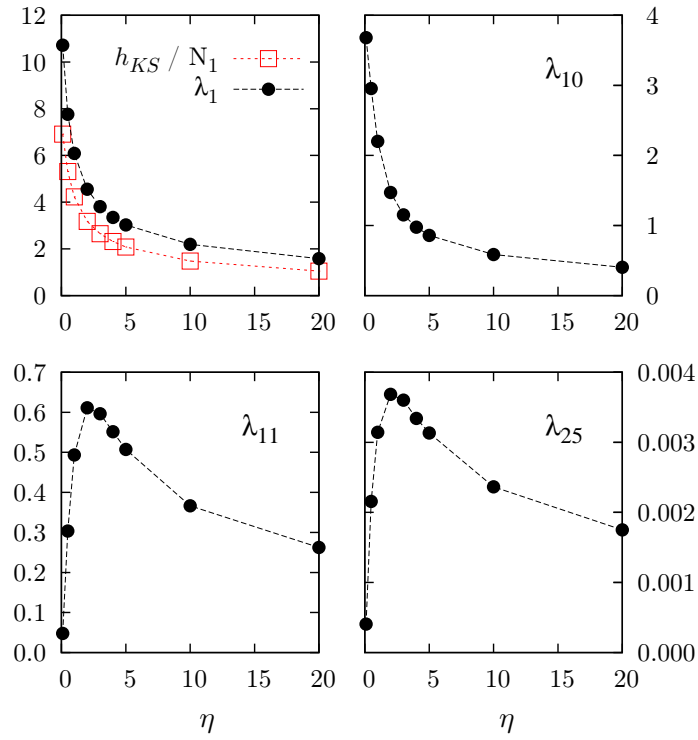


**Figure 2.11 :** Behavior of the Kolmogorov-Sinai entropy per wanderer,  $h_{KS}/N_1$ , and of selected Lyapunov exponents as a function of  $\eta$  for a small system ( $N_1 = 10$  wanderers,  $N_2 = 40$  disk scatterers, and for a box length  $L = 20$ ) in equilibrium ( $\Delta T = 0$ ).

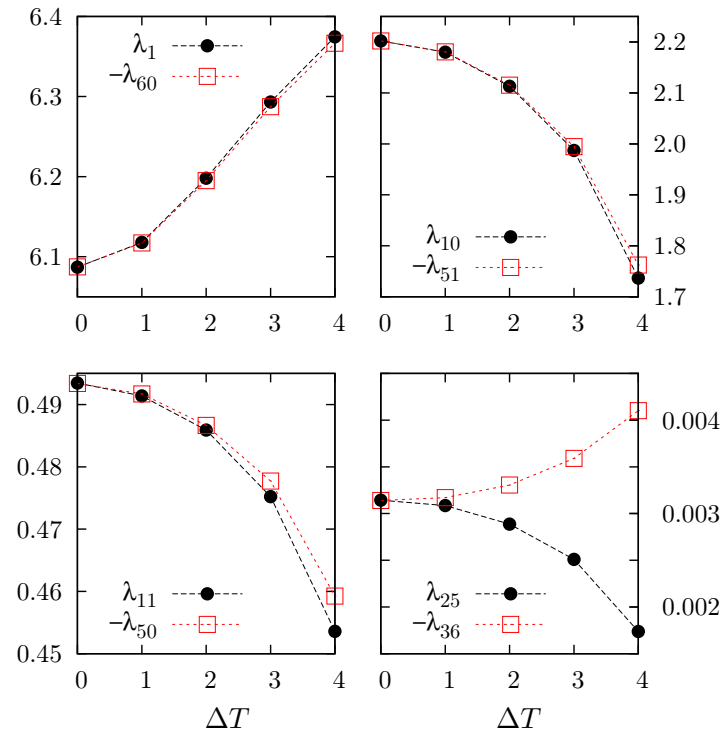


**Figure 2.12 :** Violation of the conjugate pairing relation for selected Lyapunov exponents as a function of  $\Delta T$ , where  $\eta = 1$ , for a small system ( $N_1 = 10$  wanderers,  $N_2 = 40$  disk scatterers, and for a box length  $L = 20$ ).

Not unexpectedly,  $\lambda_1$  strongly depends on the coupling parameter  $\eta$ .

To show more clearly the dependence of the Lyapunov spectrum on the parameter  $\eta$ , the system is studied in equilibrium,  $\Delta T = 0$ . We show in Fig. 2.11 the behavior of the Kolmogorov-Sinai entropy per wanderer,  $h_{KS}/N_1$ , as well as of the Lyapunov exponents selected above. All other exponents pertaining to the same branch (unstable or stable) behave in a similar manner.

To show the violation of conjugate pairing for  $\Delta T > 0$ , we plot the value of selected Lyapunov exponents as well as their conjugate exponents in Fig. 2.12. The conjugate pairing symmetry is significantly violated for the exponents mostly affected by the scatterer rotation,  $\{\lambda_{11}, \dots, \lambda_{25}\}$ , whereas the large exponents, mostly affected by the wanderer particles, do not show a significant deviation.

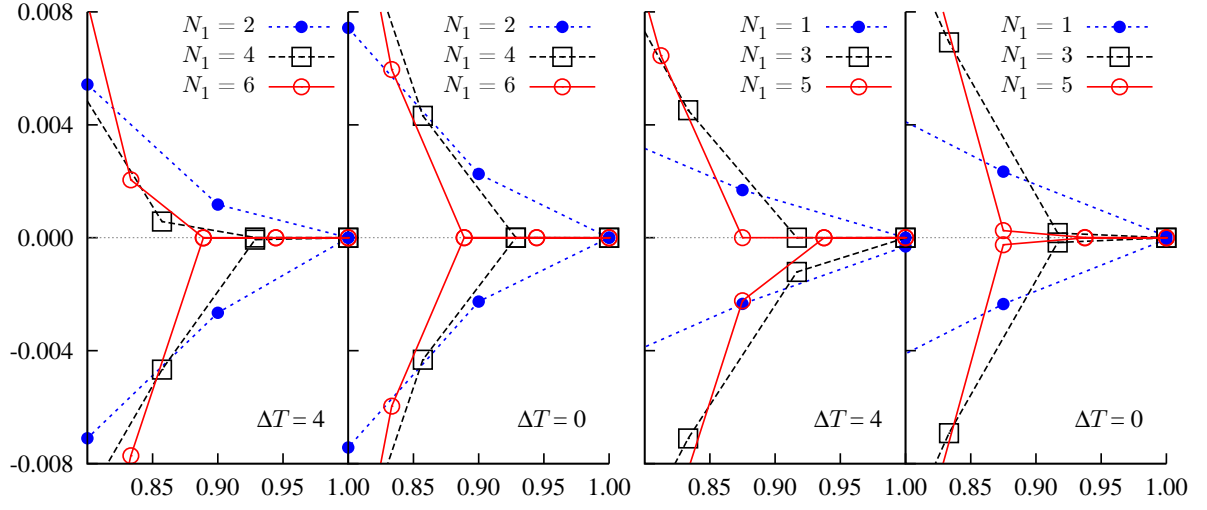
## 2.4.2 Vanishing Lyapunov exponents and conjugate pairing relation

To determine the dependence of the vanishing Lyapunov exponents on the number of wanderers, we performed a series of simulations with a small number of wanderers,  $N_1 \in \{1, \dots, 6\}$  for the thermostated model with  $\Delta T \in \{0, 4\}$ . For this purpose, it is advantageous to use only few wanderers ( $N_2 = 12$ ). The parameter  $\eta$  is set to unity. Fig. 2.13 shows an enlargement of the Lyapunov spectra around the vanishing exponents. To illustrate the conjugate pairing symmetry  $\lambda_i = \lambda_{D+1-i}$  for equilibrium systems, we plot conjugate exponent pairs with the same index  $i$  for conjugate pairs on the abscissa, where now  $i \in \{1, \dots, D/2\}$ . At  $i = D/2$ , two vanishing Lyapunov exponents are superposed.

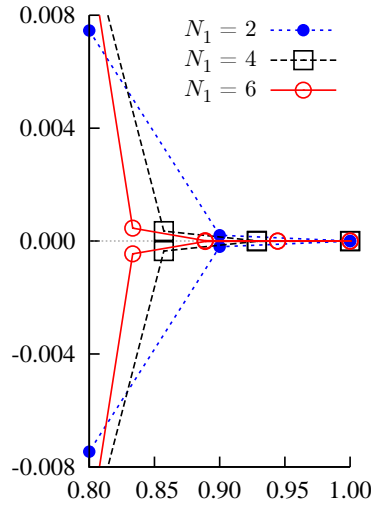
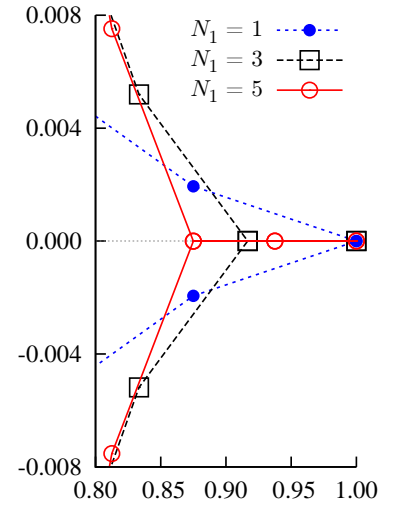
We found a different behavior for systems involving either an even or odd number of wanderers:

- For an even number of wanderers (the two left-hand panels in Fig. 2.13), it can be seen that the number of vanishing exponents is equal to the number of wanderers in the system. In particular, at the equilibrium state ( $\Delta T = 0$ ) the spectra are symmetric. As expected, the symmetry is broken for the non-equilibrium state ( $\Delta T = 4$ ).
- For an odd number of wanderers (the two right-hand panels in Fig. 2.13), in the non-equilibrium state ( $\Delta T = 4$ ), the symmetry is also broken and the number of vanishing exponents is equal to the number of wanderers. By contrast, for equilibrium systems ( $\Delta T = 0$ ), a competition between the conjugate pairing symmetry ( $\lambda_i = \lambda_{D+1-i}$ ) and the number of wanderers occurs. Manifestly in this case, the symmetry prevails (since the number of vanishing exponents does not equal the number of wanderers, as can be seen on the right-hand panel in the figure). We note a second surprising point for the equilibrium case:



$\lambda(2i/D)$ 

**Figure 2.13 :** Enlargement of the Lyapunov spectra for the thermostated modified Lorentz gas (with  $N_2 = 12$  disk scatterers and where the length of the box  $L = 6$ ) for various  $\Delta T$ , with a small number  $N_1$  of wanderer particles, and with  $\eta = 1$ . Reduced Lyapunov indices,  $2i/D$ , are used on the abscissa. For an even number of wanderers (the two panels on the left-hand side): the number of vanishing exponents is equal to the number of wanderers; for on odd number of wanderers (the two panels on the right-hand side): the number of vanishing exponents is equal to the number of wanderers only for the non-equilibrium case ( $\Delta T = 4$ ). (See main text for more details.)

 $\lambda(2i/D)$  $\lambda(2i/D)$ 

**Figure 2.14 :** Enlargement of the Lyapunov spectra for the modified Lorentz gas (with  $N_2 = 12$  disk scatterers and where the length of the box  $L = 6$ ), with a small number  $N_1$  of wanderer particles, and with  $\eta = 1$ . Here, periodic boundary conditions both in the vertical and in the horizontal direction are used. For an even number of wanderers (left-hand side): the number of vanishing exponents is equal to the number  $N_1$  of wanderers; for an odd number of wanderers (right-hand side): the number of vanishing exponents is equal to  $N_1 + 1$ . Reduced indices  $2i/D$  are used on the abscissa.

- If we consider only one wanderer we observe two null exponents (which is in line with Nöther's theorem).
- If we consider three wanderers we observe also two null exponents, and for five wanderers we find four null exponents. The adjacent positive and negative exponents are, however, close to zero.

We performed analogous simulations with periodic boundary conditions also in the horizontal direction (instead of thermostat walls parallel to the  $y$ -axis), where the energy is now conserved and set to  $(N_1 + N_2/2)k_B T^*$ . For the case of an even number of wanderers (left panel in Fig. 2.14) the same result is observed as for the thermostated system at equilibrium ( $\Delta T = 0$ ): the number of vanishing exponents equals the number of the wanderers. For the cases of an odd number of wanderers (right panel in Fig. 2.14) we observe a different behavior:

- If we consider only one wanderer we observe two vanishing exponents (as above).
- But if we consider three wanderers we observe four vanishing exponents, and for five wanderers we find six null exponents.

The experimental result for the number of vanishing exponents is very complicated indeed and not completely understood. The fact that this number agrees (more or less) with the number of wanderer particles points to a phase-space constraint, which we have not been able to identify. The computation of covariant Lyapunov vectors may possibly help and will be carried out in the future.

## 2.5 Chaos and transport

The Lyapunov spectra for non-equilibrium conditions are only slightly shifted from those of the equilibrium system. For  $\Delta T > 0$  the sum of all Lyapunov exponents is negative due to the collisions of wanderers with the thermostats, and thus a multifractal attractor in the phase space appears. We characterize this phenomenon by computing the dimensionality reduction  $\Delta D = D - D_{KY}$ , where  $D_{KY}$  is the Kaplan-Yorke dimension [30]. We show in Fig. 2.15 that  $\Delta D$  for a given  $\Delta T$  varies inversely proportional to the length  $L$  of the box. The simulations have been performed for systems of  $N_2 = 2L$  disk scatterers and  $N_1 = 5L/2$  wanderers. In Sec. 2.3, it has been observed that the heat flux  $J$  is also proportional to  $1/L$ , and we find that  $\Delta D$  is proportional to  $J$ .

In Table 2.1, some of our results are collected for the modified Lorentz gas model consisting of

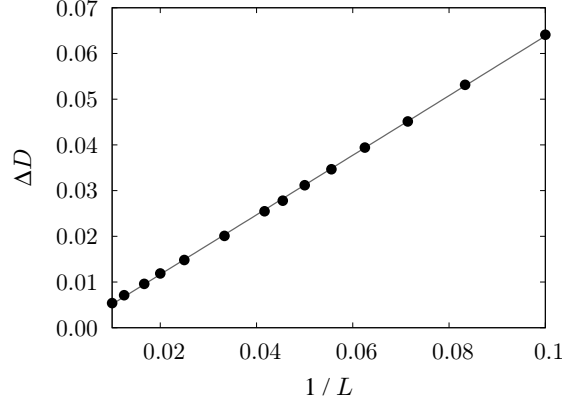


**Figure 2.15 :** Dimensionality reduction  $\Delta D$  as a function of the inverse of the box length,  $1/L$ . The number  $N_2$  of disk scatterers is equal to  $2L$ , and the number  $N_1$  of wanderers is equal to  $5L/2$ . The boundary-temperature difference  $\Delta T = 4$ , whereas the medial temperature  $T^* \equiv (T_1 + T_2)/2$  is fixed to 3. The coupling parameter  $\eta = 1$ .

$N_1 = 10$  wanderers and  $N_2 = 20$  scatterers. We give the heat flux  $Q$ , the dimensionality reduction  $\Delta D$ , the sum of the full Lyapunov exponents  $\sum_{i=1}^D \lambda_i$ , the maximum Lyapunov exponent  $\lambda_1$ , the Kolmogorov-Sinai entropy per point-particle  $h_{KS}/N_1$  (only for equilibrium), the energy per point-particle  $\langle K_1 \rangle/N_1$ , and twice the energy per disk-scatterer  $2\langle K_2 \rangle/N_2$ . The dependence of these quantities on the coupling parameter  $\eta$  and on the temperature difference between the two thermostats  $\Delta T = T_2 - T_1$  is indicated.  $T^* \equiv (T_1 + T_2)/2$  is fixed to 3.

**Table 2.1 :** Simulation results for the thermostated modified Lorentz gas of  $N_1 = 10$  wanderers and  $N_2 = 20$  rotating scatterers, which is shown in Fig. 2.5. The parameter  $\eta$  is dimensionless. The difference between the right and the left boundary temperatures,  $\Delta T$ , is given in units of  $K/k_B$ , where  $K$  is the energy of our system, and  $J$  is the heat flux.  $\lambda_1$  is the maximum Lyapunov exponent [units:  $(K/m\sigma^2)^{1/2}$ ],  $\sum_{i=1}^{4N} \lambda_k$  is the sum over all exponents, and  $h_{KS}/N_1$  is the Kolmogorov-Sinai entropy per point-particle.  $\Delta D = D - D_{KY}$  is the dimensionality reduction, where  $D_{KY}$  is the Kaplan-Yorke (information) dimension and  $D$  the phase-space dimension of the system.

$\eta$	$\Delta T$	$Q$	$\Delta D$	$\sum_{i=1}^D \lambda_i$	$\lambda_1$	$h_{KS}/N_1$
0.5	0	0.0000	0.00000	0.0000	7.610	6.915
	1	0.0234	0.00079	-0.0062	7.789	
	2	0.0459	0.00337	-0.0265	7.861	
	3	0.0672	0.00868	-0.0689	7.947	
	4	0.0854	0.01972	-0.1577	8.006	
1.0	0	0.0000	0.00000	0.0000	6.087	4.227
	1	0.0205	0.00089	-0.0054	6.118	
	2	0.0405	0.00377	-0.0233	6.197	
	3	0.0593	0.00968	-0.0608	6.293	
	4	0.0757	0.02197	-0.1399	6.375	
20.0	0	0.0000	0.00000	0.0000	1.582	1.050
	1	0.0053	0.00088	-0.0014	1.592	
	2	0.0106	0.00377	-0.0061	1.622	
	3	0.0158	0.00977	-0.0163	1.667	
	4	0.0209	0.02532	-0.0387	1.717	

## 2.6 Localization for large systems in microcanonical equilibrium

Another interesting point is the understanding of the manner how the translational part (pertaining to the wanderers) and the rotational part (due to the scatterers) are related. The strength of the coupling between the two parts gives an estimate to what extent the tangent space can be divided into two distinct parts. In this section, periodic boundary conditions are used also in the  $x$ -direction in order to discard the effect of the thermostat walls. We consider a system consisting of  $N_1 = 200$  wanderers and  $N_2 = 200$  scatterers, where the length  $L$  of the box is equal to 10. The energy of the system is set to  $(N_1 + N_2/2)k_B T^*$ , where  $T^* = 3$ .

It is well known for momentum-conserving systems [31] that only a small percentage of wanderers (or scatterers) contributes to the maximum exponential growth, and the perturbation is therefore confined to a small subdomain of space. This localization gets even more pronounced for larger systems until the thermodynamic limit is reached. In contrast, the perturbations belonging to the smallest non-vanishing exponents are spread out on the entire physical space. For a specific class of systems (i.e. smooth hard disks and smooth hard spheres), the small non-vanishing exponents form orthogonal periodic structures in space, the Lyapunov modes, if a sufficiently large number of particles is considered. The Lyapunov modes are a consequence of the existence of the “central manifold” (see Chap. 8). For this specific class of systems, the central manifold is always orthogonal to the stable and unstable subspaces, i.e. the non-exponentially growing (or decaying) perturbation vectors of the tangent space stay always orthogonal to the exponentially growing (or decaying) perturbation vectors during the time evolution. Note that this property is lost if the particles are allowed to rotate as for rough hard disks. This will be treated in Chap. 8.

In Fig. 2.16 we plot, as a snapshot, the projection of the maximum perturbation vector onto the subspaces spanned by the phase variables pertaining to each wanderer  $n$ ,  $\delta\vec{q}_n^2 + \delta\vec{p}_n^2$ , and for each scatterer  $s$ ,  $\delta\omega_s^2$ . The snapshot is taken of a well-relaxed system to ensure that initial conditions do not interfere. We observe that the maximum Lyapunov exponent is strongly localized for both the wanderers and the scatterers, and, in addition, they are both independent from each other. If instead of a snapshot, one follows the projections of Fig 2.16 during the time evolution, the two localized peaks deform and move around in the entire accessible physical space.

To measure the localization property of a system, it is common to use the following definition [32] : First, the contribution of an individual wanderer  $n$  to a particular perturbation vector is

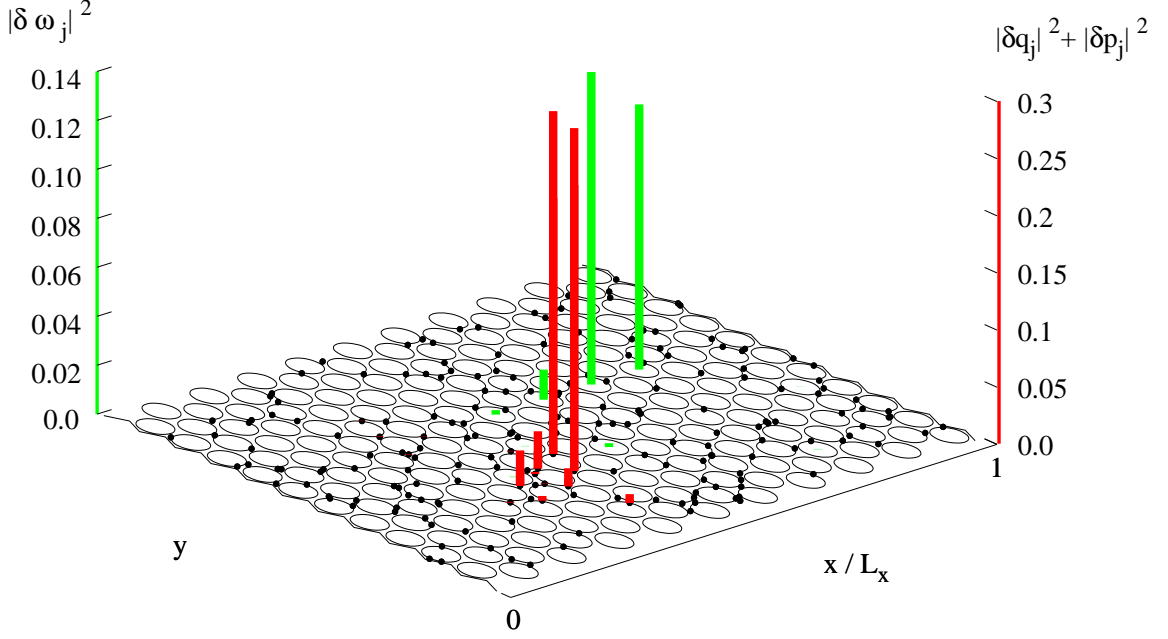


**Figure 2.16 :** For a modified Lorentz gas consisting of  $N_1 = 200$  wanderers and  $N_2 = 200$  scatterers (the length of box  $L = 10$ ), where the coupling parameter  $\eta = 1$ , and with periodic boundary conditions, we show the localization of the rotational and transversal components in the physical  $xy$ -plane, for the maximum Lyapunov exponent.

defined as the square of the projection of  $\delta\Gamma$  onto the subspace pertaining to this wanderer,

$$\mu_n = \frac{\delta \vec{q}_n^2 + \delta \vec{p}_n^2}{\sum_{k=1}^{N_1} (\delta \vec{q}_k^2 + \delta \vec{p}_k^2)} .$$

This quantity acts like a probability measure of the wanderer  $n$  contributing to the perturbation  $\delta\Gamma$ . The localization measure  $W^{(q,p)}$  (to which for simplicity we shall refer to as “localization”) is defined according to the time-averaged Shannon entropy for the “probability” distributions  $\mu_n$ :

$$W^{(q,p)} = \frac{1}{N_1} \exp \left[ - \left\langle \sum_{n=1}^{N_1} \mu_n \ln \mu_n \right\rangle \right] , \text{ and } 1/N_1 \leq W^{(q,p)} \leq 1 ,$$

where the lower and upper bounds apply to complete localization and delocalization, respectively. In the same way we define the contribution of an individual disk-scatterer  $s$  to a particular perturbation vector as the square of the projection of  $\delta\Gamma$  onto the subspace pertaining to this disk scatterer,

$$\mu_s = \frac{\delta \omega_s^2}{\sum_{k=1}^{N_2} \delta \omega_k^2} .$$

The localization  $W^{(\omega)}$  is thus defined as

$$W^{(\omega)} = \frac{1}{N_2} \exp \left[ - \left\langle \sum_{s=1}^{N_2} \mu_s \ln \mu_s \right\rangle \right] , \text{ and } 1/N_2 \leq W^{(\omega)} \leq 1 .$$

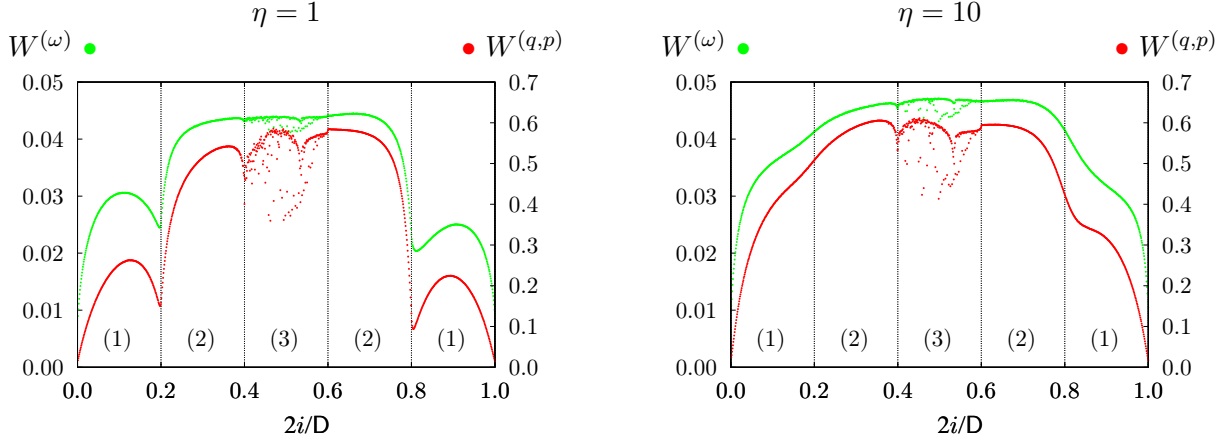


**Figure 2.17 :** Normalized localization  $W$  for the full perturbation vector set, as function of the normalized Lyapunov index  $2i/D$ , for the same model described in Fig. 2.16, for the coupling parameters  $\eta \in \{1, 10\}$ .

In Fig. 2.17, we show the localizations  $W^{(q,p)}$  and  $W^{(\omega)}$  as a function of the normalized Lyapunov indices  $2i/D$ , for two different values of the parameter  $\eta$ . One observes that the transversal part of the perturbation vectors is strongly localized for the large Lyapunov exponents (1) and is relatively well spread out on the entire physical space for the small (2) and null (3) exponents. Even though we observe the same general form for the rotational part, it seems that this part is more or less strongly localized for all Lyapunov indices (note the scale in Fig. 2.17). In Fig. 2.9, we observed a jump between the Lyapunov exponents  $\lambda_{N_1}$  and  $\lambda_{N_1+1}$ , which disappears progressively for growing coupling parameter  $\eta$ . Concomitantly, one notes in Fig. 2.17 that, for large  $\eta$ , the localization becomes a monotonic increasing (decreasing) function of the Lyapunov index  $i$  for positive (negative) Lyapunov exponents.

## 2.7 Conclusion

Our results are well in line with those reported by Mejía-Monasterio *et al.* [8, 9] who originally introduced the modified Lorentz gas. The model has been investigated more recently focussing on the mathematical description [33, 34, 35, 36]. These studies assume a Hamiltonian character of the wanderer-scatterer collisions, in which case the Boltzmann master equation is derived from the Liouville equation.

In order to test that the wanderer-scatterer collisions derive from a Hamiltonian description, we considered the modified Lorentz gas with periodic boundary conditions in both directions to eliminate the influence of the thermostat. The equations that govern the collisions comply with the conservation of energy and of angular momentum. We found that the localization spectra (Fig. 2.17) are not symmetric ( $W_{D+1-i}^{(q,p)} \neq W_i^{(q,p)}$ ), which is a clear indication for the non-

Hamiltonian character of the system. We shall come back to this point in the last chapter of this thesis. The rough-hard-disk system of Chap. 8 shows similar asymmetries and was analyzed in more detail. We indeed show there that the Hamiltonian character is broken due to the rotational degrees of freedom. Its equations derive from the conservation of energy and angular momentum, as is the case for the modified Lorentz gas, and in addition from the conservation of transversal momentum. However, the conservation of the transversal momentum does not influence the Hamiltonian character of a system. We suggest that the non-Hamiltonian character is due to the angular momentum constraint. This can be seen as a (non-holonomic) constraint implying a “mixing” of the position and of the velocity of the particles, which breaks down the symplectic structure of the tangent space. Our observations corroborate the remark of Gaspard and Gilbert concerning the modified Lorentz gas [37, p. 3].

## 2.8 Appendix: Wanderer-scatterer collisions for the three-dimensional modified Lorentz gas

To determine the transformation map of wanderer-scatterer collisions in the phase space as well as the respective linearized map in the tangent space, we first consider the three-dimensional modified Lorentz gas, and then reduce it to the two-dimensional model.

If the  $N_1$  wanderers, which are located at  $\{\vec{q}_n\}_{n=1}^{N_1}$ , move with transversal momenta  $\{\vec{p}_n\}_{n=1}^{N_1}$ , and if the  $N_2$  spherical scatterers rotate with angular velocities  $\{\vec{\omega}_s\}_{s=1}^{N_2}$ , the state vector is written as

$$\mathbf{\Gamma} = \left( \{\vec{q}_n\}_{n=1}^{N_1}, \{\vec{p}_n\}_{n=1}^{N_1}, \{\vec{\omega}_s\}_{s=1}^{N_2} \right) ,$$

where the angular positions of the spherical scatterers do not appear because of their isotropy. In the same way, considering the associated perturbation vectors  $\{\delta\vec{q}_n\}_{n=1}^{N_1}$ ,  $\{\delta\vec{p}_n\}_{n=1}^{N_1}$  and  $\{\delta\vec{\omega}_s\}_{s=1}^{N_2}$ , an arbitrary Lyapunov vector is written as

$$\delta\mathbf{\Gamma} = \left( \{\delta\vec{q}_n\}_{n=1}^{N_1}, \{\delta\vec{p}_n\}_{n=1}^{N_1}, \{\delta\vec{\omega}_s\}_{s=1}^{N_2} \right) .$$

Let us consider the collision event of a wandering point-particle  $k$  of mass  $m$  with a spherical scatterer  $\ell$  of diameter  $\sigma$  (which is fixed in its center and is allowed to rotate with a moment of inertia  $I$ ). The phase point  $\mathbf{\Gamma}$  and an arbitrary tangent vector  $\delta\mathbf{\Gamma}$  of the system undergo changes only in their components belonging to the wanderer  $k$  and to the scatterer  $\ell$ .

### 2.8.1 Phase space dynamics

Unlike in Ref. [21], we cannot use directly the transformation rule for two rough spheres of Chapman *et al.* (Sec. 11.6 of Ref. [38]), because the transversal momentum is not conserved. However, we operate in a similar manner, using the conservation laws of energy and of total angular momentum.

To determine the three-dimensional “rough-hard-collision” rule between a wanderer  $k$  and a scatterer  $\ell$ , we express the outgoing transversal momentum  $\vec{p}'_k$  and the angular velocity  $\vec{\omega}'_\ell$  as function of the incoming quantities,  $\vec{p}_k$  and  $\vec{\omega}_\ell$ . For that purpose, we introduce the quantities:

$$\Delta\vec{p}_k = \vec{p}'_k - \vec{p}_k ; \quad \Delta\vec{\omega}_\ell = \vec{\omega}'_\ell - \vec{\omega}_\ell .$$



Hence, the conservation of the energy is written as follows

$$\frac{\Delta \vec{p}_k}{m} \cdot (\Delta \vec{p}_k + 2 \vec{p}_k) + I \Delta \vec{\omega}_\ell \cdot (\Delta \vec{\omega}_\ell + 2 \vec{\omega}_\ell) = 0 . \quad (2.5)$$

According to the total-angular-momentum conservation,  $\Delta \vec{\omega}_\ell = 2/(m\sigma\eta) (\Delta \vec{p}_k \times \vec{n})$  (where the unit vector  $\vec{n} = 2/\sigma (\vec{q}_k - \vec{q}_\ell)$  and the coupling parameter  $\eta = 4I/m\sigma^2$ ), each part of Eq. (2.5) can be expressed solely in terms of  $\Delta \vec{p}_k$ :

$$\Delta \vec{\omega}_\ell \cdot \Delta \vec{\omega}_\ell = \left( \frac{2}{m\sigma\eta} \right)^2 [\Delta \vec{p}_k - (\vec{n} \cdot \Delta \vec{p}_k) \vec{n}] \cdot \Delta \vec{p}_k , \quad (2.6)$$

$$\Delta \vec{\omega}_\ell \cdot \vec{\omega}_\ell = \frac{2}{m\sigma\eta} (\vec{n} \times \vec{\omega}_\ell) \cdot \Delta \vec{p}_k . \quad (2.7)$$

Since  $\Delta \vec{p}_k \neq \vec{0}$ , Eqs. (2.5), (2.6) and (2.7) yield

$$\left( 1 + \frac{1}{\eta} \right) \Delta \vec{p}_k - \frac{1}{\eta} (\vec{n} \cdot \Delta \vec{p}_k) \vec{n} + 2 \left( \vec{p}_k + \frac{\sigma}{2} (\vec{n} \times \vec{\omega}_\ell) \right) = \vec{0} . \quad (2.8)$$

If we project Eq. (2.8) onto the unit vector  $\vec{n}$ , we find  $\vec{n} \cdot \Delta \vec{p}_k = -2\vec{n} \cdot \vec{p}_k$ , which gives

$$\vec{q}'_k = \vec{q}_k , \quad (2.9)$$

$$\vec{p}'_k = \vec{p}_k - 2m\gamma \vec{g} - 2\beta (\vec{n} \cdot \vec{p}_k) \vec{n} , \quad (2.10)$$

$$\vec{\omega}'_\ell = \vec{\omega}_\ell + \frac{4\beta}{\sigma} (\vec{n} \times \vec{g}) , \quad (2.11)$$

where the constant parameters  $\gamma = \eta/(1 + \eta)$  and  $\beta = 1/(1 + \eta)$ , and where

$$\vec{g} = \frac{\vec{p}_k}{m} + \frac{\sigma}{2} (\vec{n} \times \vec{\omega}_\ell) ,$$

which corresponds to the velocity of the impact point on the surface of the scatterer.

From Eqs. (2.9) - (2.11) in three dimensions, the respective collision map for the rough scatterer-wanderer collision in two dimensions (Eqs. (2.1) - (2.3) on p. 33) follow immediately.

### 2.8.2 Tangent space dynamics

For the sake of simplicity we define by

$$\delta \mathbf{\Gamma}_{k\ell} = \left( \delta \vec{q}_k, \delta \vec{p}_k, \delta \vec{\omega}_\ell \right) ,$$

the part of an arbitrary perturbation vector  $\delta \mathbf{\Gamma}$ , which undergoes changes due to the collision. According to [11] (as mentioned in the Introduction, see p. 7), we can express, by linearization,

the new components of  $\delta\mathbf{\Gamma}'_{k\ell}$  as follows

$$\delta\vec{q}'_k = \frac{\partial\vec{q}'_k}{\partial\mathbf{\Gamma}_{k\ell}} \delta\mathbf{\Gamma}_{k\ell} + \frac{1}{m} \left( \frac{\partial\vec{q}'_k}{\partial\vec{q}_k} \vec{p}_k \delta\tau_c - \vec{p}'_k \delta\tau_c \right) , \quad (2.12)$$

$$\delta\vec{p}'_k = \frac{\partial\vec{p}'_k}{\partial\mathbf{\Gamma}_{k\ell}} \delta\mathbf{\Gamma}_{k\ell} + \frac{1}{m} \left( \frac{\partial\vec{p}'_k}{\partial\vec{q}_k} \vec{p}_k \delta\tau_c \right) , \quad (2.13)$$

$$\delta\vec{\omega}'_\ell = \frac{\partial\vec{\omega}'_\ell}{\partial\mathbf{\Gamma}_{k\ell}} \delta\mathbf{\Gamma}_{k\ell} + \frac{1}{m} \left( \frac{\partial\vec{\omega}'_\ell}{\partial\vec{q}_k} \vec{p}_k \delta\tau_c \right) , \quad (2.14)$$

where,  $\delta\tau_c = -(\delta\vec{q}_k \cdot \vec{n})/(\vec{p}_k \cdot \vec{n})$  is the infinitesimal time shift between the collision of the reference and the perturbed trajectories. Using directly the results of Eqs. (2.9) - (2.11), it yields

$$\begin{aligned} \frac{\partial\vec{q}'_k}{\partial\mathbf{\Gamma}_{k\ell}} \delta\mathbf{\Gamma}_{k\ell} &= \delta\vec{q}_k , \\ \frac{\partial\vec{p}'_k}{\partial\mathbf{\Gamma}_{k\ell}} \delta\mathbf{\Gamma}_{k\ell} &= \delta\vec{p}_k - 2m\gamma\delta\vec{g} - 2\beta \left[ (\delta\vec{n} \cdot \vec{p}_k + \vec{n} \cdot \delta\vec{p}_k) \vec{n} + (\vec{n} \cdot \vec{p}_k) \delta\vec{n} \right] , \\ \frac{\partial\vec{\omega}'_\ell}{\partial\mathbf{\Gamma}_{k\ell}} \delta\mathbf{\Gamma}_{k\ell} &= \delta\vec{\omega}_\ell + \frac{4\beta}{\sigma} (\delta\vec{n} \times \vec{g} + \vec{n} \times \delta\vec{g}) . \end{aligned}$$

The second terms of the Eqs. (2.12) - (2.14) are given by

$$\begin{aligned} \frac{\partial\vec{q}'_k}{\partial\vec{q}_k} \vec{p}_k \delta\tau_c - \vec{p}'_k \delta\tau_c &= \left[ 2m\gamma\vec{g} + 2\beta(\vec{n} \cdot \vec{p}_k) \vec{n} \right] \delta\tau_c , \\ \frac{\partial\vec{p}'_k}{\partial\vec{q}_k} \vec{p}_k \delta\tau_c &= -2m\gamma \frac{\partial\vec{g}}{\partial\vec{q}_k} \vec{p}_k \delta\tau_c \\ &\quad - 2\beta \left[ \left\{ \left( \frac{\partial\vec{n}}{\partial\vec{q}_k} \vec{p}_k \delta\tau_c \right) \cdot \vec{p}_k \right\} \vec{n} + (\vec{n} \cdot \vec{p}_k) \left( \frac{\partial\vec{n}}{\partial\vec{q}_k} \vec{p}_k \delta\tau_c \right) \right] , \\ \frac{\partial\vec{\omega}'_\ell}{\partial\vec{q}_k} \vec{p}_k \delta\tau_c &= \frac{4\beta}{\sigma} \left[ \left( \frac{\partial\vec{n}}{\partial\vec{q}_k} \vec{p}_k \delta\tau_c \right) \times \vec{g} + \vec{n} \times \left( \frac{\partial\vec{g}}{\partial\vec{q}_k} \vec{p}_k \delta\tau_c \right) \right] . \end{aligned}$$

Here,

$$\begin{aligned} \frac{\partial\vec{n}}{\partial\vec{q}_k} \vec{p}_k \delta\tau_c &= \frac{2}{\sigma} \vec{p}_k \delta\tau_c , & \frac{\partial\vec{g}}{\partial\vec{q}_k} \vec{p}_k \delta\tau_c &= (\vec{p}_k \delta\tau_c) \times \vec{\omega}_\ell , \\ \delta\vec{n} &= \frac{2}{\sigma} \delta\vec{q}_k , & \delta\vec{g} &= \frac{\delta\vec{p}_k}{m} + \delta\vec{q}_k \times \vec{\omega}_\ell + \frac{\sigma}{2} \vec{n} \times \delta\vec{\omega}_\ell . \end{aligned}$$

We define

$$\delta\vec{q}_c = \delta\vec{q}_k + \frac{\vec{p}_k}{m} \delta\tau_c , \quad \delta\vec{g}_c = \frac{\delta\vec{p}_k}{m} + \delta\vec{q}_c \times \vec{\omega}_\ell + \frac{\sigma}{2} \vec{n} \times \delta\vec{\omega}_\ell ,$$

where  $\delta\vec{q}_c$  corresponds to the shift in configuration space between the collision points of the reference and of the satellite trajectories, and  $\delta\vec{g}_c$  follows from  $\delta\vec{g}$  by replacing  $\delta\vec{q}$  by  $\delta\vec{q}_c$ . We thus obtain for the post-collisional components of the perturbation vector for the wanderer  $k$

and the spherical scatterer  $\ell$

$$\delta \vec{q}'_k = \delta \vec{q}_k + \left[ \gamma \vec{g} + \frac{2\beta}{m} (\vec{n} \cdot \vec{p}_k) \vec{n} \right] \delta \tau_c, \quad (2.15)$$

$$\delta \vec{p}'_k = \delta \vec{p}_k - 2m\gamma \delta \vec{g}_c - \frac{4\beta}{\sigma} \left[ (\delta \vec{q}_c \cdot \vec{p}_k) \vec{n} + \frac{\sigma}{2} (\vec{n} \cdot \delta \vec{p}_k) \vec{n} + (\vec{n} \cdot \vec{p}_k) \delta \vec{q}_c \right], \quad (2.16)$$

$$\delta \vec{\omega}'_\ell = \delta \vec{\omega}_\ell + \frac{4\beta}{\sigma^2} \left[ \delta \vec{q}_c \times \vec{g} + \frac{\sigma}{2} (\vec{n} \times \delta \vec{g}_c) \right]. \quad (2.17)$$

If the moment of inertia is set to zero (i.e.  $\gamma = 0$  and  $\beta = 1$ ), the linearized collision map of the simple Lorentz gas is recovered, with the important requirement that the angular velocity perturbations are discarded.

Restricting these linearized collision maps to the two-dimensional case of a wanderer collision with a disk, one obtains the equations which we used for the computation of the Lyapunov spectrum of the modified Lorentz gas in Sec. 2.4.

## References

- [1] J.B. Fourier, *Théorie analytique de la chaleur* (Didot, Paris, 1822).
- [2] B. Moran, Wm.G. Hoover, and S. Bestiale, J. Stat. Phys. **48**, 709 (1987).
- [3] Wm.G. Hoover, B. Moran, C.G. Hoover, and W.J. Evans, Phys. Letter A **133**, 114 (1988).
- [4] H.A. Posch, Ch. Dellago, Wm.G. Hoover, and O. Kum, in *Pioneering Ideas for the Physical and Chemical Sciences: Josef Loschmidts Contributions and Modern Developments in Structural Organic Chemistry, Atomistics and Statistical Mechanics*, edited by W. Fleischhacker and T. Schönfeld (Plenum, New York, 1997) p. 233.
- [5] Wm.G. Hoover, J. Chem. Phys. **109**, 4164 (1998).
- [6] J.L. Lebowitz and H. Spohn, J. Stat. Phys. **19**, 633 (1978).
- [7] J.L. Lebowitz and H. Spohn, J. Stat. Phys. **28**, 539 (1982).
- [8] C. Mejía-Monasterio, H. Larralde, and F. Leyvraz, Phys. Rev. Lett. **86**, 5417 (2001).
- [9] H. Larralde, F. Leyvraz, and C. Mejía-Monasterio, J. Stat. Phys. **113**, 197 (2003).
- [10] B.L. Holian, Wm.G. Hoover, and H.A. Posch, Phys. Rev. Lett. **59**, 10 (1987).
- [11] Ch. Dellago, H.A. Posch, and Wm.G. Hoover, Phys. Rev. E **53**, 1485 (1996).

- [12] H.A. Posch and Wm.G. Hoover, Phys. Rev. E **58**, 4344 (1998).
- [13] D.J. Evans and G.P. Morriss, *Statistical Mechanics of NonEquilibrium Liquids* (Cambridge University Press, 2nd ed., 2008).
- [14] Wm.G. Hoover, *Time reversibility, computer simulation, and chaos* (World Scientific, Singapore, 1999).
- [15] H. van Beijeren, private communication.
- [16] N.I. Chernov and J.L. Lebowitz, J. Stat. Phys. **86**, 953 (1997).
- [17] A. Dhar and D. Dhar, Phys. Rev. Lett. **82**, 480 (1999).
- [18] G. Benettin, L. Galgani, A. Giorgilli, and J.M. Strelcyn, *Part I: Theory*, Meccanica **15**, 9 (1980).
- [19] G. Benettin, L. Galgani, A. Giorgilli, and J.M. Strelcyn, *Part II: Numerical application*, Meccanica **15**, 9 (1980).
- [20] I. Shimada and T. Nagashima, Prog. Theor. Phys. **61**, 1605 (1979).
- [21] J.A. van Meel and H.A. Posch, Phys. Rev. E **80**, 016206 (2009).
- [22] P. Gaspard, *Chaos, Scattering, and Statistical Mechanics* (Cambridge University Press, 1998).
- [23] D. Ruelle, Publ. Math. de l'IHÉS **50**, 27 (1979).
- [24] F. Ginelli, P. Poggi, A. Turchi, H. Chaté, R. Livi, and A. Politi, Phys. Rev. Lett. **99**, 130601 (2007).
- [25] H. Bosetti and H.A. Posch, Chem. Phys. **375**, 296 (2010).
- [26] Ch. Dellago and H.A. Posch, Phys. Rev. E **55**, R9 (1997).
- [27] N.S. Krylov, *Works on the Foundations of Statistical Mechanics* edited by A.S. Wightman and P.A. Anderson (Princeton University Press, Princeton, 1979) p.239; Appendix by Y.G. Sinai.
- [28] M. Falcioni, U.M.B. Marconi, and A. Vulpiani, Phys. Rev. A **44**, 2263 (1991).
- [29] J.B. Pesin, Russian Math. Surveys **32**, 55 (1977).

- 
- [30] J.L. Kaplan and J.A. Yorke, in *Functional differential Equations and Approximation of Fixed Points*, Lecture Notes in Mathematics **vol. 730**, edited by H.O. Walther and H.O. Peitzen (Springer-Verlag, Berlin, 1979) p. 204.
  - [31] Ch. Forster, R. Hirschl, H.A. Posch, and Wm.G. Hoover, *Physica D* **187**, 294 (2004).
  - [32] T. Taniguchi and G.P. Morriss, *Phys. Rev E* **68**, 046203 (2003).
  - [33] J.P. Eckmann and L.S. Young, *Europhys. Lett.* **68**, 790 (2004).
  - [34] J.P. Eckmann and L.S. Young, *Commun. Math. Phys.* **262**, 237 (2006).
  - [35] K.K. Lin and L.S. Young, *J. Stat. Phys.* **128**, 607 (2007).
  - [36] K. Ravishankar and L.S. Young, *J. Stat. Phys.* **128**, 641 (2007).
  - [37] P. Gaspard and T. Gilbert, *New. J. Phys.* **10**, 103004 (2008).
  - [38] S. Chapman and T.G. Cowling, *The Mathematical Theory of Non-Uniform Gases* (Cambridge University Press, New York, 3rd ed., 1990).



## Part II

# Tangent bundle dynamics and its consequences

### Contents

3	Covariant Lyapunov vectors for rigid disk systems	61
4	Covariant Lyapunov vectors for the field-free Lorentz gas	105
5	Time-reversal symmetry for simple models in/out of thermal equilibrium	119
6	Symmetry properties of Lyapunov vectors and local exponents	145
7	Domination and convergence of Lyapunov spectra for smooth-hard-disk systems	149
8	How rotation breaks the Hamiltonian character of rough-hard-disk systems	157





This chapter has been published as  
**H. Bosetti and H.A. Posch,**  
*Covariant Lyapunov vectors for rigid disk systems,*  
**Chem. Phys. 375, p. 296 (2010).**  
 Sec. 3.8 was not included in this publication  
 and has been added here.

# CHAPTER 3

## Covariant Lyapunov vectors for rigid disk systems

### Contents

---

3.1	Introduction . . . . .	<b>62</b>
3.2	Phase-space and tangent-space dynamics . . . . .	<b>63</b>
3.3	Numerical considerations . . . . .	<b>65</b>
3.4	A simple example: the Hénon map . . . . .	<b>67</b>
3.5	Systems of hard disks . . . . .	<b>67</b>
3.6	Conclusion . . . . .	<b>88</b>
3.7	Acknowledgements . . . . .	<b>89</b>
3.8	Appendix . . . . .	<b>90</b>
	References . . . . .	<b>102</b>

---

### Abstract

We carry out extensive computer simulations to study the Lyapunov instability of a two-dimensional hard-disk system in a rectangular box with periodic boundary conditions. The system is large enough to allow the formation of Lyapunov modes parallel to the  $x$ -axis of the box. The Oseledec splitting into covariant subspaces of the tangent space is considered by computing the full set of covariant perturbation vectors co-moving with the flow in tangent space. These vectors are shown to be transversal, but generally not orthogonal to each other. Only the angle between covariant vectors associated with immediate adjacent Lyapunov exponents in the Lyapunov spectrum may become small, but the probability of this angle to vanish approaches zero. The stable and unstable manifolds are transverse to each other and the system is hyperbolic.

### 3.1 Introduction

Lyapunov exponents measure the exponential growth, or decay, of infinitesimal phase-space perturbations of a chaotic dynamical system. For a  $D$ -dimensional phase space, there are  $D$  exponents, which, if ordered according to size,  $\lambda_i \geq \lambda_{i+1}$ , are referred to as the Lyapunov spectrum. The classical algorithm for the computation is based on the fact that almost all volume elements of dimension  $d \leq D$  in tangent space (with the exception of elements of measure zero) asymptotically evolve with an exponential rate which is equal to the sum of the first  $d$  Lyapunov exponents. Such a  $d$ -dimensional subspace may be spanned by  $d$  orthonormal vectors, which may be constructed by the Gram-Schmidt procedure and, therefore, are referred to as Gram-Schmidt (GS) vectors. The GS vectors are not covariant, which means that at any point in phase space they are not mapped by the linearized dynamics into the GS vectors at the forward images of that point [1]. As a consequence, they are not invariant with respect to the time-reversed dynamics. Due to the periodic re-orthonormalization of the GS vectors only the radial dynamics is exploited for the computation of the exponents, whereas the angular information is discarded.

Although the angular dynamics is not a universal property and may depend, for example, on the choice of the coordinate system [2], it would be advantageous for many applications, to span the subspaces mentioned above by covariant vectors and to study also the angular dynamics of and between these vectors. It has the additional advantage to preserve the time-reversal symmetry for these tangent vectors, a property not displayed by the GS vectors. Recently, an efficient numerical procedure was developed by Ginelli *et al.* [1] for the computation of covariant Lyapunov vectors. Here, we apply their algorithm to a two-dimensional system of rigid disks.

The choice of hard elastic particles is motivated by the fact that their dynamics is comparatively simple, and their ergodic, structural and dynamical properties are well known and are thought to be typical of more realistic physical systems [3]. Secondly, hard-particle systems in two and three dimensions serve as reference systems for the most successful perturbation theories of dense gases and liquids [4, 5]. Finally, the combination of a Lyapunov analysis with novel statistical methods for rare events [6] seems particularly promising for the study of such rare transformations in systems, for which hard core interactions are at the root.

The paper is organized as follows. After an introduction of the basic concepts for the dynamics of phase-space perturbations in Sec. 3.2, we summarize in Sec. 3.3 the features and our numerical implementation of the algorithm of Ginelli *et al.* [1] for the computation of covariant vectors and covariant subspaces. In Sec. 3.4, the Hénon map serves as a simple two-dimensional illustration. The hard-disk model is introduced in Sec. 3.5. In this work we restrict ourselves to 198 disks,

a number which is dictated by computational economy, but still large enough to allow the study of Lyapunov modes. In Sec. 3.5.1 we study the relative orientations of Gram-Schmidt and covariant vectors, which give rise to the same Lyapunov exponents. Next, in Sec. 3.14, we compare the localization properties in physical space for these two sets of perturbation vectors. The configuration and momentum space projections of the perturbation vectors – Gram-Schmidt or covariant – are the topic of Sec. 3.5.3. The central manifold (or null subspace) and its dependence on the intrinsic continuous symmetries – translation invariance with respect to time and space – is discussed in Sec. 3.5.4. Although the null subspace is completely orthogonal to the unstable and stable subspaces, it is essential for a proper understanding of the Lyapunov modes [7, 8]. Sec. 3.5.5 is devoted to a discussion of these modes and how they are represented by the covariant vectors. In Subsec. 3.5.6 we compute the angles between the covariant modes and test for tangency between covariant Oseledec subspaces. In Sec. 3.6 we conclude with a summary.

## 3.2 Phase-space and tangent-space dynamics

The dynamics of a system of hard disks is that of free flight, interrupted by elastic binary collisions. If  $\Gamma_0$  denotes the state of the system at time 0, the state at time  $t$  is given by  $\Gamma_t = \phi^t(\Gamma_0)$ , where  $\phi^t : \mathbf{X} \rightarrow \mathbf{X}$  defines the flow in the phase space  $\mathbf{X}$ . Similarly, if  $\delta\Gamma_0$  is a vector in tangent space  $\mathbf{TX}$  at  $\Gamma_0$ , at time  $t$  it becomes  $\delta\Gamma_t = D\phi^t|_{\Gamma_0}\delta\Gamma_0$ , where  $D\phi^t$  defines the tangent flow. It is represented by a  $D \times D$  matrix, where  $D$  is the dimension of phase space. A subspace  $\mathbf{E}^{(i)}$  of the phase space is said to be covariant if

$$D\phi^t|_{\Gamma_0}\mathbf{E}^{(i)}(\Gamma_0) = \mathbf{E}^{(i)}(\phi^t(\Gamma_0)). \quad (3.1)$$

This definition also applies to covariant vectors, if  $\mathbf{E}^{(i)}$  is one-dimensional. Loosely speaking, covariant subspaces (vectors) are co-moving (co-rotating in particular) with the tangent flow. An analogous relation holds for the time-reversed flow.

Next we consider the decomposition of the tangent space into subspaces according to the *multiplicative ergodic theorem* of Oseledec [9, 10, 11]. Here, we closely follow Ref. [7].

The first part of the multiplicative ergodic theorem asserts that the real and symmetric matrices

$$\Lambda_{\pm} = \lim_{t \rightarrow \pm\infty} \left( [D\phi^t|_{\Gamma}]^{\dagger} D\phi^t|_{\Gamma} \right)^{1/2|t|} \quad (3.2)$$

exist for (almost all) phase points  $\Gamma$ . Here,  $\dagger$  denotes transposition. The eigenvalues of  $\Lambda_+$  are

ordered according to  $\exp(\lambda^{(1)}) > \dots > \exp(\lambda^{(\ell)})$ , where the  $\lambda^{(j)}$  are the Lyapunov exponents, which appear with multiplicity  $m^{(j)}$ . For symplectic systems as in our case,  $\lambda^{(j)} = -\lambda^{(\ell+1-j)}$ , which is referred to as conjugate pairing. Similarly, the eigenvalues of  $\Lambda_-$  are  $\exp(-\lambda^{(\ell)}) > \dots > \exp(-\lambda^{(1)})$ . The eigenspaces of  $\Lambda_{\pm}$  associated with  $\exp(\pm\lambda^{(j)})$  are denoted by  $\mathbf{U}_{\pm}^{(j)}$ . They are pairwise orthogonal but *not* covariant. If the  $\lambda^{(j)}$  are degenerate with multiplicity  $m^{(j)} = \dim \mathbf{U}_{\pm}^{(j)}$ , all multiplicities sum to  $\mathbf{D}$ , the dimension of the phase space. Since the matrices  $\Lambda_{\pm}$  are symmetrical, each of the two sets of eigenspaces,  $\{\mathbf{U}_{\pm}^{(j)}\}$ , completely span the tangent space,

$$\mathbf{TX}(\mathbf{\Gamma}) = \mathbf{U}_{\pm}^{(1)}(\mathbf{\Gamma}) \oplus \dots \oplus \mathbf{U}_{\pm}^{(\ell)}(\mathbf{\Gamma}). \quad (3.3)$$

The eigenspaces  $\mathbf{U}_{\pm}^{(j)}$  are not covariant, but the subspaces

$$\mathbf{U}_{+}^{(j)} \oplus \dots \oplus \mathbf{U}_{+}^{(\ell)} \quad \text{and} \quad \mathbf{U}_{-}^{(1)} \oplus \dots \oplus \mathbf{U}_{-}^{(j)}, \quad j \in \{1, \dots, \ell\}, \quad (3.4)$$

are. They are, respectively, the most stable subspace of dimension  $\sum_{i=j}^{\ell} m^{(i)}$  of  $\Lambda_{+}$ , and the most-unstable subspace of dimension  $\sum_{i=1}^j m^{(i)}$  of  $\Lambda_{-}$  (corresponding to the most stable subspace of that dimension in the past).

The second part of Oseledec' theorem asserts that for (almost) every phase-space point  $\mathbf{\Gamma}$  there exists another decomposition of the tangent space into *covariant subspaces*  $\mathbf{E}^{(j)}(\mathbf{\Gamma})$  referred to as Oseledec splitting,

$$\mathbf{TX}(\mathbf{\Gamma}) = \mathbf{E}^{(1)}(\mathbf{\Gamma}) \oplus \dots \oplus \mathbf{E}^{(\ell)}(\mathbf{\Gamma}). \quad (3.5)$$

For  $\delta\mathbf{\Gamma} \in \mathbf{E}^{(j)}(\mathbf{\Gamma})$  the respective Lyapunov exponent follows from

$$\lim_{t \rightarrow \pm\infty} \frac{1}{|t|} \log \|D\phi^t|_{\mathbf{\Gamma}} \delta\mathbf{\Gamma}\| = \pm\lambda^{(j)} \quad \forall j \in \{1, \dots, \ell\}. \quad (3.6)$$

The subspaces  $\mathbf{E}^{(j)}$  are covariant (see Eq. (3.1)) but, in general, not orthogonal. According to Ruelle [10], they are related to the eigenspaces  $\mathbf{U}_{\pm}^{(j)}$  of  $\Lambda_{\pm}$ :

$$\mathbf{E}^{(j)} = \left( \mathbf{U}_{-}^{(1)} \oplus \dots \oplus \mathbf{U}_{-}^{(j)} \right) \cap \left( \mathbf{U}_{+}^{(j)} \oplus \dots \oplus \mathbf{U}_{+}^{(\ell)} \right). \quad (3.7)$$

This equation is at the heart of the construction of covariant vectors according to Ginelli *et al.* as described in the next section. Furthermore, one can show that

$$\mathbf{F}^{(j)} \equiv \mathbf{E}^{(1)} \oplus \dots \oplus \mathbf{E}^{(j)} = \mathbf{U}_{-}^{(1)} \oplus \dots \oplus \mathbf{U}_{-}^{(j)} \quad (3.8)$$

are covariant subspaces.

### 3.3 Numerical considerations

Numerical methods probe the tangent space by a set of  $D$  tangent vectors, such that the Lyapunov exponents are repeated with multiplicities,  $\lambda_1 \geq \dots \geq \lambda_D$ . Here, the lower index is referred to as the Lyapunov index. The relation between the  $\lambda^{(j)}$  and  $\lambda_i$  is given by

$$\lambda^{(j)} = \lambda_{f^{(j-1)+1}} = \dots = \lambda_{f^{(j)}},$$

where  $f^{(j)} = m^{(1)} + \dots + m^{(j)}$  is the sum of all subspace dimensions up to  $j$ .

For notational convenience in the following, the vectors  $\mathbf{g}_k^j$ ,  $j = 1, \dots, D$ , spanning the tangent space at time  $t_k$ , are arranged as column vectors of a  $D \times D$  matrix  $\mathbf{G}_k \equiv (\mathbf{g}_k^1 | \dots | \mathbf{g}_k^D)$ . The same convention is used below for other spanning vector sets such as  $\overline{\mathbf{G}}_k \equiv (\overline{\mathbf{g}}_k^1 | \dots | \overline{\mathbf{g}}_k^D)$  and  $\mathbf{V}_k \equiv (\mathbf{v}_k^1 | \dots | \mathbf{v}_k^D)$ .

In the classical algorithm of Benettin *et al.* [12] and Shimada and Nagashima *et al.* [13] for the computation of Lyapunov exponents, an orthonormal set of tangent vectors  $\mathbf{G}_{k-1}$  at time  $t_{k-1}$  is evolved to a time  $t_k \equiv t_{k-1} + \tau$ , ( $\tau > 0$ ),

$$\overline{\mathbf{G}}_k = \mathbf{J}_{k-1}^\tau \mathbf{G}_{k-1},$$

where  $\mathbf{J}_{k-1}^\tau$  is the Jacobian of the evolution map taking the phase space point  $\mathbf{\Gamma}_{k-1}$  at time  $t_{k-1}$  to  $\mathbf{\Gamma}_k$  at time  $t_k$ . The column vectors of  $\overline{\mathbf{G}}_k$  at time  $t_k$  generally are not orthonormal any more and need to be re-orthonormalized with a Gram-Schmidt procedure. This gives the matrix  $\mathbf{G}_k$  with column vectors  $\{\mathbf{g}^j\}_k$ , which form the next orthonormal Gram-Schmidt (GS) basis at time  $t_k$ . These vectors are pairwise orthogonal but not covariant. Each GS renormalization step is equivalent to a so-called QR decomposition of the matrix  $\overline{\mathbf{G}}_k$ ,  $\overline{\mathbf{G}}_k = \mathbf{G}_k \mathbf{R}_k$ , where the matrix  $\mathbf{R}_k$  is upper triangular [14]. The diagonal elements of  $\mathbf{R}_k$  are required for the accumulative computation of the Lyapunov exponents. This procedure is iterated until convergence for the Lyapunov exponents is obtained.

For the computation of a covariant set of vectors  $\{\mathbf{v}^j\}_0$  spanning the tangent space for the phase point  $\mathbf{\Gamma}_0 \equiv \mathbf{\Gamma}(0)$  at, say, time  $t_0$ , Ginelli *et al.* [1] start with a well-relaxed set of GS vectors at  $t_0$  and follow the dynamics forward for a sufficiently long time up to  $t_\omega = t_0 + \omega\tau$ , storing  $\mathbf{G}_k$  and  $\overline{\mathbf{G}}_k$  (or, equivalently,  $\mathbf{R}_k$ ) for  $t_k = t_0 + k\tau$ ,  $k = 0, \dots, \omega$  along the way. At  $t_\omega$  a set of unit tangent vectors  $\{\mathbf{v}^j\}_\omega$  is constructed according to

$$\mathbf{v}_\omega^j \in \mathbf{S}_\omega^j \equiv \text{span} \{\mathbf{g}_\omega^1, \dots, \mathbf{g}_\omega^j\} \quad \forall j \in \{1, \dots, D\} \quad , \quad (3.9)$$

which serve as starting vectors for a backward iteration from  $t_\omega$  to time  $t_0$ . The vector  $\mathbf{v}_k^j$  will stay in  $\mathbf{S}_k^j$  at any intermediate time  $t_k$ , because  $\mathbf{S}_k^j$  is the most stable subspace of dimension  $j$  for the time-reversed iteration. Arranging these vectors again as column vectors of a matrix  $\mathbf{V}_k$  and expressing them in the GS basis at time  $t_k$ , one has  $\mathbf{V}_k = \mathbf{G}_k \mathbf{C}_k$ , where the matrix  $\mathbf{C}_k$  is again upper triangular with elements  $[\mathbf{C}_k]_{i,j} = \mathbf{g}_k^i \cdot \mathbf{v}_k^j$ . If, at any step  $n$ ,  $\mathbf{C}_{k-1}$  is constructed from  $\mathbf{C}_k$  according to  $\mathbf{C}_{k-1} = [\mathbf{R}_k]^{-1} \mathbf{C}_k$ , Ginelli *et al.* have shown that  $\mathbf{V}_k = \mathbf{J}_{k-1} \mathbf{V}_{k-1}$  and, hence, the respective column vectors of this matrix follow the natural tangent-space dynamics without re-orthogonalization. They are covariant but not orthogonal in general. At this stage of the algorithm, renormalization of  $\mathbf{v}_{k-1}^j$  is still required to escape the exponential divergence of the vector norms without affecting their orientation. After reaching  $t_0$  at the end of the iteration, the vectors  $\mathbf{v}_0^j$  point into their proper orientations in tangent space such that, according to Eq. (3.7),  $\text{span}(\mathbf{v}_0^1, \dots, \mathbf{v}_0^{f(j)}) = \mathbf{E}^{(1)}(\Gamma_0) \oplus \dots \oplus \mathbf{E}^{(j)}(\Gamma_0)$  is the most-unstable subspace of dimension  $f(j) \equiv m^{(1)} + \dots + m^{(j)}$  of the tangent space at the space point  $\Gamma_0$ , going forward in time. If there are degeneracies (as in the presence of Lyapunov modes to be discussed below), the Oseledec subspace  $\mathbf{E}^{(j)}$  is spanned according to

$$\mathbf{E}^{(j)} = \mathbf{v}^{f^{(j-1)}+1} \oplus \dots \oplus \mathbf{v}^{f^{(j)}}, \quad (3.10)$$

where, as in the following, we omit the arguments for the phase-space point. If there are no degeneracies,  $\mathbf{v}^{f^{(j)}} = \mathbf{E}^{(j)}$ . Similarly, the Gram-Schmidt vectors may be expressed in terms of the eigenspaces of  $\Lambda_-$  [15, 16, 7],

$$\mathbf{U}_-^{(j)} = \mathbf{g}^{f^{(j-1)}+1} \oplus \dots \oplus \mathbf{g}^{f^{(j)}}, \quad (3.11)$$

for nondegenerate subspaces one finds

$$\mathbf{U}_-^{(j)} = \mathbf{g}^{f^{(j)}}. \quad (3.12)$$

The drawback of this algorithm for many-particle systems is the large storage requirement for the matrices  $\mathbf{G}_k$  and  $\overline{\mathbf{G}}_k$  (or, equivalently,  $\mathbf{R}_k$ ) for the intermediate times  $t_k = t_0 + k\tau$ ,  $k = 0, \dots, \omega$ , because  $\tau$  must not be chosen too large (containing not more than, say, 20 particle collisions). At the expense of computer time, this can be bypassed by storing the matrices only for times separated by, say,  $100\tau$  intervals and recomputing the forward dynamics in between when required during the time-reversed iteration. In this case, also the phase-space trajectory needs to be stored.

### 3.4 A simple example: the Hénon map

To illustrate the foregoing algorithm, we apply it to a simple two-dimensional example, the Hénon map [17],

$$\begin{aligned}x_{k+1} &= a - x_k^2 + b y_k, \\y_{k+1} &= x_k,\end{aligned}$$

with  $a = 1.4$  and  $b = 0.3$ . In Fig. 3.1 the Hénon attractor is shown (black line), which is known to coincide with its unstable manifold. An approximation of the stable manifold is shown by the dotted lines. At the point 0 the initial GS basis is indicated by the two orthogonal vectors in blue, where one, as required, points into the direction of the unstable manifold. If these vectors are evolved forward in time with the GS method for a few hundred steps, the two orthogonal GS vectors at the point  $\omega$  are obtained. Taking these vectors as the initial vectors  $\mathbf{v}_\omega^1$  and  $\mathbf{v}_\omega^2$ , the consecutive backward iteration yields the covariant vectors at point 0 indicated in red. As expected, one is parallel to the unstable manifold, the other parallel to the stable manifold at that point.

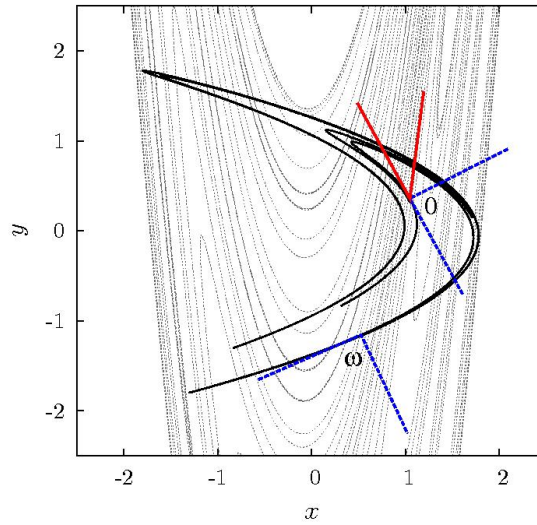


**Figure 3.1 :** The Hénon attractor (black line) and a finite-length approximation of its stable manifold (dotted line) are shown. The red vectors are the covariant vectors at the phase point 0 as explained in the main text. The blue vectors are Gram-Schmidt vectors.

### 3.5 Systems of hard disks

Now we turn to the study of a two-dimensional system of hard disks in a box with periodic boundaries, where the particles suffer elastic hard collisions (without roughness), and move along

straight lines in between collisions. The case of rough hard disks is the topic of a forthcoming publication (Chap. 8).

The Lyapunov instability of hard-disk systems has been studied in detail in the past [18, 19, 20, 21, 22]. Here, we are mainly concerned with the differences encountered with the GS and covariant vectors, which, as we have seen, give rise to identical Lyapunov spectra. To facilitate comparison with our previous work, we consider reduced units for which the particle diameter  $\sigma$ , the particle mass  $m$  and the kinetic energy per particle,  $K/N$ , are unity. Here,  $K$  is the total energy, which is purely kinetic, and  $N$  denotes the number of particles. Lyapunov exponents are given in units of  $\sqrt{K/Nm\sigma^2}$ . If not otherwise stated, our standard system consists of  $N = 198$  particles at a density  $\rho \equiv N/(L_x L_y) = 0.7$  and a simulation box with an aspect ratio  $L_y/L_x = 2/11$ , which is periodic in  $x$  and  $y$ . The choice of such a small aspect ratio facilitates the observation of the Lyapunov modes to be discussed later. As usual, the total momentum is set to zero.

The state of the system is given by the coordinates and momenta of all the particles,

$$\mathbf{\Gamma} = \{\vec{q}_n, \vec{p}_n; n = 1, \dots, N\}.$$

Similarly, an arbitrary tangent vector  $\delta\mathbf{\Gamma}$  - either a Gram-Schmidt vector  $\mathbf{g}$  or a covariant vector  $\mathbf{v}$  - consists of the respective coordinate and momentum perturbations,

$$\delta\mathbf{\Gamma} = \{\delta\vec{q}_n, \delta\vec{p}_n; n = 1, \dots, N\}. \quad (3.13)$$

The time evolution of these vectors and the construction of the map from one Gram-Schmidt step to the next has been discussed before [18, 23].

Fig. 3.2 shows the Lyapunov spectrum for this system computed both in forward direction with the GS vectors (blue line) and in backward direction with the covariant vectors (red line). The typical time of the simulation in the forward direction is for  $t_0 + t_\omega = 2.5 \times 10^5 \tau$ , where  $\tau = 0.6$  is the largest interval between two successive Gram-Schmidt re-orthonormalizations, which does not affect the spectrum. The backward simulation is for a time  $t_\omega - t_0 = 2.5 \times 10^4 \tau$ . The time  $t_0$  (at least of the order of  $1 \times 10^4 \tau$ ) is required for the preparation of the relaxed initial state at  $t_0$ . It can be observed in the figure that the unstable directions in the future correspond well to the stable directions in the past and vice versa. Of course, if the sequence of covariant vectors is followed in the forward direction of time, the spectrum is identical to the classical GS results (blue line in Fig. 3.2).



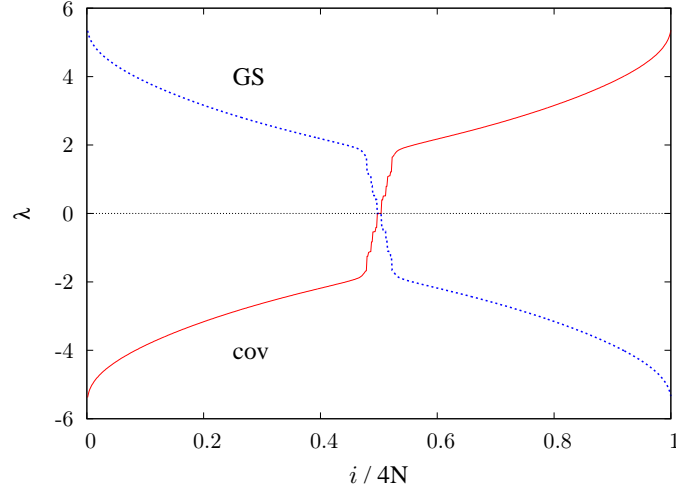


**Figure 3.2 :** Lyapunov spectrum for the 198 disk system described in the main text. The spectrum calculated in the forward direction with the GS method is shown by the blue line, the one calculated in the backward direction with the covariant vectors by the red line. Reduced indices  $i/4N$  are used on the abscissa. Although the spectrum is defined only for integer  $i$ , solid lines are drawn for clarity.

### 3.5.1 Covariant versus Gram-Schmidt vectors

Whereas the time evolution of the GS vectors is determined by the exponential growth of infinitesimal volume elements belonging to subspaces  $\mathbf{g}^1 \oplus \dots \oplus \mathbf{g}^i$  for  $i \in \{1, \dots, D\}$  according to  $\exp\left(t \sum_{j=1}^i \lambda_j\right)$ , the growth of an infinitesimal perturbation representing a covariant vector  $\mathbf{v}^i$  is directly proportional to  $\exp(t \lambda_i)$ , for all  $i$ . Thus, it is interesting to compare the relative orientations of respective vectors giving rise to the same exponent. In the left panel of Fig. 3.3 the difference in orientation of the two types of vectors is demonstrated by a plot of  $|\mathbf{g}^i \cdot \mathbf{v}^i|$  as a function of  $i$ . The black line is an average over 100 frames separated by time intervals of  $250\tau$ . Since for tangent vectors only their direction and not the sense of direction is important, an absolute value is taken (here and for analogous cases below), otherwise the scalar product might average to zero over long times, with equal numbers of vectors pointing into opposite directions. For the unstable directions in the left half of the left panel, one observes a rapid decrease of the scalar product with  $i$  and, hence a rapid increase of the angle between respective covariant and GS vectors. This decrease is repeated for the stable directions in the right half of the figure. These two parts are separated by the mode region, an enlargement of which is shown in the right panel of Fig. 3.3 and which will be dealt with in more detail below.

In Fig. 3.4 we show similar projections (time averages of absolute values of scalar products as before) for selected covariant vectors with the whole Gram-Schmidt vector set. One observes that the covariant vectors  $\mathbf{v}^j$  belong to the GS subspace  $\mathbf{g}^1 \oplus \dots \oplus \mathbf{g}^j$ , for all  $j \in \{1, \dots, 4N\}$  and, thus, give rise to the upper-triangular property of the matrix  $\mathbf{R}$  in the QR-decomposition

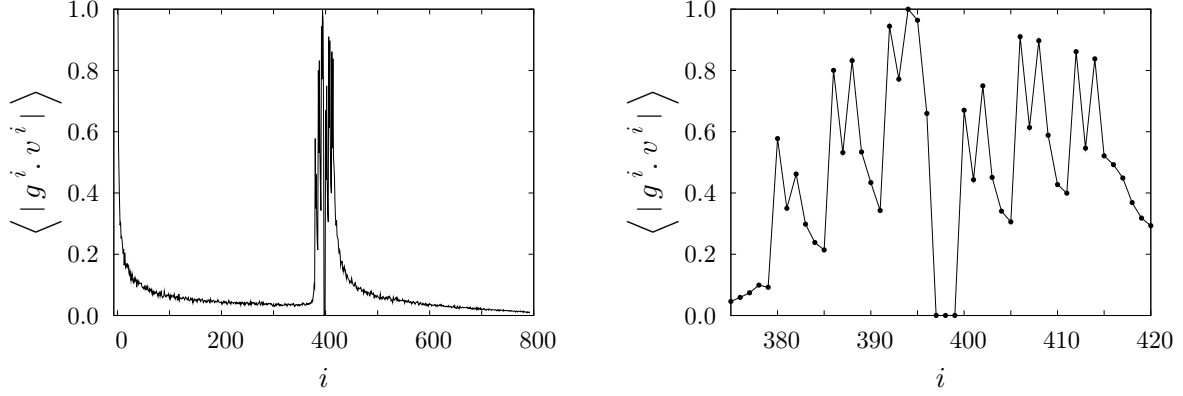


**Figure 3.3 :** Plot of the scalar product norm,  $\langle |g^i \cdot v^i| \rangle$ , for GS and covariant vectors giving rise to the same Lyapunov exponent  $\lambda_i$ , as a function of  $i$ . The line is a time average as discribed in the main text. Left panel: full range of Lyapunov exponents; Right panel: enlargement of the central part.

mentioned above. The curves in the figure strongly depend on the choice of  $j$ :

- If it belongs to the unstable subspace  $\mathbf{E}^u$  but does not represent a Lyapunov mode (top-left panel for  $j = 370$ ), there is no obvious orientational correlation with any of the GS vectors with index  $i < j$ . For  $i = j = 1$  corresponding to the maximum exponent, the covariant and GS vectors are identical. If, however, the covariant vector represents a Lyapunov mode as in the bottom-left panel for  $j = 393$ , then its angle with the respective GS vector may become smaller, giving rise to a scalar product closer to unity.
- If the covariant vector belongs to the stable subspace  $\mathbf{E}^s$  but does not represent a mode as for  $j = 700$  in the top-right panel of Fig. 3.4, it has non-vanishing components in the GS basis for all  $i \leq j$  with the exception of the zero subspace  $2N - 2 \leq i \leq 2N + 3$ , which is strictly orthogonal. With the exception of the step at the conjugate index  $i = 4N + 1 - j = 93$ , the origin of which is not fully understood, there is no indication of orientational correlations between the covariant vector with any of the GS vectors for  $i \leq j$ . If, however, the covariant vector represents a mode as for  $j = 400$  in the lower-right panel of the figure, there is strong orientational correlation not only with the respective GS vector with  $i = 400$ , but also with its conjugate pair at  $4N + 1 - i$  ( $= 393$  in our example).

It is interesting to note that the leading GS and covariant vectors in the null subspace are always identical (up to an irrelevant sign):  $v^{2N-2} = g^{2N-2}$ .

### 3.5.2 Localization

The maximum (minimum) Lyapunov exponent is the rate constant for the fastest growth (decay) of a phase-space perturbation and is dominated by the fastest dynamical events, a locally-enhanced collision frequency. It is not too surprising that the associated tangent-vector com-

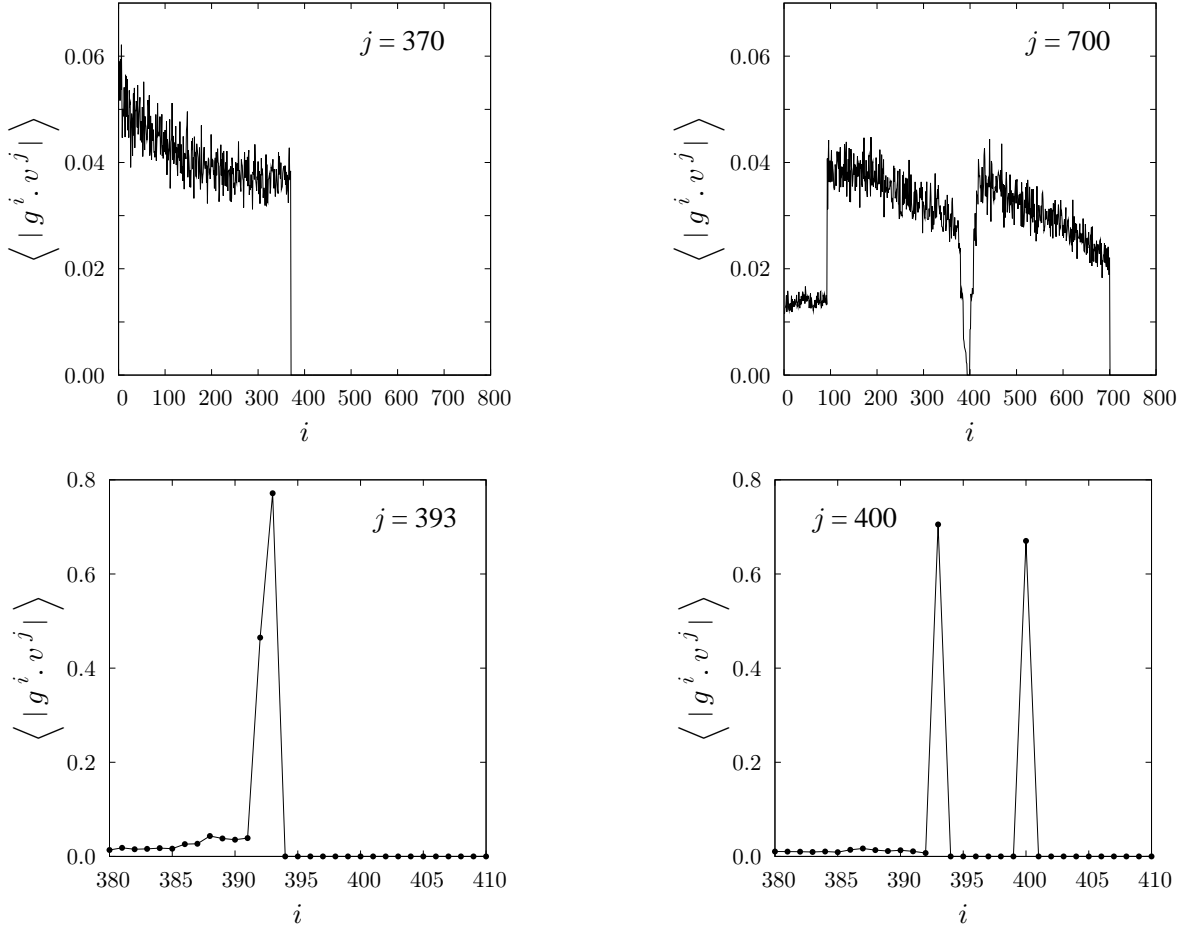


**Figure 3.4 :** Time averaged absolute value of the scalar product of selected covariant vectors  $v^j$  (as indicated by the labels) with the whole set of Gram-Schmidt vectors  $g^i$  as a function of  $i$ .

ponents are significantly different from zero for only a few strongly-interacting particles at any instant of time. Thus, the respective perturbations are strongly localized in physical space. This property persists in the thermodynamic limit such that the fraction of tangent-vector components contributing to the generation of  $\lambda_1$  follows a power law  $\propto N^{-\eta}$ ,  $\eta > 0$ , and converges to zero for  $N \rightarrow \infty$  [24, 25, 20, 26]. The localization becomes gradually worse for larger indices  $i > 1$ , until it ceases to exist and (almost) all particles collectively contribute to the coherent Lyapunov modes to be discussed below. Similar observations for spatially extended systems have been made by various authors [27, 28, 29, 21, 22], which were consequently explained in terms of simple models [30, 31]. We also mention Ref. [32], where the tangent-space dynamics of the first Lyapunov vector  $g^1$  for various one-dimensional Hamiltonian lattices is compared to that for the Kardar-Parisi-Zhang model of spatio-temporal chaos. The unexpected differences found for the scaling properties are traced back to the existence of long-range correlations, both in space and time, in the Hamiltonian chains, the origin of which, however, could not be fully disclosed. The same correlations are conjectured to be responsible for a slow  $1/\sqrt{N}$  convergence of  $\lambda_1$

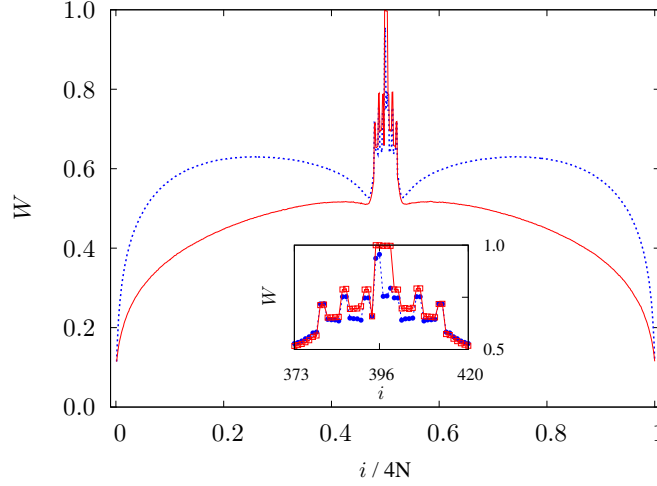


**Figure 3.5 :** Localization spectra  $W$  for the complete set of Gram-Schmidt vectors (blue) and covariant vectors (red). The details of the hard-disk system are given in Sec. 3.5. Reduced indices  $i/4N$  are used on the abscissa. In the inset a magnification of the central mode region is shown.

towards its thermodynamic limit [32], which is also observed for hard-disk systems [18].

Up to now, all considerations concerning localization were based on the Gram-Schmidt vectors. Here, we demonstrate the same property for the covariant vectors. According to Eq. (3.13) we define the contribution of an individual disk  $n$  to a particular perturbation vector as the square of the projection of  $\delta\mathbf{\Gamma}$  onto the subspace pertaining to this disk,

$$\mu_n = (\delta\vec{q}_n)^2 + (\delta\vec{p}_n)^2.$$

Since  $\delta\mathbf{\Gamma}$  is either a GS vector or a covariant vector both of which are normalized, one has  $\sum_{n=1}^N \mu_n = 1$ , and  $\mu_n$  may be interpreted as a kind of action probability of particle  $n$  contributing to the perturbation in question. It should be noted that for the definition of  $\mu_n$  the Euclidean norm is used and that all localization measures depend on this choice. Qualitatively, this is still sufficient to demonstrate localization. From all the localization measures introduced [29, 24], the most common is due to Taniguchi and Morriss [21, 22],

$$W = \frac{1}{N} \exp[S], \quad S = \left\langle - \sum_{n=1}^N \mu_n \ln \mu_n \right\rangle. \quad (3.14)$$

Here,  $S$  is the Shannon entropy for the "probability" distribution  $\mu_n$ , and  $\langle \dots \rangle$  denotes a time average.  $W$  is bounded according to  $1/N \leq W \leq 1$ , where the lower and upper bounds apply to complete localization and delocalization, respectively. In Fig. 3.5, we compare  $W$  obtained for the full set of Gram-Schmidt vectors (blue curve) to that of all the covariant vectors (red curve). The spectra are obtained by identifying  $\delta\mathbf{\Gamma}$  with all vectors of the respective sets,  $i = 1, \dots, 4N$ . Not

too surprisingly, the localization is stronger for the covariant vectors, whose direction in tangent space is solely determined by the tangent flow and is not affected by renormalization constraints. Another interesting feature is the symmetry  $W_i = W_{4N+1-i}$ , which is a direct consequence of the symplectic nature of the flow (see Chap. 8).

### 3.5.3 Tangent space projections

It is interesting to see how much the coordinate and momentum subspaces contribute to a particular tangent vector  $\delta\mathbf{\Gamma}$  (see Eq. 3.13), which may be a Gram-Schmidt vector  $\mathbf{g}^i$  or a covariant vector  $\mathbf{v}^i$ , both associated with the same Lyapunov exponent  $\lambda_i$ . The time-averaged squared projections of  $\delta\mathbf{\Gamma}$  onto the coordinate and momentum subspaces  $\mathbf{Q}$  and  $\mathbf{P}$ , respectively, are given by

$$\eta_q = \left\langle \sum_{n=1}^N (\delta\vec{q}_n)^2 \right\rangle, \quad \eta_p = \left\langle \sum_{n=1}^N (\delta\vec{p}_n)^2 \right\rangle \quad (3.15)$$

and are plotted in Fig. 3.6 for the whole set of Gram-Schmidt vectors, and in Fig. 3.7 for the whole set of covariant vectors,  $i = 1, \dots, 4N$ . One notes that for the Gram-Schmidt case the contributions of  $\eta_q$  and  $\eta_p$  to a vector  $\mathbf{g}^i$  and its conjugate  $\mathbf{g}^{4N+1-i}$  are interchanged, whereas for the covariant vectors  $\mathbf{v}^i$  and  $\mathbf{v}^{4N+1-i}$  they are the same. This is particularly noticeable for the expanded central regions in the respective right panels of Figs. 3.6 and 3.7.

### 3.5.4 Central manifold and vanishing exponents

The dynamics of a closed particle system such as ours is strongly affected by the inherent continuous symmetries, which leave the Lagrangian and, hence, the equations of motion invariant. The symmetries relevant for our two-dimensional system with periodic boundaries are the homogeneity of time (or invariance with respect to time translation), and the homogeneity of space (or invariance with respect to space translations in two independent directions). Each of these symmetries is associated with two vector fields with sub-exponential growth (or decay) and, therefore, gives rise to two vanishing Lyapunov exponents [33]. At any phase-space point  $\mathbf{\Gamma}$ , the six vectors span a six-dimensional subspace  $\mathcal{N}(\mathbf{\Gamma})$  of the tangent space  $\mathbf{TX}(\mathbf{\Gamma})$ , which is referred to as null space or central manifold. This subspace is covariant. If the  $4N$  components of the state vector are arranged as

$$\mathbf{\Gamma} = (q_x^1, q_y^1, \dots, q_x^N, q_y^N; p_x^1, p_y^1, \dots, p_x^N, p_y^N) \quad , \quad (3.16)$$

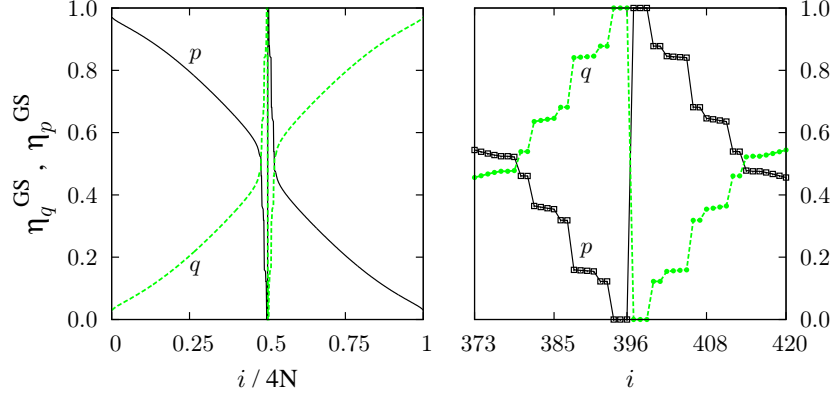


**Figure 3.6 :** Mean squared projections for the full Gram-Schmidt vector set,  $i = 1, \dots, 4N$ , onto the coordinate subspace  $\mathbf{Q}$ ,  $\eta_q^{GS}$  (green line), and the momentum subspace  $\mathbf{P}$ ,  $\eta_p^{GS}$  (black line), for the 198-particle system defined above. Left panel: full spectrum; Right panel: magnification of the central mode-carrying region.

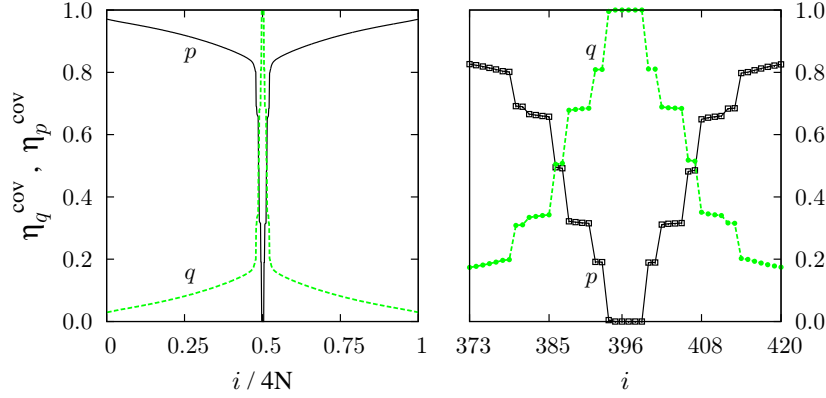


**Figure 3.7 :** Mean squared projections for the full covariant vector set,  $i = 1, \dots, 4N$ , onto the coordinate subspace  $\mathbf{Q}$ ,  $\eta_q^{cov}$  (green line), and the momentum subspace  $\mathbf{P}$ ,  $\eta_p^{cov}$  (black line), for the 198-disk system defined above. Left panel: full spectrum; Right panel: magnification of the central mode-carrying region.

the six orthogonal spanning vectors, which are the generators of the elementary symmetry transformations, are given by [20, 7]

$$\mathbf{e}_1 = \frac{1}{\sqrt{2K}} (p_x^1, p_y^1, \dots, p_x^N, p_y^N; 0, 0, \dots, 0, 0) , \quad (3.17)$$

$$\mathbf{e}_2 = \frac{1}{\sqrt{N}} (1, 0, \dots, 1, 0; 0, 0, \dots, 0, 0) , \quad (3.18)$$

$$\mathbf{e}_3 = \frac{1}{\sqrt{N}} (0, 1, \dots, 0, 1; 0, 0, \dots, 0, 0) , \quad (3.19)$$

$$\mathbf{e}_4 = \frac{1}{\sqrt{2K}} (0, 0, \dots, 0, 0; p_x^1, p_y^1, \dots, p_x^N, p_y^N) , \quad (3.20)$$

$$\mathbf{e}_5 = \frac{1}{\sqrt{N}} (0, 0, \dots, 0, 0; 1, 0, \dots, 1, 0) , \quad (3.21)$$

$$\mathbf{e}_6 = \frac{1}{\sqrt{N}} (0, 0, \dots, 0, 0; 0, 1, \dots, 0, 1) . \quad (3.22)$$

$\mathbf{e}_1$  corresponds to a change of the time origin,  $\mathbf{e}_4$  to a change of energy,  $\mathbf{e}_2$  and  $\mathbf{e}_3$  to an (infinitesimal) uniform translation of the origin in the  $x$ - and  $y$ -directions, respectively, and  $\mathbf{e}_5$  and  $\mathbf{e}_6$  to a perturbation of the total momentum in the  $x$ - and  $y$ -directions, respectively. The six vanishing Lyapunov exponents are located in the center of the Lyapunov spectrum with indices  $2N - 2 \leq i \leq 2N + 3$ . The first three of these vectors have non-vanishing components only for the position perturbations in the  $2N$ -dimensional configuration subspace  $\mathbf{Q}$ , the remaining only for the momentum perturbations in the  $2N$ -dimensional momentum subspace  $\mathbf{P}$ . They are related by  $\mathbf{e}_j = \mathcal{J} \mathbf{e}_{j+3}$  for  $j \in \{1, 2, 3\}$ , where  $\mathcal{J}$  is the symplectic (skew-symmetric) matrix.

Let us consider the projection matrices  $\alpha$  and  $\beta$  of the GS and covariant vectors, respectively, onto the natural basis,

$$\alpha_{i,j} = \mathbf{g}^i \cdot \mathbf{e}_j; \quad \beta_{i,j} = \mathbf{v}^i \cdot \mathbf{e}_j, \quad j \in \{1, \dots, 6\} \quad i \in \{2N - 2, \dots, 2N + 3\}.$$

For  $i \notin \{2N - 2, \dots, 2N + 3\}$  these components vanish. Without loss of generality, we consider in the following example a system with only  $N = 4$  particles in a periodic box, which is relaxed for  $t_0 = 10^6$  time units, followed by a forward and backward iteration lasting for  $t_\omega - t_0 = 10^5$  time units. Very special initial conditions for the backward iteration,  $\mathbf{v}_\omega^i = \mathbf{g}_\omega^i$  for  $i = 1, \dots, 4N (= 16)$ , are used. The projections at the time  $t_0$  are given in Table 3.1 for the GS vectors, in Table 3.2 for the covariant vectors.

**Table 3.1 :** Instantaneous projection matrix  $\alpha$  of Gram-Schmidt vectors (for  $i \in \{2N - 2, \dots, 2N + 3\}$ ) onto the natural basis  $\{\mathbf{e}_j, 1 \leq j \leq 6\}$  of the central manifold. The system contains  $N = 4$  disks. The powers of 10 are given in square brackets.

$i$	$\alpha_{i,1}$	$\alpha_{i,2}$	$\alpha_{i,3}$	$\alpha_{i,4}$	$\alpha_{i,5}$	$\alpha_{i,6}$
$2N - 2$	-0.766	0.582	0.273	-0.766[-6]	0.582[-6]	0.273[-6]
$2N - 1$	0.256	-0.114	0.960	0.256[-6]	-0.114[-6]	0.960[-6]
$2N$	0.590	0.805	-0.062	0.590[-6]	0.805[-6]	-0.062[-6]
$2N + 1$	-0.611[-6]	0.782[-6]	-0.121[-6]	0.611	-0.782	0.121
$2N + 2$	0.575[-6]	0.544[-6]	0.611[-6]	-0.575	-0.544	-0.611
$2N + 3$	-0.543[-6]	-0.304[-6]	0.783[-6]	0.543	0.304	-0.783

A comparison of the two tables reveals the following:

- The six orthogonal GS vectors  $\mathbf{g}^i; i = 2N - 2, \dots, 2N + 3$  completely span the null subspace (the squared elements for each rows add up to unity in Table 3.1). The same is true for the six non-orthogonal covariant vectors  $\mathbf{v}^i; i = 2N - 2, \dots, 2N + 3$  in Table 3.2.
- The first three covariant and Gram-Schmidt vectors completely agree. This is a consequence of the special initial conditions for the former at the time  $t_\omega$  as mentioned above. During the

**Table 3.2 :** Instantaneous projection matrix matrix  $\beta$  for the the six central covariant vectors onto the natural basis  $\{\mathbf{e}_j, 1 \leq j \leq 6\}$  of the central manifold. The system contains  $N = 4$  particles. The powers of 10 are given in square brackets.

$i$	$\beta_{i,1}$	$\beta_{i,2}$	$\beta_{i,3}$	$\beta_{i,4}$	$\beta_{i,5}$	$\beta_{i,6}$
$2N - 2$	-0.766	0.582	0.273	-0.766[-6]	0.582[-6]	0.273[-6]
$2N - 1$	0.256	-0.114	0.960	0.256[-6]	-0.114[-6]	0.960[-6]
$2N$	0.590	0.805	-0.062	0.590[-6]	0.805[-6]	-0.062[-6]
$2N + 1$	-0.611	0.782	-0.121	0.611 [-5]	-0.782 [-5]	0.121 [-5]
$2N + 2$	0.575	0.544	0.611	-0.575 [-5]	-0.544[-5]	-0.611[-5]
$2N + 3$	-0.543	-0.304	0.783	0.543 [-5]	0.304 [-5]	-0.783[-5]

backward iteration the three covariant vectors stay in their respective subspaces and remain parallel to the GS vectors (which were stored during the forward phase of the algorithm). At  $t_0$  they are still identical to their GS counterparts. The first vectors always agree,  $\mathbf{v}_0^{2N-2} = \mathbf{g}_0^{2N-2}$ , even if less special initial conditions conforming to Eq. 3.9 are used.

- Equivalent components have the same mantissa but may differ by a factors of  $10^5$  or  $10^6$ , which are related to the duration of the relaxation phase  $t_0$  and of the forward-backward iteration time  $t_\omega - t_0$ .

The explanation for this behavior (see Sec. 3.8.1) is obtained by a repeated explicit application of the linearized maps for the free streaming and consecutive collision of particles [23, 18] to the six basis vectors  $\{\mathbf{e}_j\}$ . One finds that

$$D\phi_{\mathbf{\Gamma}_0}^t \mathbf{e}_j(\mathbf{\Gamma}_0) = \mathbf{e}_j(\mathbf{\Gamma}_t), \quad (3.23)$$

$$D\phi_{\mathbf{\Gamma}_0}^t \mathbf{e}_{j+3}(\mathbf{\Gamma}_0) = t \mathbf{e}_j(\mathbf{\Gamma}_t) + \mathbf{e}_{j+3}(\mathbf{\Gamma}_t), \quad (3.24)$$

for  $j \in \{1, 2, 3\}$ . Eq. (3.24) implies that any perturbation vector with non-vanishing components parallel to  $\mathbf{e}_4$ ,  $\mathbf{e}_5$ , or  $\mathbf{e}_6$  will rotate towards  $\mathbf{e}_1$ ,  $\mathbf{e}_2$ , and  $\mathbf{e}_3$ , respectively. It follows (i) that the null subspace  $\mathcal{N}(\mathbf{\Gamma})$  is covariant; (ii) that the subspaces  $\mathcal{N}_1 = \text{span}\{\mathbf{e}_1\}$ ,  $\mathcal{N}_2 = \text{span}\{\mathbf{e}_2\}$  and  $\mathcal{N}_3 = \text{span}\{\mathbf{e}_3\}$  are separately covariant (from Eq. (3.23)); that, as was already noted in Ref. [7],  $\mathcal{N}$  can be further decomposed into the three two-dimensional covariant subspaces  $\mathcal{N}_p = \text{span}\{\mathbf{e}_1, \mathbf{e}_4\}$ ,  $\mathcal{N}_x = \text{span}\{\mathbf{e}_2, \mathbf{e}_5\}$ , and  $\mathcal{N}_y = \text{span}\{\mathbf{e}_3, \mathbf{e}_6\}$ .

### 3.5.5 Lyapunov modes

We have seen in Sec. 3.14 that the perturbation vectors are less and less localized, the smaller the Lyapunov exponents become, until they are coherently spread out over the physical space and form periodic spatial patterns with a well-defined wave vector  $\mathbf{k}$ . This collective patterns are referred to as Lyapunov modes. The modes were observed for hard-particle systems in one,



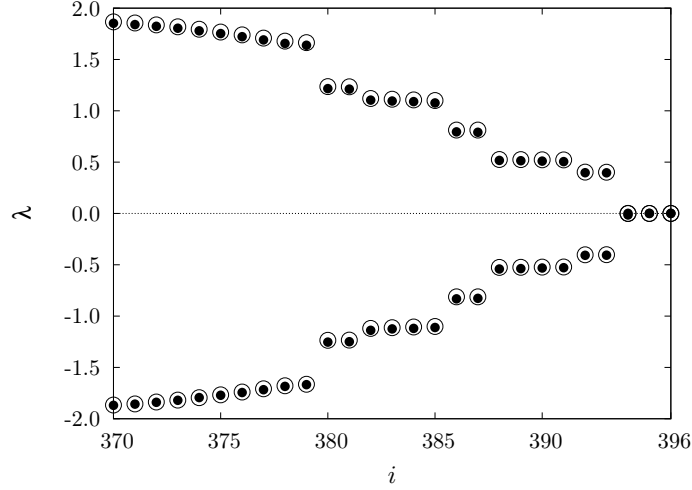


**Figure 3.8 :** Enlargement of the mode regime for the Lyapunov spectrum depicted in Fig. 3.2. The open symbols indicate exponents computed from the Gram-Schmidt vectors, the full dots are for exponents obtained from the covariant vectors.

two and three dimensions [7, 19, 21, 22, 34], for hard planar dumbbells [35, 36, 24] and for one and two-dimensional soft particles [37, 38, 26]. A formal classification of the modes is given in Ref. [7]. Physically, they are interpreted as periodic modulations with wave number ( $k \neq 0$ ) of the null modes associated with the elementary continuous symmetries and conservation laws. Since this modulation involves the breaking of such symmetries, the modes have been interpreted as Goldstone modes [8]. Theoretical approaches are based on random matrix theory [39, 40], periodic orbit expansion [41], and kinetic theory [42, 43, 8].

So far the numerical work on Lyapunov modes has been exclusively concerned with the orthonormal Gram-Schmidt vectors  $\{\mathbf{g}^i\}$ ,  $i = 1, \dots, 4N$ . The purpose of this section is to point out some differences one encounters, if the modes for the Gram-Schmidt and covariant vectors are compared.

Fig. 3.8 shows an enlargement of the mode-carrying region for the Lyapunov spectrum of Fig. 3.2. In order to emphasize the conjugate pairing symmetry  $\lambda_i = -\lambda_{4N+1-i}$  for symplectic systems, conjugate exponent pairs are plotted with the same index  $i$  on the abscissa, where now  $i \in \{1, \dots, 2N\}$ . The open circles are computed from the Gram-Schmidt vectors in the forward direction of time, the dots from the covariant vectors during the time-reversed iteration. Considering the size of the system ( $N = 198$ ), the agreement is excellent.

The steps in the spectrum due to degenerate exponents is a clear indication for the presence of Lyapunov modes. According to the classification in our previous work [7], the steps with a two-fold degeneracy are transverse (T) modes – T(1,0), T(2,0) and T(3,0) from right to left in Fig. 3.2. Similarly, the steps with a four-fold degeneracy of the exponents are longitudinal-

momentum (LP) modes – LP(1,0), LP(2,0) and LP(3,0) again from the right. The arguments  $(n_x, n_y)$  account for the number of periods of the sinusoidal perturbations in the  $x$  and  $y$ -directions. Since our simulation cell is rather narrow, only wave vectors  $\mathbf{k}$  parallel to the  $x$ -axis of the (periodic) cell appear, leaving 0 for the second argument [7]. As usual, “transverse” and “longitudinal” refer to the spatial polarization with respect to  $\mathbf{k}$  of the wave-like pattern.

One of our early observations, which greatly facilitates the classification of the modes for the Gram-Schmid vectors [7], is that in the limit  $N \rightarrow \infty$  the cosine of the angle  $\Theta$  between the  $2N$ -dimensional vectors of the position perturbations and momentum perturbations converges to +1 for the smallest positive, and to -1 for the smallest negative exponents. See the blue line in Fig. 3.9. Furthermore, the relation

$$\delta \mathbf{p} = C_{\pm} \delta \mathbf{q} \quad (3.25)$$

holds with known constants  $C_{\pm}$ .

This means that these vectors are nearly parallel or anti-parallel for large  $N$  and that the mode classification may be based solely on  $\delta \mathbf{q}$ . Somewhat surprisingly, this property does not strictly hold anymore for the covariant vectors. This is shown by the red line in Fig. 3.9, where  $\cos(\Theta)$  is seen to differ significantly from  $\pm 1$  for all  $i$  outside of the null subspace (for which  $394 \leq i \leq 399$ ). Unfortunately, this has dire consequences for the representation of the covariant vector modes, since they cannot be purely understood as a vector field of the position perturbations only as in the GS case. For the purpose of this paper, however, we restrict to the GS-based classification of Ref. [7].

**Table 3.3 :** Basis vectors of  $(n_x, 0)$  modes for a hard disk system in a rectangular box with periodic boundaries. We use the notation  $c_x = \cos(k_x x)$ , and  $s_x = \sin(k_x x)$ , where the wave vector is given by  $\mathbf{k} = (k_x, k_y) = (2\pi n_x / L_x, 0)$ . Here  $n_x \in \{1, 2, 3\}$ .

$\mathbf{n}$	Basis of $\mathbf{T}(\mathbf{n})$	Basis of $\mathbf{L}(\mathbf{n})$	Basis of $\mathbf{P}(\mathbf{n})$
$\begin{pmatrix} n_x \\ 0 \end{pmatrix}$	$\begin{pmatrix} 0 \\ c_x \end{pmatrix}, \begin{pmatrix} 0 \\ s_x \end{pmatrix}$	$\begin{pmatrix} c_x \\ 0 \end{pmatrix}, \begin{pmatrix} s_x \\ 0 \end{pmatrix}$	$\begin{pmatrix} p_x \\ p_y \end{pmatrix} s_x, \begin{pmatrix} p_x \\ p_y \end{pmatrix} c_x$

Transverse modes are two-dimensional subspaces (for the periodic boundary conditions and a rectangular box), for which two orthogonal basis vectors are given in Table 3.3. As an example, we show in the panels on the left-hand side of Fig. 3.10 snapshots of the mode T(1,0) for the index  $i = 393$ , namely plots of  $\delta q_y$  as a function of  $q_x$  (top-left), and of  $\delta p_y$  as a function of  $q_x$  (bottom-left). The respective plots for the  $x$  components fluctuate around zero, as expected, and are not shown. Analogous plots for the mode T(2,0) with  $i = 387$  are shown in the panels on the right-hand side. The blue points are for GS vectors, the red squares for the respective covariant

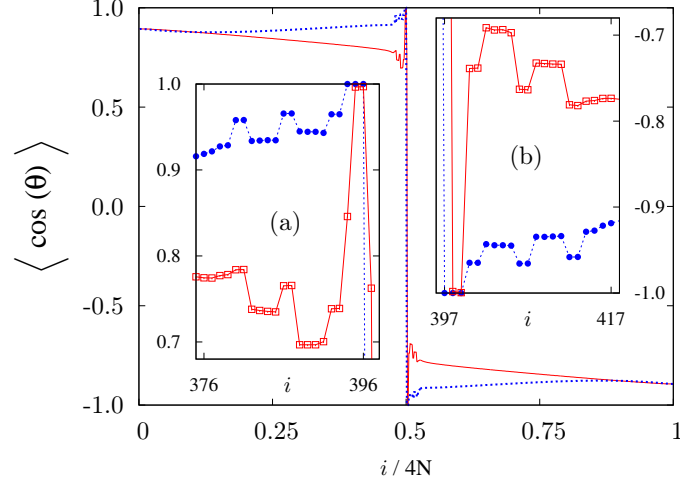


**Figure 3.9 :** Time averaged value of  $\cos(\Theta) = (\delta \mathbf{q} \cdot \delta \mathbf{p}) / (\|\delta \mathbf{q}\| \|\delta \mathbf{p}\|)$  as a function of the Lyapunov index  $i$  for a system with  $N = 198$  hard disks. Here,  $\delta \mathbf{q} \in \mathbf{Q}$  and  $\delta \mathbf{p} \in \mathbf{P}$  are the  $2N$ -dimensional vectors of all position perturbations respective all momentum perturbation for the Gram-Schmidt vectors  $\mathbf{g}^i$  (blue line) and the covariant vectors  $\mathbf{v}^i$  (red line). The insets are magnifications of the mode-carrying region.

vectors. It is interesting to note that the scatter of the points for the position perturbations is smaller for the covariant modes (red squares) than for the GS modes (blue dots). A fit shows that the residuals for the covariant modes are smaller by about a factor of two in comparison to Gram-Schmidt. Quite the opposite is true for the momentum perturbations in the bottom row of panels. Although the proportionality of Eq. (3.25) still holds, the scatter of the red squares for the covariant vectors is larger than that of the blue dots for the GS vectors. Such a behavior is always observed and is not simple numerical noise. The reason for this behavior is related to the previous discussion in connection with Fig. 3.9 but still needs further clarification.

Longitudinal (L) and associated momentum (P) modes share the same degenerate Lyapunov exponent  $\lambda^{(i)}$ , and generally appear superimposed in experimental vectors. With a rectangular box and periodic boundaries, they form four-dimensional LP perturbations. The superposition varies periodically with time. This “dynamics” has been identified as a rotation of the pure L and P vectors in the standard frame. For details we refer to previous work in Ref. [7]. The patterns for the pure L mode are easily recognizable as sine and cosine functions, but those for the P modes are not. As is evident from the spanning vectors for L(1,0) and P(1,0) also listed in Table 3.3, the P modes are proportional to the instantaneous velocities of all particles, which does not at all constitute a smooth vector field. For a pattern to be recognizable, these velocities need to be “divided out”. A full mode reconstruction is required as is described for the case of Gram-Schmidt vectors in Ref. [7], see Sec. 3.8.2. Here we carry out an analogous reconstruction in terms of the covariant vectors and compare them to the GS modes. In Fig. 3.11 two of the reconstructed patterns for L and P modes belonging to the four-dimensional LP(1,0) subspace

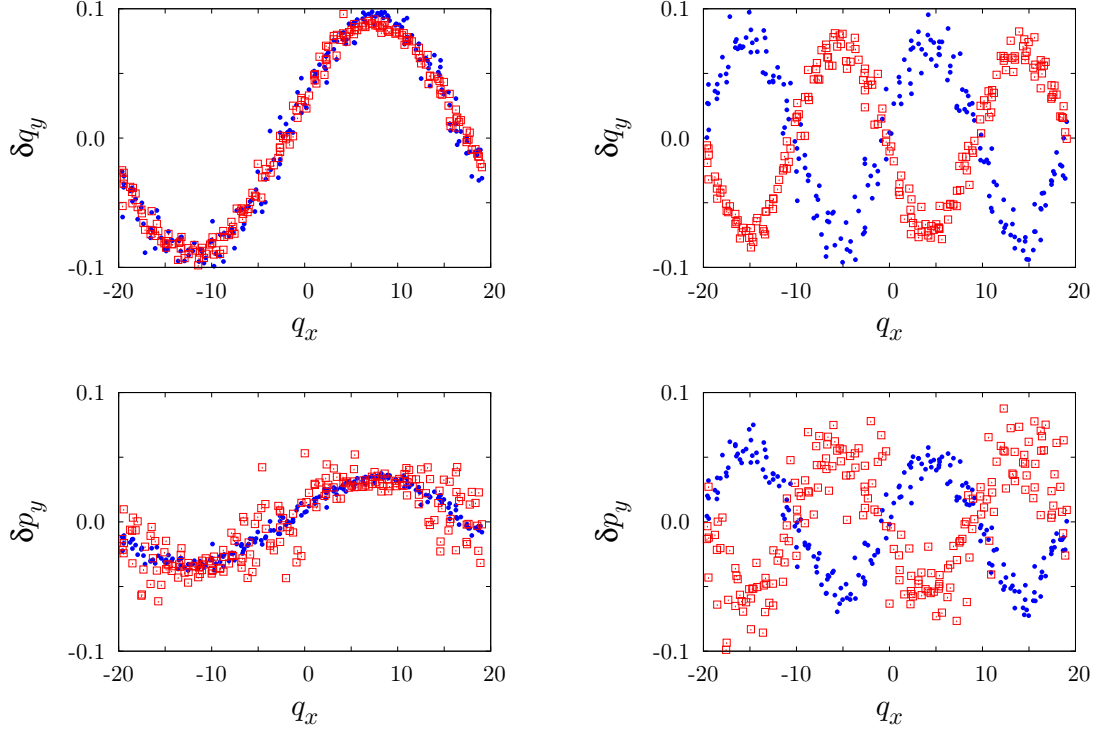


**Figure 3.10 :** Instantaneous transverse Lyapunov modes T(1,0) for index  $i = 393$  (left panels), and T(2,0) for index  $i = 387$  (right panels) for the 198-disk system. In the panels at the top (bottom) the  $y$ -coordinate perturbations  $\delta q_y$  ( $y$ -momentum perturbations  $\delta p_y$ ) of all particles are plotted as a function of their  $x$  coordinate,  $q_x$ , in the simulation cell. The wave vector is parallel to the  $x$  axis. The blue dots are for Gram-Schmidt vectors, the red squares for covariant vectors.

with indices  $i \in \{388, 389, 390, 391\}$  are shown. The blue dots are for GS modes, the red squares for covariant modes. To judge the quality of the reconstruction, we have included in the top-right panel also the  $\delta q_y$  versus  $q_x$  curve, which vanishes nicely as required.

For comparison, Fig. 3.12 gives results for a completely analogous reconstruction, where instead of the position perturbations as in Fig. 3.11, the corresponding momentum perturbations are used. For this example cosine patterns were selected, whereas in Fig. 3.11 sine patterns were used. As before, blue dots refer to GS vectors, red squares to covariant vectors.

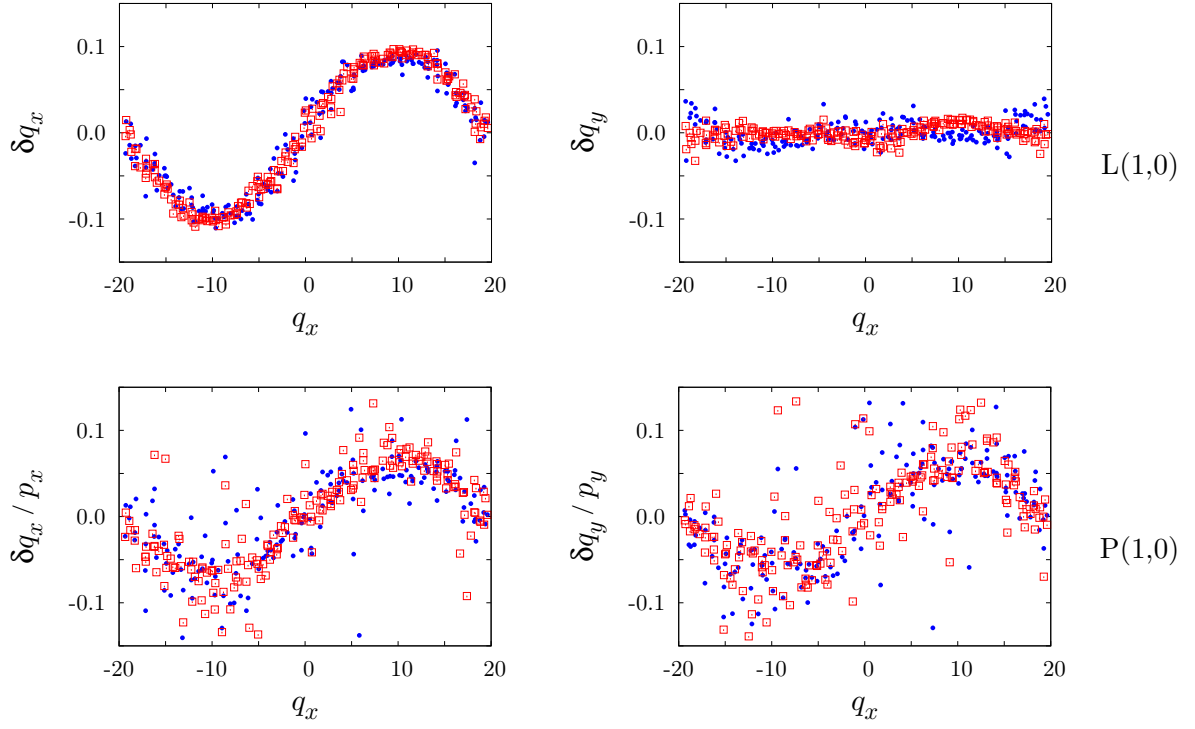


**Figure 3.11 :** Reconstructed position perturbations of the pure L(1,0) mode (top panels) and P(1,0) mode (bottom panels). Only the patterns proportional to  $\sin(2\pi q_x/L_x)$  are shown. Blue dots: Gram-Schmidt vectors; Red squares: covariant vectors. For details we refer to the main text.

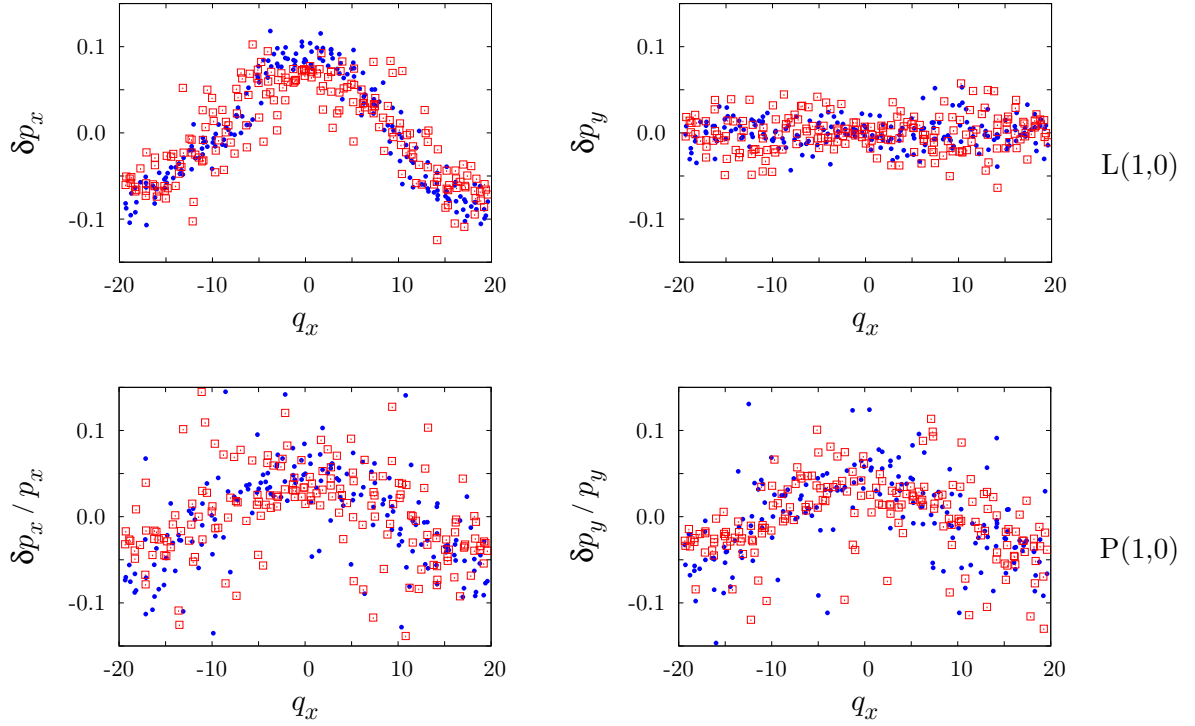


**Figure 3.12 :** Reconstructed momentum perturbations for the pure L(1,0) mode (top panels) and P(1,0) mode (bottom panels) depicted already in Fig. 3.11. Only the patterns proportional to  $\cos(2\pi q_x/L_x)$  are shown. Blue dots: Gram-Schmidt vectors; Red squares: covariant vectors.

### 3.5.6 Transversality

From the Lyapunov spectrum of Fig. 3.2 and the magnification of its central part in Fig. 3.8, the following inequalities are read off,

$$\lambda_1 > \cdots \geq \lambda_{2N-3} > \left[ \lambda^{(0)} \right] > \lambda_{2N+4} \geq \cdots > \lambda_{4N} , \quad (3.26)$$

where the equal sign applies for the degenerate exponents belonging to modes.  $[\lambda^0] = 0$  is sixfold degenerate in our case. Conjugate pairing assures that  $\lambda_i = -\lambda_{4N+1-i}$ . The Oseledec splitting provides us with the following structure of the tangent space,

$$\mathbf{TX} = \mathbf{E}^u \oplus \mathcal{N} \oplus \mathbf{E}^s, \quad (3.27)$$

where  $\mathbf{E}^u = \mathbf{v}^1 \oplus \cdots \oplus \mathbf{v}^{2N-3}$  and  $\mathbf{E}^s = \mathbf{v}^{2N+4} \oplus \cdots \oplus \mathbf{v}^{4N}$  are the covariant unstable and stable subspaces, respectively, and  $\mathcal{N}$  is the null subspace or central manifold. The question arises whether the system is hyperbolic, which implies that the angles between the stable manifold  $\mathbf{E}^s$  and the unstable manifold  $\mathbf{E}^u$  are bounded away from zero for all phase points (due to the existence of a central manifold this is referred to as partial hyperbolicity in the mathematical literature [44]). Even more, we may ask whether the angles between all Oseledec subspaces and, hence between all covariant vectors, are bounded away from zero for all phase-space points. To find an answer to that question, we compute in the following the scalar products for all covariant vector pairs and present representative results. (This procedure reminds us of the so-called coherence angles introduced by d'Alessandro and Tenenbaum [45, 46], measuring the angular distance between a physically interesting direction and the direction of maximum perturbation expansion).

The lines in Figure 3.13 depict the product norms  $\langle |\mathbf{v}^j \cdot \mathbf{v}^i| \rangle$  for selected covariant vectors  $\mathbf{v}^j$  with all other covariant vectors  $\mathbf{v}^i$ ,  $i \neq j$ . As before, a time average is performed. The panels on the left-hand side provide three examples for  $\mathbf{v}^j$  from the unstable manifold outside of the mode regime ( $j = 1, 200$ , and  $370$  from top-left to bottom-left, respectively), and similarly on the right-hand side from the stable manifold outside of the mode regime ( $j = 420, 600$ , and  $792$  from bottom-right to top-right, respectively). One immediately observes that the stable and unstable subspaces are not orthogonal. As has been mentioned in Sec. 3.5.4 and is also convincingly demonstrated in the following Fig. 3.14, the null subspace  $\mathcal{N}$  is orthogonal to both  $\mathbf{E}^u$  and  $\mathbf{E}^s$ . For two covariant vectors from the same subspace,  $\mathbf{E}^u$  or  $\mathbf{E}^s$ , however, the scalar product does not vanish indicating considerable non-orthogonality. But at the same time it is also well bounded away from unity, which means that the two vectors do not become parallel

either. However, one possible exception may be the covariant vector pairs  $(\mathbf{v}^j, \mathbf{v}^{j+1})$  for adjacent Lyapunov exponents in the spectrum. In these cases, the scalar product reaches a pronounced maximum in all of the six panels of Fig. 3.13 which may still allow these vectors to become parallel occasionally. This will be discussed further below.

So far we have considered only vectors  $\mathbf{v}^j$  outside of the mode regime. The case of covariant vectors representing modes is treated separately in Fig. 3.14, where, as before, time-averaged scalar product norms  $\langle |\mathbf{v}^j \cdot \mathbf{v}^i| \rangle$  for  $i \neq j$  are plotted as a function of  $i$ . The panels on the left-hand side are for  $j$  belonging to unstable transversal modes, the panels on the right-hand side for  $j$  belonging to unstable LP pairs. The curves for the conjugate stable modes just look like the mirror images around the central index. Each vector representing a T or LP-mode has significant contributions to the scalar product only for covariant vectors belonging to the same degenerate exponent and – to a lesser extent – the corresponding conjugate (negative) exponents (where the latter is not true anymore for the LP(3,0) modes in the bottom-right panel of Fig. 3.14, where no peak around  $i = 414$  is discernible).

The covariant vectors belonging to transverse (or to LP) modes span covariant Oseledec subspaces  $\mathbf{E}^{(i)}$  with a dimension  $m^{(i)}$  equal to 2 (respective 4). To ease the notation, we refer to them as  $\mathbf{E}^{(X)}$  in the following, where  $X$  is either T( $n_x, 0$ ) or LP( $n_x, 0$ ) with  $n_x \in \{1, 2, 3\}$ . The conjugate Oseledec subspaces,  $\mathbf{E}^{(X)*}$ , have the same dimension and are spanned by the respective conjugate covariant vectors. Fig. 3.14 shows that the covariant vectors spanning any of the subspaces  $\mathbf{E}^{(X)}$  or  $\mathbf{E}^{(X)*}$  have a rather small but finite angular distance and, thus, are transversal. The Oseledec subspaces representing modes are themselves transversal to all other subspaces of the Oseledec splitting, but to a varying degree. The angular distances in tangent space are generally large except between conjugate subspaces  $\mathbf{E}^{(X)}$  and  $\mathbf{E}^{(X)*}$ , for which the scalar products of their spanning vectors may become surprisingly large.

To check more carefully for transversality even in this case, we show in Fig. 3.15 the probability distribution for the minimum angle between the conjugate subspaces  $\mathbf{E}^{(X)}$  and  $\mathbf{E}^{(X)*}$ , where  $X$  stands for the T and LP modes as indicated by the labels. This angle  $\Phi$  is computed from the smallest principal angle between the two subspaces [47, 48]. If the covariant vectors belonging to  $\mathbf{E}^{(X)}$  and  $\mathbf{E}^{(X)*}$  are arranged as the column vectors of matrices  $\mathbf{V}$  and  $\mathbf{V}^*$ , respectively, the QR decompositions  $\mathbf{V} = \mathbf{Q}\mathbf{R}$  and  $\mathbf{V}^* = \mathbf{Q}^*\mathbf{R}^*$  of the latter provide matrices  $\mathbf{Q}$  and  $\mathbf{Q}^*$ , with which the matrix  $\mathbf{M} = \mathbf{Q}^T\mathbf{Q}^*$  is constructed. The singular values of  $\mathbf{M}$  are equal to the cosines of the principal angles, of which  $\Phi$  is the minimum angle. Since  $\Phi$  is never very small, this method works well and does not need more complicated refinements [47, 48, 49]. It is seen that all distributions are well bounded away from zero indicating transversality for the respective subspaces.

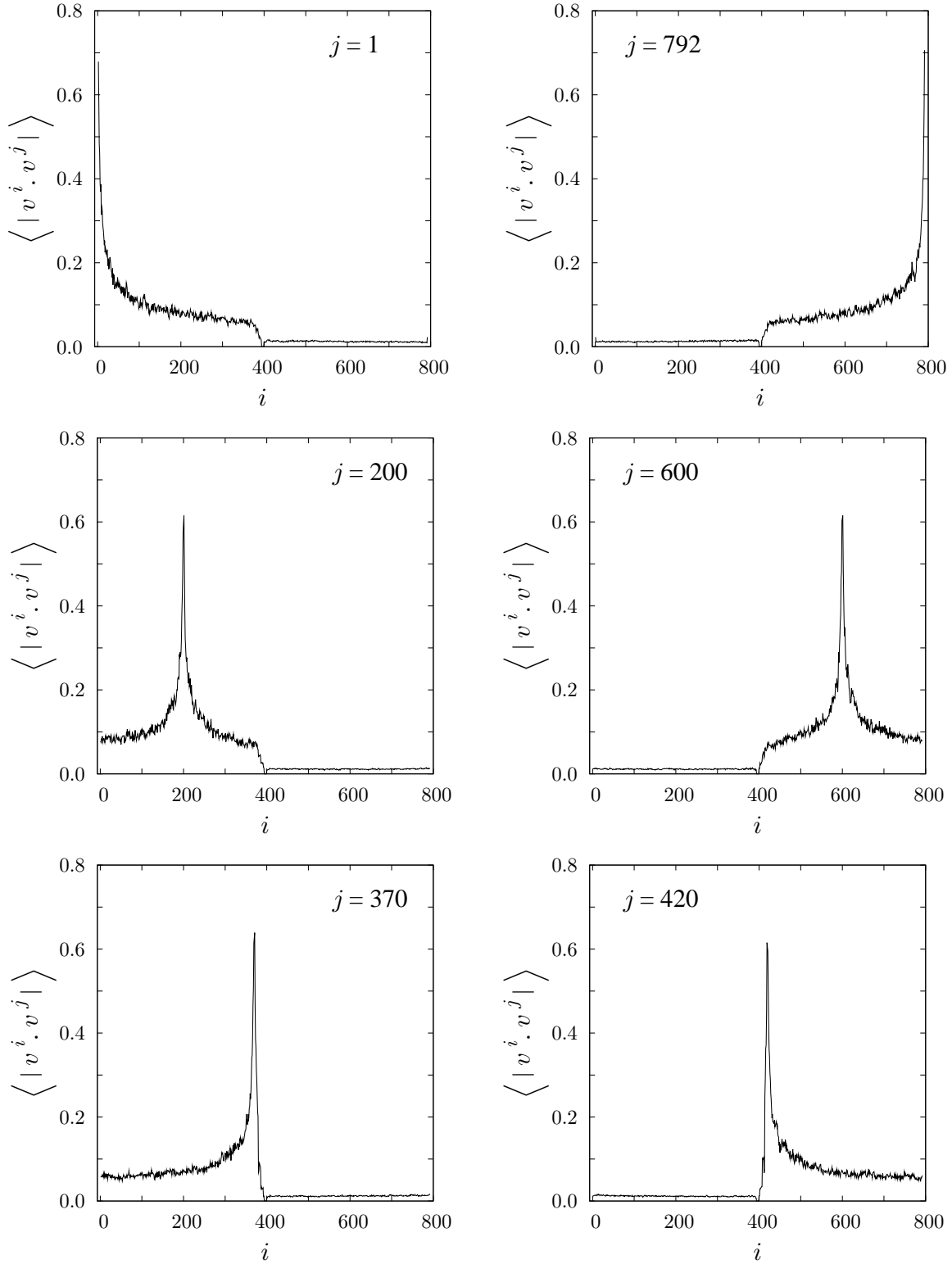


**Figure 3.13 :** The lines are time averaged (100 frames separated by 150 time units) absolute values of the scalar product of a specified covariant vector  $v^j$  with all the remaining covariant vectors  $v^{i \neq j}$  as a function of  $i$ . Left panels from top to bottom:  $j = 1, 200$ , and  $370$  belonging to the unstable manifold; Right panels from bottom to top:  $j = 420, 600$ , and  $792$  from the stable manifold.



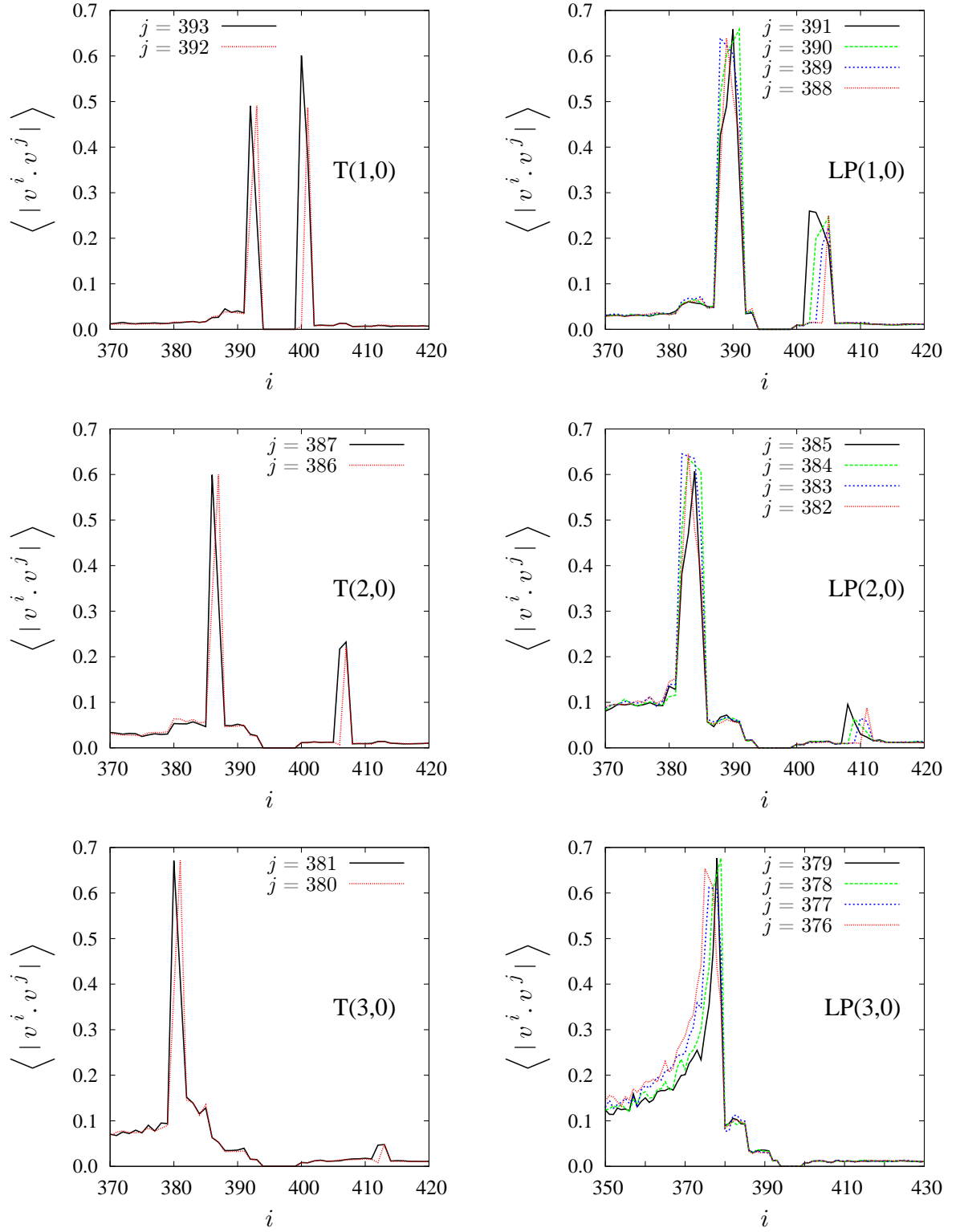


**Figure 3.14 :** The lines are time averaged (100 events separated by 150 time units) absolute values for the scalar product of covariant vectors  $v^j$  (as specified by the label  $j$ ) with all the remaining covariant vectors  $v^{i \neq j}$  as a function of  $i$ . The abscissa is restricted to the mode regime.  $j$  is for modes from the unstable subspace with positive exponents only. For the respective conjugate modes from the stable subspace, the curves in all panels are just the mirror images around the center as in Fig. 3.13.

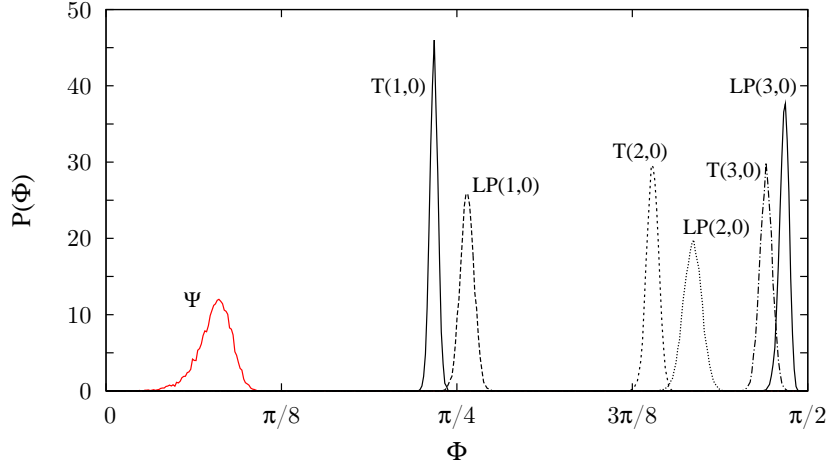


**Figure 3.15 :** Probability distributions for the minimum angle between the Oseledec subspace  $\mathbf{E}^{(X)}$  and its conjugate subspace  $\mathbf{E}^{(X)*}$ . Here,  $X \in \{T(n_x, 0), LP(n_x, 0)\}$  with  $n_x = 1, 2, 3$  specifies the modes as indicated by the labels. The probability distribution  $\Psi$  for the minimum angle between the stable and unstable manifolds  $\mathbf{E}^s$  and  $\mathbf{E}^u$  is shown by the red line.

Finally, we concentrate on the minimum angle between the full unstable subspace  $\mathbf{E}^u = \mathbf{v}^1 \oplus \dots \oplus \mathbf{v}^{393}$  and its conjugate stable counterpart  $\mathbf{E}^s = \mathbf{v}^{400} \oplus \dots \oplus \mathbf{v}^{792}$ , using the same method as before. These subspaces include the mode-carrying vectors studied before. The probability distribution for the minimum angle is denoted by  $\Psi$  and is also shown in Fig. 3.15 (red line). Also this distribution is well bounded away from zero and indicates transversality between  $\mathbf{E}^s$  and  $\mathbf{E}^u$ . We conclude that for finite  $N$  the hard-disk systems are (partially) hyperbolic in phase space.

In Fig. 3.13 it was observed that the scalar products between covariant vectors with adjacent indices are rather large and possibly may allow tangencies. To study this point more carefully, we follow a suggestion of G. Morriss and consider the angle  $\Theta = \cos^{-1} |\mathbf{v}^i \cdot \mathbf{v}^j|$  between the vectors  $\mathbf{v}^i \in \mathbf{F}^{(J)}$  and  $\mathbf{v}^j \in \mathbf{F}^{(J)}$ , for which  $i - j$  is a specified positive integer. The probability distributions for angles with  $i - j = 1, 2, 4, 20, 50$  are shown in Fig. 3.16, and for  $i - j = 100, 200, 300$  in the inset of the same figure. Whereas the probabilities for  $i - j > 1$  are bounded away from zero, the distribution for  $i - j = 1$  seems to converge to zero for  $\Theta \rightarrow 0$ .

An even more demanding test is given in Fig 3.17, where the minimum of  $\Theta$  for given  $i - j > 0$  is plotted as a function of  $i - j$ . The inset provides a magnification of the most interesting region. One observes that the minimum of the angle  $\Theta$  between covariant vectors specifying Oseledec subspaces with  $i - j = 1$  may indeed become very small, but this happens with extremely small probability. Our numerical evidence is consistent with the assumption that the angle becomes zero with vanishing probability.

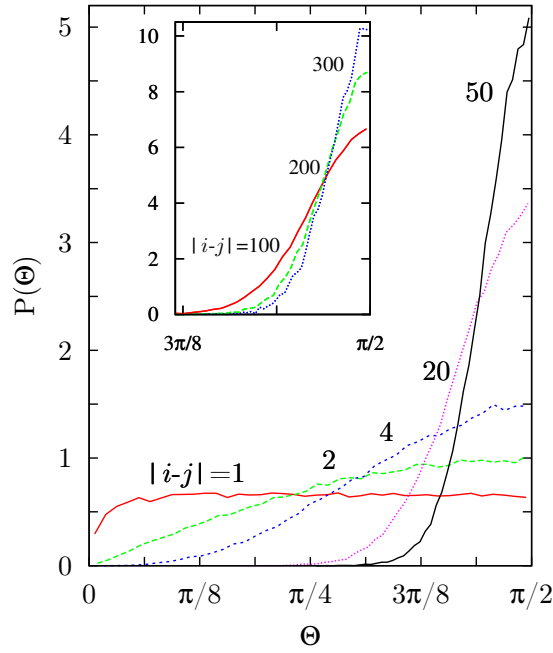


**Figure 3.16 :** Probability distributions for the angles  $\Theta$  between all covariant vectors  $\mathbf{v}^i$  and  $\mathbf{v}^j$  from  $\mathbf{F}^{(370)} = \mathbf{v}^1 \oplus \dots \oplus \mathbf{v}^{370}$  with prescribed separation  $i - j$  of their indices as indicated by the labels.

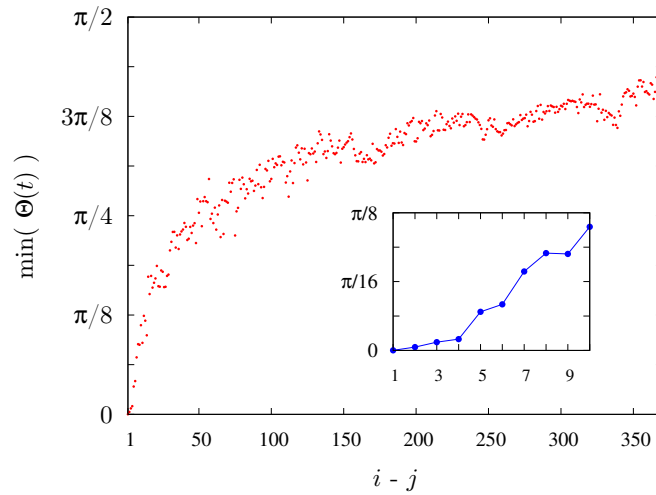


**Figure 3.17 :** Plot of the minimum angle between different covariant vectors  $\mathbf{v}^i$  and  $\mathbf{v}^j$  from the unstable subspace without the mode-affected directions,  $\mathbf{F}^{(370)} = \mathbf{v}^1 \oplus \dots \oplus \mathbf{v}^{370}$ , as a function of their index difference  $i - j$ .

### 3.6 Conclusion

A comparison of the covariant vectors with corresponding orthonormal Gram-Schmidt vectors reveal similarities, but also significant differences. The vectors associated with the maximum Lyapunov exponent are identical,  $\mathbf{v}^1 = \mathbf{g}^1$ , and also the leading vectors in the central manifold agree,  $\mathbf{v}^{2N-2} = \mathbf{g}^{2N-2}$ . All the other corresponding vectors generally point into different tangent-space directions. Whereas the GS vectors are pairwise orthogonal by construction, the covariant vectors are not. Most notably, the perturbation contributions from the particles' positions and momenta are significantly different and even exhibit a different symmetry between vectors from the stable and unstable manifold as in Fig. 3.6. For the covariant vectors these contributions agree in accordance with the time-reversal symmetry required for them, whereas for the Gram-Schmidt vectors these contributions are interchanged. Another significant difference is the degree of localization in physical space for the non-degenerate perturbations. As Fig. 3.5 shows, the covariant vectors are much more localized than the GS vectors in accordance with the fact that they are not dynamically constrained by re-orthogonalization.

From a theoretical point of view, an interesting result is that no tangencies occur between the respective unstable and stable manifolds  $\mathbf{E}^u$  and  $\mathbf{E}^s$ . In Fig. 3.15 the probability distribution  $\Psi$  of the minimum angle between stable and unstable subspaces (including the Lyapunov modes) is well bounded away from zero, and even more so for the vectors belonging to unstable respective stable modes. Thus, a hard-disk system with  $N = 198$  particles as in our case is (partial) hyperbolic for all points in phase space. We even find that all Oseledec subspaces are pairwise transversal with non-vanishing angles between them.

We speculate that for  $N \rightarrow \infty$  the distribution for the minimum angle between  $\mathbf{E}^u$  and  $\mathbf{E}^s$  may possibly reach the origin in Fig. 3.15. To clarify this point further studies are required.

The concept of hyperbolicity is closely linked with the notion of dominated Oseledec splitting for all phase space points [44]. We may rewrite Eq. (3.6) for the Lyapunov exponents, expressed in terms of the covariant vectors, according to

$$\lambda_i = \lim_{\mathcal{K} \rightarrow \infty} \frac{1}{\mathcal{K}} \sum_{k=0}^{\mathcal{K}-1} \frac{1}{\tau} \ln \|D\phi^\tau|_{\Gamma(t_k)} \mathbf{v}^i(\Gamma(t_k))\|, \quad (3.28)$$

where  $t_k \equiv k\tau$ , and  $\tau$  is the short time interval between consecutive re-normalizations of the covariant vectors. Here,  $\lambda_\ell$  is expressed as a time average of a quantity

$$\Lambda_i^{\text{cov}}(\Gamma(t_n)) = \frac{1}{\tau} \ln \|D\phi^\tau|_{\Gamma(t_{k-1})} \mathbf{v}^i(\Gamma(t_{k-1}))\|, \quad (3.29)$$

which is referred to as local (or time-dependent) Lyapunov exponent, and is a function of the instantaneous phase point  $\Gamma(\mathbf{t})$ . The Oseledec splitting is said to be dominated, if the local Lyapunov exponents, when averaged over a finite time  $\Delta$ , do not change their order in the spectrum for any  $\Delta$  larger than some *finite*  $\Delta_0 > 0$  (see Chap. 7). This is a very strong condition on the fluctuations of the local exponents [50, 51]. For symplectic systems it is known that the domination of the splitting implies that the system is (partially) hyperbolic [44]. But it is not clear whether the converse is true in our case. The discussion of this point is deferred to a forthcoming publication (Chap. 8).

The number and the dimension of the Oseledec subspaces are constant in phase space. There is no entanglement of subspaces, which has been identified as one of the main reasons for the occurrence of well-established Lyapunov modes [50]. We refer to Ref. [51] (Chap. 5) for a discussion of a simple but physically-relevant model, for which the dimensions of the stable and unstable manifolds frequently change along the trajectory.

An interesting extension of this work is the study of rough hard particles allowing for energy exchange between translational and rotational degrees of freedom (Chap. 8). Arguably, this is the simplest model of a molecular fluid. No Lyapunov modes are found in this case [52]. An analysis in terms of covariant vectors is presently under way and will be published separately.

### 3.7 Acknowledgements

We dedicate this work to Peter Hänggi on the occasion of his 60th birthday. His insight and enthusiasm for science is a continuous source of inspiration. We also gratefully acknowledge stimulating discussions with Francesco Ginelli, Gary Morriss, Antonio Politi, Günter Radons, and Hong-liu Yang. Our work was supported by the Austrian Wissenschaftsfonds (FWF), grant P 18798-N20.

### 3.8 Appendix\*

#### 3.8.1 Zero Modes dynamics

In this Appendix we justify Eqs. (3.23) and (3.24) for the dynamics of the six natural basis vectors (Eqs. (3.17) - (3.22)) spanning the central manifold. For convenience, we use the notation

$$\mathbf{e}_j = \frac{1}{\sqrt{(\delta \mathbf{q}^j)^2 + (\delta \mathbf{p}^j)^2}} (\delta \mathbf{q}^j ; \delta \mathbf{p}^j)$$

for the basis vectors, and

$$\mathbf{\Gamma} = (\mathbf{q} ; \mathbf{p})$$

for the state point, where  $\mathbf{q} = (\vec{q}_1, \dots, \vec{q}_N)$  and  $\mathbf{p} = (\vec{p}_1, \dots, \vec{p}_N)$  are  $2N$ -dimensional vectors in the configuration and momentum spaces, respectively. The time evolution of the state vector and of an arbitrary perturbation vector follows the phase flow and the tangent flow, respectively:

$$\mathbf{\Gamma}_t = \phi^t \mathbf{\Gamma}_0 \quad \text{and} \quad \delta \mathbf{\Gamma}_t = D\phi_{\mathbf{\Gamma}_0}^t \delta \mathbf{\Gamma}_0 .$$

Both flows are characterized by a sequence of free flights interrupted by elastic collisions at times  $\{\tau_1, \tau_2, \dots, \tau_\zeta\}$ ,

$$\begin{aligned} \phi^t &= \phi^{t-\tau_\zeta} \mathcal{M} \dots \phi^{\tau_2-\tau_1} \mathcal{M} \phi^{\tau_1-\tau_0} , \\ D\phi_{\mathbf{\Gamma}_0}^t &= D\phi_{\mathbf{\Gamma}_0}^{t-\tau_\zeta} \mathcal{S} \dots D\phi_{\mathbf{\Gamma}_0}^{\tau_2-\tau_1} \mathcal{S} D\phi_{\mathbf{\Gamma}_0}^{\tau_1-\tau_0} , \end{aligned}$$

where the discrete maps  $\mathcal{M}$  and  $\mathcal{S}$  govern the respective transformation at each collision in the phase and tangent space. The free flight between collisions at  $\tau_1$  and  $\tau_2$  is trivially given by

$$\begin{aligned} \phi^{\tau_2-\tau_1} \mathbf{\Gamma} &\begin{cases} \vec{q}_n(\tau_2) = \vec{q}_n(\tau_1) + (\tau_2 - \tau_1) \vec{p}_n(\tau_1)/m , \\ \vec{p}_n(\tau_2) = \vec{p}_n(\tau_1) , \end{cases} \\ D\phi^{\tau_2-\tau_1} \delta \mathbf{\Gamma} &\begin{cases} \delta \vec{q}_n(\tau_2) = \delta \vec{q}_n(\tau_1) + (\tau_2 - \tau_1) \delta \vec{p}_n(\tau_1)/m , \\ \delta \vec{p}_n(\tau_2) = \delta \vec{p}_n(\tau_1) , \end{cases} \end{aligned}$$

where the particle mass  $m$  is considered equal to unity. Since  $\delta \vec{p}_n = \vec{0}$ ,  $\forall n \in \{1, \dots, N\}$ , for  $\mathbf{e}_1$ ,  $\mathbf{e}_2$  and  $\mathbf{e}_3$  (Eqs. (3.17) - (3.19)), one has

$$D\phi^{\tau_2-\tau_1} \mathbf{e}_j(\tau_1) = \mathbf{e}_j(\tau_2) \quad \forall j \in \{1, 2, 3\} .$$

---

\*This section is not included in the original publication in Chem. Phys. **375**, p. 296 (2010).

Since  $\delta \vec{q}_n = \vec{0}$ ,  $\forall n \in \{1, \dots, N\}$ , for  $\mathbf{e}_4$ ,  $\mathbf{e}_5$  and  $\mathbf{e}_6$  (Eq. (3.20) - (3.22)), writing these last three vectors as

$$\mathbf{e}_{j+3}(\tau_1) = \frac{1}{\|\delta \mathbf{p}^{j+3}(\tau_1)\|} \left( \mathbf{0}; \delta \mathbf{p}^{j+3}(\tau_1) \right) \quad \forall j \in \{1, 2, 3\} ,$$

implies

$$\begin{aligned} D\phi^{\tau_2 - \tau_1} \mathbf{e}_{j+3}(\tau_1) &= \frac{1}{\|\delta \mathbf{p}^{j+3}(\tau_1)\|} \left( (\tau_2 - \tau_1) \delta \mathbf{p}^{j+3}(\tau_1); \delta \mathbf{p}^{j+3}(\tau_1) \right) \\ &= (\tau_2 - \tau_1) \left( \frac{\delta \mathbf{p}^{j+3}(\tau_1)}{\|\delta \mathbf{p}^{j+3}(\tau_1)\|}; \mathbf{0} \right) + \left( \mathbf{0}; \frac{\delta \mathbf{p}^{j+3}(\tau_1)}{\|\delta \mathbf{p}^{j+3}(\tau_1)\|} \right) \\ &= (\tau_2 - \tau_1) \mathcal{J} \mathbf{e}_{j+3}(\tau_1) + \mathbf{e}_{j+3}(\tau_1) \\ &= (\tau_2 - \tau_1) \mathbf{e}_j(\tau_1) + \mathbf{e}_{j+3}(\tau_1) \quad \forall j \in \{1, 2, 3\} . \end{aligned}$$

Now we turn our attention to the transformations for a collision between the disks  $k$  and  $\ell$ . Let  $\vec{q} = \vec{q}_k - \vec{q}_\ell$  and  $\delta \vec{q} = \delta \vec{q}_k - \delta \vec{q}_\ell$  denote the respective relative positions in the phase space and in the tangent space, similarly,  $\vec{p} = \vec{p}_k - \vec{p}_\ell$  and  $\delta \vec{p} = \delta \vec{p}_k - \delta \vec{p}_\ell$  the relative momenta. According to [18], immediately after the collision, the vectors  $\mathbf{\Gamma}$  and  $\delta \mathbf{\Gamma}$  are transformed according to

$$\mathcal{M} \mathbf{\Gamma} \left\{ \begin{array}{l} \mathcal{M}_q \mathbf{q} \left\{ \begin{array}{l} \vec{q}'_n = \vec{q}_n \quad \forall n \in \{1, \dots, N\} , \\ \vec{p}'_n = \vec{p}_n \quad \forall n \notin \{k, \ell\} , \\ \vec{p}'_\ell = \vec{p}_\ell + \frac{1}{\sigma^2} (\vec{p} \cdot \vec{q}) \vec{q} , \\ \vec{p}'_k = \vec{p}_k - \frac{1}{\sigma^2} (\vec{p} \cdot \vec{q}) \vec{q} , \end{array} \right. \end{array} \right. \quad (3.30)$$

$$\mathcal{S} \delta \mathbf{\Gamma} \left\{ \begin{array}{l} \mathcal{S}_q \delta \mathbf{q} \left\{ \begin{array}{l} \delta \vec{q}'_n = \delta \vec{q}_n \quad \forall n \notin \{k, \ell\} , \\ \delta \vec{q}'_\ell = \delta \vec{q}_\ell + \frac{1}{\sigma^2} (\delta \vec{q} \cdot \vec{q}) \vec{q} , \\ \delta \vec{q}'_k = \delta \vec{q}_k - \frac{1}{\sigma^2} (\delta \vec{q} \cdot \vec{q}) \vec{q} , \end{array} \right. \\ \mathcal{S}_p \delta \mathbf{p} \left\{ \begin{array}{l} \delta \vec{p}'_n = \delta \vec{p}_n \quad \forall n \notin \{k, \ell\} , \\ \delta \vec{p}'_\ell = \delta \vec{p}_\ell + \frac{1}{\sigma^2} (\delta \vec{p} \cdot \vec{q}) \vec{q} + \frac{1}{\sigma^2} \left[ (\vec{p} \cdot \vec{q}) \delta \vec{q}_c + (\vec{p} \cdot \delta \vec{q}_c) \vec{q} \right] , \\ \delta \vec{p}'_k = \delta \vec{p}_k - \frac{1}{\sigma^2} (\delta \vec{p} \cdot \vec{q}) \vec{q} - \frac{1}{\sigma^2} \left[ (\vec{p} \cdot \vec{q}) \delta \vec{q}_c + (\vec{p} \cdot \delta \vec{q}_c) \vec{q} \right] , \end{array} \right. \end{array} \right. \quad (3.31)$$

where the displacement of the collision point between the reference and the satellite trajectory is given by  $\delta \vec{q}_c = \delta \vec{q} - \vec{p}(\delta \vec{q} \cdot \vec{q})/(\vec{p} \cdot \vec{q})$ , which is perpendicular to  $\vec{q}$  (see Fig. 3.18).

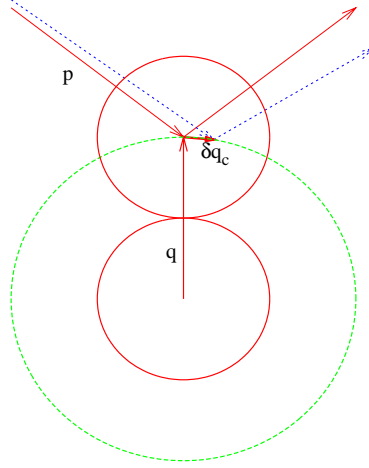


**Figure 3.18 :** Collision in relative coordinates.

According to Eqs. (3.30) and (3.31), we obtain

$$\begin{aligned} \mathcal{S} \mathbf{e}_1(\Gamma_0) &= \frac{1}{\sqrt{(\delta \mathbf{q}^1)^2 + (\delta \mathbf{p}^1)^2}} (\mathcal{S}_q \delta \mathbf{q}^1 ; \mathcal{S}_p \delta \mathbf{p}^1) \\ &= \frac{1}{\sqrt{2K}} (\mathcal{M}_p \mathbf{p} ; \emptyset) \equiv \mathbf{e}'_1(\Gamma_0) . \end{aligned} \quad (3.32)$$

For  $\mathbf{e}_2$  and  $\mathbf{e}_3$ , for which  $\delta \vec{q} \equiv \delta \vec{q}_\ell - \delta \vec{q}_k = \vec{0}$  and  $\delta \vec{p}_n = \vec{0}$ ,  $\forall n \in \{1, \dots, N\}$ , Eq. (3.31) gives

$$\mathcal{S} \mathbf{e}_2(\Gamma_0) = \mathbf{e}_2(\Gamma_0) \quad \text{and} \quad \mathcal{S} \mathbf{e}_3(\Gamma_0) = \mathbf{e}_3(\Gamma_0) . \quad (3.33)$$

Correspondingly, for  $\mathbf{e}_5$  and  $\mathbf{e}_6$ , for which  $\delta \vec{p} \equiv \delta \vec{p}_\ell - \delta \vec{p}_k = \vec{0}$  and  $\delta \vec{q}_n = \vec{0}$ ,  $\forall n \in \{1, \dots, N\}$ , Eq. (3.31) yields

$$\mathcal{S} \mathbf{e}_5(\Gamma_0) = \mathbf{e}_5(\Gamma_0) \quad \text{and} \quad \mathcal{S} \mathbf{e}_6(\Gamma_0) = \mathbf{e}_6(\Gamma_0) . \quad (3.34)$$

For  $\mathbf{e}_4$  we have  $\delta \vec{q}_n = \vec{0}$ ,  $\forall n \in \{1, \dots, N\}$ , and from Eqs. (3.30) and (3.31) we obtain

$$\begin{aligned} \mathcal{S} \mathbf{e}_4(\Gamma_0) &= \frac{1}{\sqrt{(\delta \mathbf{q}^4)^2 + (\delta \mathbf{p}^4)^2}} (\mathcal{S}_q \delta \mathbf{q}^4 ; \mathcal{S}_p \delta \mathbf{p}^4) \\ &= \frac{1}{\sqrt{2K}} (\emptyset ; \mathcal{M}_p \mathbf{p}) \equiv \mathbf{e}'_4(\Gamma_0) . \end{aligned} \quad (3.35)$$

Finally, an alternative application of the maps for free flight and collision to the six basis vectors  $\{\mathbf{e}_j, 1 \leq j \leq 6\}$  gives

$$D\phi_{\Gamma_0}^t \mathbf{e}_j(\Gamma_0) = \mathbf{e}_j(\Gamma_t) , \quad (3.36)$$

$$D\phi_{\Gamma_0}^t \mathbf{e}_{j+3}(\Gamma_0) = t \mathbf{e}_j(\Gamma_t) + \mathbf{e}_{j+3}(\Gamma_t) , \quad (3.37)$$

for  $j \in \{1, 2, 3\}$  as stated in Eqs. (3.23) and (3.24).



Next, we consider the time evolution of an arbitrary perturbation vector  $\delta\mathbf{\Gamma}^c$  in the central manifold. Initially,

$$\delta\mathbf{\Gamma}_0^c = \sum_{j=1}^6 a_0^j \mathbf{e}_j(\mathbf{\Gamma}_0) .$$

According to Eqs. (3.36) and (3.37), it will reorient for large times  $t$  towards the Q-space,

$$\begin{aligned} \delta\mathbf{\Gamma}_t^c &\equiv \sum_{j=1}^6 a_t^j \mathbf{e}_j(\mathbf{\Gamma}_t) = \sum_{j=1}^3 (a_0^j + t a_0^{j+3}) \mathbf{e}_j(\mathbf{\Gamma}_t) + a_0^{j+3} \mathbf{e}_{j+3}(\mathbf{\Gamma}_t) , \\ \lim_{t \gg 1} \delta\mathbf{\Gamma}_t^c &= \sum_{j=1}^3 t a_0^{j+3} \mathbf{e}_j(\mathbf{\Gamma}_t) + a_0^{j+3} \mathbf{e}_{j+3}(\mathbf{\Gamma}_t) . \end{aligned}$$

For large times,

$$a_t^{j+3} = \frac{a_t^j}{t} \quad \forall j \in [1, 3] .$$

This behavior determines the projection matrix  $\beta$  in Table 3.2. With  $t \rightarrow \infty$  the vectors  $\mathbf{e}_4$ ,  $\mathbf{e}_5$  and  $\mathbf{e}_6$  converge towards the subspace spanned by  $\mathbf{e}_1$ ,  $\mathbf{e}_2$  and  $\mathbf{e}_3$ .

We note that for the first three vectors belonging to the central manifold  $\{\mathbf{e}_j, 1 \leq j \leq 3\}$  the convergence in the P-part depends on the relaxation time  $t_0$ , whereas for the last three vectors  $\{\mathbf{e}_j, 4 \leq j \leq 6\}$  this convergence depends on the forward-backward iteration time  $t_\omega - t_0$ . The reason for this is that for the first three vectors the convergence is already obtained with the G-S vectors during the relaxation time (see Table 3.1), whereas during the forward and backward iterations the changes are compensated. For the last three vectors the components are only generated during the backward iteration.

### 3.8.2 Reconstruction of the LP-modes from the experimental GS and covariant vectors (see Table 3.3)

Here we explain how we approximate the typical basis vectors for the various LP modes from the experimental GS and covariant vectors. This method was first used in Ref. [7] for GS vectors, where the mode classification is based only on  $\delta\mathbf{q}$ , since  $\delta\mathbf{q}$  and  $\delta\mathbf{p}$  are observed to be either parallel (for the unstable branch) or anti-parallel (for the stable branch) in the mode region for sufficiently large systems (see Fig. 3.9). Here, the method is also applied to the covariant vectors, and the  $\delta\mathbf{q}$  and  $\delta\mathbf{p}$  parts are treated separately since  $\delta\mathbf{q}$  and  $\delta\mathbf{p}$  are not strictly parallel (see Fig. 3.9).

Because the hard disks are enclosed in a rectangular box with periodic boundary conditions, the  $\text{LP}(n_x, 0)$  spaces have a dimension of 4 (the spectrum indicates a four-fold degeneracy).

Each  $\text{LP}(n_x, 0)$  space is assumed to be a superposition of the 2-dimensional subspaces  $\text{L}(n_x, 0)$  and  $\text{P}(n_x, 0)$ . Each  $\text{L}(n_x, 0)$ - and  $\text{P}(n_x, 0)$ -mode consists of a pair of  $2N$ -dimensional spanning vectors (cosine and sine part), which are denoted  $(\varphi_c^L, \varphi_s^L)$  and  $(\varphi_c^P, \varphi_s^P)$ , respectively. According to Table 3.3, the typical basis vectors are defined as

$$\varphi_c^L = \frac{1}{z_c^L} (c_1, 0, \dots, c_N, 0) \quad \text{and} \quad \varphi_s^L = \frac{1}{z_s^L} (s_1, 0, \dots, s_N, 0) \quad ,$$

$$\varphi_c^P = \frac{1}{z_c^P} (p_x^1 c_1, p_y^1 c_1, \dots, p_x^N c_N, p_y^N c_N) \quad \text{and} \quad \varphi_s^P = \frac{1}{z_s^P} (p_x^1 s_1, p_y^1 s_1, \dots, p_x^N s_N, p_y^N s_N) \quad ,$$

where  $z_c^L$ ,  $z_s^L$ ,  $z_c^P$  and  $z_s^P$  are normalization factors, and where  $c_n = \cos(k_x q_x^n)$  and  $s_n = \sin(k_x q_x^n)$  corresponding to the  $n$ -th particle. From now on, the four  $2N$ -dimensional spanning vectors are indifferently denoted by  $\varphi \equiv (\varphi_1, \dots, \varphi_{2N})$ , omitting the subscripts and superscripts for the sake of simplicity.

We denote by  $\psi^1$ ,  $\psi^2$ ,  $\psi^3$  and  $\psi^4$  the four experimental perturbation vectors of  $2N$  dimensions (since  $\delta \mathbf{q}$  and  $\delta \mathbf{p}$  are considered separately) associated with each tangent subspace  $\text{LP}(n_x, 0)$ , for  $1 \leq n_x \leq 3$ . We give as example the expression of  $\{\psi^j\}_{j=1}^4$  associated to  $\text{LP}(1, 0)$  in the configuration space (i.e. the  $\delta \mathbf{q}$  part):

$$\psi^1 = \frac{\delta \mathbf{q}^{388}}{\|\delta \mathbf{q}^{388}\|} \quad , \quad \psi^2 = \frac{\delta \mathbf{q}^{389}}{\|\delta \mathbf{q}^{389}\|} \quad , \quad \psi^3 = \frac{\delta \mathbf{q}^{390}}{\|\delta \mathbf{q}^{390}\|} \quad , \quad \psi^4 = \frac{\delta \mathbf{q}^{391}}{\|\delta \mathbf{q}^{391}\|} \quad ,$$

where  $\delta \mathbf{q}^i = (\vec{q}_1^i, \dots, \vec{q}_N^i)$  is the  $2N$ -dimensional configuration part of the perturbation vector  $\delta \mathbf{\Gamma}_i \equiv (\delta \mathbf{q}^i; \delta \mathbf{p}^i)$ ,  $i$  corresponding to the Lyapunov index. The Lyapunov indices corresponding to the set  $\{\psi^j\}_{j=1}^4$ , for each  $\text{LP}(n_x, 0)$  space, are shown in Fig. 3.14.

For each of the four typical basis vectors  $\varphi$ , we find its best approximation from the linear combination of the measured vectors  $\{\psi^j\}_{j=1}^4$ :

$$\varphi \approx \alpha_1 \psi^1 + \alpha_2 \psi^2 + \alpha_3 \psi^3 + \alpha_4 \psi^4 \quad ,$$

where  $\psi^j \equiv (\psi_1^j, \dots, \psi_{2N}^j)$ . Numerically, the best values for the constants  $\{\alpha_j\}_{j=1}^4$  are computed using the least-square method, and chi-square is calculated as usual:

$$\chi^2 = \sum_{k=1}^{2N} (\varphi_k - \alpha_1 \psi_k^1 - \alpha_2 \psi_k^2 - \alpha_3 \psi_k^3 - \alpha_4 \psi_k^4)^2 \quad .$$

The conditions  $\partial \chi^2 / \partial \alpha_j = 0$ , for all  $j \in \{1, 2, 3, 4\}$ , directly give the following matrix equal-

ity:

$$\underbrace{\begin{pmatrix} \sum_k \psi_k^1 \varphi_k \\ \sum_k \psi_k^2 \varphi_k \\ \sum_k \psi_k^3 \varphi_k \\ \sum_k \psi_k^4 \varphi_k \end{pmatrix}}_{\mathbf{B}} = \underbrace{\begin{pmatrix} \sum_k (\psi_k^1)^2 & \sum_k \psi_k^1 \psi_k^2 & \sum_k \psi_k^1 \psi_k^3 & \sum_k \psi_k^1 \psi_k^4 \\ \sum_k \psi_k^2 \psi_k^1 & \sum_k (\psi_k^2)^2 & \sum_k \psi_k^2 \psi_k^3 & \sum_k \psi_k^2 \psi_k^4 \\ \sum_k \psi_k^3 \psi_k^1 & \sum_k \psi_k^3 \psi_k^2 & \sum_k (\psi_k^3)^2 & \sum_k \psi_k^3 \psi_k^4 \\ \sum_k \psi_k^4 \psi_k^1 & \sum_k \psi_k^4 \psi_k^2 & \sum_k \psi_k^4 \psi_k^3 & \sum_k (\psi_k^4)^2 \end{pmatrix}}_{\mathbf{A}} \begin{pmatrix} \alpha_1 \\ \alpha_2 \\ \alpha_3 \\ \alpha_4 \end{pmatrix}.$$

The investigated constants are then simply found as

$$\begin{pmatrix} \alpha_1 \\ \alpha_2 \\ \alpha_3 \\ \alpha_4 \end{pmatrix} = \mathbf{A}^{-1} \mathbf{B}.$$

This algorithm was used to reconstruct the different basis vectors of the L-mode and the P-mode: the classification of the modes is shown for the  $\delta \mathbf{q}$  and  $\delta \mathbf{p}$  parts of the GS and covariant vectors, and only for the corresponding positive Lyapunov exponents.

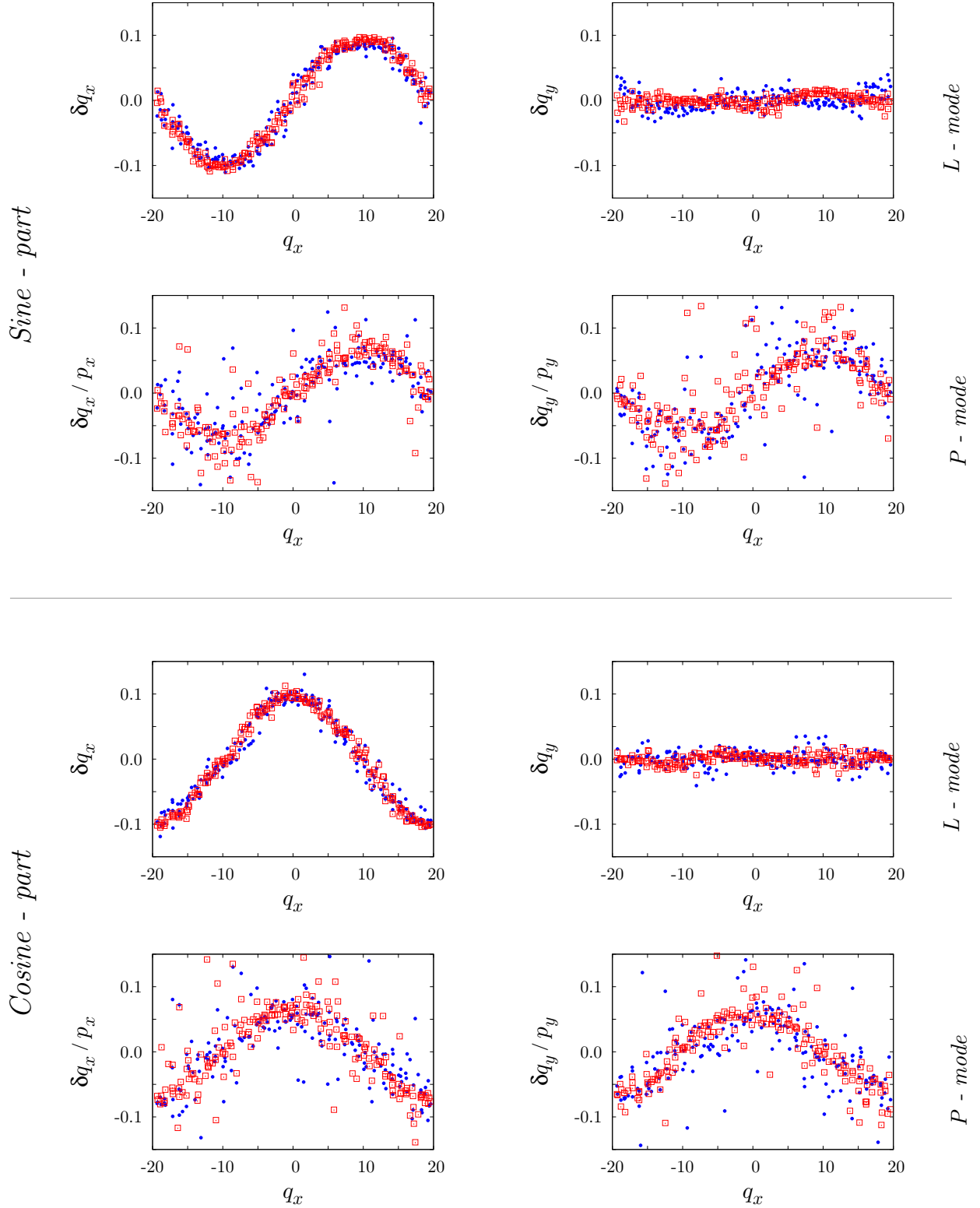


**Figure 3.19 :** Reconstruction of the  $\delta \mathbf{q}$  part for LP(1,0) ( $\bullet$  GS vectors,  $\square$  covariant vectors).

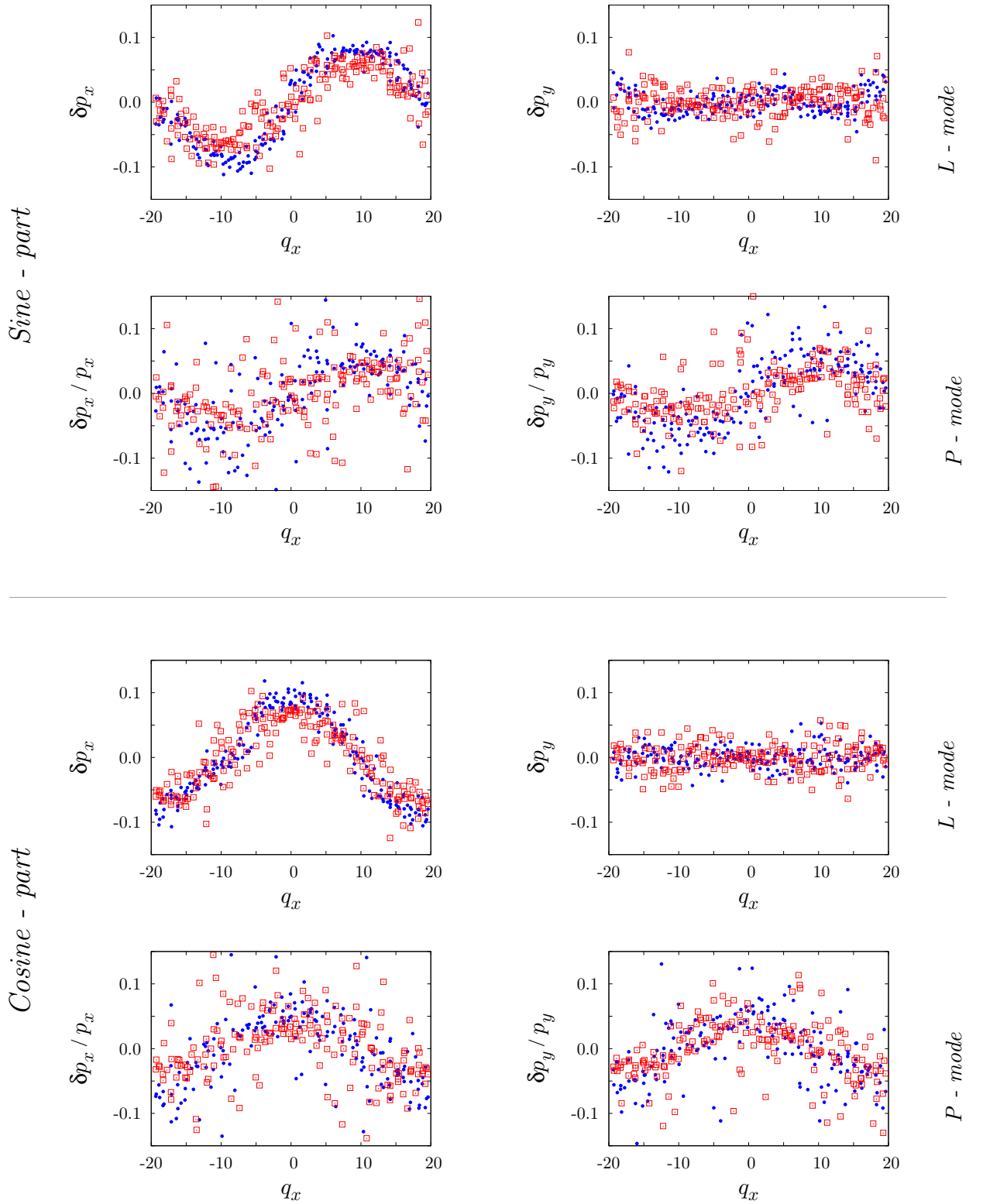


**Figure 3.20 :** Reconstruction of the  $\delta \mathbf{p}$  part for LP(1,0) (● GS vectors, □ covariant vectors).

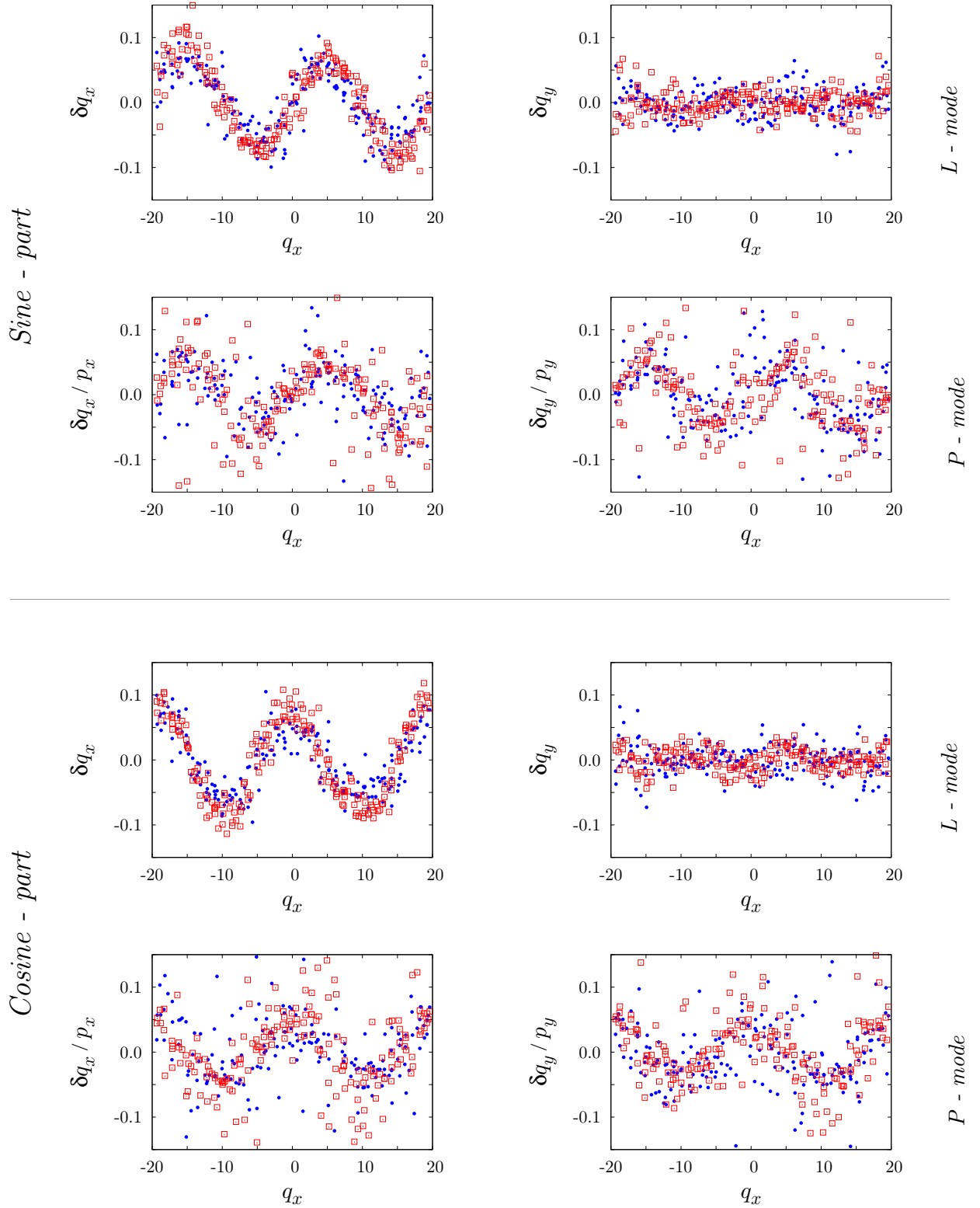


**Figure 3.21** : Reconstruction of the  $\delta q$  part for LP(2,0) ( $\bullet$  GS vectors,  $\square$  covariant vectors).

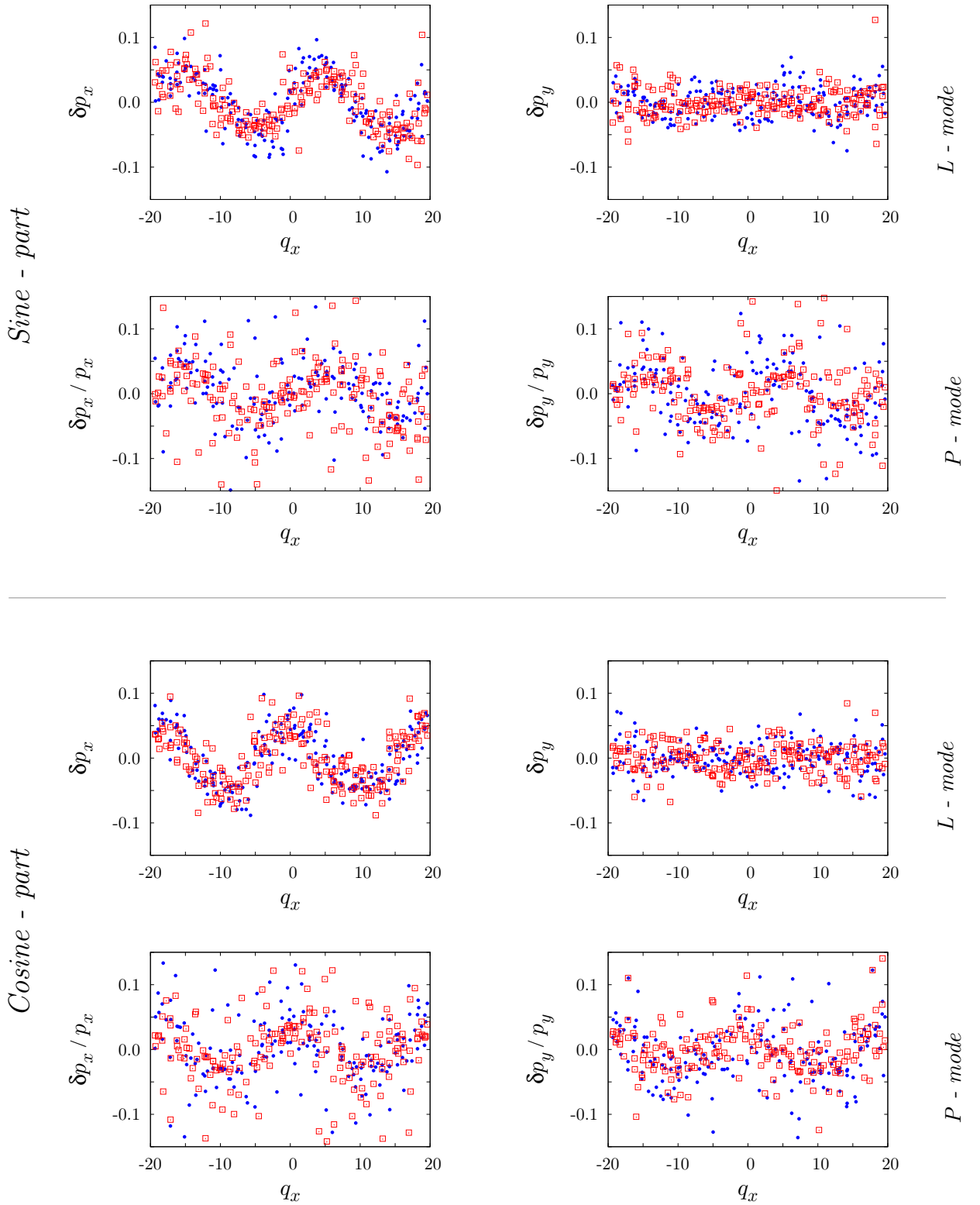


**Figure 3.22 :** Reconstruction of the  $\delta \mathbf{p}$  part for LP(2,0) ( $\bullet$  GS vectors,  $\square$  covariant vectors).

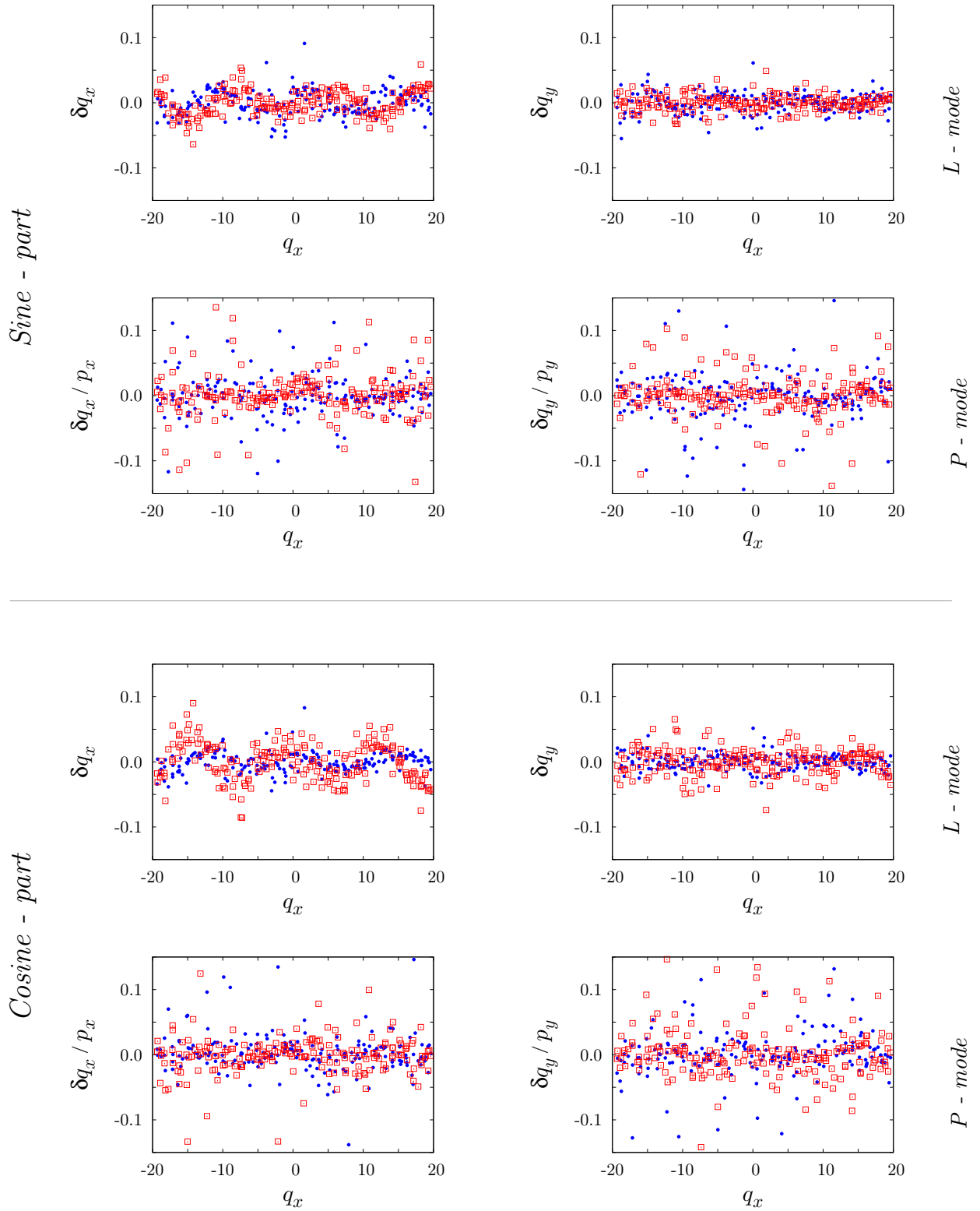


**Figure 3.23 :** Reconstruction of the  $\delta \mathbf{q}$  part for LP(3,0) (• GS vectors, □ covariant vectors).



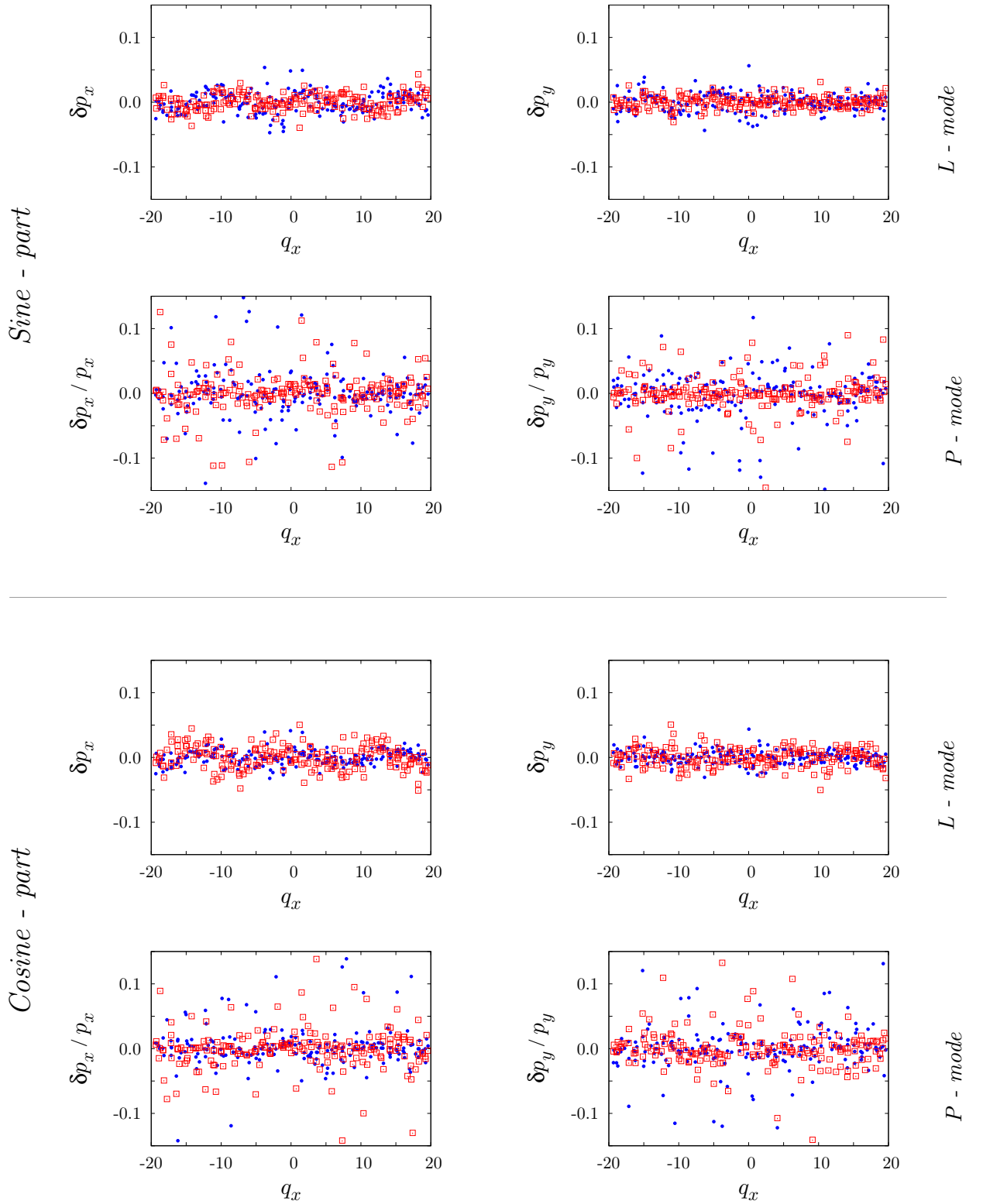


**Figure 3.24 :** Reconstruction of the  $\delta \mathbf{p}$  part for LP(3,0) (● GS vectors, □ covariant vectors).

## References

- [1] F. Ginelli, P. Poggi, A. Turchi, H. Chaté, R. Livi, and A. Politi, *Phys. Rev. Lett.* **99**, 130601 (2007).
- [2] Wm.G. Hoover, C.G. Hoover, and H.A. Posch, *Phys. Rev. A* **41**, 2999 (1990).
- [3] D. Szász (editor), *Hard Ball Systems and the Lorentz Gas*, Encyclopedia of Mathematical Sciences **101** (Springer-Verlag, Berlin, 2000).
- [4] J.A. Barker and D. Henderson, *J. Chem. Phys.* **47**, 4714 (1967).
- [5] J.P. Hansen and I.R. McDonald, *Theory of simple liquids* (Academic Press, London, 1991).
- [6] Ph. Geiger and Ch. Dellago, *Chem. Phys.* **375**, 309 (2010).
- [7] J.P. Eckmann, Ch. Forster, H.A. Posch, and E. Zabey, *J. Stat. Phys.* **118**, 813 (2005).
- [8] A. de Wijn and H. van Beijeren, *Phys. Rev. E* **70**, 016207 (2004).
- [9] V.I. Oseledec, *Trudy Moskov. Mat. Obsc.* **19**, 179 (1968). English transl. *Trans. Moscow Math. Soc.* **19**, 197 (1968).
- [10] D. Ruelle, *Publ. Math. de l'IHÉS* **50**, 27 (1979).
- [11] J.P. Eckmann and D. Ruelle, *Rev. Mod. Phys.* **57**, 617 (1985).
- [12] G. Benettin, L. Galgani, A. Giorgilli, and J.-M. Strelcyn, *Meccanica* **15**, 21 (1980).
- [13] I. Shimada and T. Nagashima, *Prog. Theor. Phys.* **61**, 1605 (1979).
- [14] W.H. Press, S.A. Teukolsky, T. Vetterling, and B.P. Flannery, *Numerical Recipes in Fortran 77: The Art of Scientific Computing* (Cambridge University Press, 2nd ed., 1999).
- [15] S.V. Ershov and A.B. Potapov, *Physica D* **118**, 167 (1998).
- [16] B. Legras and R. Vautard, *Proceedings of the Seminar on Predictability, ECWF Seminar vol. 1*, edited by T. Palmer (EC MWF Reading, UK, 1996) p 1.
- [17] M. Hénon, *Comm. Math. Phys.* **50**, 69 (1976).
- [18] Ch. Dellago, H.A. Posch, and Wm.G.Hoover, *Phys. Rev. E* **53**, 1485 (1996).
- [19] H.A. Posch and R. Hirschl, in *Hard Ball Systems and the Lorentz Gas*, Encyclopaedia of Mathematical Sciences **vol. 101**, edited by D. Szász (Springer-Verlag, Berlin, 2000) p. 269.

- [20] Ch. Forster, R. Hirschl, H.A. Posch, and Wm.G. Hoover, *Physica D* **187** 294 (2004).
- [21] T. Taniguchi and G.P. Morriss, *Phys. Rev E* **68**, 026218 (2003).
- [22] T. Taniguchi and G.P. Morriss, *Phys. Rev E* **68**, 046203 (2003).
- [23] Ch. Dellago and H.A. Posch, *Physica A*, **240**, 68 (1997).
- [24] Lj. Milanović and H.A. Posch, *J. Mol. Liquids* **96 - 97**, 221 (2002).
- [25] H.A. Posch and Ch. Forster, *Lecture Notes on Computational Science – ICCS 2002*, edited by P.M.A. Slood, C.J.K. Tan, J.J.Dongarra, and A.G. Hoekstra (Springer-Verlag, Berlin, 2002) p. 1170.
- [26] Ch. Forster and H.A. Posch, *New J. Phys.* **7**, 32 (2005).
- [27] P. Manneville, in *Macroscopic Modelling of Turbulent Flows*, *Lecture notes in Physics* **vol. 230**, edited by Araki *et al.* (Springer-Verlag, Berlin, 1985) p. 319.
- [28] R. Livi and S. Ruffo, in *Nonlinear Dynamics*, edited by G. Turchetti (World Scientific, Singapore, 1989) p. 220.
- [29] M. Falcioni, U.M.B. Marconi, and A. Vulpiani, *Phys. Rev. A* **44**, 2263 (1991).
- [30] R. van Zon and H. van Beijeren, *J. Stat. Phys.* **109**, 641 (2002).
- [31] T. Taniguchi and G.P.Morriss, *Phys. Rev. E* **73**, 036208 (2006).
- [32] A. Pikovsky and A. Politi, *Phys. Rev. E* **63**, 036207 (2001).
- [33] P. Gaspard, *Chaos, Scattering, and Statistical Mechanics* (Cambridge University Press, 1998).
- [34] Wm.G. Hoover, H.A. Posch, Ch. Forster, Ch. Dellago, and M. Zhou, *J. Stat. Phys.* **109**, 765 (2002).
- [35] Lj. Milanović, H.A. Posch and Wm.G. Hoover, *Mol. Phys.* **95**, 281 (1998).
- [36] Lj. Milanović, H.A. Posch and Wm.G. Hoover, *Chaos* **8**, 455 (1998)
- [37] G. Radons and H.L. Yang, *arXiv:nlin.CD/0404028*.
- [38] H.L. Yang and G. Radons, *Phys. Rev. E* **71**, 036211 (2005).
- [39] J.P. Eckmann and O. Gat, *J. Stat. Phys.* **98**, 775 (2000).
- [40] T. Taniguchi and G.P. Morriss, *Phys. Rev. E* **65**, 056202 (2002).

- [41] T. Taniguchi, C.P. Dettmann, and G.P. Morriss, *J. Stat. Phys.* **109**, 747 (2002).
- [42] S. McNamara and M. Mareschal, *Phys. Rev E* **64**, 051103 (2001).
- [43] M. Mareschal and S. McNamara, *Physica D* **187**, 311 (2004).
- [44] J. Bochi and M. Viana, *Ann. I. H. Poincaré* **19**, 1 (2002).
- [45] M. D'Alessandro and A. Tenenbaum, *Phys. Rev. E* **52**, R2141 (1995).
- [46] M. D'Alessandro, A. D'Aquino, and A. Tenenbaum, *Phys. Rev. E* **62**, 4809 (2000).
- [47] P.V. Kuptsov and S.P. Kuznetsov, *Phys. Rev. E* **80**, 016205 (2009).
- [48] A. Björck and G.H. Golub, *Mathem. of Computation* **27**, 579 (1973).
- [49] A.V. Knyazev and E.M. Argentati, *SIAM J. Sci. Comput.* **23**, 2008 (2002).
- [50] H.L. Yang and G. Radons, *Phys. Rev. Lett.* **100**, 024101 (2008).
- [51] H. Bosetti, H.A. Posch, Ch. Dellago, and W. G. Hoover, *Phys. Rev. E* **82**, 046218 (2010).
- [52] J.A. van Meel and H.A. Posch, *Phys. Rev. E* **80**, 016206 (2009).

# CHAPTER 4

## Covariant Lyapunov vectors for the field-free Lorentz gas

### Contents

---

4.1	Introduction . . . . .	105
4.2	Phase-space and tangent-space dynamics . . . . .	107
4.3	Gram-Schmidt vectors and covariant vectors . . . . .	109
4.4	Projections onto coordinate and momentum subspaces . . . . .	111
4.5	Hyperbolicity . . . . .	112
4.6	Poincaré map representation of covariant vectors . . . . .	112
4.7	Appendix . . . . .	115
	References . . . . .	116

---

### 4.1 Introduction

The isokinetic periodic Lorentz gas is a popular model for studying irreversible processes in classical chaotic systems. In the simplest two-dimensional equilibrium version, it consists of an infinite array of hard disk scatterers, periodically arranged on a triangular lattice (see Fig. 4.1), and a single point particle, which suffers hard elastic collisions with the scatterers and moves freely along straight paths in between. It may be easily driven into a stationary non-equilibrium state by accelerating the point particle with a homogeneous external field in, say, the  $x$ -direction and, simultaneously, keeping the kinetic energy fixed by a Gaussian thermostat [1]. For such a state the Sinai-Ruelle-Bowen measure is known to exist and to be a multifractal object in phase space [2].

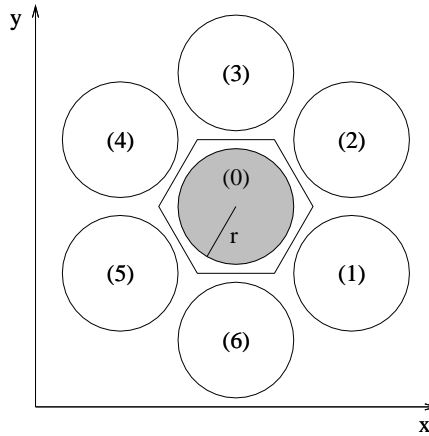


**Figure 4.1 :** Disk arrangement for the planar periodic Lorentz gas. The hexagonal basis cell of the corresponding Sinai billiard with the (shaded) scatterer inside is also shown. The numbering in the scheme is used below to locate the scatterer hit by the trajectory before it collides with the central disk (0).

The model may also be viewed as a Sinai billiard within a hexagonal basis cell with periodic boundaries and a single scatterer inside (shaded in Fig. 4.1). If the point particle leaves the hexagon at a particular point, the periodic boundaries assure its return at the homologous point. In the following we always have this billiard interpretation in mind.

Since the (purely kinetic) energy is conserved, the phase space is essentially three-dimensional. If a Poincaré map is constructed from one collision with the central scatterer to the next [3], the rectangle spanned by the Birkhoff coordinates  $\alpha$  and  $\sin \beta$ , defined by the collision depicted in Fig. 4.2, is uniformly covered by successive applications of the map [1]. This is a consequence of the ergodicity of the model, which is theoretically well known [4].

The driven thermostated Lorentz gas has some unique features thought to be typical for more-complicated many body systems of relevance for physics [1, 5, 6, 7]: (i) The equations of motion and the associated Poincaré map, both at and away from equilibrium, remain exactly time reversible and invertible, respectively; (ii) In equilibrium an arbitrary volume element in phase space is dynamically conserved. In the non-equilibrium steady state, however, it shrinks, on average, with a rate given by the (negative) sum of all Lyapunov exponents; (iii) For not too-strong driving fields, the support of this measure is the full phase space, and the system is ergodic. Although the system is not strictly hyperbolic, the hyperbolic tangencies are statistically insignificant. The Lorentz gas may be treated even as an Anosov-like system and obeys the steady-state Galavotti-Cohen fluctuation theorem [8, 9].

In the following we restrict to the field-free equilibrium case. We use reduced units for which the scatterer diameter  $\sigma$ , the point particle mass  $m$ , and the point particle (kinetic) energy,  $K = p^2/2m$ , are unity. The unit of time is  $(m\sigma^2/K)^{1/2}$ . In these units, the center-to-center

separation of the scatterers is  $b = 2\sigma/\sqrt{3}$ , which corresponds to the limiting case of a finite horizon.

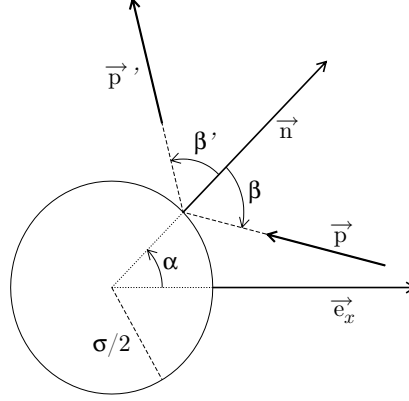


**Figure 4.2 :** Definition of the Birkhoff coordinates  $\alpha$  and  $\sin \beta$  for a collision of the point particle with the scattering disk.  $\vec{p}$  and  $\vec{p}'$  are the pre- and post-collisional momentum vectors of the particle, and  $\vec{n}$  is a unit normal vector at the impact point.

## 4.2 Phase-space and tangent-space dynamics

Between successive collisions, the point particle moves along a smooth trajectory, which follows from the motion equations. At an elastic collision, the state vector is instantaneously mapped to another state in phase space. The corresponding linearized motion equations and linearized collision map for an infinitesimal perturbation in tangent space have been derived by Dellago *et al.* [10, 11]. Here we apply an elegant matrix formulation due to de Wijn and van Beijeren [12] (which was already used in [13]) by considering as an elementary step the map from a state immediately after a collision to the state immediately after the next collision, which happens a time  $\tau$  later. An initial state vector  $\mathbf{\Gamma}_0 = (\vec{q}_0, \vec{p}_0)^\dagger$ , and an initial tangent vector  $\delta\mathbf{\Gamma}_0 = (\delta\vec{q}_0, \delta\vec{p}_0)^\dagger$  (where the superscript  $\dagger$  means here transposed), are transformed by the elementary step as follows,

$$\mathbf{\Gamma}'_\tau \equiv \mathcal{M}_\phi^\tau \mathbf{\Gamma}_0 = \begin{pmatrix} I & 0 \\ 0 & \mathcal{K}(\mathbf{\Gamma}_0) \end{pmatrix} \begin{pmatrix} I & \tau I \\ 0 & I \end{pmatrix} \mathbf{\Gamma}_0, \quad (4.1)$$

$$\delta\mathbf{\Gamma}'_\tau \equiv \mathcal{S}_\phi^\tau \delta\mathbf{\Gamma}_0 = \begin{pmatrix} \mathcal{K}(\mathbf{\Gamma}_0) & 0 \\ \mathcal{G}(\mathbf{\Gamma}_0) & \mathcal{K}(\mathbf{\Gamma}_0) \end{pmatrix} \begin{pmatrix} I & \tau I \\ 0 & I \end{pmatrix} \delta\mathbf{\Gamma}_0, \quad (4.2)$$

where the  $2 \times 2$  sub-matrices  $\mathcal{K}(\mathbf{\Gamma}_0)$  and  $\mathcal{G}(\mathbf{\Gamma}_0)$  are defined by

$$\mathcal{K}(\mathbf{\Gamma}_0) = I - \frac{8}{\sigma^2} \vec{q}_0 \vec{q}_0^\dagger, \quad (4.3)$$

$$\mathcal{G}(\mathbf{\Gamma}_0) = -\frac{8}{\sigma^2} (\vec{p}_0 \cdot \vec{q}_0) \left( I + \frac{\vec{q}_0 \vec{p}_0^\dagger}{\vec{p}_0 \cdot \vec{q}_0} \right) \left( I - \frac{\vec{p}_0 \vec{q}_0^\dagger}{\vec{p}_0 \cdot \vec{q}_0} \right). \quad (4.4)$$

The last factor in Eq. (4.4) denotes the displacement of the collision point of the perturbed trajectory with respect to that of the reference trajectory,

$$\delta \vec{q}_c = \left( I - \frac{\vec{p} \vec{q}^\dagger}{\vec{p} \cdot \vec{q}} \right) \delta \vec{q} . \quad (4.5)$$

The field-free periodic Lorentz gas has two vanishing Lyapunov exponents and, hence, a two-dimensional central manifold. Due to the time-translation invariance property of the motion equations and the conservation of energy [14], perturbation vectors in this invariant subspace do not grow or shrink exponentially with time. The respective marginal unit vectors

$$\mathbf{e}_2 = \frac{1}{\|\vec{p}\|} \begin{pmatrix} \vec{p} \\ \vec{0} \end{pmatrix} \quad \text{and} \quad \mathbf{e}_3 = \frac{1}{\|\vec{p}\|} \begin{pmatrix} \vec{0} \\ \vec{p} \end{pmatrix} \quad (4.6)$$

provide a natural basis for the central manifold. By adding the unit vector

$$\mathbf{e}_1 = \frac{1}{\|\vec{p}\|} \begin{pmatrix} \vec{p}^\perp \\ \vec{0} \end{pmatrix} \quad \text{and} \quad \mathbf{e}_4 = \frac{1}{\|\vec{p}\|} \begin{pmatrix} \vec{0} \\ \vec{p}^\perp \end{pmatrix} , \quad (4.7)$$

where  $\vec{p}^\perp = D^{\pi/2} \vec{p}$  (the matrix  $D^{\pi/2}$  refers to an anticlockwise rotation of angle  $\pi/2$ ), one obtains a set of orthonormal vectors  $\{\mathbf{e}_k\}_{k=1}^4$  spanning the full tangent space at any instant of time. Applying the elementary iteration step in tangent space, Eq. (4.2), to these basis vectors, one observes that  $\mathbf{e}_2$  is preserved by the dynamics, but  $\mathbf{e}_3$  rotates towards  $\mathbf{e}_2$  :

$$\mathcal{S}_\phi^\tau \mathbf{e}_2(0) = \begin{pmatrix} \vec{p}'_0 \\ \vec{0} \end{pmatrix} \equiv \mathbf{e}'_2(0) , \quad (4.8)$$

$$\mathcal{S}_\phi^\tau \mathbf{e}_3(0) = \begin{pmatrix} \tau \vec{p}'_0 \\ \vec{p}'_0 \end{pmatrix} \equiv \tau \mathbf{e}'_2(0) + \mathbf{e}'_3(0) , \quad (4.9)$$

since the outgoing momentum at the impact point is given by  $\vec{p}'_0 = \mathcal{K}(\Gamma_0) \vec{p}_0$ , and  $\mathcal{G}(\Gamma_0) \vec{p}_0 = \vec{0}$ . In addition, we find that

$$\mathcal{S}_\phi^\tau \mathbf{e}_i(0) \cdot \mathcal{S}_\phi^\tau \mathbf{e}_j(0) = \mathbf{0} , \quad i \in \{1, 4\} \text{ and } j \in \{2, 3\} , \quad (4.10)$$

i.e. the orthogonality between  $\mathbf{e}_1 \oplus \mathbf{e}_4$  and  $\mathbf{e}_2 \oplus \mathbf{e}_3$  is preserved by the dynamics. The fact that  $\mathbf{e}_3$  rotates towards  $\mathbf{e}_2$  (Eq. (4.9)) is completely analogous to Eq. (3.24) for hard disk systems, where the basis vectors  $\mathbf{e}_4$ ,  $\mathbf{e}_5$  and  $\mathbf{e}_6$  are found to rotate towards the subspace spanned by  $\mathbf{e}_1$ ,  $\mathbf{e}_2$  and  $\mathbf{e}_3$  (see Chap. 3).



### 4.3 Gram-Schmidt vectors and covariant vectors

Next, we introduce the set of Gram-Schmidt (GS) vectors,  $\{\mathbf{g}_i(\mathbf{\Gamma}_{t_0})\}_{i=1}^4$ , and the set of covariant vectors,  $\{\mathbf{v}_i(\mathbf{\Gamma}_{t_0})\}_{i=1}^4$ , at the phase-space point  $\mathbf{\Gamma}_{t_0}$ . GS vectors are *orthonormal* unit vectors co-moving with the tangent flow, such that the first vector always points in the direction of maximum phase-space expansion, the second vector into a direction with fastest-possible phase-space expansion but orthogonal to the first vector, and so forth. In the classical algorithm for the computation of Lyapunov exponents [15, 16, 11], orthonormality of the vectors is achieved by periodic applications of the Gram-Schmidt procedure. For time-continuous systems and even more elegantly, a differential approach with motion equations may be used, which involve Lagrange multipliers keeping these vectors orthonormal at all times [17, 18, 19]. If the simulation starts at time zero with arbitrary initial conditions, the Gram-Schmidt vectors  $\mathbf{g}_i(\mathbf{\Gamma}_{t_0})$  will have reached their proper phase-space directions at a phase point  $\mathbf{\Gamma}_{t_0}$  after a sufficiently-long relaxation time  $t_0$ . Covariant vectors, on the other hand, are strictly co-moving with the flow in tangent space. They are regularly normalized, but their orientation is not affected. In general, they are not pairwise orthogonal. According to the theorem of Oseledec [20, 21, 22], their physical significance lies in the fact that they span subspaces which are covariant with the flow. The algorithm for the computation of covariant vectors is much more involved [23, 24, 25] and requires the computation of the Gram-Schmidt vectors in the forward time interval  $t_0 \leq t \leq t_\omega$ . At  $t_\omega \gg t_0$ , the Gram-Schmidt vectors  $\{\mathbf{g}_i(\mathbf{\Gamma}_{t_\omega})\}_{i=1}^4$  are taken as initial condition for a set of vectors  $\{\mathbf{v}_i(\mathbf{\Gamma}_{t_\omega})\}_{i=1}^4$ , which, when iterated backward along the trajectory according to the algorithm of Ginelli *et al.*, gradually converge towards the set of covariant vectors  $\{\mathbf{v}_i(\mathbf{\Gamma}_{t_0})\}_{i=1}^4$  at the phase point  $\mathbf{\Gamma}_{t_0}$ . For non-degenerate Lyapunov exponents the covariant vectors are unique. In the following we are interested in these vectors at  $\mathbf{\Gamma}_{t_0}$  and omit the arguments, if not required.

Thus,  $\mathbf{v}_1$  and  $\mathbf{v}_4$  span the (one-dimensional) unstable and stable manifolds, respectively, and  $\mathbf{v}_2$  and  $\mathbf{v}_3$  provide another spanning set for the two-dimensional central manifold (which is covariant). These vectors satisfy

$$\mathbf{g}_1 = \mathbf{v}_1; \quad \mathbf{g}_1 \oplus \mathbf{g}_4 = \mathbf{v}_1 \oplus \mathbf{v}_4 = \mathbf{e}_1 \oplus \mathbf{e}_4; \quad \mathbf{g}_2 \oplus \mathbf{g}_3 = \mathbf{v}_2 \oplus \mathbf{v}_3 = \mathbf{e}_2 \oplus \mathbf{e}_3 . \quad (4.11)$$

As an illustration, we expand in Table 4.1 the Gram-Schmidt vectors, and in Table 4.2 the respective covariant vectors, in the natural basis  $\{\mathbf{e}_k\}_{k=1}^4$ . The time  $t_0 = 10^3$  after startup is large enough for all Gram-Schmidt vectors to have relaxed to their proper orientations. Similarly  $t_\omega - t_0 = 10^2$  suffices for the covariant vectors to relax sufficiently well. One directly observes that

$$\mathbf{g}_2 = \pm \mathbf{e}_2 \quad \text{and} \quad \mathbf{g}_3 = \pm \mathbf{e}_3 , \quad (4.12)$$

**Table 4.1 :** Projection of all GS-vectors  $\{\mathbf{g}_i, 1 \leq i \leq 4\}$  – at time  $t_0 = 10^3$  – onto the natural basis  $\{\mathbf{e}_k, 1 \leq k \leq 4\}$ .

$i$	$\mathbf{g}_i \cdot \mathbf{e}_1$	$\mathbf{g}_i \cdot \mathbf{e}_2$	$\mathbf{g}_i \cdot \mathbf{e}_3$	$\mathbf{g}_i \cdot \mathbf{e}_4$	$\sum_{k=1}^4 (\mathbf{g}_i \cdot \mathbf{e}_k)^2$
1	-0.2539303	0.0000000	0.0000000	-0.9672225	1.0000000
2	0.0000000	-1.0000000	0.0000000	0.0000000	1.0000000
3	0.0000000	0.0000000	1.0000000	0.0000000	1.0000000
4	0.9672225	0.0000000	0.0000000	-0.2539303	1.0000000

**Table 4.2 :** Projection of the whole covariant vector set  $\{\mathbf{v}_i, 1 \leq i \leq 4\}$  – at time  $t_0 = 10^3$  – onto the natural basis  $\{\mathbf{e}_k, 1 \leq k \leq 4\}$ .  $t_\omega - t_0 = 10^2$ .

$i$	$\mathbf{v}_i \cdot \mathbf{e}_1$	$\mathbf{v}_i \cdot \mathbf{e}_2$	$\mathbf{v}_i \cdot \mathbf{e}_3$	$\mathbf{v}_i \cdot \mathbf{e}_4$	$\sum_{k=1}^4 (\mathbf{v}_i \cdot \mathbf{e}_k)^2$
1	-0.2539303	0.0000000	0.0000000	-0.9672225	1.0000000
2	0.0000000	1.0000000	0.0000000	0.0000000	1.0000000
3	0.0000000	0.99995000	0.0099995	0.0000000	1.0000000
4	0.2013094	0.0000000	0.0000000	-0.9795277	1.0000000

due to the dynamics in the central manifold as a consequence of the Eqs. (4.8) - (4.9) in combination with the Gram-Schmidt procedure used at constant time intervals. Furthermore,

$$\mathbf{g}_1 = \pm \mathbf{v}_1 \quad \text{and} \quad \mathbf{g}_2 = \pm \mathbf{v}_2 . \quad (4.13)$$

The last equality is a direct consequence of the initial conditions mentioned above for the backward iteration of the covariant vectors. One further observes that the central manifold (spanned by  $\mathbf{e}_2 \oplus \mathbf{e}_3$ ) is always perpendicular to the unstable subspace (parallel to  $\mathbf{g}_1 = \mathbf{v}_1$ ) and the stable subspace (parallel to  $\mathbf{v}_4$ ). The most relevant observation is that the central manifold is “almost completely” contained just in one marginal direction, namely  $\mathbf{e}_2$ , which is parallel to the flow  $\dot{\mathbf{\Gamma}}$  (respective  $\mathbf{v}_2$ ). As a consequence of Eqs. (4.8) - (4.9), one finds

$$\mathbf{v}_3(t_0) \cdot \mathbf{e}_2(t_0) = \pm \sqrt{\frac{1}{1 + 1/(t_\omega - t_0)^2}} \quad \text{and} \quad \mathbf{v}_3(t_0) \cdot \mathbf{e}_3(t_0) = \pm \sqrt{\frac{1}{1 + (t_\omega - t_0)^2}} ,$$

for any finite  $t_\omega > t_0$ . Strict convergence of the covariant vectors is obtained for  $t_\omega \rightarrow \infty$ , for which  $\mathbf{v}_3 \rightarrow \mathbf{v}_2$ . Thus, the direction perpendicular to the constant (kinetic) energy surface effectively disappears for large  $t_\omega$ , and the null subspace has only one effective dimension. This subtlety can be avoided by replacing  $p_y = \pm \sqrt{2m(K - p_x^2/2m)}$  and working only in a three-dimensional phase space. Then the central manifold is one-dimensional and parallel to the flow.

## 4.4 Projections onto coordinate and momentum subspaces

Up to now the speed of the point particle of the Lorentz gas was set to unity, since the trajectory in physical space is not affected by the speed. In this section we make an exemption in order to observe how a variation of the energy affects the time-averaged relative contributions of the coordinate and momentum subspaces to the perturbation vectors. To that effect we define squared projection components [26, 27]

$$\eta_q^i = \left\langle (\delta \vec{q}_i)^2 \right\rangle, \quad \eta_p^i = \left\langle (\delta \vec{p}_i)^2 \right\rangle, \quad (4.14)$$

where, the subscript  $q$  and  $p$  refer to the coordinate and momentum subspaces, respectively, and the superscript  $i$  denotes the Lyapunov index.  $\langle \cdot \rangle$  indicates a time average. Since  $\eta_q^i + \eta_p^i = 1$ , we show in Fig. 4.3 the momentum dependence of the squared contributions only for the spatial part of  $\mathbf{g}_1 = \mathbf{v}_1$ , associated with the maximum Lyapunov exponent. Since the first two Gram-Schmidt and covariant vectors agree, so do their squared projections onto the  $p$  and  $q$  subspaces. For the third and fourth vectors, however, the squared projections are different, as is shown in Fig. 4.4. In fact, the role of the position and momentum subspaces is interchanged: for GS vectors, the anti-symmetry (with respect to the conjugate negative branch) reveal the Hamiltonian aspect of the system, whereas the symmetry for covariant vectors is due to the time-reversible phase-space structure. This will be explained in detail in Chap. 8.

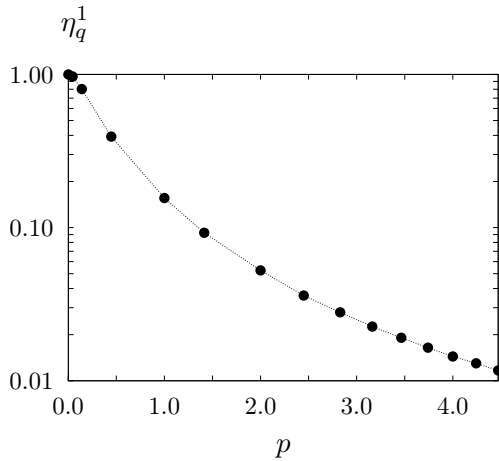


**Figure 4.3 :** Semi-log plot of the squared projections  $\eta_q^1$  as a function of the momentum  $p$  of the point particle. Gram-Schmidt and covariant-vector results agree.

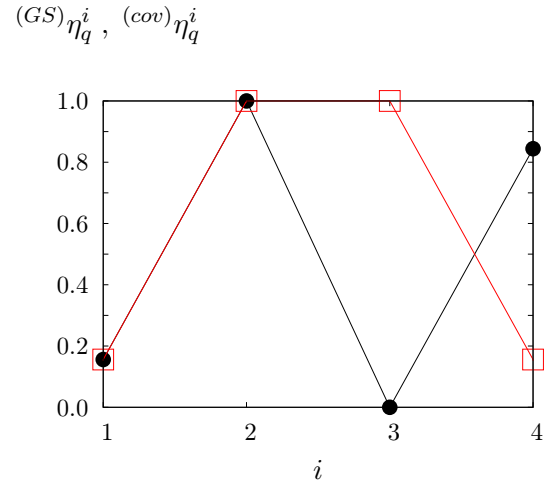


**Figure 4.4 :** Comparison of the squared projections onto the coordinate subspace for Gram Schmidt vectors (black full dots) and covariant vectors (red open squares), where  $p = 1$ .  $i$  on the abscissa denotes the Lyapunov index.

## 4.5 Hyperbolicity

The Oseledec splitting is a decomposition of the tangent space into covariant subspaces. If this decomposition is unique at every phase-space point, and if the dimensions of the stable and unstable subspaces are the same everywhere in phase space, the system is said to be hyperbolic. The Lorentz gas is known to have that property [2]. Hyperbolicity implies that there are no homoclinic tangencies. In view of later applications to related models, we demonstrate this behavior in Fig. 4.5, where the probability density  $P(\Phi)$  of the angle between the stable and unstable manifolds (which is the angle between the covariant vectors  $\mathbf{v}_1$  and  $\mathbf{v}_4$ ) is shown.  $P(\Phi)$  is well bounded away from zero, which indicates that the stable and unstable directions never become parallel. The fine structure in this distribution is a consequence of the lattice structure of the scattering disks. This will become clear below.

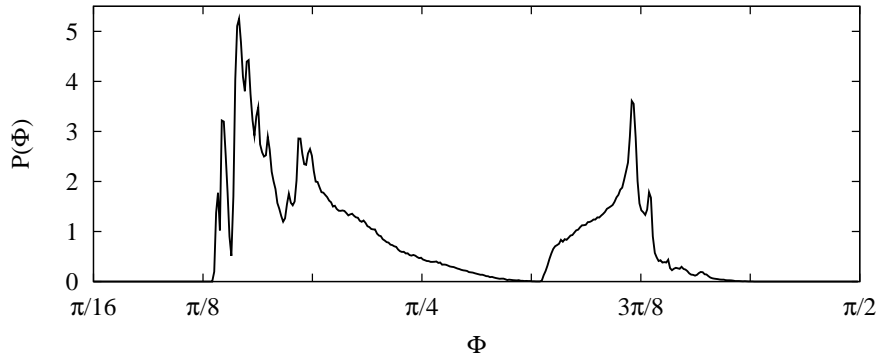


**Figure 4.5 :** Probability distribution of the angle  $\Phi$  between the stable and the unstable direction for the field-free Lorentz gas. One million collisions are used to generate this density.

## 4.6 Poincaré map representation of covariant vectors

Here we use Birkhoff coordinates  $\alpha$  and  $\sin \beta'$  as defined in Fig. 4.2 for a collision of the point particle with the scatterer. If  $\vec{n}$  denotes the unit vector normal to the scatterer surface at the collision point,  $\alpha$  is the angle between  $\vec{n}$  and the  $x$  axis. Similarly,  $\beta'$  is the angle between the outgoing momentum  $\vec{p}'$  and  $\vec{n}$ . A Poincaré map from one collision to the next may be constructed in the rectangle  $[0 \leq \alpha \leq 2\pi, -1 \leq \sin \beta' \leq 1]$ . For clarity and without loss of generality, in the following figures the upper bound of  $\alpha$  is restricted to  $\pi$ . For any collision at the point  $(q_x, q_y)$ , these coordinates become

$$\alpha = k\pi + \tan^{-1}\left(\frac{q_y}{q_x}\right) \quad \text{with } k = \begin{cases} 0 & \text{if } q_x > 0 \text{ and } q_y > 0, \\ 1 & \text{if } q_x < 0, \\ 2 & \text{if } q_x > 0 \text{ and } q_y < 0, \end{cases} \quad \text{and} \quad \sin \beta' = \frac{\vec{p}' \cdot \vec{t}}{\|\vec{p}'\|},$$

where  $\vec{t}$  is the unit tangent vector at the impact point, which is obtained from  $\vec{n}$  by a counter-clockwise rotation of  $\pi/2$ . For any perturbation vector  $\{\delta\vec{q}, \delta\vec{p}'\}$  immediately after a collision, its projection onto the Poincaré plane becomes a vector  $(\delta\alpha, \delta(\sin\beta'))$ , where

$$\delta\alpha = \frac{\delta\vec{q} \cdot \vec{t}}{\sigma/2} \quad \text{and} \quad \delta(\sin\beta') = \frac{1}{\|\vec{p}'\|} (\delta\vec{p}' \cdot \vec{t} + \vec{p}' \cdot \delta\vec{t}) . \quad (4.15)$$

In these equations  $\vec{t}$  and its associated tangent-space projection,  $\delta\vec{t}$ , are given by

$$\vec{t} = \begin{pmatrix} 0 & -1 \\ 1 & 0 \end{pmatrix} \frac{\vec{q}}{\sigma/2} , \quad \delta\vec{t} = \begin{pmatrix} 0 & -1 \\ 1 & 0 \end{pmatrix} \frac{\delta\vec{q}}{\sigma/2} .$$

In Fig. 4.6 the vector fields for the covariant-vector projections onto the Poincaré plane are shown for 5000 consecutive collisions immediately after each collision. The top and bottom panels refer to the projections for  $\mathbf{v}_1$  and  $\mathbf{v}_4$ , which indicate the unstable and stable directions, respectively. The whole map is separated into various domains according to the nearest scattering disk, at which the collision would take place, if no periodic boundaries were used. If the next-neighbor disks are labeled according to Fig. 4.1, the respective domains in the Poincaré plane are indicated in Fig. 4.7. The boundaries of these domains are explicitly given in the Appendix and are marked by the red lines in Fig. 4.6. The intermediate regions – with the vectors indicated in blue – refer to collisions, which do not take place with neighboring disks but with second-next-neighbor disks. There, due to the longer free path, the stable and unstable manifolds point into markedly different directions than for next-neighbor-disk collisions. No possible collisions with other disks exist. The middle panel of Fig. 4.6 refers to the central manifold spanned by  $\mathbf{v}_2$  and  $\mathbf{v}_3$ . As pointed out in Sec. 4.3, the two vectors coincide (for  $t_\omega \rightarrow \infty$ ) and point into the direction of the phase-space flow. This requires  $\sin\beta'$  to vanish, and the respective perturbation vectors are indeed parallel to the  $\alpha$  axis.

The symmetry observed between the two vector fields due to the expanding and contracting directions of the 4-dimensional phase-space underlines the time-reversible property of the phase-space structure. The expanding direction (parallel to  $\mathbf{v}_1$ ) in the time-forward iteration becomes the contracting direction in the time-backward iteration, and similarly, the contracting direction (parallel to  $\mathbf{v}_2$ ) becomes the expanding direction. This fact is studied in more detail for simple particle systems in the following chapter and in Ref. [25].

All these considerations are for the field-free equilibrium case. If a weak field along the  $x$ -direction is switched on, the phase-space probability density and the respective Poincaré map become multifractal objects [1].

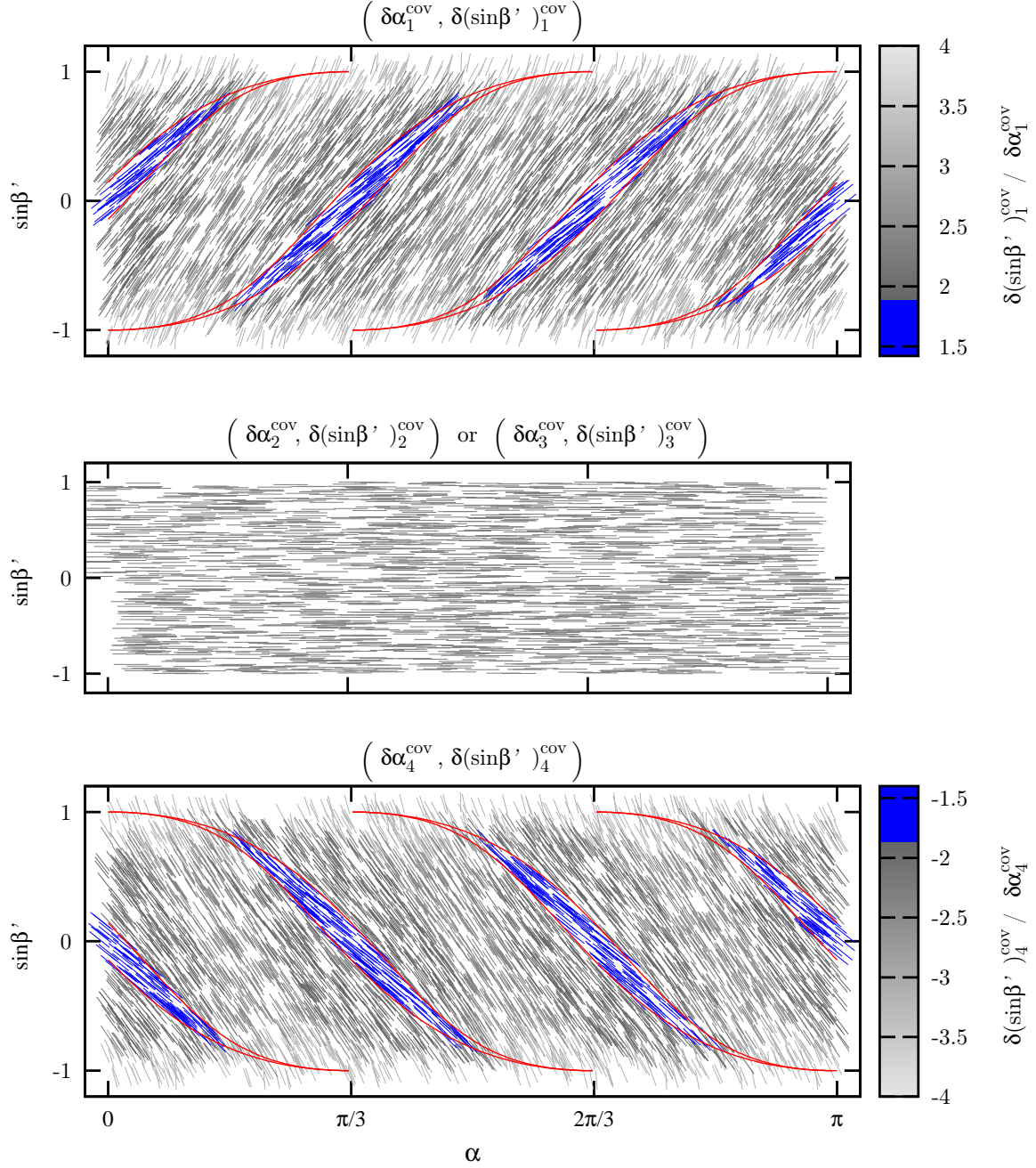


**Figure 4.6 :** For the simple periodic Lorentz gas with finite horizon: In the collisional  $(\alpha, \sin \beta')$ -plane, the various vector fields  $(\delta \alpha_i^{\text{cov}}, \delta(\sin \beta')_i^{\text{cov}})$  are shown. For each Lyapunov index  $i \in \{1, 2, 3, 4\}$ , the covariant vector field is constructed for 5,000 collisions immediately after the collision events (the vectors are normalized immediately after the collision and before  $\alpha$  and  $\sin \beta'$  are calculated).

## 4.7 Appendix

In the unfolded representation of the periodic Lorentz gas any trajectory of the point particle hitting the central scatterer (with label (0) in Fig. 4.1) originates either from a collision with a next neighbor (with labels (1) to (6) in Fig. 4.1) or from a collision with a scatterer of the second-nearest neighbor shell. In the Poincaré plane of the central scatterer in Fig. 4.7, the labels of the various domains refer to the next neighbor disk, with which the foregoing collision occurred. The narrow domains are from foregoing collision with a disk from the second-nearest neighbor shell. The boundaries between these domains in the Poincaré plane  $(\alpha, \sin \beta')$  may be expressed by functions  $\sin \chi_\ell^+(\alpha)$  and  $\sin \chi_\ell^-(\alpha)$  in terms of the angle  $\alpha$  (defined in Fig. 4.2). Simple geometrical considerations give

$$\chi_\ell^\pm = \theta_\ell \pm \sin^{-1} \left( \frac{\sigma/2}{\sqrt{b^2 + \frac{\sigma^2}{4} - b\sigma \cos(\frac{\pi}{6} - \theta_\ell)}} \right) \mp \cos^{-1} \left( \frac{\sigma - \frac{\sigma}{2} \cos(\theta_\ell)}{\sqrt{b^2 + \frac{\sigma^2}{4} - b\sigma \cos(\frac{\pi}{6} - \theta_\ell)}} \right),$$

where  $b = 2\sigma/\sqrt{3}$  and

$$\theta_\ell = \alpha - \frac{\pi}{3}\ell \quad \text{with} \quad \begin{cases} \alpha \in [0, \pi/3] & \text{for } \ell = 0, \\ \alpha \in [0, 2\pi/3] & \text{for } \ell = 1, \\ \alpha \in [\pi/3, 2\pi/3] & \text{for } \ell = 2, \\ \alpha \in [2\pi/3, \pi] & \text{for } \ell = 3. \end{cases}$$

$(\sin \chi_\ell^+(\alpha), \sin \chi_\ell^-(\alpha)) ; \ell = 0, 1, 2, 3$

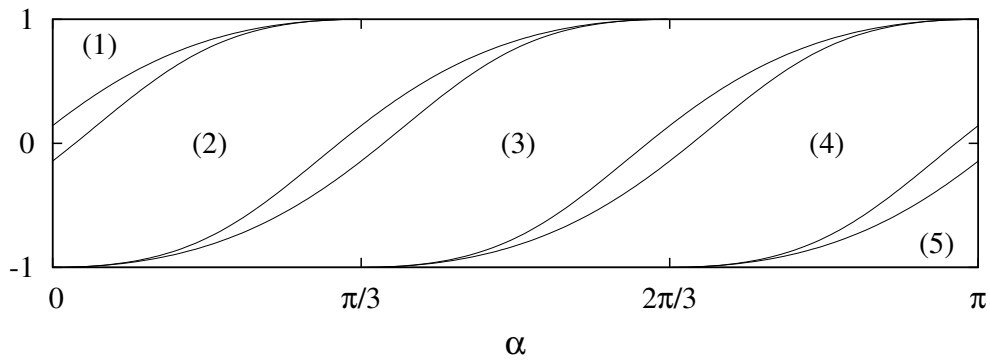


**Figure 4.7 :** In the Poincaré map, the lines indicate the boundaries of the collision domains according to the geometry of the scatterers (see the labelling scheme in 4.1). They are given by  $\sin \chi_\ell^+(\alpha)$  and  $\sin \chi_\ell^-(\alpha)$  defined in the text.

## References

- [1] B. Moran, Wm.G. Hoover, and S. Bestiale, J. Stat. Phys. **48**, 709 (1987).
- [2] N.I. Chernov, G.L. Eyink, J.L. Lebowitz, and Ya. G. Sinai., Comm. Math. Phys. **154**, 569 (1993).
- [3] J. Lloyd, M. Niemeyer, L. Rondoni, and G.P. Morriss, Chaos **5**, 536 (1995).
- [4] Y.G. Sinai Funktsional Anal, i Prilozhen. **13:3**, 46 (1979). English transl. Functional Anal. Appl. **13:3**, 192 (1979).
- [5] Wm.G. Hoover, B. Moran, C.G. Hoover, and W.J. Evans, Phys. Letter A **133**, 114 (1988).
- [6] H.A. Posch, Ch. Dellago, Wm.G. Hoover, and O. Kum, in *Pioneering Ideas for the Physical and Chemical Sciences: Josef Loschmidts Contributions and Modern Developments in Structural Organic Chemistry, Atomistics and Statistical Mechanics*, W. Fleischhacker and T. Schönfeld, eds. ,(Plenum, New York, 1997) p. 233.
- [7] Wm.G. Hoover, J. Chem. Phys. **109**, 4164 (1998).
- [8] G. Gallavotti and E.G.D. Cohen, Phys. Rev. Lett. **74**, 2694 (1995)
- [9] G. Gallavotti and E.G.D. Cohen, J. Stat. Phys. **80**, 931 (1995).
- [10] Ch. Dellago and H.A. Posch, Phys. Rev. E **52**, 2401 (1995).
- [11] Ch. Dellago, H.A. Posch, and Wm.G.Hoover, Phys. Rev. E **53**, 1485 (1996).
- [12] A.S. de Wijn and H. van Beijeren, Phys. Rev. E **70**, 016207 (2004).
- [13] T. Chung, D. Truant, and G.P. Morriss, Phys. Rev. E **81**, 066208 (2010).
- [14] P. Gaspard, *Chaos, Scattering, and Statistical Mechanics* (Cambridge University Press, 1998).
- [15] G. Benettin, L. Galgani, A. Giorgilli, and J.M. Strelcyn, Meccanica **15**, 21 (1980).
- [16] A. Wolf, j.B. Swift, H.L. Swinney, and J.A. Vastano, Physica D **16**, 285 (1985).
- [17] H.A. Posch and Wm.G. Hoover, Phys. Rev. A **38**, 473 (1988).
- [18] I. Goldhirsch, P.L. Sulem, and S.A. Orszag, Physica D **27**, 311 (1987).
- [19] H.A. Posch and Wm.G. Hoover, Physica D **187**, 281 (2004).



- 
- [20] V.I. Oseledec, Trudy Moskov. Mat. Obsc. **19**, 179, (1968). English transl. Trans. Moscow Math. Soc. **19**, 197 (1968).
  - [21] D. Ruelle, Publ. Math. de l'IHÉS **50**, 27 (1979).
  - [22] J.P. Eckmann and D. Ruelle, Rev. Mod. Phys. **57**, 617 (1985).
  - [23] F. Ginelli, P. Poggi, A. Turchi, H. Chaté, R. Livi, and A. Politi, Phys. Rev. Lett. **99**, 130601 (2007).
  - [24] H. Bosetti and H.A. Posch, Chem. Phys. **375**, 296 (2010).
  - [25] H. Bosetti, H. A. Posch, Ch. Dellago, and Wm.G. Hoover, Phys. Rev. E **82**, 046218 (2010).
  - [26] Lj. Milanovic and H.A. Posch, J. Mol. Liquids **96 - 97**, 221 (2002).
  - [27] T. Taniguchi and G.P.Morriss, Phys. Rev. E **73**, 036208 (2006).



This chapter is based on the following publication:  
H. Bosetti, H.A. Posch, Ch. Dellago, and Wm.G. Hoover,  
*Time-reversal symmetry and covariant Lyapunov vectors  
for simple particle models in and out of thermal equilibrium,*  
[Phys. Rev. E 82, 046218 \(2010\)](#).

Sec. 5.6 has been added.

## CHAPTER 5

# Time-reversal symmetry and covariant Lyapunov vectors for simple particle models in and out of thermal equilibrium

### Contents

---

5.1	Introduction . . . . .	<a href="#">120</a>
5.2	Covariant Lyapunov vectors and local Lyapunov exponents . . . . .	<a href="#">120</a>
5.3	Differential approach to local Lyapunov exponents . . . . .	<a href="#">126</a>
5.4	Numerical considerations . . . . .	<a href="#">126</a>
5.5	Doubly-thermostated oscillator . . . . .	<a href="#">128</a>
5.6	Local Lyapunov exponents for symplectic systems . . . . .	<a href="#">136</a>
5.7	Concluding remarks . . . . .	<a href="#">140</a>
5.8	Acknowledgements . . . . .	<a href="#">141</a>
	References . . . . .	<a href="#">141</a>

---

### Abstract

Recently, a new algorithm for the computation of covariant Lyapunov vectors and of corresponding local Lyapunov exponents has become available. Here we study the properties of these still unfamiliar quantities for a number of simple models, including an harmonic oscillator coupled to a thermal gradient with a two-stage thermostat, which leaves the system ergodic and fully time reversible. We explicitly demonstrate how time-reversal invariance affects the perturbation vectors in tangent space and the associated local Lyapunov exponents. We also find that the local covariant exponents vary discontinuously along directions transverse to the phase flow.

## 5.1 Introduction

Recently, many concepts and methods of dynamical systems theory have turned out to be very useful for the characterization and understanding of physical systems in and out of thermodynamic equilibrium. For example, for a class of stationary non-equilibrium systems, the spectrum of Lyapunov exponents is a convenient tool for studying the collapse of the phase-space probability distribution onto fractal measures with an information dimension smaller than the dimension of phase space. In this case, stationarity is achieved with time-reversible thermostats [1, 2]. Stationary non-equilibrium systems with stochastic thermostats may be formulated along similar lines [3].

The aim of this paper is to apply the hitherto rather unfamiliar concept of covariant Lyapunov vectors and their associated local Lyapunov exponents to some simple and pedagogical systems in equilibrium and in non-equilibrium stationary states to sharpen the intuition for more demanding applications. The systems studied include a harmonic oscillator subjected to a two-stage chain of Nosé-Hoover-type thermostats with a temperature which varies with the position of the particle.

The paper is organized as follows: In the next section we provide the basic theoretical concepts and definitions required for our numerical work. In particular, the covariant vectors and their classical counterparts, the Gram-Schmidt vectors, are introduced, and their dynamical evolution is discussed. Sec. 5.3 is devoted to an alternative differential-equation based method for the evolution of orthonormal perturbation vectors, which may be interpreted as continuous re-orthonormalization. In Sec. 5.4 we specify the protocol for our numerical work, both forward and backward in time. Our main example, a doubly-thermostated oscillator in a space-dependent thermal field, is treated in various subsections of Sec. 5.5. Sec. 5.6 is devoted to symplectic systems, with regular trajectories on a torus or with chaotic behavior, for which the differences of the symmetry properties for the local Gram-Schmidt and covariant Lyapunov exponents are most pronounced. We conclude in Sec. 5.7 with some remarks, which also concern the stationary fluctuation theorem for thermostated systems.

## 5.2 Covariant Lyapunov vectors and local Lyapunov exponents

If  $\Gamma(t)$  denotes the state of a dynamical system of dimension  $D$ , its evolution equations are given by

$$\dot{\Gamma} = \mathcal{F}(\Gamma), \quad (5.1)$$

where  $\mathbf{F}$  is a (generally nonlinear) vector-valued function of dimension  $D$ . An arbitrary perturbation vector  $\delta\mathbf{\Gamma}(t)$  in tangent space evolves according to the linearized equations

$$\dot{\delta\mathbf{\Gamma}} = \mathcal{D}_{\mathbf{\Gamma}} \delta\mathbf{\Gamma}, \quad (5.2)$$

where the dynamical (Jacobian) matrix  $\mathcal{D}_{\mathbf{\Gamma}}$  is given by

$$\mathcal{D}_{\mathbf{\Gamma}} = \frac{\partial \mathcal{F}}{\partial \mathbf{\Gamma}}.$$

The stability of a trajectory in a  $D$ -dimensional phase space is determined by a set of  $D$  (global) Lyapunov exponents, which are the *time-averaged* logarithmic rates of the growth or decay of the norm of some perturbation vectors, which must be oriented ‘properly’ in tangent space at the initial time. Formally, let  $\mathbf{\Gamma}(0)$  denote the state of the system at time 0, the state at time  $t$  is given by  $\mathbf{\Gamma}(t) = \phi^t(\mathbf{\Gamma}(0))$ , where the map  $\phi^t : \mathbf{\Gamma} \rightarrow \mathbf{\Gamma}$  defines the flow in the phase space  $\mathbf{\Gamma}$ . Similarly, if  $\delta\mathbf{\Gamma}(0)$  is a vector in the tangent space at the phase point  $\mathbf{\Gamma}(0)$ , at time  $t$ , it becomes  $\delta\mathbf{\Gamma}(t) = D\phi^t|_{\mathbf{\Gamma}(0)} \delta\mathbf{\Gamma}(0)$ , where  $D\phi^t$  defines the tangent flow. It is represented by a real but generally nonsymmetric  $D \times D$  matrix. The multiplicative ergodic theorem of Oseledec [4, 5, 6] asserts that there exist ‘properly oriented’ normalized vectors  $\mathbf{v}^\ell(\mathbf{\Gamma}(0))$  in tangent space, which evolve according to

$$D\phi^t|_{\mathbf{\Gamma}(0)} \mathbf{v}^\ell(\mathbf{\Gamma}(0)) = \mathbf{v}^\ell(\mathbf{\Gamma}(t)), \quad (5.3)$$

and which generate the Lyapunov exponents on the way,

$$\pm\lambda_\ell = \lim_{t \rightarrow \pm\infty} \frac{1}{|t|} \ln \| D\phi^t|_{\mathbf{\Gamma}(0)} \mathbf{v}^\ell(\mathbf{\Gamma}(0)) \| \quad (5.4)$$

for all  $\ell \in \{1, \dots, D\}$ , both forward and backward in time (for time-reversible systems). (Strictly speaking, this formulation is only correct for nondegenerate exponents  $\lambda_\ell$ . If two such exponents become identical, the respective vectors must be replaced by a covariant subspace spanned by the vectors. Since in our applications below, this happens only for the symplectic systems in thermodynamic equilibrium discussed in Sec. 5.6, there is no danger of misinterpretation, and we avoid the additional notational complexity. The case of degenerate exponents is treated in detail in Ref. [7] (Chap. 3). Because of the property described by Eq. (5.3), the vectors  $\mathbf{v}^\ell$  are called *covariant*. Loosely speaking, covariant vectors are co-moving (co-rotating in particular) with the tangent flow. As will be shown below, this property of co-rotation is responsible for the fact that the evolution of their length in the forward and backward directions of time (for time-reversible systems) is intimately connected, a symmetry not enjoyed by other perturbation vectors. For numerical reasons, it is still necessary to *normalize* the vectors periodically at times

$t_k \equiv k\tau$ , such that Eq. (5.4) becomes

$$\lambda_\ell = \lim_{\mathcal{K} \rightarrow \infty} \frac{1}{\mathcal{K}\tau} \sum_{k=0}^{\mathcal{K}-1} \ln \|D\phi^\tau|_{\Gamma_k} \mathbf{v}^\ell(\Gamma_k)\|, \quad (5.5)$$

where we use the abbreviated notation  $\Gamma(t_k) \equiv \Gamma_k$ .  $\|\mathbf{v}^\ell(\Gamma_k)\| = 1$  at the beginning of each interval of length  $\tau$ . Generally its norm differs from unity at the end of the interval.

Up to very recently, no practical algorithm for the computation of the covariant vectors was available. The classical algorithm for the computation of Lyapunov exponents [8, 9] is based on the fact that almost all volume elements of dimension  $d \leq D$  in tangent space (with the exception of elements of measure zero) asymptotically evolve with an exponential rate, which is equal to the sum of the first  $d$  Lyapunov exponents. Such a  $d$ -dimensional subspace may be spanned by  $d$  orthonormal vectors, which are constructed by the Gram-Schmidt re-orthonormalization procedure and, therefore, are referred to as Gram-Schmidt (GS) vectors  $\mathbf{g}^\ell(\Gamma(t))$ . The evolution during the time interval  $\tau = t_k - t_{k-1}$ ,

$$D\phi^\tau|_{\Gamma_{k-1}} \mathbf{g}^\ell(\Gamma_{k-1}) \equiv \bar{\mathbf{g}}^\ell(\Gamma_k), \quad (5.6)$$

generates a set of non-orthonormal vectors,  $\{\bar{\mathbf{g}}^\ell(\Gamma_k), \ell = 1, \dots, D\}$ , which after Gram-Schmidt re-orthonormalization [10, 11],

$$\begin{aligned} \mathbf{g}^1(\Gamma_k) &= \frac{\bar{\mathbf{g}}^1(\Gamma_k)}{\|\bar{\mathbf{g}}^1(\Gamma_k)\|}, \\ \mathbf{g}^\ell(\Gamma_k) &= \frac{\bar{\mathbf{g}}^\ell(\Gamma_k) - \sum_{i=1}^{\ell-1} (\bar{\mathbf{g}}^\ell(\Gamma_k) \cdot \mathbf{g}^i(\Gamma_k)) \mathbf{g}^i(\Gamma_k)}{\|\bar{\mathbf{g}}^\ell(\Gamma_k) - \sum_{i=1}^{\ell-1} (\bar{\mathbf{g}}^\ell(\Gamma_k) \cdot \mathbf{g}^i(\Gamma_k)) \mathbf{g}^i(\Gamma_k)\|}, \end{aligned}$$

(where  $\ell$  consecutively assumes the values  $1, \dots, D$ ) become the orthonormal starting vectors for the next interval. The vectors  $\mathbf{g}^\ell$  are not covariant, which means that, in general, the vectors are not mapped by the linearized dynamics into the GS vectors at the forward images of the initial phase-space point [12]. As a consequence, they are also not invariant with respect to the time-reversed dynamics. The Lyapunov exponents are computed from the normalization factors,

$$\begin{aligned} \lambda_1 &= \lim_{\mathcal{K} \rightarrow \infty} \frac{1}{\mathcal{K}\tau} \sum_{k=0}^{\mathcal{K}-1} \ln \|\bar{\mathbf{g}}^1(\Gamma_k)\|, \\ \lambda_\ell &= \lim_{\mathcal{K} \rightarrow \infty} \frac{1}{\mathcal{K}\tau} \sum_{k=0}^{\mathcal{K}-1} \ln \left\| \bar{\mathbf{g}}^\ell(\Gamma_k) - \sum_{i=1}^{\ell-1} (\bar{\mathbf{g}}^\ell(\Gamma_k) \cdot \mathbf{g}^i(\Gamma_k)) \mathbf{g}^i(\Gamma_k) \right\| \end{aligned} \quad (5.7)$$

for  $\ell = 2, \dots, D$ .

Recently, a reasonably fast algorithm for the computation of covariant Lyapunov vectors was presented by Ginelli *et al.* [12], which first requires the construction of the Gram-Schmidt vectors by a forward integration in time. In a second step, this stored information is used to obtain the covariant vectors by a backward iteration in time. For details of this algorithm we refer to their paper [12] and to our previous work [7].

A *local* Lyapunov exponent characterizes the expansion, or shrinkage, of a particular tangent vector during a (short) time interval  $\tau$ . From Eqs. (5.5) and (5.7) local exponents for the covariant and Gram-Schmidt vectors are obtained for a time  $t_k \equiv k\tau$  at the phase point  $\Gamma_k$ :

$$\Lambda_\ell^{\text{cov}}(t_k) = \frac{1}{\tau} \ln \|D\phi^\tau|_{\Gamma_{k-1}} \mathbf{v}^\ell(\Gamma_{k-1})\|, \quad (5.8)$$

for  $\ell = 1, \dots, D$ , and

$$\begin{aligned} \Lambda_1^{GS}(t_k) &= \frac{1}{\tau} \ln \|\bar{\mathbf{g}}^1(\Gamma_k)\|, \\ \Lambda_\ell^{GS}(t_k) &= \frac{1}{\tau} \ln \left\| \bar{\mathbf{g}}^\ell(\Gamma_k) - \sum_{i=1}^{\ell-1} \left( \bar{\mathbf{g}}^\ell(\Gamma_k) \cdot \mathbf{g}^i(\Gamma_k) \right) \mathbf{g}^i(\Gamma_k) \right\|, \end{aligned} \quad (5.9)$$

for  $\ell = 2, \dots, D$ .

Since the spaces

$$\mathbf{v}^1 \oplus \dots \oplus \mathbf{v}^\ell = \mathbf{g}^1 \oplus \dots \oplus \mathbf{g}^\ell \quad (5.10)$$

are covariant subspaces of the tangent space for all  $\ell$ , we have  $\mathbf{v}^\ell(t) \in \mathbf{g}^1(t) \oplus \dots \oplus \mathbf{g}^\ell(t)$ . If  $\beta_{\ell\ell}(t)$  denotes the angle between the respective covariant and Gram-Schmidt vectors  $\mathbf{v}^\ell(t)$  and  $\mathbf{g}^\ell(t)$  at the specified time, the component of the normalized vector  $\mathbf{v}^\ell(t_{k-1})$  in the direction of  $\mathbf{g}^\ell(t_{k-1})$  is given by  $\cos \beta_{\ell\ell}(t_{k-1})$ . During  $\tau$ , this component grows by a factor  $\exp\{\Lambda_\ell^{GS}\tau\}$ , whereas the norm of the vector itself grows by  $\exp\{\Lambda_\ell^{\text{cov}}\tau\}$ . At the end of the interval, equating the vector components of  $\mathbf{v}^\ell(t_k)$  in the *new* direction of the re-orthonormalized vector  $\mathbf{g}^\ell(t_k)$ , one obtains

$$\Lambda_\ell^{GS}(t_k) = \Lambda_\ell^{\text{cov}}(t_k) + \frac{1}{\tau} \ln \frac{\cos \beta_{\ell\ell}(t_k)}{\cos \beta_{\ell\ell}(t_{k-1})}, \quad (5.11)$$

$\ell = 1, \dots, D$ . This relates the local exponents for the GS and covariant vectors.

If we consider the limit  $\tau \rightarrow 0$  implying continuous re-orthonormalization of the  $\mathbf{g}^\ell$  and normalization of the  $\mathbf{v}^\ell$ , Eq. (5.11) becomes

$$\Lambda_\ell^{GS}(t) = \Lambda_\ell^{\text{cov}}(t) - \tan \beta_{\ell\ell}(t) \frac{d\beta_{\ell\ell}}{dt}.$$

This is most easily achieved with a matrix of Lagrange multipliers constraining the vectors to

unit length and enforcing orthogonality of the  $\mathbf{g}^\ell$  [13, 14, 15]. We shall return to this point in the following section.

For time-continuous systems, these relations are general and are not restricted to any particular model. Below they will be applied to a variety of models mentioned in the introduction.

The global exponents are the time averages of the local exponents over a long trajectory tracing out the whole ergodic phase space component, and are the same for the covariant and Gram-Schmidt cases,

$$\lambda_\ell = \lim_{\mathcal{K} \rightarrow \infty} \frac{1}{\mathcal{K}} \sum_{k=0}^{\mathcal{K}-1} \Lambda_\ell^{\text{cov}}(t_k) = \lim_{\mathcal{K} \rightarrow \infty} \frac{1}{\mathcal{K}} \sum_{k=0}^{\mathcal{K}-1} \Lambda_\ell^{GS}(t_k).$$

Whereas the global Lyapunov exponents do not depend on the particular metric and the choice of the coordinate system, the local exponents do. This will become apparent in Sec. 5.6 for a scaled harmonic oscillator. For particular applications of the local exponents this must be kept in mind.

All systems we consider here are invariant with respect to time reversal. This property leaves the equations of motion in phase and tangent space unchanged if the signs of all momentum-like variables *and* of time are reversed, but leaving all position variables unchanged. This implies that there exists a smooth isometry  $\mathcal{T}$  of phase space, such that  $\mathcal{T}\phi^t = \phi^{-t}\mathcal{T}$ . In practice, an integration of the equations of motion backward in time is carried out with reversed momentum-like variables and a positive time step. After reaching the endpoint, the signs of all momentum-like variables need to be reversed again and the time variable properly adjusted. Alternatively, and even more easily, the integration of the motion equations may proceed without changing the sign of the momentum-like variables but with a negative time step. There is also no sign change after reaching the end point in this case. A comparison of both methods yields identical results. Where necessary, we indicate the forward and backward directions of time by upper indexes (+) and (−), respectively. If this index is omitted, the forward direction is implied.

We have mentioned already that the classical algorithm invoking Gram-Schmidt re-orthonormalization carefully keeps track of the time evolution of  $d$ -dimensional volume elements,  $\delta\mathcal{V}_d$ , for any  $d \leq D$ , which proceeds according to [2, 16]

$$\frac{d \ln \delta\mathcal{V}_d(t)}{dt} = \sum_{\ell=1}^d \Lambda_\ell^{GS}(t).$$

If the total phase volume is conserved as for symplectic systems, the following sum rule for the



Gram-Schmidt local exponents holds at all times:

$$\sum_{\ell=1}^D \Lambda_{\ell}^{GS}(t) = 0. \quad (5.12)$$

In this symplectic case we can even say more. For each positive local GS exponent there is a local negative GS exponent such that their pair sum vanishes [17],

$$^{(+)}\Lambda_{\ell}^{GS}(t) = -^{(+)}\Lambda_{D+1-\ell}^{GS}(t), \quad (5.13)$$

$$^{(-)}\Lambda_{\ell}^{GS}(t) = -^{(-)}\Lambda_{D+1-\ell}^{GS}(t). \quad (5.14)$$

As indicated, such a symplectic local pairing symmetry exists both forward and backward in time. But, generally, the GS local exponents do not show the symmetry with respect to time-reversal invariance. Thus,

$$^{(-)}\Lambda_{\ell}^{GS}(t) \neq -^{(+)}\Lambda_{D+1-\ell}^{GS}(t). \quad (5.15)$$

No such symmetries exist for non-symplectic systems. Examples are provided below.

The situation is very different for the covariant local Lyapunov exponents. In their case, the vectors are still re-normalized, but the angles between them remain unchanged, which effectively destroys all information concerning the  $d$ -dimensional volume elements. Thus, no symmetries analogous to Eqs. (5.13) and (5.14) exist. Instead, the re-normalized covariant vectors faithfully preserve the time-reversal symmetry of the equations of motion, which is reflected by

$$^{(-)}\Lambda_{\ell}^{\text{cov}}(t) = -^{(+)}\Lambda_{D+1-\ell}^{\text{cov}}(t) \text{ for } \ell = 1, \dots, D, \quad (5.16)$$

regardless, whether the system is symplectic or not. This means that an expanding co-moving direction is converted into a collapsing co-moving direction by an application of the time-reversal operation. Of course, the forward and backward local exponents in Eq. (5.16) refer to the same phase space point  $\mathbf{\Gamma}(t)$ .

These symmetry properties may be considered the main conceptual differences between the Gram-Schmidt and covariant viewpoints.

Before leaving this section, a short remark concerning the commonly-used term “time-dependent exponent” seems in order. Primarily, this quantity is a function of the phase point and should only be called a “local” exponent. Its value may be different whether the phase point is reached from the past, forward in time (+), or from the future, backward in time (−).

### 5.3 Differential approach to local Lyapunov exponents

Equation (5.9) precisely reflects the numerical procedure for the computation of local GS exponents for finite time intervals  $\tau$ . But it is also possible to obtain a differential version for  $\tau \rightarrow 0$ . Goldhirsch *et al.* derived a full set of differential equations for the Gram-Schmidt vectors  $\mathbf{g}^\ell$  [13],

$$\dot{\mathbf{g}}^1 = \mathcal{D}_{\mathbf{r}} \mathbf{g}^1 - R_{11} \mathbf{g}^1, \quad (5.17)$$

$$\dot{\mathbf{g}}^\ell = \mathcal{D}_{\mathbf{r}} \mathbf{g}^\ell - R_{\ell\ell} \mathbf{g}^\ell - \sum_{m=1}^{\ell-1} (R_{\ell m} + R_{m\ell}) \mathbf{g}^m, \quad (5.18)$$

where in the last equation  $\ell = 2, \dots, D$ . We have demonstrated [14, 15] that the matrix elements

$$R_{\ell m}(\mathbf{\Gamma}(t)) = (\mathbf{g}^\ell)^\dagger \mathcal{D}_{\mathbf{r}} \mathbf{g}^m \quad (5.19)$$

may be understood as Lagrange multipliers enforcing the orthonormalization constraints  $\mathbf{g}^\ell \cdot \mathbf{g}^m = \delta_{\ell m}$  (equal to unity for  $\ell = m$ , and zero otherwise). Here  $\dagger$  means transposition. Most importantly, the diagonal elements are the local Gram-Schmidt exponents:

$$\Lambda_\ell^{GS}(\mathbf{\Gamma}(t)) \equiv R_{\ell\ell}(\mathbf{\Gamma}(t)) = (\mathbf{g}^\ell)^\dagger \mathcal{D}_{\mathbf{r}} \mathbf{g}^\ell. \quad (5.20)$$

This expression nicely underlines the local nature of the exponents.

We have verified for the doubly-thermostated heat conduction model discussed in Sec. 5.5 below that the direct integration of the Eqs. (5.17) and (5.18) provide local GS exponents according to Eq. (5.20), which agree extremely well with the results obtained from a direct application of the GS algorithm, Eq. (5.9), for a reasonably-small time interval  $\tau$ . This agreement also persists for the time-reversed dynamics.

### 5.4 Numerical considerations

In this section we remark on a few aspects of our implementation of the algorithm for the computation of the covariant Lyapunov vectors, which we apply in the following sections. Reduced units are used for the various models treated below. For convenience, we specify already here the adopted values (in reduced units) for some time parameters:  $t_\omega = 6 \times 10^4$ ,  $t_\alpha = 5 \times 10^4$ , and  $t_0 = 100$ . Their meaning is explained below. For the integration of the equations of motion, a 4th-order Runge-Kutta algorithm with a time step  $dt = 0.001$  is used. This time step is chosen

such that the trajectory is correct to double-precision accuracy. For the interval between successive Gram-Schmidt re-orthonormalization steps – respective covariant vector normalizations – we choose  $\tau = 10dt = 0.01$ . This number is a (very conservative) compromise between the achieved reduction in storage requirements as outlined below, and the precision of integration forward and backward over the same interval. The time  $t_0$  is chosen such that in the interval  $-t_0 \leq t \leq t_0$  accurate Gram-Schmidt and covariant Lyapunov vectors are available.

The simulations are carried out with the following protocol:

**Phase 1 (forward integration from  $-t_\omega$  to  $+t_\omega$ ):** Starting with arbitrary initial conditions at a time  $-t_\omega$  and using a positive integration time step  $dt > 0$ , the evolution of the reference trajectory  $\mathbf{\Gamma}(t)$  and of the full set of Gram-Schmidt vectors is computed in the forward direction of time up to a time  $+t_\omega$ . The reference trajectory and the Gram-Schmidt vectors are stored for every 10 time steps,  $10dt = \tau$ , along the way. The Gram-Schmidt vectors are used in phase 2 for the construction of the covariant vectors, and the reference trajectory is required in phase 3 for the computation of the time-reversed Gram-Schmidt vectors. The Lyapunov spectrum  $\{^{(+)}\lambda^{GS}\}$  is accumulated for times  $-t_\alpha \leq t \leq t_\omega$ , for which the orientations of the Gram-Schmidt vectors are fully relaxed.

**Phase 2 (backward iteration from  $t_\omega$  to  $-t_0$ ):** Starting at  $t_\omega$ , the covariant vectors are computed by iterating back to a time  $-t_0$ . The details of this algorithm are given in Ref. [7]. Since the *forward* GS-vectors, stored during phase 1, are now used in reversed order, the consecutive order of the covariant vectors  $\dots, \mathbf{v}^\ell(t_k), \mathbf{v}^\ell(t_{k-1}), \dots$  has to be reversed for the computation of the corresponding local exponent,

$$^{(+)}\Lambda_\ell^{\text{cov}}(t_k) = \frac{1}{\tau} \ln \frac{\|\mathbf{v}^\ell(t_k)\|}{\|\mathbf{v}^\ell(t_{k-1})\|},$$

or, alternatively, the sign of the local exponents must be reversed. The time averaging for the global Lyapunov spectrum  $\{^{(+)}\lambda_\ell^{\text{cov}}\}$  is carried out for times  $t_\alpha \geq t \geq -t_0$ .

The following two phases are only required for the computation of the local *time-reversed* Gram-Schmidt and covariant exponents.

**Phase 3 (backward integration from  $t_\omega$  to  $-t_\omega$ ):** With arbitrary initial conditions at time  $t_\omega$ , the Gram-Schmidt tangent space dynamics is followed backward in time up to  $-t_\omega$ . To counteract the Lyapunov instability, it is essential for this computation to use the *same* reference trajectory stored in phase 1, where the sign of the momentum-like variables ( $p, z$ , and  $x$  for the doubly-thermostated oscillator) is left unchanged, but with the time step reversed to  $-0.001$ . For an accurate computation of the backward GS vectors, the reference trajectory at *every* integration

step is required. Since in phase 1 this information was stored for only every 10th step (to save computer storage), the forward reference trajectory is piece-wise re-computed with stored phase-space points as initial conditions. The backward Gram-Schmidt vectors are again stored for every 10th time step replacing the forward vectors of phase 1. If time is reversed, the stable directions become unstable and *vice versa*. The Lyapunov spectrum  $\{^{(-)}\lambda_\ell^{GS}\}$  is accumulated in the interval  $t_\alpha \geq t \geq -t_\omega$ .

**Phase 4 (forward iteration from  $-t_\omega$  to  $+t_0$ ):** Analogous to phase 2, in this final stage the covariant Lyapunov vectors for the *reversed time direction* are computed with the help of the time-reversed Gram-Schmidt vectors from phase 3. The respective Lyapunov spectrum  $\{^{(-)}\lambda_\ell^{\text{cov}}\}$  is accumulated for times  $-t_\alpha \leq t \leq t_0$ .

It may be noticed that in the interval  $-t_0 \leq t \leq +t_0$  all local properties are available with the Gram-Schmidt and covariant vectors fully relaxed both forward and backward in time. Therefore, the detailed analysis of local (time-dependent) Lyapunov exponents in the following sections is carried out in this regime.

## 5.5 Doubly-thermostated oscillator

### 5.5.1 Description of the model

Here we consider a simple model which already has many ingredients in common with much more involved physical systems. It exhibits chaotic equilibrium and stationary non-equilibrium states and collapses onto a limit cycle for very strong driving. It consists of a one-dimensional harmonic oscillator, which is coupled to two consecutive stages of Nosé-Hoover thermostats with a space-dependent temperature  $T(q)$ . The equilibrium version of this model was first considered by Martyna, Klein and Tuckerman [18]. Its non-equilibrium properties were consecutively studied by us in some detail [19, 20], but without considering covariant vectors. This paper is also intended to augment this work correspondingly.

The equations of motion, expanded with two thermostat variables  $z$  and  $x$ , are [19, 20]

$$\begin{aligned}\dot{q} &= p, \\ \dot{p} &= -q - zp, \\ \dot{z} &= p^2 - T(q) - zx, \\ \dot{x} &= z^2 - T(q),\end{aligned}$$

where the position dependent temperature is given by

$$T(q) = 1 + \varepsilon \tanh(q).$$

The control parameter  $\varepsilon$  coincides with the temperature gradient at  $q = 0$ . These equations are written in the most simple reduced form with all arbitrary parameters of the model set equal to unity. The system is not symplectic. On average, the oscillator picks up energy from the thermostat whenever it is in a region of high temperature ( $q > 0$ ), and releases it again in low-temperature regions ( $q < 0$ ).

### 5.5.2 Global properties

For a typical non-equilibrium state, ( $\varepsilon = 0.25$ ), the global Lyapunov spectrum was computed by four independent methods, applying the protocol outlined in Sec. 5.4:

**Phase 1** : GS exponents in forward direction of time,

$$\{^{(+)}\lambda_{\ell}^{GS}\} = \{0.053_1, 0.0000_1, -0.034_4, -0.086_7\},$$

**Phase 2** : covariant exponents in forward direction of time,

$$\{^{(+)}\lambda_{\ell}^{\text{cov}}\} = \{0.053_6, 0.0000_1, -0.035_1, -0.086_2\},$$

**Phase 3** : GS exponents in backward direction of time,

$$\{^{(-)}\lambda_{\ell}^{GS}\} = \{0.086_7, 0.034_4, 0.0000_3, -0.053_1\},$$

**Phase 4** : covariant exponents in backward direction of time,

$$\{^{(-)}\lambda_{\ell}^{\text{cov}}\} = \{0.087_1, 0.033_7, 0.00000_1, -0.052_5\}.$$

The last digit of each number is rounded accordingly. Considering the smallness of the exponents and the rather involved numerical procedures, the agreement between the independently-determined global spectra is very satisfactory. A comparison of the forward and backward dynamics reveals the theoretically expected symmetry for the global Lyapunov exponents [5, 21],

$$^{(-)}\lambda_{\ell} = -^{(+)}\lambda_{D+1-\ell} \text{ for } \ell = 1, \dots, D. \quad (5.21)$$

If the temperature gradient  $\varepsilon$  is varied over a wide range, significant changes of the spectrum become evident. This is shown in the left panel of Fig. 5.1. There exist a number of distinct regimes with different qualitative behavior.

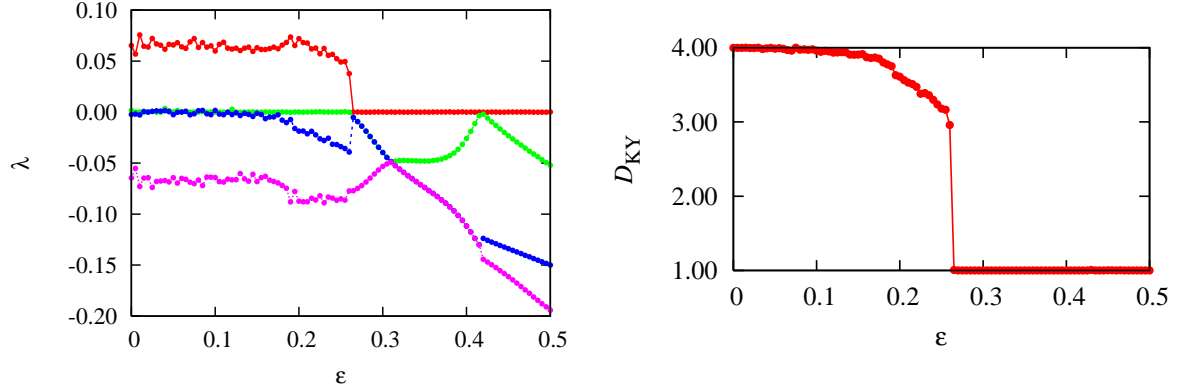


**Figure 5.1 :** Temperature-gradient dependence of all four Lyapunov exponents (left panel) and of the Kaplan-Yorke dimension (right panel) for the doubly-thermostated oscillator. For  $\varepsilon > \varepsilon_c = 0.26314$ , the trajectory collapses onto a limit cycle.

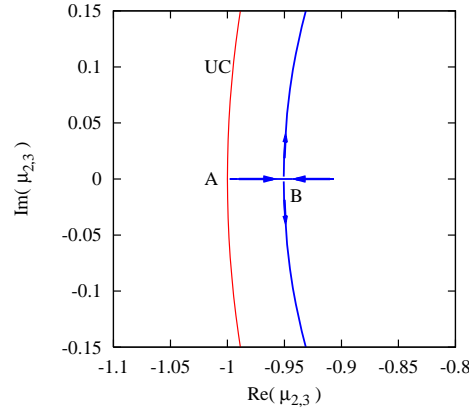


**Figure 5.2 :** Floquet multipliers  $\mu_2$  and  $\mu_3$  in the complex plain for  $\varepsilon \geq 0.26312$ . UC denotes the unit circle, and A is the bifurcation point. The multipliers are complex conjugate to each other for  $\varepsilon > 0.26319$  as indicated by B.

For  $\varepsilon \lesssim 0.18$ , the spectrum changes but little with  $\varepsilon$ , and the Kaplan-Yorke dimension is only weakly reduced with respect to the full phase space dimension, as is shown in the right panel of Fig. 5.1. The dissipation due to the weak heat current influences the appearance of the chaotic phase-space trajectory very little. An example of a projection of such a trajectory onto the  $qpz$ -subspace is provided in the top-left panel of Fig. 5.3. For  $0.18 \lesssim \varepsilon < 0.26$ , the trajectory is more and more attracted to a weakly unstable periodic orbit (see the bottom-left panel of Fig. 5.3), which for  $\varepsilon_c \approx 0.26312$  turns into a stable limit cycle as shown in the top-right panel of Fig. 5.3. The nature of this transition may be established by considering the Floquet multipliers  $\mu_\ell$ ,  $\ell = 1, \dots, 4$  for the fixed points of the Poincaré map, defined by  $q = 0$ , for  $\varepsilon \geq \varepsilon_c \approx 0.26312$ . Whereas  $\mu_1 = 1$  and  $\mu_4 < 0$ , a single multiplier  $\mu_2$  crosses the unit circle on the real axis at the point A corresponding to  $\varepsilon_c$  in Fig. 5.2. Such a behavior is characteristic of a period doubling bifurcation [22], where, possibly, the chaotic attractor disappears in a boundary crisis bifurcation. Increasing  $\varepsilon$  further, the Floquet multipliers  $\mu_{2,3}$  vary as indicated by the arrows and

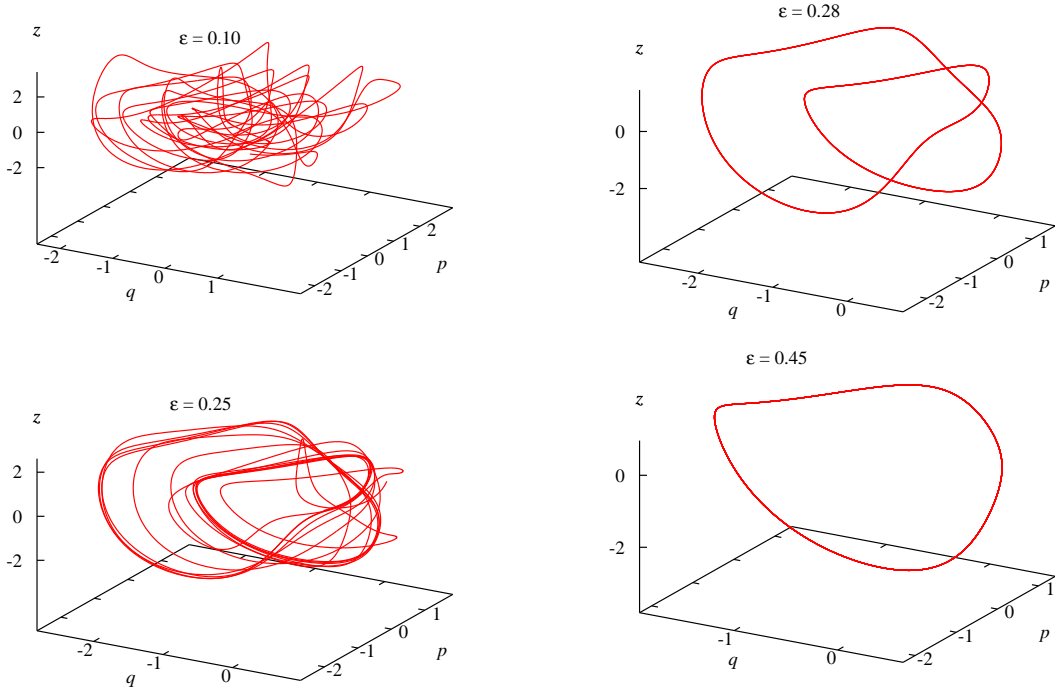


**Figure 5.3 :** Projection of a short chaotic trajectory for  $\varepsilon = 0.10$  (top-left),  $\varepsilon = 0.25$  (bottom-left),  $\varepsilon = 0.28$  (top-right) and  $\varepsilon = 0.45$  (bottom-right) onto the  $qpz$ -subspace.

become complex conjugate to each other for  $\varepsilon \approx 0.26319$  (point B in Fig. 5.2). For  $\varepsilon \approx 0.417$ , there is another transition changing the two-loop limit cycle into a single-loop orbit, this is illustrated in the bottom-right panel of Fig. 5.3.

### 5.5.3 Local Lyapunov exponents

In Fig. 5.4 we apply Eq. (5.11) to the doubly-thermostated oscillator in a stationary chaotic state,  $\varepsilon = 0.25$ . For  $\ell = 1$  the respective time-dependent exponents are identical and are not shown. The case  $\ell = 2$  is treated in the figure. The dashed green line denotes the covariant local exponent, the smooth red line is for the local GS-exponents, which is directly obtained from the simulation invoking Gram-Schmidt re-orthonormalization. The time interval  $\tau$  is 0.01. The blue points for  $\Lambda_\ell^{GS}(t)$  are computed with Eq. (5.11), where the covariant exponent  $\Lambda_\ell^{\text{cov}}(t)$  and the angle  $\beta_{\ell\ell}(t)$  are taken from the simulation. The agreement is convincing. Similar results are also obtained for  $\ell = 3$  and 4 (not shown).

In the right panel of Fig. 5.5 we demonstrate, for  $\ell = 2$ , the general time-reversal symmetry for the local (time dependent) covariant exponents (see Eq. (5.16)) which also gives rise to the symmetry of the global (time-averaged) exponents already encountered in Eq. (5.21). For  $\ell = 1$

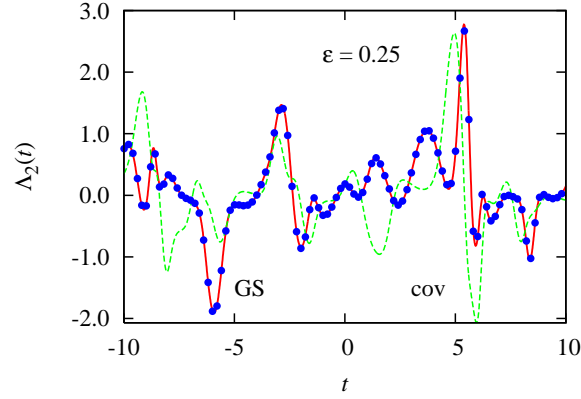


**Figure 5.4 :** Time-dependence of the local Lyapunov exponents  $\Lambda_2(t)$  in the forward direction of time for the doubly-thermostated oscillator with  $\epsilon = 0.25$ . The smooth red curve denotes Gram-Schmidt exponents, directly obtained with a re-orthonormalization procedure, the blue points are computed with Eq. (5.11), using the covariant time-dependent exponents  $\Lambda_\ell^{\text{cov}}$  (also shown as green dashed line) and the angles  $\beta_{\ell\ell}$  as input. For clarity, only every 20th point is depicted.

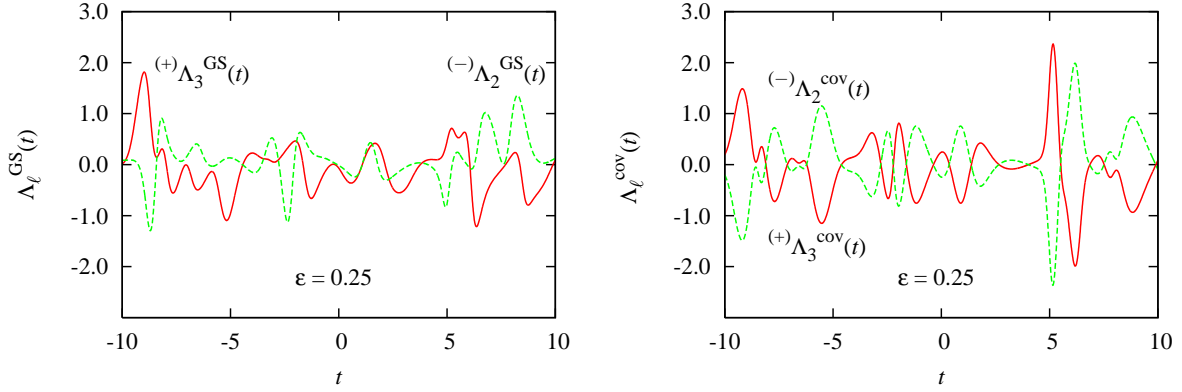


**Figure 5.5 :** Doubly-thermostated oscillator for  $\epsilon = 0.25$ . Left panel: The Gram-Schmidt local Lyapunov exponents do not display time-reversal symmetry. Right panel: Display of time-reversal symmetry by the covariant local exponents,  $(+)\Lambda_\ell^{\text{cov}} = -(-)\Lambda_{D+1-\ell}^{\text{cov}}$  for  $\ell = 2$ , Analogous curves are obtained for the other  $\ell$ , but are not shown.

the symmetry is also fully obeyed but not shown.

As emphasized already in Eq. (5.15), the local Gram-Schmidt exponents generally do not have this symmetry. This is explicitly shown in the left panel of Fig. 5.5. See also Ref. [19], where the same observation was made. Only the subspaces in Eq. (5.10) spanned by consecutive Gram-Schmidt vectors have a simple dynamical interpretation, but not the GS-vectors themselves. The orthonormal GS-vectors are oriented such that for the tangent space, tangent to the phase flow at the phase point  $\mathbf{\Gamma}(t)$ , the subspaces  $(-)\mathbf{g}^1(t) \oplus \dots \oplus (-)\mathbf{g}^\ell$ , with  $\ell \in \{1, \dots, D\}$ , are the most unstable subspaces of dimension  $\ell$  going from time  $t$  to  $-\infty$  (i.e. the most stable subspaces of dimension  $\ell$  in the future). Although time reversal converts a most stable subspace of dimension  $\ell$  into the most unstable subspace with the same dimension, and *vice versa*, there



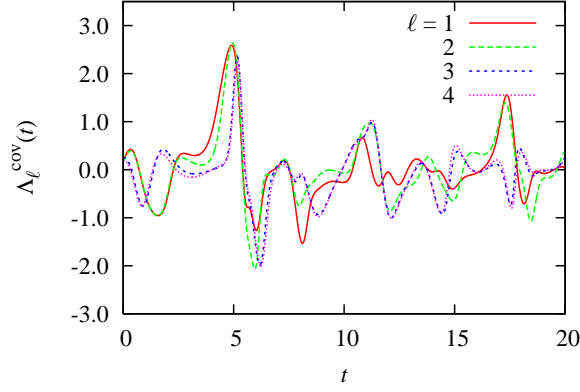


**Figure 5.6 :** Doubly-thermostated oscillator with  $\epsilon = 0.25$ : Time dependence of all four local covariant Lyapunov exponents.

is no obvious correlation of the instantaneous Lyapunov exponents  $(-)\Lambda_\ell^{GS}(t)$  and  $(+)\Lambda_{D+1-\ell}^{GS}(t)$  for  $\ell = 1, \dots, D$ .

It is interesting to follow the time dependence of the covariant local exponents, or more correctly expressed, their variation for consecutive state points along the phase space trajectory (see Fig. 5.6). One observes that the order of the exponents fluctuates and may even be totally reversed with  $\Lambda_1^{\text{cov}}(t)$  being most negative and  $\Lambda_4^{\text{cov}}(t)$  most positive. Also the dimension of the stable and unstable manifolds changes along the trajectory. This indicates that the system is far from being hyperbolic. We address this point more closely in the following subsection.

#### 5.5.4 Hyperbolicity

We infer from Eq. (5.11) that the difference between the local covariant and Gram-Schmidt exponents stems from the fact that the angle between the respective vectors deviates significantly from zero and varies with time. But also the angles between covariant vectors,  $\alpha_{ij}(t) \equiv \arccos[(\mathbf{v}^i \cdot \mathbf{v}^j)/\|\mathbf{v}^i\|\|\mathbf{v}^j\|]$  significantly change with time. This is demonstrated in the right panel of Fig. 5.7 for the same non-equilibrium state ( $\epsilon = 0.25$ ) of the doubly-thermostated oscillator discussed previously. There is an intermittent tendency of any two pairs of vectors to get parallel or antiparallel to each other. The probability distributions for these angles,  $\pi(\alpha_{ij})$ , are shown in the left panel of Fig. 5.7 and confirm this observation. Although the angles  $\alpha$  do not become strictly zero – the vectors could not separate anymore after such an event, which is not observed – the large probability for angles close to zero or  $\pi$  is noticeable. As was mentioned before, the associated local covariant exponents are out of order for most of the time as in Fig. 5.6. If  $P_i$  denotes the probability for  $\Lambda_i^{\text{cov}}$  to be out of order with respect to any of the other exponents, one finds for the doubly-thermostated oscillator ( $\epsilon = 0.25$ )  $\{P_1, \dots, P_4\} = \{0.650, 0.813, 0.840, 0.645\}$ .

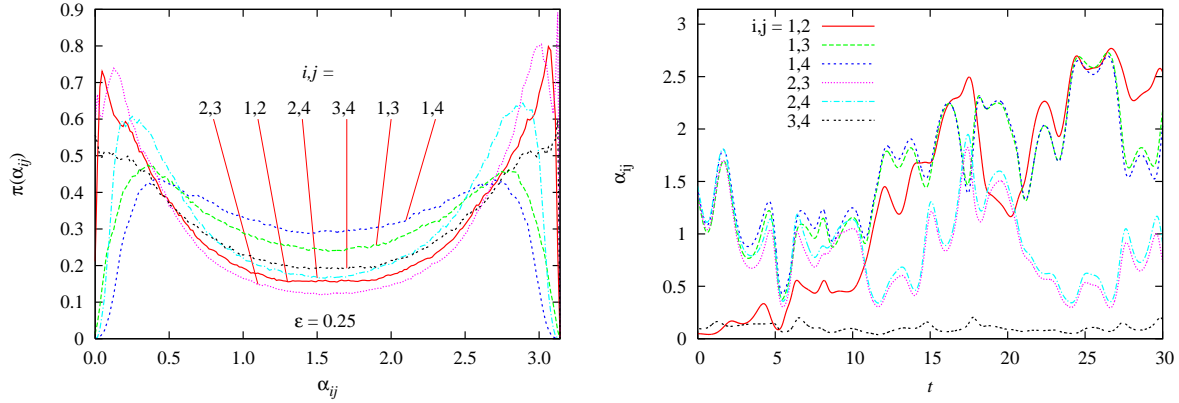


**Figure 5.7 :** Doubly-thermostated oscillator with  $\epsilon = 0.25$ . Left panel: Probability distributions for the angles  $\alpha_{ij}$  between covariant vector pairs specified by the labels. Right panel: Time evolution of the angles  $\alpha_{ij}$  between the covariant vectors  $\mathbf{v}^i$  and  $\mathbf{v}^j$ .

This clearly demonstrates the strong entanglement between the covariant vectors. If the local exponents are time averaged along the trajectory for time intervals  $\Delta$ , the analogous probabilities  $\bar{P}_i^\Delta$  for the time-averaged exponents  ${}^{\text{cov}}\bar{\Lambda}_i^\Delta$  scale according to  $\bar{P}^\Delta \propto \Delta^{-\gamma_i}$  with  $\gamma > 0$  for large-enough  $\Delta$ . This shows that the domination of the Oseledec splitting is violated for finite times.

Such a behavior is in contrast to the covariant dynamics of hard-disk systems, for which the covariant vectors tend to avoid becoming parallel or antiparallel [7]. Thus, whereas the hard-disk system is hyperbolic, the doubly-thermostated oscillator is not.

### 5.5.5 Singularities of the local Lyapunov exponents

In the direction of the flow, the local Lyapunov exponents clearly are smooth functions of the time and, hence, of the phase-space position along the trajectory, see Fig. 5.4. But transverse to the flow this need not be the case. Indeed, for the periodic Lorentz gas it was noted by Gaspard [23, 24] that the local stretching factors are discontinuous transverse to the flow. Since this model involves hard elastic collisions of point particles with space-fixed scatterers, the observed discontinuity might still be thought to be a consequence of the discontinuous nature of the flow. However, Dellago and Hoover showed [25] that this is not the case. They found a discontinuous local exponent  $\Lambda_1^{GS}$  along a path transverse to the flow even for a time-continuous Hamiltonian system, a chaotic pendulum on a spring. Of course, their result also applies to  $\Lambda_1^{\text{cov}}$  for that model. Here we provide evidence for the doubly-thermostated oscillator in equilibrium ( $\epsilon = 0$ ) that all local covariant exponents are discontinuous along directions transverse to the flow.

For this simulation we slightly modify the protocol of Sec. 5.4.

**Phase 0:** Starting at a phase point  $\Gamma_s$  at time zero, the reference trajectory is followed backward in time to  $-t_\omega = -60,000$  and is periodically stored for intervals  $\tau$  along the way.

**Phase 1:** The next phase is identical to phase 1 of Sec. 5.4 with one essential difference: For  $-t_\omega \leq t \leq 0$ , the previously-stored reference trajectory is now used in the forward direction of time for the computation of the Gram-Schmidt vectors, which assures that the trajectory precisely arrives at  $\Gamma_s$  at time zero in spite of the inherent Lyapunov instability. For  $0 \leq t \leq t_\omega$  the simulation proceeds as in phase 1 of Sec. 5.4.

**Phase 2:** This is identical to phase 2 of Sec. 5.4 and provides us with the covariant vectors and the respective local exponents in the interval  $-t_0 < t < t_0$  and at the time  $t = 0$  in particular, when the state coincides with the selected phase point  $\Gamma_s$ .

The whole procedure is repeated for starting points  $\Gamma_s \equiv \Gamma_0 + s \times (0, 0, 1, 0)$  on a straight line parallel to the  $z$ -axis, which is parametrized by  $s$ . This line is transversal to the flow, as may be expected from Fig. 5.3.

As an example, we plot in the left panel of Fig. 5.8 the local covariant exponent  $\Lambda_4^{\text{cov}}(t)$  as a function of time for 500 initial points  $\Gamma_s$  separated by  $\Delta s = 1 \times 10^{-4}$ . It should be noted that the scale on the  $t$  axis, converted into distances along the trajectory, is about 200 times coarser than that on the  $s$  axis. The red line for  $t = 0$  connects the local exponents for the selected initial states  $\Gamma_s$ . This curve for  $\Lambda_4^{\text{cov}}(t)$  is also reproduced in the right panel of Fig. 5.8 together with an analogous result for  $\Lambda_1^{\text{cov}}(t)$ . Both curves exhibit singularities on many scales showing singular fractal character. There are no obvious correlations between the two curves. The singularities are due to bifurcations in the past history of the trajectory. In view of Fig. 5.3, such a bifurcation may be visualized, for example, by a transition of the trajectory from the neighborhood of an unstable periodic orbit to the neighborhood of another with a different number of loops.

One may raise the question (as has been done by one of the referees), how reliable the curves in Fig. 5.8 are in view of the chaotic nature of the flow and problems of shadowing due to the finite computational accuracy. An increase of the Runge-Kutta integration time step  $dt$  by a factor of four has no noticeable effect (less than 0.1%) in Fig. 5.8, which also proved completely insensitive to a reduction of the relaxation time  $t_\omega$  of the algorithm by a factor of two and of an increase of the time  $\tau$  between successive re-orthonormalization steps by the same factor. This robustness, however, does not apply to the local exponents  $\Lambda_2^{\text{cov}}$  and  $\Lambda_3^{\text{cov}}$  (not shown), which belong to the two-dimensional central manifold for this equilibrium system. The respective covariant vectors span this subspace, but their precise orientations and their local exponents are affected by details of the algorithm and do not have direct physical significance.

For non-equilibrium stationary states the singular character of the local exponents in transverse

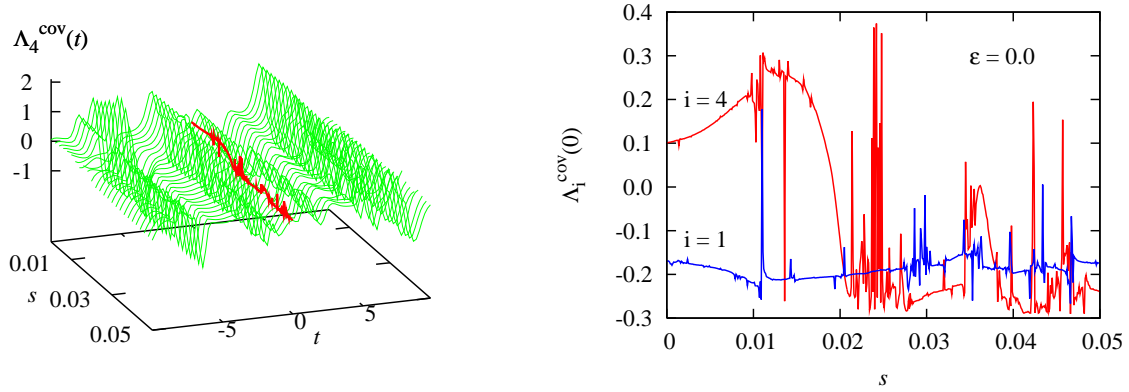


**Figure 5.8 :** Covariant local Lyapunov exponent,  $\Lambda_4^{\text{cov}}$ , for the doubly-thermostated oscillator in equilibrium. Left panel: Time dependence along trajectories, which, for  $t = 0$ , are at the specified initial points  $\Gamma_s$  introduced in the main text. These phase points lie on a straight line transverse to the flow, and  $s$  specifies the precise position. The variation of the local exponent along this straight line is shown as a red curve. Right panel: The red curve is a magnified view of the red line of the left panel, representing the variation of  $\Lambda_4^{\text{cov}}$  along a straight line transverse to the flow in the phase space. The blue line is an analogous curve for  $\Lambda_1^{\text{cov}}$ .

directions is expected to be even more pronounced, since even the phase-space probability density becomes a multifractal object [1, 14]. For the covariant exponent this cannot be shown with the present algorithm. The reason is that during the time-reversed simulation in phase 0, the phase volumes collapse yielding negative Lyapunov exponent sums. Since in phase 1 this trajectory is followed in the opposite direction, the respective phase volumes *expand* providing a positive sum of Lyapunov exponents, but only up to time zero. For positive times the reference trajectory is calculated anew from the motion equations, again yielding *contracting* phase volumes. Thus, the character of the flow changes at  $t = 0$  and the Gram-Schmidt vectors at first are non-relaxed and point into wrong directions for positive times. Since these vectors are required for the computation of covariant vectors at and near zero time, the algorithm cannot be used to obtain the covariant vectors and respective local exponents at a pre-determined point  $\Gamma_s$  in phase space. For equilibrium states this restriction does not apply and the local exponents may be computed for pre-specified phase-space points.

## 5.6 Local Lyapunov exponents for symplectic systems\*

So far we have omitted to mention that we use a particular metric in phase space. Whereas the global exponents are independent of the metric, the local exponents, covariant or Gram-Schmidt, clearly are not. We demonstrate this with the most simple symplectic example, a scaled harmonic

\*This section is not included in the original publication in Phys. Rev. E **82**, 046218 (2010).

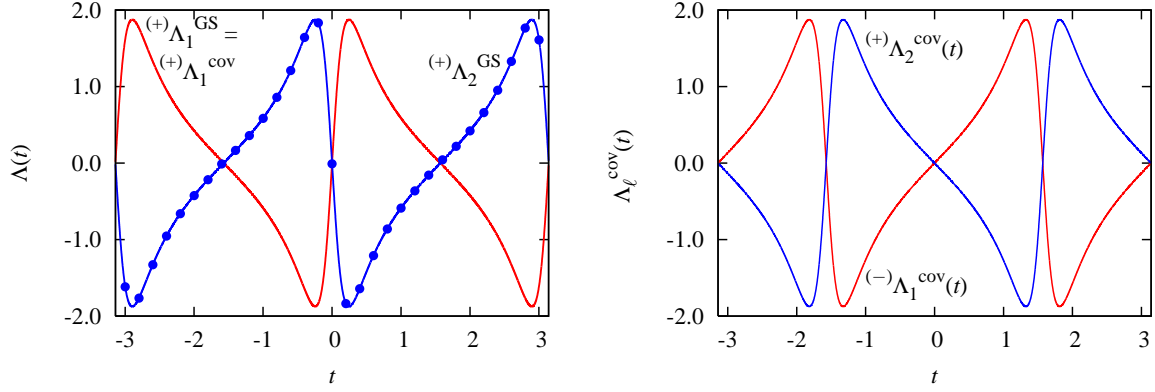


**Figure 5.9 :** Scaled harmonic oscillator with  $s = 2$ : Time dependence of the local Lyapunov exponents. Left panel: The smooth red lines are local GS exponents for  $\ell = 1$  and 2 as indicated by the labels. The results from direct simulation and from theory are undistinguishable on this scale. The points indicate the reconstruction of  $(+)\Lambda_2^{\text{GS}}$  with the help of Eq. (5.11), where  $(+)\Lambda_2^{\text{cov}}$  is shown in the right panel. Note that the GS and covariant exponents for  $\ell = 1$  are identical. Right panel: Demonstration of the time-reversal invariance for the covariant exponents.

oscillator [26, 27] with Hamiltonian

$$H_s(p, q) = \frac{1}{2} \left[ \left( \frac{p}{s} \right)^2 + (sq)^2 \right]$$

and equations of motion

$$\dot{q} = s^{-2}p, \quad \dot{p} = -s^2q, \quad (5.22)$$

where  $s$  is a scaling parameter. For the ‘natural’ scaling,  $s = 1$ , the global and local exponents vanish. But for the scaled case,  $s \neq 1$ , the local Lyapunov exponents do not. They depend on the metric and, for that matter, on the choice of the coordinate system, be it Cartesian or polar.

Let us look at this model in a little more detail, since the dynamical matrix

$$\mathcal{D}_\Gamma = \begin{pmatrix} 0 & s^{-2} \\ -s^2 & 0 \end{pmatrix}$$

for this linear model does not depend on the phase point and allows for a complete analytical solution [27] for the tangent vector dynamics. Still, the model is a bit peculiar, since there is no global exponential ordering of tangent vectors familiar from the Gram-Schmidt algorithm, and the considerations of Sec. 5.4 lose their meaning. Any (unit) vector, with arbitrary initial condition (phase), which is a solution of Eq. (5.17), may be taken as the first Gram-Schmidt vector (or covariant vector for that matter). We fix this arbitrary phase by requiring that  $\mathbf{g}^1$  coincides with the normalized phase-space velocity, which is associated with a vanishing exponent

and is a solution of Eq. (5.17), as may be explicitly shown. Thus,

$$\mathbf{g}^1 \equiv \begin{pmatrix} \delta q_1 \\ \delta p_1 \end{pmatrix} = \left[ \left( \frac{p}{s^2} \right)^2 + (s^2 q)^2 \right]^{-1/2} \begin{pmatrix} p/s^2 \\ -s^2 q \end{pmatrix}, \quad (5.23)$$

where we denote the perturbation components of  $\mathbf{g}^1$  by  $\delta q_1$  and  $\delta p_1$ ). From the constrained motion equation (5.17) one obtains

$$\dot{\delta q}_1 = s^{-2} \delta p_1 - R_{11} \delta q_1 \quad (5.24)$$

$$\dot{\delta p}_1 = -s^2 \delta q_1 - R_{11} \delta p_1. \quad (5.25)$$

Since  $\mathbf{g}^1$  is constrained to unit length,  $\delta q_1 \dot{\delta q}_1 + \delta p_1 \dot{\delta p}_1 = 0$ , and noting that  $\Lambda_1^{GS} \equiv R_{11}$ , we obtain from these equations

$$\Lambda_1^{GS} = (s^{-2} - s^2) \delta q_1 \delta p_1. \quad (5.26)$$

Insertion of  $\delta q_1$  and  $\delta p_1$  from Eq. (5.23) yields an analytic expression for the local Gram-Schmidt exponent  $\Lambda_1^{GS}$  as a function of the phase-space point  $(q, p)$ . The second Gram-Schmidt vector is perpendicular to the first, and its associated GS exponents immediately follow from the conservation of phase-space volume:

$$\Lambda_2^{GS}(q, p) = -\Lambda_1^{GS}(q, p).$$

In the left panel of Fig. 5.9 the local Gram-Schmidt exponents for the scaled harmonic oscillator for  $s = 2$  are shown as a function of time. The initial conditions  $q(0) = 0$  and  $p(0) = 1$  are used, for which the solution of Eq. (5.22) becomes

$$q(t) = s^{-2} \sin t, \quad p(t) = \cos t.$$

Both computer simulation results and the theoretical expressions for  $\Lambda_1^{GS}$  and  $\Lambda_2^{GS}$  are shown, which agree so well that they cannot be distinguished and appear only as a single smooth red line in the figure.

The upper and lower bounds of the local exponents are also easily obtained from Eq. (5.26) [27],

$$\Lambda_{\min, \max} = \pm(s^{+2} - s^{-2})/2.$$

The extrema are attained whenever the components  $\delta q$  and  $\delta p$  of the respective perturbation vectors contribute equally,  $\delta p = \pm \delta q$ . For  $s = 2$  we find  $\Lambda_{\min, \max} = \pm 1.875$  in full agreement

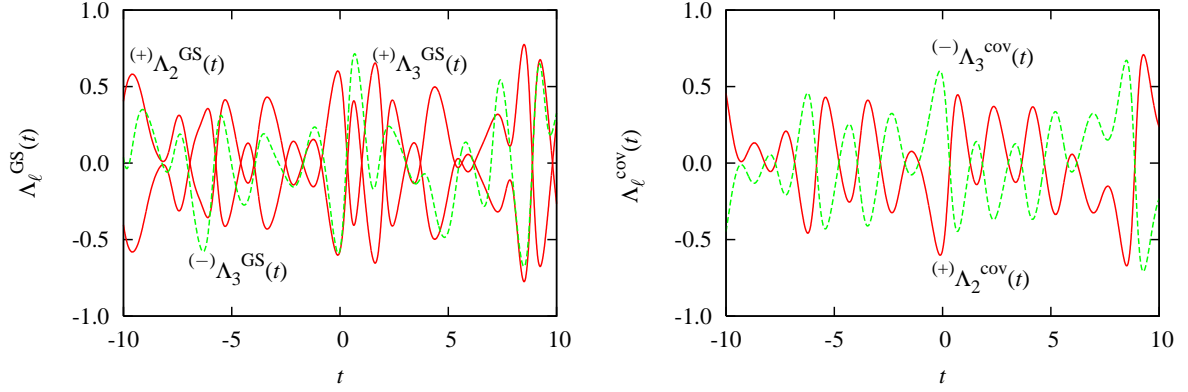


**Figure 5.10 :** Local Lyapunov exponents for the Hénon-Heiles system with energy  $H = 1/6$ . Left panel: Illustration of the symplectic local pairing symmetry, Eq. (5.13), for the Gram-Schmidt exponents  $(+)\Lambda_2^{GS}$  and  $(+)\Lambda_3^{GS}$  (smooth red lines). Here,  $D = 4$ . Also the inequality Eq. (5.15) applies ( $\ell = 2$ ), as the dashed green line for  $(-)\Lambda_3^{GS}$  certifies. Right panel: Verification of the time-reversal invariance property (5.16) for the covariant vectors specified.

with Fig. 5.9.

The undetermined phases we encountered with the Gram-Schmidt vectors also carry over to the covariant vectors. But since the latter are computed with the help of the former, the choice of phase for  $\mathbf{g}^1$  also fixes that for  $\mathbf{v}^1$  and  $\mathbf{v}^2$ . In the right panel of Fig. 5.9 the covariant exponent  $\Lambda_2^{cov}(t)$  is shown as it is obtained from the simulation. If this function is used to reconstruct  $\Lambda_2^{GS}(t)$  with the help of Eq. (5.11), the (blue) dots in the left panel of Fig. 5.9 are obtained, where  $\cos(\beta_{22}) = \mathbf{g}^2 \cdot \mathbf{v}^2$  is also taken from the simulation. The agreement is very good. In the right panel of Fig. 5.9 we also plot  $(-)\Lambda_1^{cov}(t)$  for the time-reversed dynamics. The time-reversal symmetry of Eq. (5.16),

$$(-)\Lambda_1^{cov}(t) = -(+)\Lambda_2^{cov}(t),$$

is nicely displayed.

As a slightly more involved example, we compute the four local Lyapunov exponents for the symplectic Hénon-Heiles system [28] with Hamiltonian

$$H = \frac{1}{2}(p_x^2 + p_y^2) + \frac{1}{2}(x^2 + y^2) + x^2y - \frac{1}{3}y^3. \quad (5.27)$$

For an energy  $H = 1/6$ , the system is known to be chaotic (with a Lyapunov spectrum  $\{0.1277, 0, 0, -0.1277\}$ ), where the trajectory visits most of the accessible phase space [29, 30]. Using the protocol of Sec. 5.4, we compute the GS and covariant exponents and present some of the results in Fig. 5.10. In the left panel the symplectic local pairing symmetry of Eq. (5.13) for  $(+)\Lambda_2^{GS}$  and  $(+)\Lambda_3^{GS}$  is shown by the smooth red lines (similar to the results of Ref. [30]). The green dashed line refers to the time-reversed exponent  $(-)\Lambda_3^{GS}$  and clearly emphasizes the lack

of any time-reversal symmetry as expressed by the inequality (5.15). On the other hand, for the covariant exponents precisely this symmetry is evident from the right panel of Fig. 5.10.

To avoid confusion, we note that the ‘detailed balance symmetry’ introduced in Ref. [30] is not connected with the symplectic local pairing symmetry considered here. The former only means that for a global exponent to become zero, the positive and negative parts of the respective local exponent along the trajectory must cancel each other when integrated over time.

## 5.7 Concluding remarks

For the doubly-thermostated oscillator in a non-equilibrium stationary state, there is a single vanishing global exponent,  $\lambda_2$ , due to the time-translation invariance of the equations of motion. The corresponding covariant vector,  $\mathbf{v}^2(t)$ , needs to be parallel (or antiparallel) to the phase-space velocity  $\dot{\mathbf{\Gamma}}(t) \equiv \{\dot{q}(t), \dot{p}(t), \dot{z}(t), \dot{x}(t)\}$ . We have verified in our simulation that this is indeed the case. The remaining vectors  $\mathbf{v}^1$ ,  $\mathbf{v}^3$  and  $\mathbf{v}^4$  are oriented with angles fluctuating between 0 and  $\pi$  with respect to  $\dot{\mathbf{\Gamma}}(t)$ . The Gram-Schmidt vectors behave very differently. Whereas the vector  $\mathbf{g}^1$  is identical to  $\mathbf{v}^1$ , the vector  $\mathbf{g}^2$  is not parallel to  $\dot{\mathbf{\Gamma}}(t)$ . Instead, the vectors  $\mathbf{g}^3$  and  $\mathbf{g}^4$  are perpendicular to  $\dot{\mathbf{\Gamma}}(t)$  as expected in view of the covariant subspaces of Eq. (5.10). These observations serve as convenient consistency checks for the numerical procedure.

One of the remarkable features of the covariant local Lyapunov exponents  $\Lambda^{\text{cov}}(\mathbf{\Gamma}(t))$  is their singular behavior transverse to the phase flow, whereas they are absolutely continuous in the direction of the flow. Fig. 5.8 provides an illuminating example. The singularities are consequences of bifurcations in the past history. Still, the local exponents are point functions in the phase space in the sense that one always gets the same value at the state point in question, as long as the trajectory has been followed from far enough back and has experienced the same history. Due to the uniqueness of the solutions of differential equations there is only this path to the state point in question. The global exponents, however, are time averages of the local exponents along an (ergodic) trajectory.

A final remark concerns the doubly-thermostated driven oscillator again. In a driven system (in our case a single particle in a non-homogenous thermal field) heat and, hence, entropy is generated, which needs to be compensated by a negative entropy production in the thermostat to achieve a stationary state. The excess heat is transferred from the system to the thermostat (by the positive friction  $zp > 0$ ), where it disappears. It follows from the thermostated motion equations in Sec. 5.5.1 that the external entropy production (of the reservoir) is given by

$$\dot{S}/k \equiv \frac{\partial}{\partial \mathbf{\Gamma}} \dot{\mathbf{\Gamma}} = z + x,$$



where  $k$  is the Boltzmann constant. In the non-equilibrium situation, a full time average  $\langle z + x \rangle$  is necessarily positive. However, we have verified by simulation that finite time averages of this quantity numerically obey the steady-state fluctuation theorem originally discovered by Evans, Cohen and Morriss [31]. This theorem was given a firm theoretical basis by Gallavotti and Cohen [32, 33], by invoking the so-called ‘chaotic hypothesis’ for Anosov-like systems. Although our system is not Anosov-like, it still obeys the theorem.

## 5.8 Acknowledgements

We gratefully acknowledge stimulating discussions with Francesco Ginelli, Josef Hofbauer, Gary Morriss, Antonio Politi, and Günter Radons. Our work was supported by the FWF (Austrian Science Fund) grant P 18798-N20.

## References

- [1] B.L. Holian, Wm.G. Hoover, and H.A. Posch, Phys. Rev. Lett. **59**, 10 (1987).
- [2] Wm.G. Hoover, *Time reversibility, computer simulation, and chaos* (World Scientific, Singapore, 1999).
- [3] H.A. Posch and Wm.G. Hoover, Journal of Physics: Conference Series **31**, 9, (2006).
- [4] V.I. Oseledec, Trudy Moskov. Mat. Obsc. **19**, 179, (1968). English transl. Trans. Moscow Math. Soc. **19**, 197 (1968).
- [5] D. Ruelle, Publ. Math. de l’IHÉS **50**, 27 (1979).
- [6] J.P. Eckmann and D. Ruelle, Rev. Mod. Phys. **57**, 617 (1985).
- [7] H. Bosetti and H.A. Posch, Chem. Phys. **375**, 296 (2010).
- [8] G. Benettin, L. Galgani, A. Giorgilli, and J.M. Strelcyn, Meccanica **15**, 21 (1980).
- [9] I. Shimada and T. Nagashima, Prog. Theor. Phys. **61**, 1605 (1979).
- [10] A. Wolf, J.B. Swift, H.L. Swinney, and J.A. Vastano, Physica D **16**, 285 (1985).
- [11] W.H. Press, S.A. Teukolsky, T. Vetterling, and B.P. Flannery, *Numerical Recipes in Fortran 77: The Art of Scientific Computing* (Cambridge University Press, 2nd ed., 1999).

- [12] F. Ginelli, P. Poggi, A. Turchi, H. Chaté, R. Livi, and A. Politi, Phys. Rev. Lett. **99**, 130601 (2007).
- [13] I. Goldhirsch, P.-L. Sulem, and S.A. Orszag, Physica D **27**, 311 (1987).
- [14] H.A. Posch and Wm.G. Hoover, Phys. Rev. A **38**, 473 (1988).
- [15] H.A. Posch and Wm.G. Hoover, Physica D **187**, 281 (2004).
- [16] H.A. Posch, Ch. Dellago, Wm.G. Hoover, and O. Kum, in *Pioneering Ideas for the Physical and Chemical Sciences: Josef Loschmidt's Contributions and Modern Developments in Structural Organic Chemistry, Atomistics, and Statistical Mechanics*, W. Fleischhacker and T. Schönfeld, eds., Plenum, New York, 1997; p. 233.
- [17] H.D. Meyer, J. Chem. Phys. **84**, 3147 (1986).
- [18] G.J. Martyna, M.L. Klein, and M. Tuckerman, J. Chem. Phys. **97**, 2635 (1992).
- [19] Wm.G. Hoover, H.A. Posch, and C.G. Hoover, J. Chem. Phys. **115**, 5744 (2001).
- [20] Wm.G. Hoover, C.G. Hoover, and H.A. Posch, Comp. Meth. in Science and Technology **7**, 55 (2001).
- [21] J.P. Eckmann, Ch. Forster, H.A. Posch, and E. Zabey, J. Stat. Phys. **118**, 813 (2005).
- [22] Y.A. Kuznetsov, *Elements of Applied Bifurcation Theory, Applied Mathematical Sciences*, vol. **112** (Springer-Verlag, NewYork, 2004).
- [23] P. Gaspard, Phys. Rev. E **53**, 4379 (1996).
- [24] P. Gaspard, *Chaos, Scattering and Statistical Mechanics* (Cambridge University Press, 1998) p. 308.
- [25] Ch. Dellago and Wm.G. Hoover, Physics Lett. A **268**, 220 (2000).
- [26] Wm.G. Hoover, C.G. Hoover, and H.A. Posch, Phys. Rev. A **41**, 2999 (1990).
- [27] Wm.G. Hoover, C.G. Hoover, and F. Grond, Comp. Meth. in Science and Technology **13**, 1180 (2008).
- [28] M. Hénon, Comm. Mathem. Phys. **50**, 69 (1976).
- [29] A.J. Lichtenberg and M.A. Lieberman, *Regular and Stochastic Motion*, (Springer-Verlag, New York, 1983).
- [30] R. Ramaswamy, Eur. Phys. J. B **29**, 339 (2002).

- [31] D.J. Evans, E.G.D. Cohen, and G.P. Morriss, Phys. Rev. Lett. **71**, 2401 (1993).
- [32] G. Gallavotti and E.G.D. Cohen, Phys. Rev. Lett. **74**, 2694 (1995).
- [33] G. Gallavotti and E.G.D. Cohen, J. Stat. Physics **80**, 931 (1995).



This chapter has already appeared in print with another title:

H.A. Posch and H. Bosetti,

*Covariant Lyapunov vectors and local exponents*,

American Institute of Physics, [Conf. Proc. vol. 1332](#), p. 230 (2011),

edited by P.L. Garrido, J. Marro,

and F. de los Santos.

## CHAPTER 6

# Symmetry properties of Lyapunov vectors and local exponents

Using a doubly-thermostated heat-conducting oscillator as an example, we demonstrate how time-reversal invariance affects the perturbation vectors in tangent space and the associated local Lyapunov exponents. We also find that the local covariant exponents vary discontinuously along directions transverse to the phase flow.

For classical chaotic systems, the set of Lyapunov exponents,  $\{\lambda_\ell\}, \ell = 1, \dots, D$ , measures the exponential growth, or decay, of small (infinitesimal) perturbations of the phase-space trajectory. Here,  $D$  is the dimension of the phase space. The standard algorithms for the computation of the exponents (see Chap. 5 and Ref. [1] for a review) probe the tangent-space dynamics by a set of orthonormal Gram-Schmidt (GS) vectors  $\{\mathbf{g}_\ell\}$ . Since their orthonormality is not preserved, it must be periodically restored by a GS procedure, or continuously kept up by Lagrange-multiplier constraints. These schemes are all based on the volume changes of  $d$ -dimensional volume elements in phase space,  $d \leq D$ , but they simultaneously destroy any information concerning the angles between the perturbation vectors. Thus, symmetries concerning phase-space volumes generate symmetries of the associated local GS Lyapunov exponents<sup>\*</sup>, whereas time-reversal symmetry does not. For example, for a phase-space conserving *symplectic system* the equalities  $(+)\Lambda_\ell^{GS}(t) = -(+)\Lambda_{D+1-\ell}^{GS}(t)$  and  $(-)\Lambda_\ell^{GS}(t) = -(-)\Lambda_{D+1-\ell}^{GS}(t)$  hold, if the trajectory is followed forward or backward in time as indicated by the upper indices  $(+)$  and  $(-)$ , respectively. However, time reversal invariance of the motion equations is not reflected by the GS local exponents:  $(-)\Lambda_\ell^{GS}(t) \neq -(+)\Lambda_{D+1-\ell}^{GS}(t)$ .

---

<sup>\*</sup>Local Lyapunov exponents give the local (time-dependent) exponential rate of growth (shrinkage) of the norm for GS or covariant vectors at a phase point  $\Gamma(t)$  along the trajectory. The global exponents are time averages of the local exponents.

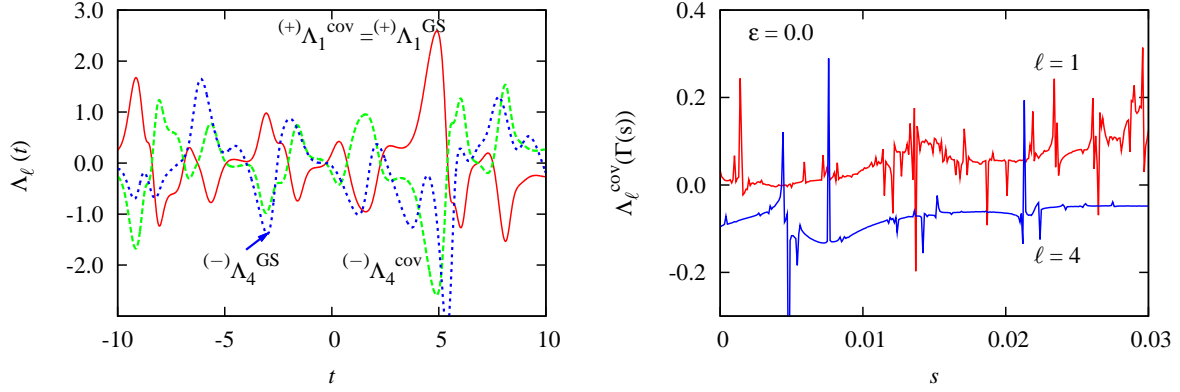


**Figure 6.1 :** Panel on the left: Time-dependent local Lyapunov exponents  $\Lambda(t)$  (as identified by the labels) for the doubly-thermostated oscillator in a non-equilibrium stationary state ( $\epsilon = 0.25$ ). Panel on the right: Fractal behavior of the local covariant exponents  $(+)\Lambda_i^{\text{cov}}$  for  $\ell \in \{1, 4\}$  along a parametric straight line transverse to the phase flow. The parameter  $s$  specifies the location  $\Gamma(s)$  in phase space. The data are for the doubly-thermostated oscillator in thermal equilibrium ( $\epsilon = 0$ ).

The multiplicative ergodic theorem of Oseledec [2, 3] asserts that there exists another spanning set of normalized vectors  $\mathbf{v}^\ell(\Gamma(0))$  in tangent space. These vectors evolve (co-rotate) with the natural tangent flow,  $\mathbf{v}^\ell(\Gamma(t)) = D\phi^t|_{\Gamma(0)} \mathbf{v}^\ell(\Gamma(0))$ , (where  $D\phi^t|_{\Gamma(0)}$  is the propagator), and directly generate the Lyapunov exponents,  $\pm\lambda_\ell = \lim_{t \rightarrow \pm\infty} (1/|t|) \ln \|D\phi^t|_{\Gamma(0)} \mathbf{v}^\ell(\Gamma(0))\|$ ,  $\ell \in \{1, \dots, D\}$ , along the way. They are referred to as covariant vectors. Generally, they are not pairwise orthogonal and span invariant manifolds, for which the local expansion (contraction) rates are given by the local covariant Lyapunov exponents  $(\pm)\Lambda_\ell^{\text{cov}}$ . In contrast to the GS exponents, they respect the time-reversal invariance of the motion equations, such that

$$(-)\Lambda_\ell^{\text{cov}}(\Gamma(t)) = -(+)\Lambda_{D+1-\ell}^{\text{cov}}(\Gamma(t)) ; \quad \ell = 1, \dots, D . \quad (6.1)$$

Local expansion forward in time implies local contraction backward in time and *vice versa*. However, they do not reflect (possible) phase-volume conservation.

Recently, reasonably efficient algorithms for the computation of covariant vectors have become available [4, 5], which were applied to a variety of systems [1, 6, 7]. In the panel on the left of the figure we demonstrate the time-reversal symmetry displayed by the local covariant exponents for a one-dimensional harmonic oscillator coupled to a position-dependent temperature  $T(q) = 1 + \varepsilon \tanh(q)$  with a two-stage Nosé-Hoover thermostat, which makes use of two thermostat variables [1]. The equations of motion are time reversible and not symplectic, and  $D = 4$ . The control parameter  $\varepsilon$  denotes the temperature gradient at the oscillator position  $q = 0$ . As the figure shows, the time-reversal symmetry of Eq. (6.1) is clearly obeyed for the maximum ( $\ell = 1$ ) and minimum ( $\ell = 4$ ) covariant exponents. Since, by construction,  $(+)\Lambda_1^{\text{GS}} \equiv (+)\Lambda_1^{\text{cov}}$  [1], one observes that no analogous relation holds for the GS exponents.

In the panel on the right of the figure it is demonstrated that the local covariant exponents show a fractal-like structure along a straight line transverse to the phase-space flow [1]. This is to be expected in view of the different past (and future) histories for trajectories passing through adjacent phase-space points transverse to the flow.

## References

- [1] H. Bosetti, H.A. Posch, Ch. Dellago, and Wm.G. Hoover, *Phys. Rev. E* **82**, 046218 (2010).
- [2] V.I. Oseledec, *Trudy Moskow. Mat. Obshch.* **19**, 179 (1968) [*Trans. Mosc. Math. Soc.* **19**, 197 (1968)].
- [3] D. Ruelle, *Publ. Math. de l'IHÉS* **50**, 27 (1979).
- [4] F. Ginelli, P. Poggi, A. Turchi, H. Chaté, R. Livi, and A. Politi, *Phys. Rev. Lett.* **99**, 130601 (2007).
- [5] C.L. Wolfe and R.M. Samelson, *Tellus* **59A**, 355 (2007).
- [6] H. Bosetti and H.A. Posch, *Chem. Phys.* **375**, 296 (2010).
- [7] M. Romero-Bastida, D. Pazó, J.M. López, and M.A. Rodríguez, *Phys.Rev. E* **82**, 036205 (2010).





## CHAPTER 7

# Domination and convergence of Lyapunov spectra for smooth-hard-disk systems

Let us consider the dynamics of smooth-hard-disk systems in the positive sense of time. The domination of the Oseledec splitting asserts that there exists a finite time  $t_s$ , from which on each Oseledec subspace – associated with an exponent  $\lambda^{(j)}$  – is uniformly more expanding than any subspace associated with a smaller Lyapunov exponent  $\lambda^{(i)}$  (i.e.,  $\forall i : i > j$ ). Therefore one obtains a Lyapunov spectrum – a plateau is only observed in the case of exponent degeneracies due to Lyapunov modes.

The mathematical definition of domination is based on the relative dynamical isolation of the Oseledec subspaces, and can also be expressed in terms of the fluctuations of the local Lyapunov exponents [1, 2] (see also Chap. 5). The Oseledec splitting is said to be dominated if these local Lyapunov exponents, when averaged over a finite time  $t_s$ , do not change their order in the spectrum for any time  $t > t_s$ . The local Lyapunov exponents and the Oseledec subspaces are computed with the algorithm of Ginelli et al. [3].

The domination of the Oseledec splitting (DOS) implies that the angles between the Oseledec subspaces are bounded away from zero [4]. Such a situation was experimentally shown to occur for coupled map lattices [1]. For rigid disk systems one also observes a strong correlation between the violation of the local order of the time-averaged Lyapunov exponent in the spectrum for short averaging times  $t$  and the relative deviation from orthogonality between Oseledec subspaces.

In order to specify the domination, we use two-dimensional smooth-hard-disk systems at a density  $\rho = 0.7$  in a box with periodic boundary conditions (in  $x$ - and  $y$ -directions) and with an aspect ratio  $L_y/L_x = 1$ . The number of particles varies,  $N \in \{9, 16, 25, 36, 100\}$ , for the different systems. As before, we consider reduced units for which the particle diameter  $\sigma$ , the particle mass

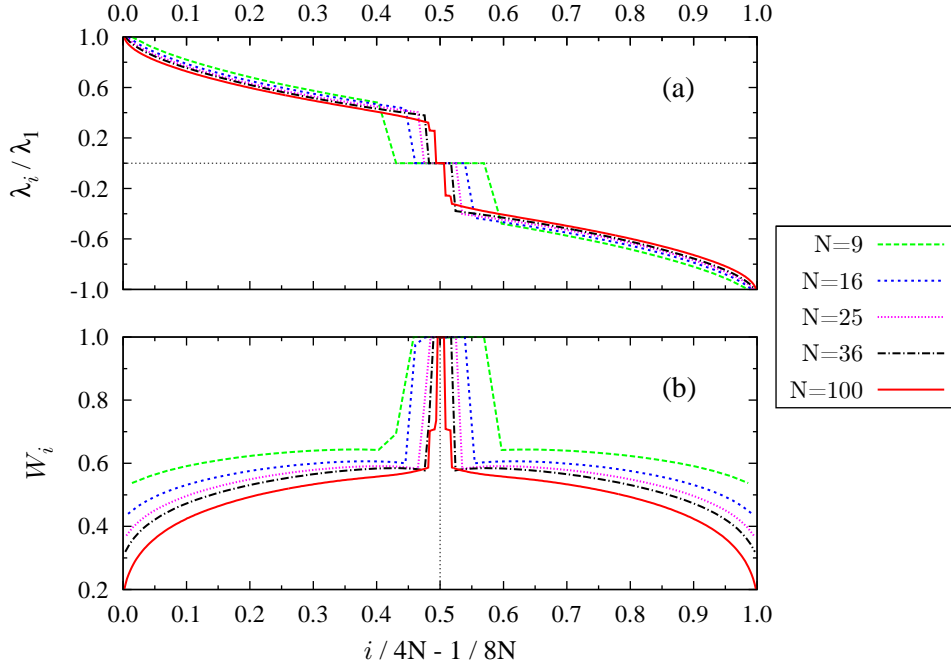


**Figure 7.1 :** The normalized Lyapunov spectra (a) and the localization spectra (b) are obtained with the covariant vectors for systems with various numbers of particles. Symmetrized reduced indices  $(i/4N - 1/8N)$  are used on the abscissa.

$m$  and the kinetic energy per particle  $K/N$  equal unity. Fig. 7.1 shows the normalized Lyapunov spectra (in the top panel) and the localization spectra (in the bottom panel) for all systems. Both sets of spectra are averages over a sufficiently long time to be considered converged. For the computation of these spectra covariant Lyapunov vectors were used (Chap. 3 and Ref. [5]). To compare spectra for various  $N$ , we use symmetrized reduced indices  $(i/4N - 1/8N)$ .

The Lyapunov spectra serve as a measure for chaos and as a reference, around which the local exponents fluctuate. Only the system with  $N = 100$  particles exhibits Lyapunov modes. Since the aspect ratio is unity, one obtains a mix of  $T(1, 0)$  and  $T(0, 1)$  belonging to the same smallest (positive and negative) Lyapunov exponents.

In the following we consider the local (time dependent) covariant Lyapunov exponents and average them over a finite time  $\mathcal{K}\tau$ ,

$$\overline{\Lambda}_i^{t=\mathcal{K}\tau} = \frac{1}{\mathcal{K}\tau} \sum_{k=0}^{\mathcal{K}-1} \ln \left\| D\phi_{\mathbf{\Gamma}_k \rightarrow \mathbf{\Gamma}_{k+1}}^{t_k \rightarrow t_{k+1}} \mathbf{v}_i(\mathbf{\Gamma}_k) \right\|, \quad (7.1)$$

for  $i = 1 \dots 4N$ , where the  $\mathbf{v}_i(\mathbf{\Gamma}_k)$  are the covariant vectors at the phase point  $\mathbf{\Gamma}_k$  at time  $t_k$ . The flow  $D\phi_{\mathbf{\Gamma}_k \rightarrow \mathbf{\Gamma}_{k+1}}^{t_k \rightarrow t_{k+1}}$  is the propagator, which maps the tangent bundle at  $\mathbf{\Gamma}_k \equiv \mathbf{\Gamma}(t_k)$  to  $\mathbf{\Gamma}_{k+1} \equiv \mathbf{\Gamma}(t_{k+1})$ . In practice,  $\tau$  corresponds to the time between two successive normalizations

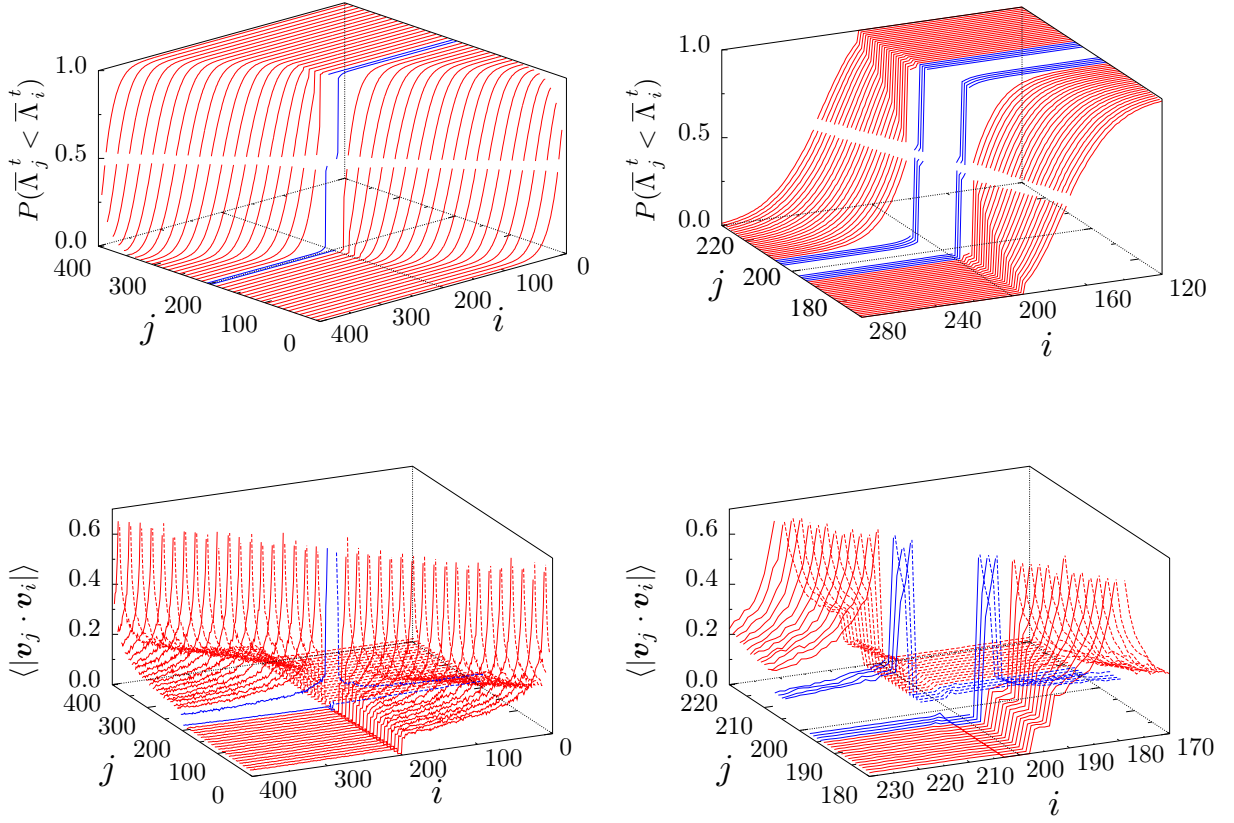


**Figure 7.2 :** Top-left panel: Domination probability  $P(\bar{\Lambda}_j^t < \bar{\Lambda}_{i \neq j}^t)$  for 100 smooth hard disks in a square box,  $\rho = 0.7$ . The averaging time  $t = 0.5$ . The blue lines are for  $j = 2N - 3$  and  $j = 2N + 4$  (corresponding to the smallest positive and negative exponents). Top-right panel: magnified view of the central region. The blue lines belong to the T(1,0) and T(0,1) modes. Bottom-left panel: Time averaged (400 events separated by 500 time units) absolute values for the scalar product of some covariant vectors  $\mathbf{v}_j$  with all the remaining covariant vectors  $\mathbf{v}_{i \neq j}$ . The blue lines are for  $j = 2N - 3$  and  $j = 2N + 4$ . Bottom-right panel: Magnified view of the central region of the bottom-left panel. The blue lines belong to the T(1,0) and T(0,1) modes.

of the covariant vector set. The global Lyapunov exponents correspond to the limit

$$\lambda_i = \lim_{\mathcal{K} \rightarrow \infty} \bar{\Lambda}_i^{t=\mathcal{K}\tau}. \quad (7.2)$$

We compute the probability  $P(\bar{\Lambda}_j^t < \bar{\Lambda}_i^t)$  for  $j \neq i$ , for an averaging time  $t$ . In the top-left panel of Fig. 7.2 this quantity is shown for some pairs  $(i, j)$  and for  $t = 0.5$ . The top-right panel provides a magnified view for all pairs  $(i, j)$  of the central region, which contains the mode regime, which is indicated by the blue lines. If the spectra were dominated without violation, the probabilities  $P(\bar{\Lambda}_j^t < \bar{\Lambda}_i^t)$  would consist of a plateau at 0 for  $j < i$  and a plateau at unity for  $j > i$ , with a sharp transition at  $i = j$ , for all large-enough  $t > t_c$ . Here,  $t_c > 0$  is some critical averaging time. Any violation for small  $t$  broadens the transition.

One observes that the transition is very sharp for the finite-time averaged local exponents belonging to the mode regime (which includes the central manifold), although the time  $t$  is rather short ( $t = 0.5$ ). This means that the local exponents in this central region are already at their proper positions in the spectrum. The fluctuations of the local exponents do not change their order any more. This is not the case for the exponents outside the mode regime, for which severe violations of the domination requirement still exist, leading to broad transitions of  $P(\bar{\Lambda}_j^t < \bar{\Lambda}_i^t)$ . Somewhat loosely we may say that the tangent space associated with the mode regime is rather well dominated as compared to the remainder of the tangent space.

The lines in the bottom panels of Fig. 7.2 depict the product norms  $\langle |\mathbf{v}_j \cdot \mathbf{v}_i| \rangle$  for the covariant vector  $\mathbf{v}_j$ ,  $j = 1, \dots, 4N$ , with all the other covariant vectors  $\mathbf{v}_i$ ,  $i \neq j$ . The bottom-right panel again provides a magnified view of the central region. Comparing the left-hand side of the top and the bottom panels, some correlations can be observed between the domination behavior, expressed by the probability  $P(\bar{\Lambda}_j^t < \bar{\Lambda}_i^t)$  (or the detailed violation probability), and the angles between covariant vectors with adjacent indices,  $|i - j| = 1, 2, \dots$ . This tendency is even more apparent for the right-hand sides of the top and the bottom panels. Note that the central manifold for such systems (smooth hard disks) is exactly orthogonal to the rest of the tangent space, and the subspaces associated with the modes (blue lines) are almost orthogonal to the rest of the tangent space. Most importantly, the local Lyapunov exponents associated with the unstable subspace (resp. with the stable subspace) never change their sign, the central manifold acts like a barrier which prevents exchanges between the stable and the unstable subspaces of the tangent space. This property of the hard-disk system does not hold in general. As we have demonstrated in Chapter 5 for the Hénon-Heiles system (Fig. 5.10), the local Lyapunov exponents fluctuate strongly such that  $\Lambda_1$  may become negative and  $\Lambda_4$  may become positive. The exponents may be strongly entangled, by which we mean that the instantaneous order of the exponents may be completely reversed as compared to the time-averaged global Lyapunov exponents.

Next we are interested in the convergence of the Lyapunov spectrum towards its long-time average. As a first step, another violation probability, called “partial”, is defined, which is the probability that for each index  $j$ , the associated local Lyapunov exponent  $\bar{\Lambda}_j^t$  is smaller than any other local exponent  $\bar{\Lambda}_i^t$ , for all  $j < i$ . In Fig. 7.3, this partial violation probability is shown for a system with 16 hard disks for various averaging times  $t$  ranging from 0.125 to 32. First of all, one notices that the smallest positive exponent for  $j = 2N - 3$ , and the last vanishing exponent for  $j = 2N + 3$ , never change position with one of the lower exponents, which confirms that there is no exchange across the central manifold: no interchanges are allowed between the local exponents for the stable subspace, the unstable subspace, and the central manifold. Secondly, one observes

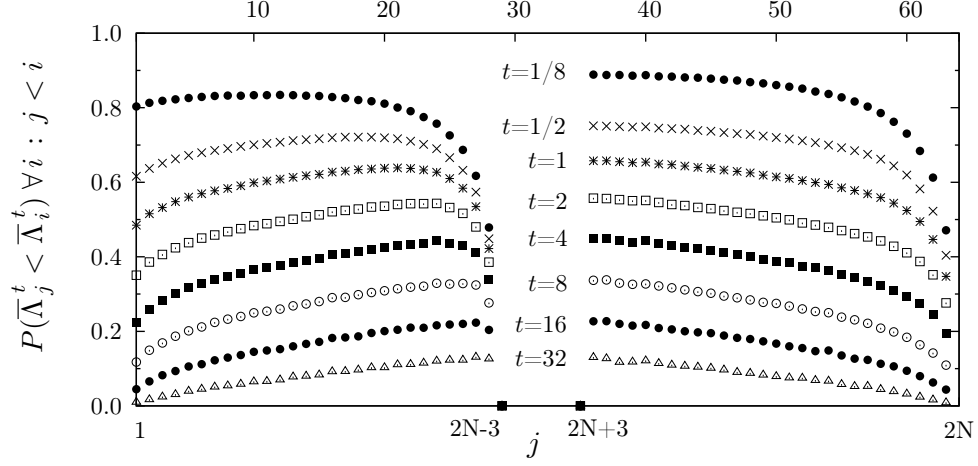


**Figure 7.3 :** Partial violation probability of the Lyapunov spectrum after different times for a system of 16 smooth hard disks.

regular smooth spectra for the various finite times considered. Finally, a slow convergence is obtained for increasing the averaging time  $t$ , but this representation is not detailed enough to give full account of the relaxation-time classification for the whole Lyapunov spectrum.

We introduce also a “total” violation probability, denoted  $\Pi(t)$ , namely the probability that at least one local Lyapunov exponent – when averaged over a time  $t > 0$  – changes the order of the local Lyapunov spectrum. The Oseledec splitting is said to be dominated, if the total violation probability converges toward zero for any time  $t$  larger than some finite time  $t_s$ .

The maximum Lyapunov exponent is the rate constant for the fastest growth of the phase-space perturbation, and depends on the binary collisions and on the velocities of the particles. It has been well established from pioneering work of Hoover, Posch and collaborators [6, 7, 8, 9, 10, 11, 12, 13] and others [14, 15, 16, 17, 18, 19], that the perturbation associated with the maximum Lyapunov exponent is strongly localized in physical space; such that non-vanishing perturbation components, which are significantly different from zero, are restricted to only few particles at any instant of time (see Chapter 3). Since there are no distinguished particles, the excited perturbed domain moves around in space, affecting succinctly all particles in a similar manner. We use this property to define a mixing process, that is concluded when, after a sufficiently long time, a large fraction of all particles has contributed to  $\lambda_1$ .

To describe this “mixing” in space, we define “cumulative particle contributions” to the perturbation  $\mathbf{v}^1 \equiv \mathbf{g}^1$  (note that the covariant and GS vectors agree in this case) by

$$\bar{\mu}_n^1(t = \mathcal{K} \tau) = \frac{1}{\mathcal{K} + 1} \sum_{k=0}^{\mathcal{K}} \left( \delta \vec{q}_n^1(t_0 + k \tau) \right)^2 + \left( \delta \vec{p}_n^1(t_0 + k \tau) \right)^2, \quad (7.3)$$

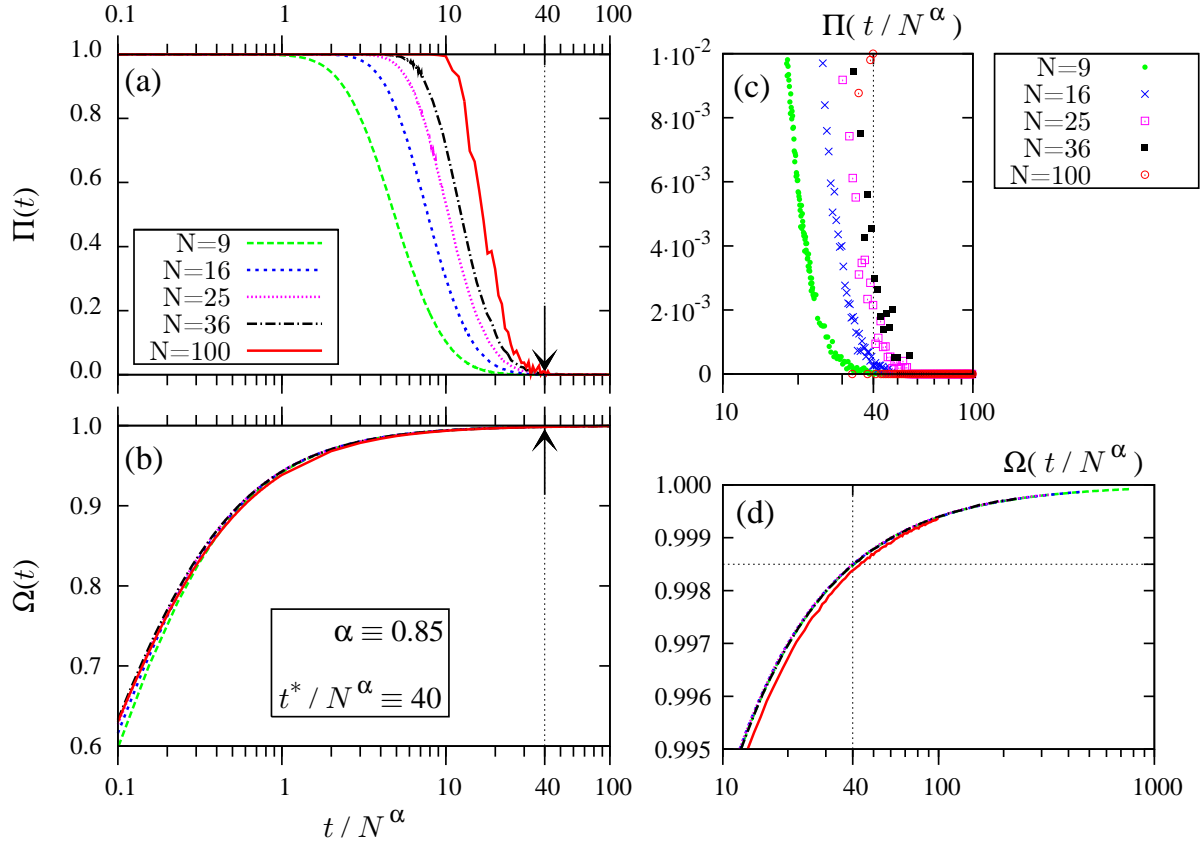


**Figure 7.4 :** The panels (a) and (b) show the total violation probability of the Lyapunov spectrum and the cumulative localization, respectively, as a function of  $t/N^\alpha$  (on a semi-log scale) for various  $N$ . The parameter  $\alpha = 0.85$  collapses all curves  $\Omega$  for various  $N$  onto a single curve. The panels on the right-hand side provide suitable magnifications.

( $\tau = 0.5$  is the time between successive Gram-Schmidt orthonormalization steps) which accumulates the contributions of the particle  $n$  over a time interval from  $t_0$  to  $t$ . For  $t \rightarrow \infty$  one has  $\mu_n^1(\infty) = 1/N$ , with each particle contributing identically. The quantity

$$\Omega(t = \mathcal{K} \tau) = \frac{1}{N} \exp \left\langle - \sum_{n=1}^N \bar{\mu}_n^1(t) \ln \bar{\mu}_n^1(t) \right\rangle_{t_0}, \quad (7.4)$$

measures the “cumulative delocalization” due to mixing. Clearly,  $\Omega(\infty) = 1$ . Here,  $\langle \rangle_{t_0}$  corresponds to the average over different starting times  $t_0$ . In practice, the starting times  $t_0$  are chosen to be separated by  $t = \mathcal{K} \tau$ .

At the initial time,  $t = 0$ , one has  $\Omega(0) = W_1$  (see Eq. 3.14 in Chapter 3). The system is spatially relaxed for cumulative localizations approaching one. We are especially interested in the convergence dynamics of the different systems (i.e., the appearances of the function  $\Omega(t)$ ) and in the time needed to consider them relaxed.

In the bottom-left panel of Fig. 7.4  $\Omega(t)$  is plotted as function of  $t/N^\alpha$ , where the scaling

parameter  $\alpha = 0.85$  is chosen such that all curves  $\Omega(t)$  for various  $N$  collapse onto a single curve. A magnification of the long-time behavior is shown in the bottom-right panel of Fig. 7.4. It is well known that the bigger the system the better is the localization of the perturbation for the maximum Lyapunov exponent [13]. Here find that the time scale for the localization to affect all particles increases with  $N^{0.85}$ , where  $N$  is the number of particles. For all practical purposes, after a time of  $t^* = 40N^{0.85}$  the local perturbation has moved around in the physical space such that  $\Omega(t)$  almost reaches unity. In the top panel of Fig. 7.4 the total violation probability  $\Pi(t)$  is plotted on the same time scale, where the top-right panel provides a magnification. One observes that  $\Pi(t)$  drops to zero for  $t \approx 40N^{0.85}$ . This shows that the violation of the spectral domination is lifted for time scales, which are connected to the speed with which the localized perturbation for  $\lambda_1$  moves around in the physical space. This time scale varies less than linearly with the number of particles.

## References

- [1] H.L. Yang and G. Radons, Phys. Rev. Lett. **100**, 024101 (2008).
- [2] H. Bosetti, H.A. Posch, Ch. Dellago, and Wm.G. Hoover, Phys. Rev. E **82**, 046218 (2010).
- [3] F. Ginelli, P. Poggi, A. Turchi, H. Chaté, R. Livi, and A. Politi, Phys. Rev. Lett. **99**, 130601 (2007).
- [4] J. Bochi and M. Viana, Ann. I. H. Poincaré **19**, 1 (2002).
- [5] H. Bosetti and H.A. Posch, Chem. Phys. **375**, 296 (2010).
- [6] Wm.G. Hoover, K. Boerker, and H.A. Posch, Phys. Rev. E **57**, 3911 (1998).
- [7] Lj. Milanović, H.A. Posch, and Wm.G. Hoover, Chaos **8**, 455 (1998).
- [8] Lj. Milanović, H.A. Posch, and Wm.G. Hoover, Mol. Phys. **95**, 281 (1998).
- [9] H.A. Posch and R. Hirschl, in *Hard Ball Systems and the Lorentz Gas*, Encyclopedia of Mathematical Sciences **vol. 101**, edited by D. Szász (Springer-Verlag, Berlin, 2000) p. 269.
- [10] Lj. Milanović and H.A. Posch, J. Mol. Liquids **96 - 97**, 221 (2002).
- [11] H.A. Posch and Ch. Forster, Lecture Notes on Computational Science – ICCS 2002, edited by P.M.A. Sloot, C.J.K. Tan, J.J.Dongarra, and A.G. Hoekstra (Springer-Verlag, Berlin, 2002) p. 1170.

- [12] Wm.G. Hoover, H.A. Posch, Ch. Forster, Ch. Dellago, and M. Zhou, J. Statist. Phys. **109**, 765 (2002).
- [13] Ch. Forster, R. Hirschl, H.A. Posch, and Wm.G. Hoover, Physica D **187**, 294 (2004).
- [14] P. Manneville, in *Macroscopic Modelling of Turbulent Flows*, Lecture Notes in Physics **vol. 230**, edited by Araki *et al.* (Springer-Verlag, New York, 1985) p. 319.
- [15] R. Livi and S. Ruffo, in Nonlinear Dynamics, edited by G. Turchetti (World Scientific, Singapore, 1989) p. 220.
- [16] M. Falcioni, U. M. B. Marconi, and A. Vulpiani, Phys. Rev. A **44**, 2263( 1991).
- [17] T. Taniguchi and G.P. Morriss, Phys. Rev E **68**, 026218 (2003).
- [18] T. Taniguchi and G.P. Morriss, Phys. Rev E **68**, 046203 (2003).
- [19] T. Taniguchi and G. P. Morriss, Phys. Rev. E **73**, 036208 (2006).



# CHAPTER 8

## How rotation breaks the Hamiltonian character of rough-hard-disk systems

### Contents

---

8.1	Introduction . . . . .	<b>157</b>
8.2	Tangent-bundle dynamics . . . . .	<b>158</b>
8.3	Systems of hard disks . . . . .	<b>159</b>
8.4	Covariant versus Gram-Schmidt vectors . . . . .	<b>166</b>
8.5	Null subspace and vanishing exponents for RHDS . . . . .	<b>174</b>
8.6	Transversality versus order violation in the local Lyapunov spectrum	<b>181</b>
8.7	The RHDS is not symplectic . . . . .	<b>184</b>
8.8	Appendix: Matrix formulation of the dynamics for SHDS . . . . .	<b>189</b>
	References . . . . .	<b>189</b>

---

### 8.1 Introduction

The Oseledec splitting can be experimentally determined by computing covariant vectors. In this chapter the covariant vectors and the Gram-Schmidt vectors are analyzed for rough-hard-disk systems (RHDS). These results are compared to respective results obtained for smooth-hard-disk systems (SHDS). We establish that the rotation of the disks deeply affects the Oseledec splitting of the tangent space. In particular, the rough-hard-disk systems are not strictly hyperbolic. We demonstrate that the rotations break the Hamiltonian character of rough-hard-disk systems.

The chapter is organized as follows. The basic concepts of the dynamics of the tangent-space

bundle are summarized in Sec. 8.2. The smooth-hard-disk system and, more thoroughly, the rough-hard-disk system are introduced in Sec. 8.3 where a matrix formulation of the system evolution is introduced. In Sec. 8.4, we compare the Gram-Schmidt vectors with the covariant Lyapunov vectors for the RHDS (which give rise to the same global Lyapunov exponents). The emphasis is on the angles between the spatial and momentum parts of the translation dynamics, on the localization of the tangent vectors in space, and on some tangent-space projections. We also show the spectra obtained for the SHDS in order to understand the transition from non-rotating (smooth) to rotating (rough) particles. The null subspace for the RHDS is the topic of Sec. 8.5, where we show that it is not strictly orthogonal to the unstable and stable subspaces. Using the covariant vector set, we show that the dynamics is converging to a sub-manifold. In Sec. 8.6 we examine the loss of isolation for the local covariant exponents, which implies that a finite-time average of local exponents may lead to a different order in the Lyapunov spectrum as compared to that of globally-averaged exponents. Furthermore, the transversality between the stable, the unstable, and the central manifolds is investigated for the SHDS and the RHDS. Sec. 8.7 is devoted to a discussion of the difference between the two models. In particular, it explains how the rotations break the Hamiltonian character for the RHDS.

## 8.2 Tangent-bundle dynamics

First we recall some basic notions in statistical mechanics and dynamical systems theory, e.g. [27, 28, 29]: (i) The concept of a phase space  $\mathbf{X}$  is tantamount to consider the full ensemble of accessible system states, denoted by the state vector  $\mathbf{\Gamma}$ . If this system is ergodic, which we assume, every infinitesimal volume element of the phase space in accord with the conserved quantities will be visited in due time. Each phase point  $\mathbf{\Gamma}$  on the hypersurface (defined by the exclusion of the subspace violating the conserved quantities) becomes equally likely; (ii) The dynamics in the phase space is characterized by the motion of a unique phase point in that space (with a fixed frame) which is not the case for the tangent space  $\mathbf{TX}_{\mathbf{\Gamma}}$ .  $\mathbf{TX}_{\mathbf{\Gamma}}$  moves with the state vector in phase space and is tangent to the hypersurface determined by the conserved quantities. It contains the complete set of perturbation vectors  $\{\delta\mathbf{\Gamma}_i\}$  which point in all accessible directions, where the state  $\mathbf{\Gamma}$  is allowed to evolve (observing the conservation rules); (iii) In order to examine also the dynamics of the perturbation vectors  $\delta\mathbf{\Gamma}$ , we have to consider the concept of the tangent bundle  $\mathbf{TX}$ , which consists of the union of the tangent spaces to  $\mathbf{X}$  at various state vectors  $\mathbf{\Gamma}$ ,  $\bigcup_{\mathbf{\Gamma} \in \mathbf{X}} \mathbf{TX}_{\mathbf{\Gamma}}$ . A point of  $\mathbf{TX}$  is a vector  $\delta\mathbf{\Gamma}$ , tangent to  $\mathbf{X}$  at some point  $\mathbf{\Gamma}(t)$ .

According to the *multiplicative ergodic theorem* of Oseledec for unstable systems [1], the dynamics of the tangent bundle induces some hierarchically dissociated sub-bundles. At some phase

point  $\Gamma$ , the sub-bundles correspond to an ensemble of dissociated subspaces, which is referred to as Oseledec splitting. The exponential growth (or decay) of the sub-bundles gives rise to the Lyapunov spectrum, whose hierarchical structure is reflected by the ordering of the exponents by size. Ginelli *et al.* [2] introduced an algorithm which permits to experimentally generate the Oseledec splitting by computing the covariant vectors  $\{\mathbf{v}_i\}$ . This method is based upon a theoretical statement, arising directly from assertions due to Ruelle [3] (see Eq. (3.7)) and to Ershov and Potapov [4] (see Eqs. (3.11) and (3.12)),

$$\mathbf{v}_i = \left( \mathbf{g}_1^{(+)} \oplus \cdots \oplus \mathbf{g}_i^{(+)} \right) \cap \left( \mathbf{g}_i^{(-)} \oplus \cdots \oplus \mathbf{g}_D^{(-)} \right), \quad (8.1)$$

where  $\{\mathbf{g}_i\}$  denotes the set of orthonormal Gram-Schmidt vectors. As usual,  $D$  is the phase space dimension. All of these vectors are associated with the same state vector  $\Gamma$ . The superscript “+” refers to the forward direction of time (i.e. the starting vector set  $\{\mathbf{g}_i^{(+)}\}$  was initially placed in the far past), whereas the superscript “−” refers to the backward direction of time (i.e. the starting vector set  $\{\mathbf{g}_i^{(-)}\}$  was initially placed in the far future).

Let  $\Gamma(t)$  denote the state of the system at time  $t$ . The flow in phase space is denoted by  $\phi^t : \mathbf{X} \rightarrow \mathbf{X}$  and the corresponding flow in tangent space by  $D\phi^t : \mathbf{TX}_{\Gamma(0)} \rightarrow \mathbf{TX}_{\Gamma(t)}$ . Then the covariant vectors  $\{\mathbf{v}_i\}$  obey

$$D\phi^t|_{\Gamma(0)} \mathbf{v}_i(\Gamma(0)) = \mathbf{v}_i(\Gamma(t))$$

for all  $i \in \{1, \dots, D\}$ , where  $\Gamma(t) = \phi^t(\Gamma(0))$ . The corresponding (global) Lyapunov exponents are time averages,

$$\lim_{t \rightarrow \pm\infty} \frac{1}{|t|} \log \| D\phi^t|_{\Gamma(0)} \mathbf{v}_i(\Gamma(0)) \| = \pm\lambda_i,$$

and due to the dynamical hierarchy, they obey:  $\lambda_1 \geq \cdots \geq \lambda_D$ .

### 8.3 Systems of hard disks

We now turn our attention to the smooth-hard-disk system (SHDS) and the rough-hard-disk system (RHDS). Due to roughness, the disks may temporarily store energy in internal degrees of freedom (rotation). The disks suffer elastic hard collisions and move along straight lines in between collisions. The systems consist of  $N$  particles at a density  $\rho$  in a box of dimension  $(L_x, L_y)$  with periodic boundaries in the  $x$ - and  $y$ -directions. As usual, we consider reduced units for which the particle diameter  $\sigma$ , the particle mass  $m$  and the kinetic energy per particle,  $K/N$ , are unity. Here,  $K$  is the total energy, which is purely kinetic. Lyapunov exponents are given in units of  $\sqrt{K/Nm\sigma^2}$ . The Lyapunov instability of SHDS has been studied in detail in

the past [5, 6, 7, 8, 9], whereas for the RHDS it has been studied only recently [10].

For the SHDS, the state vector is given by

$$\mathbf{\Gamma} = \{\vec{q}_n, \vec{p}_n\}_{n=1}^N, \quad (8.2)$$

where  $\vec{q}_n$  and  $\vec{p}_n$  denote the position and momentum vectors of particle  $n$ . For the RHDS, the state vector is given by

$$\mathbf{\Gamma} = \{\vec{q}_n, \vec{p}_n, \omega_n\}_{n=1}^N, \quad (8.3)$$

where  $\omega_n$  is the angular velocity of particle  $n$ . The orientation angles of the disks are not required for the equations of motion and are not included in the list of independent variables. This means that the Lagrangian of the system does not depend on the orientation of the particles. We shall come back to this point in Sec. 8.5. An arbitrary perturbation vector is given by

$$\delta\mathbf{\Gamma} = \{\delta\vec{q}_n, \delta\vec{p}_n\}_{n=1}^N, \quad (8.4)$$

$$\text{and } \delta\mathbf{\Gamma} = \{\delta\vec{q}_n, \delta\vec{p}_n, \delta\omega_n\}_{n=1}^N, \quad (8.5)$$

for the SHDS and the RHDS, respectively.

### 8.3.1 The rough-hard-disk system (RHDS)

The RHDS is an extension of the common SHDS, where the particles rotate and exchange translational and rotational energy at a collision. This implies a coupling between translational and rotational degrees of freedom. The “rough-hard-collision” transformation rule is established from the conservation laws for energy, linear momentum, and angular momentum. A first version of the RHDS was already introduced in the late 19<sup>th</sup> century by Bryan [11]. Explicit motion equations were given by Chapman and Cowling [12] in 1939. Initially, roughness was introduced as the maximum possible roughness in the model, where a collision reverses the relative surface velocity at the point of contact of two colliding particles. Such a model was thoroughly studied by O’Dell and Berne [13]. Subsequently, Berne and Pangali also investigated models with partial roughness [14, 15]. Here we use the maximum-roughness model of Chapman and Cowling [12].

The energy of the RHDS is purely kinetic,

$$K = \frac{1}{2} \sum_{n=1}^N \left[ \frac{(\vec{p}_n)^2}{m} + I(\omega_n)^2 \right],$$

where  $I$  is the moment of inertia, which is taken to be identical for all disks.

We first recall the collision rules for two rough hard spheres  $k$  and  $\ell$  in three dimensions [12, 10]. Let  $\vec{q} = \vec{q}_k - \vec{q}_\ell$  and  $\delta\vec{q} = \delta\vec{q}_k - \delta\vec{q}_\ell$  denote the respective relative positions in the phase space and in the tangent space, and analogously,  $\vec{p} = \vec{p}_k - \vec{p}_\ell$  and  $\delta\vec{p} = \delta\vec{p}_k - \delta\vec{p}_\ell$  the relative momenta. For convenience, we define the following quantities:  $\vec{\Omega} = \vec{\omega}_k + \vec{\omega}_\ell$ ,  $\delta\vec{\Omega} = \delta\vec{\omega}_k + \delta\vec{\omega}_\ell$ , the unit vector  $\vec{n} = \vec{q}/\sigma$ , the dimensionless moment of inertia  $\kappa = 4I/m\sigma^2$ , and the velocity of the impact point on the surface of the scatterer,

$$\vec{g} = \frac{\vec{p}}{m} + \frac{\sigma}{2} (\vec{n} \times \vec{\Omega}) .$$

During a collision, only the components associated with the colliding particles  $k$  and  $\ell$  of the vector  $\mathbf{\Gamma}$  change [10],

$$\begin{aligned} \vec{q}'_k &= \vec{q}_k , \\ \vec{q}'_\ell &= \vec{q}_\ell , \\ \vec{p}'_k &= \vec{p}_k - m\gamma \vec{g} - \beta(\vec{n} \cdot \vec{p}) \vec{n} , \\ \vec{p}'_\ell &= \vec{p}_\ell + m\gamma \vec{g} + \beta(\vec{n} \cdot \vec{p}) \vec{n} , \\ \vec{\omega}'_k &= \vec{\omega}_k + \frac{2\beta}{\sigma} (\vec{n} \times \vec{g}) , \\ \vec{\omega}'_\ell &= \vec{\omega}_\ell + \frac{2\beta}{\sigma} (\vec{n} \times \vec{g}) , \end{aligned} \tag{8.6}$$

where the prime, here and below, refers to the state immediately after the collision. The constant parameters  $\gamma = \kappa/(1 + \kappa)$  and  $\beta = 1/(1 + \kappa)$  control the coupling between translational and rotational degrees of freedom. If the moment of inertia vanishes ( $\kappa \rightarrow 0$  and  $\beta \rightarrow 0$ ) the translational and rotational degrees of freedom decouple.

Using the general equation, Eq. (11) in the Introduction, the linearization of the collision map (8.6) yields the collision map for the perturbation vectors  $\delta\mathbf{\Gamma}$  [10],

$$\begin{aligned} \delta\vec{q}'_k &= \delta\vec{q}_k + \left[ \gamma\vec{g} + \frac{\beta}{m}(\vec{n} \cdot \vec{p})\vec{n} \right] \delta\tau_c , \\ \delta\vec{q}'_\ell &= \delta\vec{q}_\ell - \left[ \gamma\vec{g} + \frac{\beta}{m}(\vec{n} \cdot \vec{p})\vec{n} \right] \delta\tau_c , \\ \delta\vec{p}'_k &= \delta\vec{p}_k - m\gamma\delta\vec{g}_c - \frac{\beta}{\sigma} [(\delta\vec{q}_c \cdot \vec{p})\vec{n} + \sigma(\vec{n} \cdot \delta\vec{p})\vec{n} + (\vec{n} \cdot \vec{p})\delta\vec{q}_c] , \\ \delta\vec{p}'_\ell &= \delta\vec{p}_\ell + m\gamma\delta\vec{g}_c + \frac{\beta}{\sigma} [(\delta\vec{q}_c \cdot \vec{p})\vec{n} + \sigma(\vec{n} \cdot \delta\vec{p})\vec{n} + (\vec{n} \cdot \vec{p})\delta\vec{q}_c] , \\ \delta\vec{\omega}'_k &= \delta\vec{\omega}_k + \frac{2\beta}{\sigma^2} [\delta\vec{q}_c \times \vec{g} + \sigma(\vec{n} \times \delta\vec{g}_c)] , \\ \delta\vec{\omega}'_\ell &= \delta\vec{\omega}_\ell + \frac{2\beta}{\sigma^2} [\delta\vec{q}_c \times \vec{g} + \sigma(\vec{n} \times \delta\vec{g}_c)] , \end{aligned} \tag{8.7}$$

where  $\delta\tau_c = -(\delta\vec{q} \cdot \vec{n})/(\vec{p} \cdot \vec{n})$  is the infinitesimal time shift between the collision of the reference and the perturbed trajectories, and  $\delta\vec{q}_c = \delta\vec{q} + \delta\tau_c \vec{p}/m$  corresponds to the shift (in configuration space) between the collision points of the reference and of the satellite trajectories. Furthermore,

$$\delta\vec{g}_c = \frac{\delta\vec{p}}{m} + \frac{1}{2} \left[ \delta\vec{q}_c \times \vec{\Omega} + \sigma(\vec{n} \times \delta\vec{\Omega}) \right] .$$

The three-dimensional maps (8.6) and (8.7) remain valid for the case of planar rough disks. In this case all position and velocity vectors are placed in the  $xy$ -plane, and all angular velocity vectors are perpendicular to this plane with a single non-vanishing  $z$ -component (denoted  $\omega_i$  for disk  $i$ ) [10]. Analogous definitions apply to the perturbation vectors.

Since the angular positions do not play any role in the dynamics, they are omitted from the list of independent variables in Eq. (8.3): If the number of particles is odd, the phase-space dimension  $D$  is also odd ( $5N$ ). If the boundaries are periodic in  $x$  and  $y$ , also the number of vanishing exponents is an odd integer. Since for symplectic systems the conjugate pairing rule applies [9], the number of vanishing Lyapunov exponents should be even. The appearance of an odd number of vanishing exponents indicates that the RHDS is not symplectic. This finding will be confirmed below both numerically and by analytic computation. We shall come back to the question of the number of vanishing Lyapunov exponents in Sec. 8.5. For the time being, the number of particles,  $N$ , is chosen an even number.

If the angular positions do not play any role in the dynamics whereas the angular velocities do, a paradox would appear if the system were Hamiltonian. The symplectic structure could not be satisfied, since the dimension of the phase space is required to be even in order to satisfy the differential 2-form: the angular velocities would not be counterbalanced by their associated coordinates, the angular positions. In summary, for the RHDS it can be said that either the angular velocities do not influence the dynamics at all, or the system is not Hamiltonian. We show below that the latter is true.

### 8.3.2 Matrix formulation of the dynamics for RHDS

#### A: The orientations of the rough disks are excluded

A matrix formulation of the collision maps for the phase- and tangent-space dynamics of Eqs. (8.6) and (8.7) is given next. For the case of the SHDS, such a procedure was suggested already in Ref. [16] by de Wijn and van Beijeren, and similarly in Ref. [17]. We assume that the components of the vectors associated with an individual particle  $n$  are arranged following

a specific order: the position, the translational momentum, and the angular velocity. They are denoted by

$$\mathbf{\Gamma}_n^\dagger(\vec{q}_n^\dagger, \vec{p}_n^\dagger, \omega_n) \quad \text{and} \quad \delta\mathbf{\Gamma}_n^\dagger(\delta\vec{q}_n^\dagger, \delta\vec{p}_n^\dagger, \delta\omega_n) ,$$

in the phase space and the tangent space, respectively. The superscript  $\dagger$  means transposition. In order to simplify the notation, we write down only the rows and columns of the matrices associated with the two colliding particles  $k$  and  $\ell$  arranged such that  $k$  and  $\ell$  are successive indices:

$$\mathbf{\Gamma}^\dagger \equiv (\dots, \mathbf{\Gamma}_k^\dagger, \mathbf{\Gamma}_\ell^\dagger, \dots) \quad \text{and} \quad \delta\mathbf{\Gamma}^\dagger \equiv (\dots, \delta\mathbf{\Gamma}_k^\dagger, \delta\mathbf{\Gamma}_\ell^\dagger, \dots) . \quad (8.8)$$

The time evolution consists in a succession of free flights, interrupted by binary collisions between particles. Let the matrix  $\mathcal{Z}(\tau)$  describe the propagator for the smooth streaming of the whole system between two successive collisions separated by a time interval  $\tau$ . It corresponds to a  $N \times N$  - block diagonal matrix, where each block on the diagonal is a  $5 \times 5$  - dimensional matrix defined as

$$\mathcal{Z}_n(\tau) = \begin{pmatrix} 1 & 0 & \tau & 0 & 0 \\ 0 & 1 & 0 & \tau & 0 \\ 0 & 0 & 1 & 0 & 0 \\ 0 & 0 & 0 & 1 & 0 \\ 0 & 0 & 0 & 0 & 1 \end{pmatrix} .$$

The matrix  $\mathcal{Z}(\tau)$  acts both on  $\mathbf{\Gamma}$  and on  $\delta\mathbf{\Gamma}$ . Let the discrete maps  $\mathcal{M}$  and  $\mathcal{S}$  govern the transformation at each collision for the phase and tangent space, respectively. They are also block diagonal matrices, and because of Eq. (8.8) yield

$$\mathcal{M} = \left( \begin{array}{c|c|c} \mathbf{I} & 0 & 0 \\ \hline 0 & \mathcal{M}_{k\ell} & 0 \\ \hline 0 & 0 & \mathbf{I} \end{array} \right) \quad \text{and} \quad \mathcal{S} = \left( \begin{array}{c|c|c} \mathbf{I} & 0 & 0 \\ \hline 0 & \mathcal{S}_{k\ell} & 0 \\ \hline 0 & 0 & \mathbf{I} \end{array} \right) .$$

The dynamics of the vectors  $\mathbf{\Gamma}$  and  $\delta\mathbf{\Gamma}$ , after  $n$  collisions, follows from

$$\begin{aligned} \mathbf{\Gamma}(t = \tau_\zeta + \dots + \tau_0) &= \mathcal{Z}(\tau_\zeta) \mathcal{M} \mathcal{Z}(\tau_{\zeta-1}) \dots \mathcal{M} \mathcal{Z}(\tau_1) \mathcal{M} \mathcal{Z}(\tau_0) \mathbf{\Gamma}(0) , \\ \delta\mathbf{\Gamma}(t = \tau_\zeta + \dots + \tau_0) &= \mathcal{Z}(\tau_\zeta) \mathcal{S} \mathcal{Z}(\tau_{\zeta-1}) \dots \mathcal{S} \mathcal{Z}(\tau_1) \mathcal{S} \mathcal{Z}(\tau_0) \delta\mathbf{\Gamma}(0) , \end{aligned}$$

where the  $\tau_i$  are time intervals between successive collisions.

With the notation suggested by Eq. (8.8), the collision matrix in phase space becomes (see

Eq. (8.6)):

$$\mathcal{M}_{k\ell} = \begin{pmatrix} \mathcal{I} & \mathbf{O} & \vec{0} & \mathbf{O} & \mathbf{O} & \vec{0} \\ \mathbf{O} & \mathcal{I} - \mathcal{A} & -\vec{a} & \mathbf{O} & \mathcal{A} & -\vec{a} \\ \vec{0}^\dagger & -\vec{b}^\dagger & 1 - \beta & \vec{0}^\dagger & -\vec{b}^\dagger & -\beta \\ \mathbf{O} & \mathbf{O} & \vec{0} & \mathcal{I} & \mathbf{O} & \vec{0} \\ \mathbf{O} & \mathcal{A} & \vec{a} & \mathbf{O} & \mathcal{I} - \mathcal{A} & \vec{a} \\ \vec{0}^\dagger & -\vec{b}^\dagger & -\beta & \vec{0}^\dagger & -\vec{b}^\dagger & 1 - \beta \end{pmatrix}, \quad (8.9)$$

where  $\mathcal{I}$  and  $\mathbf{O}$  are the  $2 \times 2$  identity and null matrices, respectively, and

$$\mathcal{A} = \gamma \mathcal{I} + \beta \vec{n} \vec{n}^\dagger, \quad \vec{a} = \frac{\sigma}{2} m \gamma \vec{t} \quad \text{and} \quad \vec{b}^\dagger = \frac{2}{m \sigma} \beta \vec{t}^\dagger.$$

$\vec{n}$  and  $\vec{t}$  are the respective normal and tangent vectors at the impact point of the collision between the particles referred to with indices  $k$  and  $\ell$ . They are defined conventionally as  $\vec{n} = (\vec{q}_k - \vec{q}_\ell)/\sigma$  and  $\vec{t} = D^{\pi/2} \vec{n}$ , where the matrix  $D^{\pi/2}$  refers to a rotation by an angle  $\pi/2$  in the anti-clockwise direction. The linearized collision map in the tangent space follows in an analogous way (see Eq. (8.7)):

$$\mathcal{S}_{k\ell} = \begin{pmatrix} \mathcal{I} - \mathcal{B} & \mathbf{O} & \vec{0} & \mathcal{B} & \mathbf{O} & \vec{0} \\ -\mathcal{C} & \mathcal{I} - \mathcal{A} & -\vec{a} & \mathcal{C} & \mathcal{A} & -\vec{a} \\ \vec{c}^\dagger & -\vec{b}^\dagger & 1 - \beta & -\vec{c}^\dagger & \vec{b}^\dagger & -\beta \\ \mathcal{B} & \mathbf{O} & \vec{0} & \mathcal{I} - \mathcal{B} & \mathbf{O} & \vec{0} \\ \mathcal{C} & \mathcal{A} & \vec{a} & -\mathcal{C} & \mathcal{I} - \mathcal{A} & \vec{a} \\ \vec{c}^\dagger & -\vec{b}^\dagger & -\beta & -\vec{c}^\dagger & \vec{b}^\dagger & 1 - \beta \end{pmatrix}, \quad (8.10)$$

where  $\vec{p} = \vec{p}_k - \vec{p}_\ell$  and  $\vec{p}_\perp = D^{\pi/2} \vec{p}$ , and

$$\begin{aligned} \vec{c}^\dagger &= \frac{2}{m \sigma^2} \beta \vec{p}_\perp^\dagger, \\ \mathcal{B} &= \frac{\gamma}{\vec{n} \cdot \vec{p}} \left( \vec{p} - \frac{\sigma}{2m} \Omega \vec{t} \right) \vec{n}^\dagger + \beta \vec{n} \vec{n}^\dagger, \\ \mathcal{C} &= -\frac{m \gamma \Omega}{2} \left( D^{\pi/2} - \frac{\vec{p}_\perp \vec{n}^\dagger}{\vec{n} \cdot \vec{p}} \right) + \frac{\beta \vec{n} \cdot \vec{p}}{\sigma} \left( \mathcal{I} + \frac{\vec{n} \vec{p}^\dagger}{\vec{n} \cdot \vec{p}} \right) \left( \mathcal{I} - \frac{\vec{p} \vec{n}^\dagger}{\vec{n} \cdot \vec{p}} \right). \end{aligned}$$

After some laborious computation, we find that the determinants for the matrix transformations  $\mathcal{M}$  and  $\mathcal{S}$  are equal to unity,

$$\det(\mathcal{M}) \equiv \det(\mathcal{M}_{k\ell}) = 1 \quad \text{and} \quad \det(\mathcal{S}) \equiv \det(\mathcal{S}_{k\ell}) = 1.$$

These relations are equivalent to saying that the collisions are phase-volume conserving. This is a necessary but not sufficient condition to qualify the transformations as symplectic. These considerations will be discussed in detail in Sec. 8.7. In the Appendix (Sec. 8.8), the matrix transformation rules for the smooth-hard-disk model are shown. They are directly recovered from



the rough-hard-disk model for  $\kappa = 0$ , if the angular-velocities are discarded altogether.

The equations in this section are used in the following to construct the time evolution of the perturbation vectors, both the Gram-Schmidt and covariant vectors, and the respective time-dependent local Lyapunov exponents. The global exponents are obtained by a time average along a long trajectory.

### B: The orientations of the rough disks are explicitly included

For completeness we give here the collision matrices in the phase and tangent spaces, when the disk orientations  $\theta_n$  are explicitly included. The respective components of the state and perturbed vectors associated with an individual particle  $n$  are arranged as

$$\mathbf{\Gamma}_n^\dagger(\vec{q}_n^\dagger, \vec{p}_n^\dagger, \omega_n, \theta_n) \quad \text{and} \quad \delta\mathbf{\Gamma}_n^\dagger(\delta\vec{q}_n^\dagger, \delta\vec{p}_n^\dagger, \delta\omega_n, \delta\theta_n) .$$

With the notation suggested by Eq. (8.8), the collision matrix in phase space becomes:

$$\mathcal{M}_{k\ell} = \begin{pmatrix} \mathcal{I} & \mathbf{O} & \vec{0} & \vec{0} & \mathbf{O} & \mathbf{O} & \vec{0} & \vec{0} \\ \mathbf{O} & \mathcal{I} - \mathcal{A} & -\vec{a} & \vec{0} & \mathbf{O} & \mathcal{A} & -\vec{a} & \vec{0} \\ \vec{0}^\dagger & -\vec{b}^\dagger & 1 - \beta & 0 & \vec{0}^\dagger & -\vec{b}^\dagger & -\beta & 0 \\ \vec{0}^\dagger & \vec{0}^\dagger & 0 & 1 & \vec{0}^\dagger & \vec{0}^\dagger & 0 & 0 \\ \mathbf{O} & \mathbf{O} & \vec{0} & \vec{0} & \mathcal{I} & \mathbf{O} & \vec{0} & \vec{0} \\ \mathbf{O} & \mathcal{A} & \vec{a} & \vec{0} & \mathbf{O} & \mathcal{I} - \mathcal{A} & \vec{a} & \vec{0} \\ \vec{0}^\dagger & -\vec{b}^\dagger & -\beta & 0 & \vec{0}^\dagger & -\vec{b}^\dagger & 1 - \beta & 0 \\ \vec{0}^\dagger & \vec{0}^\dagger & 0 & 0 & \vec{0}^\dagger & \vec{0}^\dagger & 0 & 1 \end{pmatrix} . \quad (8.11)$$

The linearized collision map in the tangent space assumes the form (see Eqs. (8.7) and (8.13)):

$$\mathcal{S}_{k\ell} = \begin{pmatrix} \mathcal{I} - \mathcal{B} & \mathbf{O} & \vec{0} & \vec{0} & \mathcal{B} & \mathbf{O} & \vec{0} & \vec{0} \\ -\mathcal{C} & \mathcal{I} - \mathcal{A} & -\vec{a} & \vec{0} & \mathcal{C} & \mathcal{A} & -\vec{a} & \vec{0} \\ \vec{c}^\dagger & -\vec{b}^\dagger & 1 - \beta & 0 & -\vec{c}^\dagger & \vec{b}^\dagger & -\beta & 0 \\ \vec{h}^\dagger & \vec{0}^\dagger & 0 & 1 & -\vec{h}^\dagger & \vec{0}^\dagger & 0 & 0 \\ \mathcal{B} & \mathbf{O} & \vec{0} & \vec{0} & \mathcal{I} - \mathcal{B} & \mathbf{O} & \vec{0} & \vec{0} \\ \mathcal{C} & \mathcal{A} & \vec{a} & \vec{0} & -\mathcal{C} & \mathcal{I} - \mathcal{A} & \vec{a} & \vec{0} \\ \vec{c}^\dagger & -\vec{b}^\dagger & -\beta & 0 & -\vec{c}^\dagger & \vec{b}^\dagger & 1 - \beta & 0 \\ \vec{h}^\dagger & \vec{0}^\dagger & 0 & 0 & -\vec{h}^\dagger & \vec{0}^\dagger & 0 & 1 \end{pmatrix} , \quad (8.12)$$

where  $\vec{h}^\dagger = \frac{2\beta}{\sigma} \left( \frac{\vec{t} \cdot \vec{p}}{m} - \frac{\sigma}{2} \Omega \right) \frac{\vec{n}^\dagger}{\vec{n} \cdot \vec{p}} .$

## 8.4 Covariant versus Gram-Schmidt vectors

We consider two-dimensional fluid-like systems consisting of  $N = 88$  hard disks at a density  $\rho = 0.7$ . The box with periodic boundary conditions has an aspect ratio  $A = 2/11$ , the same value as in our previous work on smooth hard disks (Chap. 3 and Ref. [18]), to facilitate comparison.

For the computation of the covariant vectors according to the algorithm of Ginelli *et al.* [2, 18, 19] the system was first relaxed forward in time for  $t_r = 10^5 \tau$  time units. Then, the Gram-Schmidt vectors were stored for  $t_s = 5 \cdot 10^4 \tau$  time units. Finally, the system was iterated backward in time, and covariant vectors were computed for times in the interval  $[t_r, t_r + 0.9 t_s]$ . Here,  $\tau = 0.6$  is the time difference between two successive Gram-Schmidt re-orthonormalization steps.

For  $\kappa > 0$  (three degrees of freedom per particle), the energy per particle is taken 1.5 in our reduced units. For  $\kappa = 0$  (two degrees of freedom per particle), the energy per particle is set to unity. With this choice, a comparison between the SHDS and RHDS is meaningful.

Fig. 8.1 shows the Lyapunov spectra computed with the covariant vectors for the RHDS with various values of the coupling parameter  $\kappa \in \{0, 0.1, 0.2, 0.4, 1\}$ . Fig. 8.2 shows an enlargement of the central part of these spectra. Conjugate exponent pairs are plotted with the same index  $i$  on the abscissa, where now  $i \in \{1, \dots, 5N/2\}$ . The open symbols are computed from the GS vectors in the forward direction of time, the full ones from the covariant vectors during the time-reversed iteration. Considering the size of the system ( $N = 88$ ), the agreement is excellent. The figure clearly displays the conjugate pairing symmetry  $\lambda_i = \lambda_{5N+1-i}$  expected for time reversible energy-conserving systems.

For  $\kappa > 0$  and periodic boundaries in both  $x$ - and  $y$ -directions (as is the case for the Figs. 8.1 and 8.2), there are 6 vanishing exponents, if the number  $N$  of particles is even. If this number is odd, there are 7 vanishing exponents, which is a consequence of the conjugate pairing symmetry and the fact that the phase-space dimension is odd as well ( $5N$ ), since the particle orientations do not contribute. We shall come back to this point in Sec. 8.5. However, for  $\kappa = 0$ , one obtains  $N$  additional vanishing Lyapunov exponents due to the  $N$  angular-disk velocities  $\{\omega_n\}_{n=1}^N$ , which are invariants of the system in this case. The discussion of the vanishing Lyapunov exponents is postponed to Sec. 8.5.

We can see in Fig. 8.2 the influence exerted by the moment of inertia  $I$  on the spectra. For  $I = 0$  corresponding to  $\kappa = 0$ , the steps in the spectrum due to degenerate exponents is a clear indication for the presence of Lyapunov modes. According to the classification in [20], the steps with a

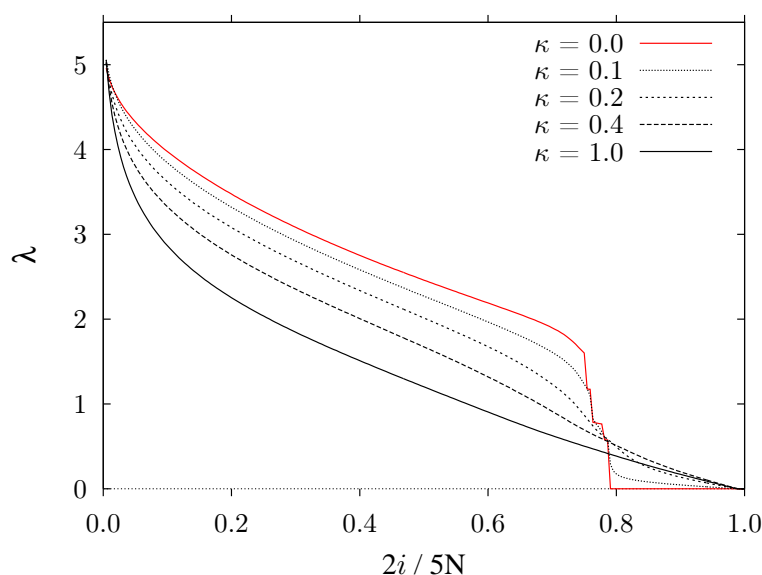


**Figure 8.1** : Lyapunov spectra for an equilibrium system consisting of a gas of 88 rough hard disks for various values of the coupling parameter ( $\kappa \in \{0, 0.1, 0.2, 0.4, 1\}$ ). The spectra are calculated with the help of the covariant vectors. Reduced indices  $2i/5N$  are used on the abscissa. Although the spectrum is defined only for integer  $i$ , lines are drawn for clarity.

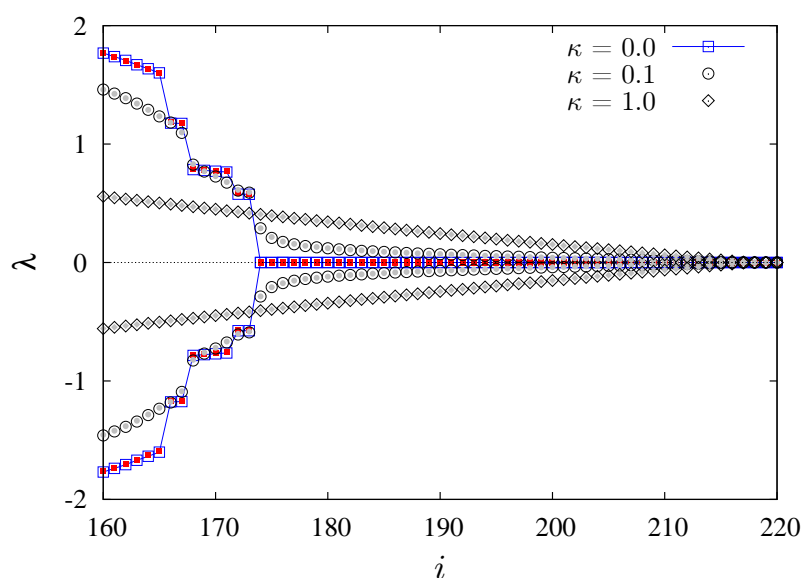


**Figure 8.2** : Enlargement of the Lyapunov spectra for the small exponents (in absolute value) of Fig. 8.1. Only the spectra for  $\kappa \in \{0, 0.1, 1\}$  are shown. The open symbols indicate exponents computed from the GS vectors, the full symbols exponents obtained from the covariant vectors. Steps can clearly be observed, the modes disappear progressively when  $\kappa$  grows and do not exist any more for a certain value of  $\kappa$  between 0.1 and 0.2.

twofold degeneracy are transverse ( $T$ ) modes –  $T(1, 0)$  and  $T(2, 0)$  from right to left in Fig. 8.2. Similarly, the steps with a fourfold degeneracy of the exponents are longitudinal-momentum ( $LP$ ) modes –  $LP(1, 0)$  and  $LP(2, 0)$  again from right to left. The arguments  $(n_x, n_y)$  account for the number of periods of the sinusoidal patterns in the  $x$ - and  $y$ -directions. Since our simulation cell is rather narrow, only modes with wave vectors  $\mathbf{k}$  parallel to the  $x$ -axis of the (periodic) cell appear, leaving 0 for the second argument. The modes for covariant vectors of smooth hard disks was studied in Chap. 3 and Ref. [18]. As usual, “transverse” and “longitudinal” refer to the spatial polarization with respect to the wave vector  $\mathbf{k}$  of the wave-like pattern. As is evident from Fig. 8.2, the mode structure in the spectra gradually disappears if  $\kappa$  is increased. This must be interpreted as a consequence of rotation-translation coupling.

#### 8.4.1 Angles between the position and momentum parts of perturbation vectors

Next, we show how differently the GS and covariant vectors span the tangent space. We consider, for each Lyapunov index  $i$ , the angle  $\theta_i$  between the spatial part and the translational-momentum part of the perturbation vector  $\delta\mathbf{\Gamma}_i$  – either a Gram-Schmidt vector  $\mathbf{g}_i$  or a covariant vector  $\mathbf{v}_i$ . Defining the  $2N$ -dimensional position vectors  $\delta\mathbf{q}_i = (\delta\vec{q}_i^1, \dots, \delta\vec{q}_i^N)$  and the  $2N$ -dimensional momentum vectors  $\delta\mathbf{p}_i = (\delta\vec{p}_i^1, \dots, \delta\vec{p}_i^N)$ , we compute  $\cos\theta_i = (\delta\mathbf{q}_i \cdot \delta\mathbf{p}_i) / (\|\delta\mathbf{q}_i\| \|\delta\mathbf{p}_i\|)$ . Note that, for the reduced units we use throughout, the positions and momenta are dimensionless. The elements of the perturbation vectors consisting of the  $N$  angular velocities of the disks are not considered.

In Fig. 8.3, the time average of  $\cos\theta_i$  is shown as a function of the Lyapunov index  $i$  for various values of the coupling parameter,  $\kappa \in \{0, 0.1, 1\}$ . As a reference, the respective result for the SHDS is also shown in the bottom-right panel of Fig. 8.3. For the covariant vectors (red curves) one immediately observes for  $\kappa > 0$  that the positive branch is anti-symmetric with respect to the conjugate negative branch,

$$\langle \cos(\theta_{D+1-i}(t)) \rangle = -\langle \cos(\theta_i(t)) \rangle \quad \forall i \in \{1, \dots, D/2\} .$$

The covariant vectors evolve according to the natural tangent bundle and obey the time-reversal symmetry prescribed by the respective dynamical rules. That means that the  $i$ -th expanding vector  $\mathbf{v}_i$  in the time-forward direction becomes the conjugate contracting vector  $-\mathbf{v}_{D+1-i}$  in the time-backward direction. The  $\langle \cos\theta \rangle$  for the GS vectors (blue curves) does not show this time-reversal symmetry. Whereas the deviations for  $\kappa = 0.1$  outside the range  $0.4 \leq i/5N \leq 0.6$  are comparatively small (bottom-left panel of Fig. 8.3), they are pronounced for  $\kappa = 1$  (top-

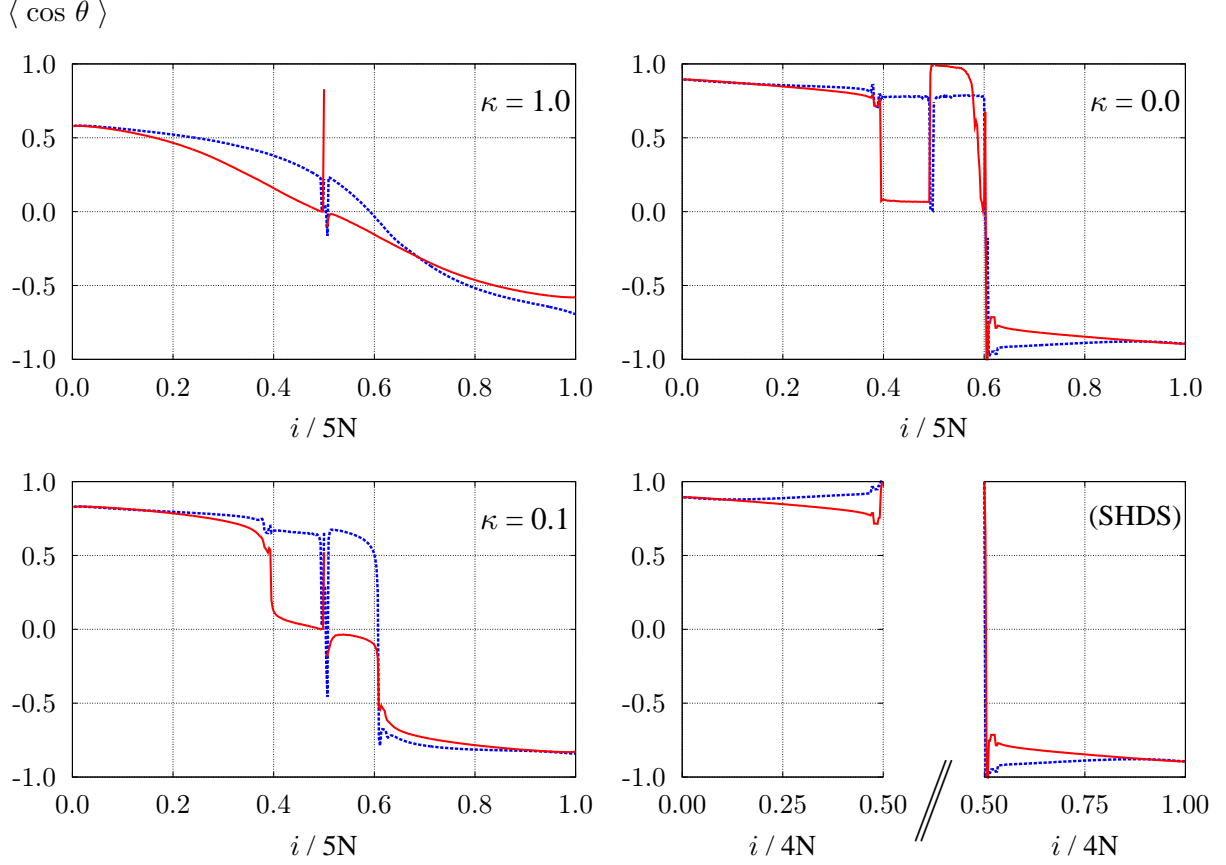


**Figure 8.3 :** Time-averaged value of  $\cos(\theta) = (\delta \mathbf{q} \cdot \delta \mathbf{p}) / (\|\delta \mathbf{q}\| \|\delta \mathbf{p}\|)$  as a function of the Lyapunov index  $i$  for a system of  $N = 88$  rough hard disks, for three different values of the coupling parameter  $\kappa \in \{0, 0.1, 1\}$ , as well as for a standard system of  $N = 88$  smooth hard disks. The density is  $\rho = 0.7$  and the aspect ratio is  $A = 2/11$ . Here,  $\delta \mathbf{q}$  and  $\delta \mathbf{p}$  are the  $2N$ -dimensional vectors of all position perturbations and of all transversal-momentum perturbations respectively, for GS vectors  $\mathbf{g}$  (blue line) and covariant vectors  $\mathbf{v}$  (red line). The case of smooth hard disks is treated in the bottom-right panel.

left panel of Fig. 8.3). This is to be expected due to the fact that the GS vectors do not obey time-reversal symmetry in general as outlined in detail in Chap. 5 and Ref. [19].

All these symmetry considerations strictly apply only to the stable and the unstable branches of the Lyapunov spectrum, where there is exponential contraction or expansion of the perturbations. The central manifolds in Fig. 8.3 (in the range  $0.4 \leq i/5N \leq 0.6$  for RHDS at  $\kappa = 0$ , and in the close vicinity of  $i/5N \sim 0.5$  for the other cases) are explicitly excluded and should be ignored.

It is interesting to note that the simple SHDS (bottom-right panel in Fig. 8.3) shows anti-symmetrical behavior of  $\langle \cos \theta \rangle$  both for the covariant vectors (as expected) and for the GS vectors. For the latter, this can only be a consequence of the symplectic symmetry of the GS vectors for Hamiltonian systems [19, 21] (see also Chap. 5). This was explicitly stated already

in Ref. [8],

$$\cos(\theta_{D+1-i}(t)) = -\cos(\theta_i(t)) \quad \forall i \in \{1, \dots, D/2\} ,$$

for any instant of time  $t$  (which is a direct consequence of Eq. (8.19) in Sec. 8.7). Therefore, also the time-averaged spectra are anti-symmetric as displayed in the bottom-right panel of Fig. 8.3.

However, the rough-hard-disk model for  $\kappa = 0$ , keeping the angular velocity variables included in the GS re-orthonormalization process, does not show this symmetry (top-right panel of Fig. 8.3). This is not a numerical artefact since the GS vectors, which do not display the expected symmetry, are used in the construction of the covariant vectors, which lead to the expected symmetry. Thus, it is not sufficient to simply put  $\kappa$  to 0 for rough disks to generate the same tangent space dynamics as found for SHDS. It is also necessary to explicitly exclude the redundant angular velocity components of the perturbation vectors from the GS re-orthonormalization procedure.

### 8.4.2 Localization of perturbation vectors

As a second example, we consider the most common localization measure for the perturbation vectors proposed by Taniguchi and Morriss [9], but here we use this measure in a slightly modified way. The aim is to better understand, how the GS vectors and the covariant vectors span the tangent space.

For each Lyapunov index we introduce two different normalized measures for the perturbation a particle  $n$  contributes to the full perturbation vector  $\delta\mathbf{\Gamma}$ ,

$$\mu_n^{(q,p,\omega)} = \frac{\delta\vec{q}_n^2 + \delta\vec{p}_n^2 + \delta\omega_n^2}{\sum_{k=1}^N (\delta\vec{q}_k^2 + \delta\vec{p}_k^2 + \delta\omega_k^2)} , \quad \mu_n^{(q,p)} = \frac{\delta\vec{q}_n^2 + \delta\vec{p}_n^2}{\sum_{k=1}^N (\delta\vec{q}_k^2 + \delta\vec{p}_k^2)} .$$

The former is used only for the RHDS, whereas the latter can be used for RHDS and SHDS. Since the conditions  $\sum_{n=1}^N \mu_n = 1$  and  $0 \leq \mu_n \leq 1$  are satisfied, the quantity  $\mu_n$  acts like a probability measure of the particle  $n$  contributing to the perturbation  $\delta\mathbf{\Gamma}$ . The localization  $W$  is defined according to the time-averaged entropy-like quantity,  $S$ , for the “probability” distributions  $\mu_n$ :

$$W = \frac{1}{N} \exp[S] , \quad S = - \left\langle \sum_{n=1}^N \mu_n \ln \mu_n \right\rangle .$$

$W$  is bounded,  $1/N \leq W \leq 1$ , where the lower and upper bounds apply to complete localization and delocalization in physical space, respectively.

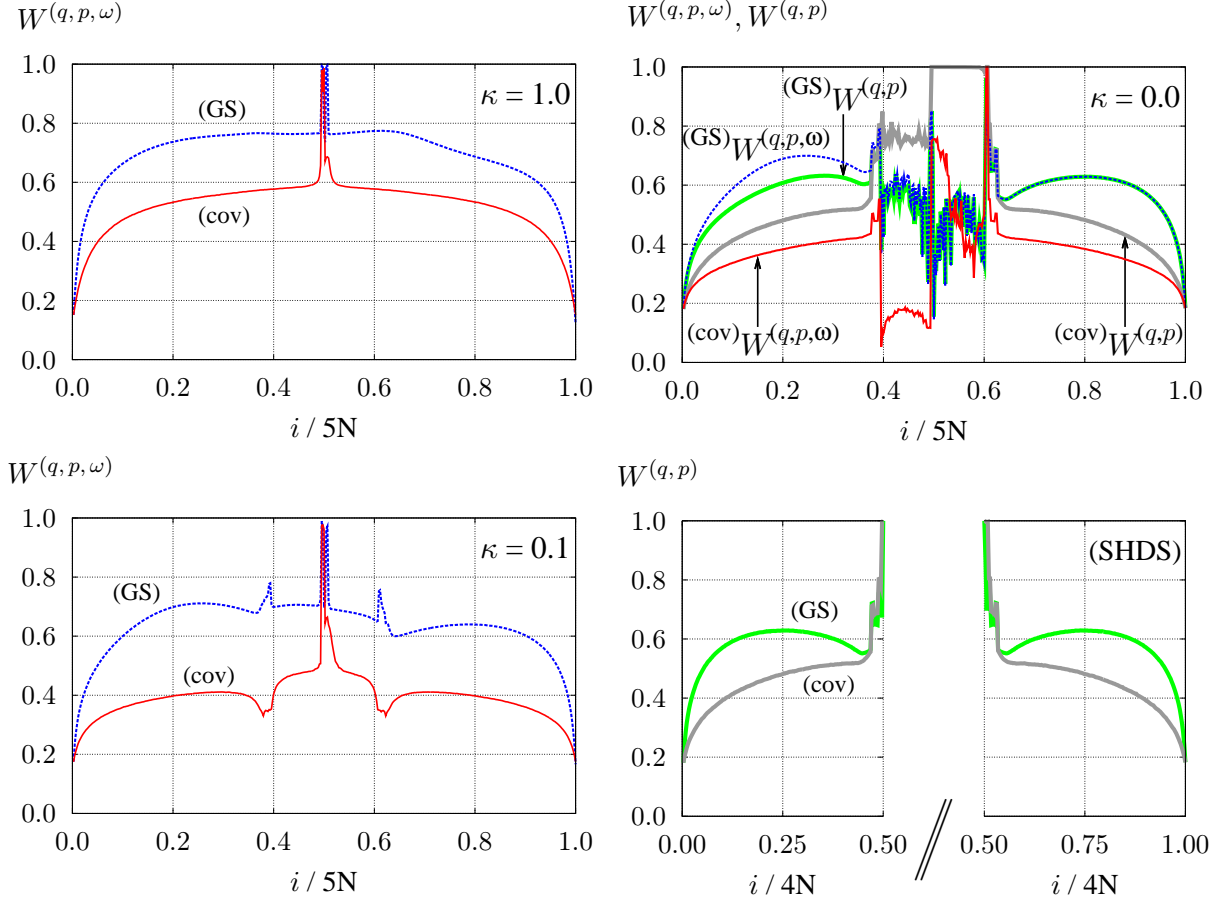


**Figure 8.4 :** Normalized localization  $W$  for the full GS vector set ( $^{(GS)}W^{(q,p,\omega)}$ : blue,  $^{(GS)}W^{(q,p)}$ : green) and for the full covariant vector set ( $^{(cov)}W^{(q,p,\omega)}$ : red,  $^{(cov)}W^{(q,p)}$ : gray) as a function of the Lyapunov index  $i$  for a system of  $N = 88$  rough hard disks at three different values of the coupling parameter ( $\kappa \in \{0, 0.1, 1\}$ ). Equivalent results for the SHDS with  $N = 88$  are shown in the bottom-right panel. The density  $\rho = 0.7$ , and the aspect ratio  $A = 2/11$ .

In Fig. 8.4, we show  $W$  as a function of the Lyapunov indices  $i$ . As in Sec. 8.4.1 the range of the central manifold in the center should be ignored. We compare  $W$  for the full set of GS vectors (blue curves) to that of all covariant vectors (red curves) for the RHDS at different values of the coupling parameter,  $\kappa \in \{0, 0.1, 1\}$ . As a reference, we show the results for the SHDS in the bottom-right panel. Not too surprisingly, the localization is stronger for covariant vectors, whose directions in tangent space are solely determined by the tangent flow and are not affected by re-orthonormalization constraints. An interesting feature is the lack of symmetry for the GS vectors:  $^{(GS)}W_i \neq ^{(GS)}W_{D+1-i}$ . However, the symmetry for the covariant vectors persists:  $^{(cov)}W_i = ^{(cov)}W_{D+1-i}$ . It also exists for the GS vectors of the SHDS (bottom-right panel of Fig. 8.4). The explanation of this symmetry is the same as the explanation furnished in Sec. 8.4.1 to understand the anti-symmetry and the lack of symmetry of  $\langle \cos \theta \rangle$  for the covariant vectors and GS vectors, respectively.

For  $\kappa = 0$ , the localization spectrum for GS vectors agrees with that for the SHDS only on the

stable branch. This confirms our conclusions already reached for  $\langle \cos \theta \rangle$ : It is not sufficient to put  $\kappa = 0$  and keep the (redundant) angular-velocity components of the perturbation vectors in the GS procedure included to recover the smooth-hard-disk case. These components need to be excluded from the GS re-orthonormalization step. Most surprisingly, even the inclusion of these components for  $\kappa = 0$  in the RHDS generates covariant localization measures, which are identical to those of SHDS. This nicely emphasizes the physical significance of the covariant vectors as compared to GS vectors, which may be considered as a more mathematical tool for the computation of global exponents.

The fact that  $^{(\text{cov})}W^{(q,p,\omega)} < ^{(\text{cov})}W^{(q,p)}$  in the top-right panel of Fig. 8.4 and  $^{(\text{cov})}W^{(q,p)}$  for RHDS ( $\kappa = 0$ ) agrees with  $^{(\text{cov})}W^{(q,p)}$  for SHDS suggests that the rotational velocities are irrelevant for this special case. We admit that it is counterintuitive that they are still relevant for the GS case (producing the asymmetry), although the GS vectors are subsequently used to generate the covariant data (which are symmetric).

### 8.4.3 Tangent space projections

Motivated to quantify how translation and rotation affects the dynamics, we consider projections of the perturbation vectors  $\delta\mathbf{\Gamma}$  onto the coordinate, the transversal-momentum and the rotational-velocity subspaces. We introduce five such measures, where the index  $n$  enumerates the disks,  $n = 1, \dots, N$ :

$$\eta_{\mathcal{X}}^{(q,p,\omega)} = \left\langle \frac{\sum_{n=1}^N \delta\vec{\mathcal{X}}_n^2}{\sum_{k=1}^N (\delta\vec{q}_k^2 + \delta\vec{p}_k^2 + \delta\omega_k^2)} \right\rangle, \quad \text{where } \{\delta\vec{\mathcal{X}}_n\}_{n=1}^N \equiv \begin{cases} \{\delta\vec{q}_n\}_{n=1}^N, \\ \text{or } \{\delta\vec{p}_n\}_{n=1}^N, \\ \text{or } \{\delta\omega_n\}_{n=1}^N. \end{cases}$$

$$\eta_{\mathcal{Y}}^{(q,p)} = \left\langle \frac{\sum_{n=1}^N \delta\vec{\mathcal{Y}}_n^2}{\sum_{k=1}^N (\delta\vec{q}_k^2 + \delta\vec{p}_k^2)} \right\rangle, \quad \text{where } \{\delta\vec{\mathcal{Y}}_n\}_{n=1}^N \equiv \begin{cases} \{\delta\vec{q}_n\}_{n=1}^N, \\ \text{or } \{\delta\vec{p}_n\}_{n=1}^N. \end{cases}$$

Obviously the first three of these measures involving  $\{\delta\vec{\mathcal{X}}_n\}_{n=1}^N$  are useful only for the RHDS, whereas the remaining quantities may be used also for SHDS.

In Fig. 8.5 we plot these measures for the Gram-Schmidt vectors in the panels on the left-hand side, and for the covariant vectors in the panels on the right-hand side. We ask the reader again to ignore the range of the central manifold in the center of all panels ( $0.4 \leq i/5N \leq 0.6$ ) for the RHDS due to the non-exponential growth/decay of perturbations in that regime. From top to bottom the panels are for  $\kappa = 1, 0.1$ , and  $\kappa = 0$ . The panels at the bottom are for the smooth-hard-disk model, which was already discussed in Chap. 3 and Ref. [18].



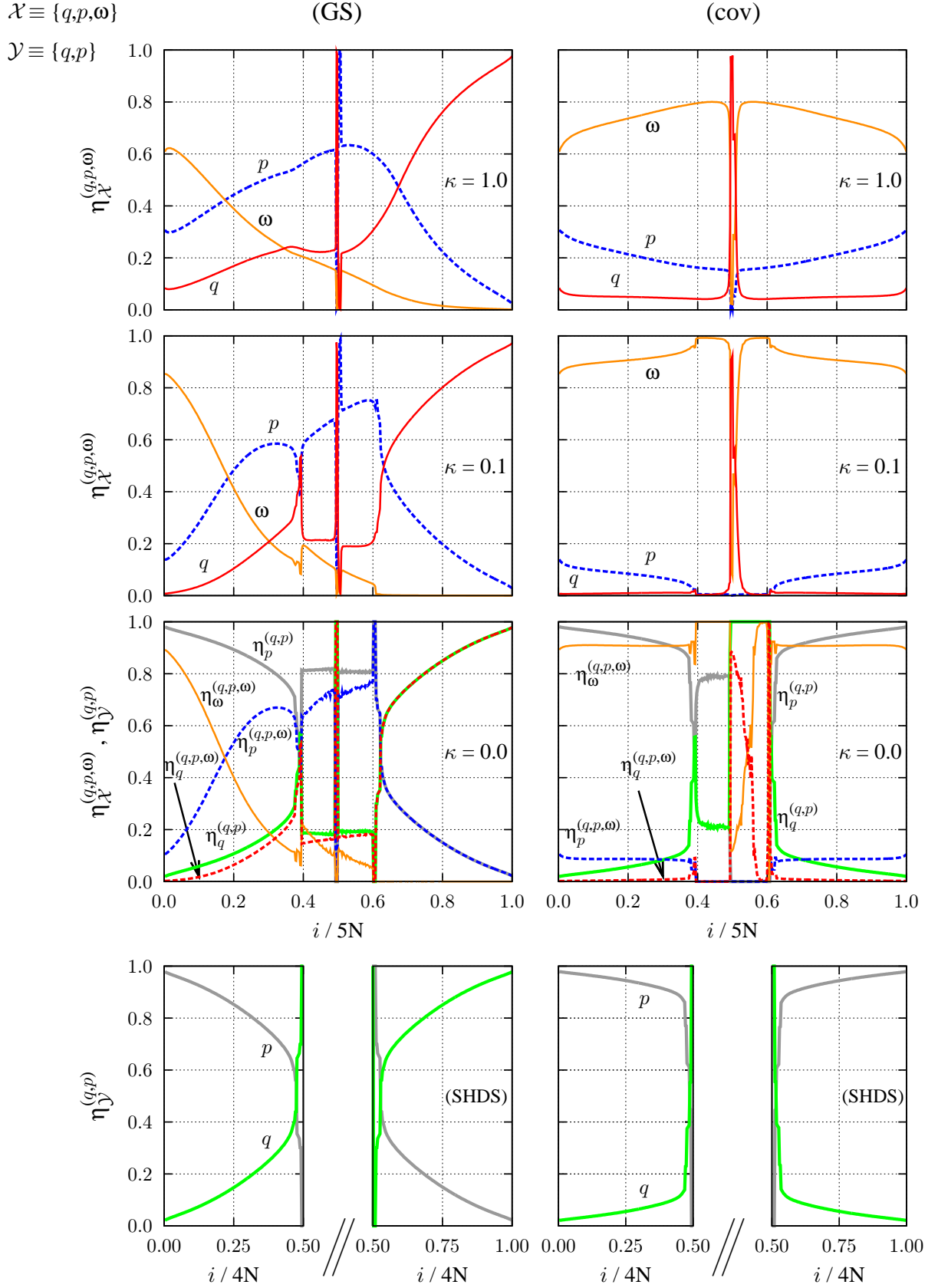


**Figure 8.5 :** Mean squared projections for the complete set of GS vectors (left-hand panels) and covariant vectors (right-hand panels) as a function of the Lyapunov index  $i$ . Parameters:  $N = 88$ ,  $\kappa \in \{1, 0.1, 0\}$  as indicated by the labels. The panels in the bottom row are for the smooth-hard-disk system for  $N = 88$ .

Let us consider the simple case of the SHDS in the bottom-row panels of Fig. 8.5. One observes for the Gram-Schmidt cases  $\eta_q^{(q,p)}$  and  $\eta_p^{(q,p)}$  for conjugate pairs  $i$  and  $5N + 1 - i$  are of equal magnitude but different sign. This anti-conjugation also persists in the central manifold. We refer to Fig. 3.6 in Chap. 3 for more details. Since the GS vectors display symplectic symmetry but not time-reversal symmetry, the anti-conjugation must be a consequence of the symplectic phase-space structure for this model. In the rough-hard-disk case, even for  $\kappa = 0$ , this anti-conjugation does not exist. This is again a strong evidence that the RHDS is not symplectic.

However, in the covariant case for the SHDS (bottom-right panel of Fig. 8.5),  $\eta_q^{(q,p)}$  and  $\eta_p^{(q,p)}$  are conjugated with equal sign. This was already observed in Fig. 3.7 of Chap. 3 (and Ref. [18]). This conjugation is a consequence of the time-reversal symmetry displayed by the covariant vectors. Since time-reversal invariance also persists for strictly rough hard disks ( $\kappa > 0$ ), the squared phase-space projections also show the conjugation property for  $\kappa > 0$  (panels on the right-hand side of Fig. 8.5).

For the covariant case  $\eta_q^{(q,p)}$  (green lines) and  $\eta_p^{(q,p)}$  (gray lines) of the RHDS with  $\kappa = 0$  (including the angular velocity part in the Gram-Schmidt re-orthonormalization procedure, but excluding these variable in the definition of  $\eta$ ) agree with the respective quantities for the strict SHDS, as expected (panels on the right-hand side). For the Gram-Schmidt case (panels on the left-hand side) they only agree for the stable branch ( $i/5N > 0.6$ ).

## 8.5 Null subspace and vanishing exponents for RHDS

The subspace of the tangent space associated with the vanishing exponents is of special interest. Let us consider some experimental results first. In Fig. 8.6 the Lyapunov spectra of a rough-hard-disk system consisting of an odd number of particles, namely  $N = 3$  disks, are shown. The panels in the top row are for periodic boundary conditions, which we exclusively used so far. The panels in the bottom row, however, are for reflecting boundary conditions, for which the tangent vectors change according to Eq. (20) of Ref. [5] for a reflection at the boundary. The essential difference is that translational momentum conservation does not apply in this case (both in  $x$ - and  $y$ -directions), which results in a reduction of the vanishing exponents by 4 with respect to the periodic-boundary case. The panels on the left-hand side of Fig. 8.6 include the orientation angles  $\{\theta_n\}_{n=1}^N$  in the list of independent variables in Eq. (8.3) and the respective perturbations  $\{\delta\theta_n\}_{n=1}^N$  in Eq. (8.5). Although the  $\{\theta_n\}_{n=1}^N$  do not affect the dynamics in the phase space at all (as discussed further below), the associated perturbations  $\{\delta\theta_n\}_{n=1}^N$  contribute to the evolution of the tangent bundle since they take part in the GS re-orthonormalization. At the collision of

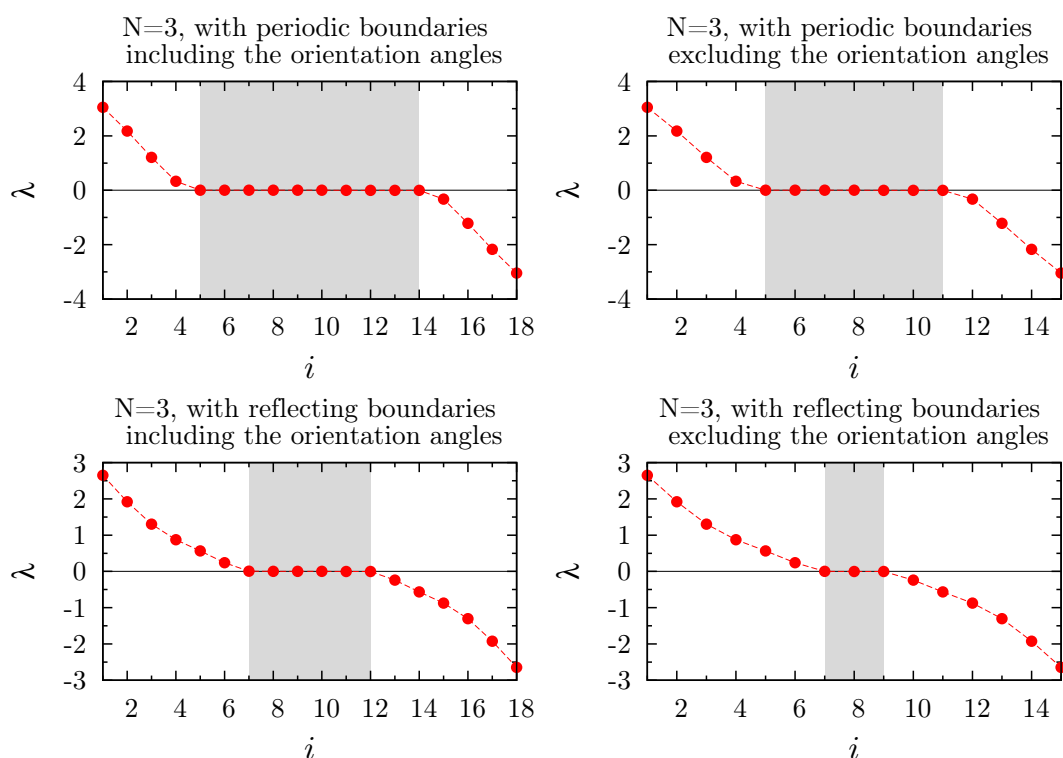


**Figure 8.6** : Lyapunov spectrum of the RHDS, with  $N = 3$  disks, for the cases of periodic and reflecting boundary conditions, where the orientation angles of the disks are either included or excluded from the phase-space and tangent-space dynamics.

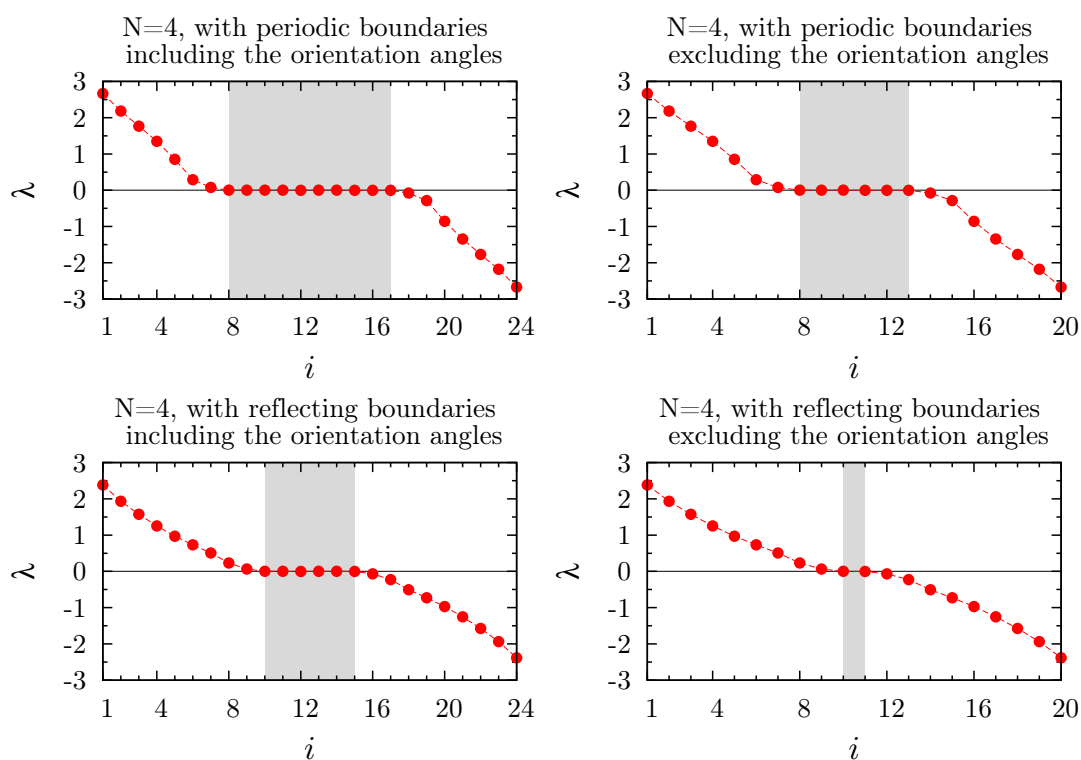


**Figure 8.7** : As for Fig. 8.6, with  $N = 4$  disks.

particles  $k$  and  $\ell$  these perturbation components change according to [5]

$$\left. \begin{aligned} \delta\theta'_k &= \delta\theta_k - \frac{2\beta}{\sigma} (\vec{n} \times \vec{g}) \delta\tau_c \\ \delta\theta'_\ell &= \delta\theta_\ell - \frac{2\beta}{\sigma} (\vec{n} \times \vec{g}) \delta\tau_c \end{aligned} \right\} \quad (8.13)$$

which augment the Eqs. (8.7) in this case. The panels on the right-hand side of Fig. 8.6 are for the standard representation of the RHSD without the explicit consideration of the disk orientations  $\{\theta_n\}_{n=1}^N$  (see Eqs. (8.6) and (8.7)).

The spectra in the analogous Fig. 8.7 are for an even number of disks,  $N = 4$ .

### A: Projection matrix for the case excluding the orientation angles

( $N = 4$ , periodic boundary conditions)

The central manifold is a consequence of the intrinsic continuous symmetries, which leave the Lagrangian and, thus, the equations of motion invariant. Our two-dimensional system with periodic boundaries provides three continuous symmetries: homogeneity of space (i.e. invariance with respect to space translations in two independent directions) and the homogeneity of time (i.e. invariance with respect to time translation). Each of these symmetries generates one conservative quantity [22]. Each symmetry produces two vector fields with sub-exponential growth (or decay) and, therefore, gives rise to two vanishing Lyapunov exponents [23]. The six vectors span, at any phase-space point  $\mathbf{\Gamma}$ , a six-dimensional subspace  $\mathcal{N}(\mathbf{\Gamma})$  of the tangent space  $\mathbf{TX}_{\mathbf{\Gamma}}$ , which is referred to as null subspace or central manifold. This subspace is covariant, but is not orthogonal to the stable and the unstable subspaces. With the  $5N$  components of the state vector arranged as

$$\mathbf{\Gamma} = (q_x^1, q_y^1, \dots, q_x^N, q_y^N; p_x^1, p_y^1, \dots, p_x^N, p_y^N; \omega_1, \dots, \omega_N) \quad ,$$

the components of an arbitrary tangent space vector  $\delta\mathbf{\Gamma}$  are arranged accordingly:

$$\mathbf{\Gamma} = (\delta q_x^1, \delta q_y^1, \dots, \delta q_x^N, \delta q_y^N; \delta p_x^1, \delta p_y^1, \dots, \delta p_x^N, \delta p_y^N; \delta\omega_1, \dots, \delta\omega_N) \quad .$$

The six orthogonal generating vectors of the continuous symmetries are written as [20]

$$\begin{aligned} \mathbf{e}_1 &= (p_x^1, p_y^1, \dots, p_x^4, p_y^4; 0, 0, \dots, 0, 0; 0, 0, 0, 0) / A \\ \mathbf{e}_2 &= (1, 0, \dots, 1, 0; 0, 0, \dots, 0, 0; 0, 0, 0, 0) / \sqrt{N} \\ \mathbf{e}_3 &= (0, 1, \dots, 0, 1; 0, 0, \dots, 0, 0; 0, 0, 0, 0) / \sqrt{N} \end{aligned}$$

$$\begin{aligned}
\mathbf{e}_4 &= (0, 0, \dots, 0, 0; p_x^1, p_y^1, \dots, p_x^4, p_y^4; I\omega_1, I\omega_2, I\omega_3, I\omega_4)/B \\
\mathbf{e}_5 &= (0, 0, \dots, 0, 0; 1, 0, \dots, 1, 0; 0, 0, 0, 0)/\sqrt{N} \\
\mathbf{e}_6 &= (0, 0, \dots, 0, 0; 0, 1, \dots, 0, 1; 0, 0, 0, 0)/\sqrt{N}
\end{aligned}$$

where  $A$  and  $B$  are normalization constraints. The orthogonality arises from the fact that the total translational momenta in  $x$ - and  $y$ -directions are set to zero and are conserved. The vector  $\mathbf{e}_1$  corresponds to a shift of the time origin,  $\mathbf{e}_4$  to a change of energy,  $\mathbf{e}_2$  and  $\mathbf{e}_3$  to a uniform translation of the origin in the  $x$ - and  $y$ -directions, respectively, and  $\mathbf{e}_5$  and  $\mathbf{e}_6$  to a uniform perturbation of the translational momentum in the  $x$ - and  $y$ -directions, respectively. The six vanishing Lyapunov exponents are located in the center of the Lyapunov spectrum with indices  $5N/2 - 3 \leq i \leq 5N/2 + 2$  (where  $N$  is even).

The projection matrices  $\alpha$  and  $\beta$  of the GS and covariant vectors onto this natural basis, are defined by

$$\alpha_{i,j} = \mathbf{g}_i \cdot \mathbf{e}_j; \quad \beta_{i,j} = \mathbf{v}_i \cdot \mathbf{e}_j; \quad \forall j \in \{1, \dots, 6\}, \quad i \in \{5N/2 - 2, \dots, 5N/2 + 3\}.$$

A small system is sufficient to study the general properties of the null subspace. We consider only  $N = 4$  rough hard disks in a periodic box, which is relaxed for  $t_r = 10^5$  time units, followed by a forward and backward iteration lasting for  $t_s = 10^4$  time units. The initial conditions for the backward iteration are  $\mathbf{v}_i(t_r + t_s) = \mathbf{g}_i(t_r + t_s)$  for  $i = 1, \dots, 5N (= 20)$ . See Sect. 3.5.4 (or Ref. [18]) for a discussion of this point. The projections at the time  $t_r$  are given in Table 8.1 for the GS vectors, in Table 8.2 for the covariant vectors.

The covariant and Gram-Schmidt vectors are different. The six orthogonal GS vectors  $\{\mathbf{g}_i; 5N/2 - 3 \leq i \leq 5N/2 + 2\}$  do not span the null subspace (the squared elements for each rows do not add up to unity in Table 8.1). The vectors  $\mathbf{e}_2, \mathbf{e}_3, \mathbf{e}_5$  and  $\mathbf{e}_6$  are entirely included in the subspace spanned by these six orthogonal GS vectors (the squared elements for the respective columns do add to unity in Table 8.1), but the vectors  $\mathbf{e}_1$  and  $\mathbf{e}_4$  are not. Thus, the null subspace spanned by  $\{\mathbf{e}_j\}_{j=1}^6$  does not agree with the subspace spanned by the orthogonal GS vectors  $\{\mathbf{g}_i; 5N/2 - 3 \leq i \leq 5N/2 + 2\}$ , since the latter is orthogonal to the stable and unstable subspaces by construction, but the null subspace is not.

In contrast, the six non-orthogonal covariant vectors  $\{\mathbf{v}_i; 5N/2 - 3 \leq i \leq 5N/2 + 2\}$  correctly span the null subspace (in Table 8.2). The components of the configuration part  $\{\beta_{i,j}; j = 2, 3\}$  are equivalent to the corresponding component of the momentum part (i.e.  $\beta_{i,j+3}$ ). They have (almost) the same mantissa but differ by a factor of  $10^5$  or  $10^4$ . These factors are related to the duration of the relaxation phase  $t_r = 10^5$  and of the forward-backward iteration time  $t_s = 10^4$ .

**Table 8.1** : RHDS for  $N = 4$  disks: Instantaneous projection matrix  $\alpha$  of GS vectors (for  $i \in \{5N/2 - 2, \dots, 5N/2 + 3\}$ ) onto the natural basis  $\{\mathbf{e}_j, 1 \leq j \leq 6\}$  of the null subspace. We use a coupling parameter  $\kappa = 0.2$ . The powers of 10 are given in square brackets.

$i$	$\alpha_{i,1}$	$\alpha_{i,2}$	$\alpha_{i,3}$	$\alpha_{i,4}$	$\alpha_{i,5}$	$\alpha_{i,6}$	$\sum_j (\alpha_{i,j})^2$
$5N/2 - 2$	-0.9902[-1]	-0.4653	-0.8689	-0.5300[-5]	-0.4653[-5]	-0.8689[-5]	0.9813
$5N/2 - 1$	0.5488	-0.3529	0.7182[-2]	0.2939[-4]	-0.3529[-5]	0.7195[-7]	0.4258
$5N/2$	0.1818	0.8118	-0.4950	0.9690[-5]	0.8117[-5]	-0.4951[-5]	0.9370
$5N/2 + 1$	0.2281[-4]	0.8248[-7]	0.2534[-6]	-0.8068	-0.1324[-1]	-0.2284[-1]	0.6517
$5N/2 + 2$	0.5757[-6]	-0.7350[-5]	-0.6776[-5]	-0.2035[-1]	0.7350	0.6776	0.9998
$5N/2 + 3$	0.1785[-6]	0.6779[-5]	-0.7351[-5]	-0.6310[-2]	-0.6779	0.7351	1.0000
$\sum_i (\alpha_{i,j})^2$	0.3441	1.0000	1.0000	0.6514	1.0000	1.0000	

**Table 8.2** : RHDS for  $N = 4$  disks: Instantaneous projection matrix  $\beta$  of covariant vectors (for  $i \in \{5N/2 - 2, \dots, 5N/2 + 3\}$ ) onto the natural basis  $\{\mathbf{e}_j, 1 \leq j \leq 6\}$  of the null subspace. We use a coupling parameter  $\kappa = 0.2$ . The powers of 10 are given in square brackets.

$i$	$\beta_{i,1}$	$\beta_{i,2}$	$\beta_{i,3}$	$\beta_{i,4}$	$\beta_{i,5}$	$\beta_{i,6}$	$\sum_j (\beta_{i,j})^2$
$5N/2 - 2$	-0.2803	-0.4532	-0.8462	-0.5161[-5]	-0.4532[-5]	-0.8462[-5]	1.0000
$5N/2 - 1$	0.9747	-0.2233	-0.8146[-2]	0.1796[-4]	-0.2233[-5]	-0.8139[-7]	1.0000
$5N/2$	0.4349	0.7688	-0.4688	0.7971[-5]	0.7688[-5]	-0.4689[-5]	1.0000
$5N/2 + 1$	-0.9982	-0.3016[-1]	-0.5204[-1]	0.1838[-3]	0.3016[-5]	0.5204[-5]	1.0000
$5N/2 + 2$	-0.6617[-2]	-0.7350	-0.6780	0.1218	0.7350[-4]	0.6780[-4]	1.0000
$5N/2 + 3$	-0.2049[-2]	0.6780	-0.7351	0.3781	-0.6779[-4]	0.7351[-4]	1.0000

The explanation for this behavior is obtained by a repeated explicit application of the linearized maps for the free streaming and consecutive collision of particles [24, 5] to the six basis vectors  $\{\mathbf{e}_j, 1 \leq j \leq 6\}$ . Similar to SHDS [18], one finds that the tangent flow  $D\phi^t : \mathbf{TX}_{\Gamma(0)} \rightarrow \mathbf{TX}_{\Gamma(t)}$  acts on the six orthogonal vectors spanning the null subspace according to

$$D\phi_{\Gamma_0}^t \mathbf{e}_j(\Gamma_0) = \mathbf{e}_j(\Gamma_t), \quad (8.14)$$

$$D\phi_{\Gamma_0}^t \mathbf{e}_{j+3}(\Gamma_0) = t \mathbf{e}_j(\Gamma_t) + \mathbf{e}_{j+3}(\Gamma_t), \quad (8.15)$$

for  $j \in \{1, 2, 3\}$ . And finally, one has  $\beta_{i,j} \approx \beta_{i,j+3} t_s$  or  $\beta_{i,j} \approx \beta_{i,j+3} t_r$  for  $j = 2, 3$ , since, during the backward iteration, the vectors  $\mathbf{e}_2(t)$ ,  $\mathbf{e}_3(t)$ ,  $\mathbf{e}_5(t)$  and  $\mathbf{e}_6(t)$  are entirely included in the subspace spanned by the six orthogonal vectors  $\{\mathbf{g}_i(t); 5N/2 - 3 \leq i \leq 5N/2 + 2\}$ . One also has  $\beta_{i,1} \approx \beta_{i,4} (0.543 t_s)$  or  $\beta_{i,1} \approx \beta_{i,4} (0.543 t_r)$ , since the vectors  $\mathbf{e}_1(t)$  and  $\mathbf{e}_4(t)$  are not entirely included in the latter subspace, but the factor 0.543 cannot be easily related to the vectors  $\mathbf{e}_1(t_r)$  and  $\mathbf{e}_4(t_r)$ .

Eq. (8.14) shows that the subspaces  $\mathcal{N}_1 = \text{span}\{\mathbf{e}_1\}$ ,  $\mathcal{N}_2 = \text{span}\{\mathbf{e}_2\}$  and  $\mathcal{N}_3 = \text{span}\{\mathbf{e}_3\}$  are separately covariant. Eq. (8.15) implies that any perturbation vector with non-vanishing components parallel to  $\mathbf{e}_4$ ,  $\mathbf{e}_5$ , or  $\mathbf{e}_6$  will rotate towards  $\mathbf{e}_1$ ,  $\mathbf{e}_2$ , and  $\mathbf{e}_3$ . It follows thus that the null subspace  $\mathcal{N}(\Gamma)$  is covariant and, more precisely, that  $\mathcal{N}$  can be further decomposed into the three two-dimensional covariant subspaces  $\mathcal{N}_p = \text{span}\{\mathbf{e}_1, \mathbf{e}_4\}$ ,  $\mathcal{N}_x = \text{span}\{\mathbf{e}_2, \mathbf{e}_5\}$ , and  $\mathcal{N}_y = \text{span}\{\mathbf{e}_3, \mathbf{e}_6\}$  [18].

We conclude that for the RHDS the null subspace is not orthogonal to the stable and unstable subspaces. Only four of its directions associated with the homogeneity of space (or momentum conservation) are orthogonal to the stable and unstable subspaces. One might be tempted to argue that such a behavior is caused by the fact that the orientation angles of the particles have not been considered at all. In the following we treat this most general representation and show that this is not the case.

### B: Projection matrix for the case including the orientation angles

( $N = 4$ , periodic boundary conditions)

Now the state vector has  $6N$  components which are arranged according to

$$\mathbf{\Gamma} = (q_x^1, q_y^1, \dots, q_x^4, q_y^4; p_x^1, p_y^1, \dots, p_x^4, p_y^4; \omega_1, \omega_2, \omega_3, \omega_4; \theta_1, \theta_2, \theta_3, \theta_4) .$$

Similarly, the perturbation vectors become

$$\delta\mathbf{\Gamma} = (\delta q_x^1, \delta q_y^1, \dots, \delta q_x^4, \delta q_y^4; \delta p_x^1, \delta p_y^1, \dots, \delta p_x^4, \delta p_y^4; \delta\omega_1, \delta\omega_2, \delta\omega_3, \delta\omega_4; \delta\theta_1, \delta\theta_2, \delta\theta_3, \delta\theta_4) .$$

In addition to the continuous symmetry we have considered before, one has to account for the fact that the Lagrangian does not depend on the orientation angles of each particles. Hence, the symmetry transformation  $(\vec{q}, \vec{p}, \omega, \theta) \mapsto (\vec{q}, \vec{p}, \omega, \theta + \varepsilon \theta)$  gives rise to a generator  $(\vec{0}, \vec{0}, 0, 1)$  for each particle. The  $6 + N$  vectors spanning the null subspace become (here,  $N = 4$ ):

$$\begin{aligned} \mathbf{e}'_1 &= (p_x^1, p_y^1, \dots, p_x^4, p_y^4; 0, 0, \dots, 0, 0; 0, 0, 0, 0; \omega_1, \omega_2, \omega_3, \omega_4)/A \\ \mathbf{e}_2 &= (1, 0, \dots, 1, 0; 0, 0, \dots, 0, 0; 0, 0, 0, 0; 0, 0, 0, 0)/2 \\ \mathbf{e}_3 &= (0, 1, \dots, 0, 1; 0, 0, \dots, 0, 0; 0, 0, 0, 0; 0, 0, 0, 0)/2 \\ \mathbf{e}_4 &= (0, 0, \dots, 0, 0; p_x^1, p_y^1, \dots, p_x^4, p_y^4; I\omega_1, I\omega_2, I\omega_3, I\omega_4; 0, 0, 0, 0)/B \\ \mathbf{e}_5 &= (0, 0, \dots, 0, 0; 1, 0, \dots, 1, 0; 0, 0, 0, 0; 0, 0, 0, 0)/2 \\ \mathbf{e}_6 &= (0, 0, \dots, 0, 0; 0, 1, \dots, 0, 1; 0, 0, 0, 0; 0, 0, 0, 0)/2 \\ \mathbf{e}_7 &= (0, 0, \dots, 0, 0; 0, 0, \dots, 0, 0; 0, 0, 0, 0; 1, 0, 0, 0) \\ \mathbf{e}_8 &= (0, 0, \dots, 0, 0; 0, 0, \dots, 0, 0; 0, 0, 0, 0; 0, 1, 0, 0) \\ \mathbf{e}_9 &= (0, 0, \dots, 0, 0; 0, 0, \dots, 0, 0; 0, 0, 0, 0; 0, 0, 1, 0) \\ \mathbf{e}_{10} &= (0, 0, \dots, 0, 0; 0, 0, \dots, 0, 0; 0, 0, 0, 0; 0, 0, 0, 1) \end{aligned}$$

where  $A$  and  $B$  are normalization factors.  $\mathbf{e}'_1$  follows from the invariance with respect to time translation,  $\mathbf{e}_4$  is a consequence of energy conservation,  $\mathbf{e}_2$ ,  $\mathbf{e}_3$ ,  $\mathbf{e}_5$  and  $\mathbf{e}_6$  follow from the ho-

**Table 8.3 :** RHDS for  $N = 4$  disks: Instantaneous projection matrix  $\alpha$  of GS vectors and projection matrix  $\beta$  of covariant vectors (for  $i \in \{3N - 4, \dots, 3N + 5\}$ ) onto the natural basis  $\{e_j, 1 \leq j \leq 10\}$  of the null subspace. We use a coupling parameter  $\kappa = 0.2$ .

$i$	$\alpha_{i,1}$	$\alpha_{i,2}$	$\alpha_{i,3}$	$\alpha_{i,4}$	$\alpha_{i,5}$	$\alpha_{i,6}$	$\alpha_{i,7}$	$\alpha_{i,8}$	$\alpha_{i,9}$	$\alpha_{i,10}$	$\sum_j (\alpha_{i,j})^2$
8	0.6950	0.3737[-9]	0.2068[-8]	0.2899[-11]	0.1885[-12]	0.1090[-11]	-0.2359	-0.7222[-1]	-0.5732[-1]	-0.1623	0.5736
9	0.3070	0.4727	0.5870	0.7491[-4]	0.4727[-4]	0.5870[-4]	0.5843[-8]	-0.2156	0.1833	-0.1008	0.7525
10	0.3306	-0.6549	-0.2651	0.8075[-4]	-0.6549[-4]	-0.2651[-4]	0.5751[-8]	-0.2322	0.1972	-0.1085	0.7130
11	0.1209	0.5897	-0.7650	0.2939[-4]	0.5896[-4]	-0.7651[-4]	0.1853[-8]	-0.8506[-1]	0.7233[-1]	-0.3976[-1]	0.9615
12	0.2873	0.9285[-4]	-0.1085[-3]	0.1016[-3]	0.8345[-8]	-0.1116[-7]	0.8707[-9]	0.3680	0.3907[-1]	-0.2554	0.2848
13	-0.2320	-0.4883[-3]	0.2448[-3]	-0.2624[-3]	-0.5166[-6]	-0.1150[-4]	0.8838[-9]	-0.1134[-8]	0.2177	-0.1404	0.1209
14	0.3798[-1]	0.2424[-6]	-0.6930[-6]	0.4413[-1]	0.7198[-2]	0.7425[-2]	-0.1414[-9]	0.6002[-10]	0.6242[-1]	0.5328[-1]	0.1023[-1]
15	0.1890[-2]	0.1600[-4]	0.1603[-4]	-0.9586	-0.1586	-0.1602	-0.6286[-11]	0.3766[-11]	0.2851[-2]	0.2446[-2]	0.9698
16	0.1318[-4]	0.2092[-4]	-0.9698[-4]	-0.1236	-0.2092	0.9698	0.2433[-12]	-0.2113[-12]	-0.5017[-6]	-0.6097[-6]	0.9995
17	-0.2908[-4]	0.9649[-4]	0.1839[-4]	0.1847	-0.9649	-0.1839	-0.1163[-12]	-0.2341[-12]	-0.3110[-6]	-0.2565[-6]	0.9990
$\sum_i (\alpha_{i,j})^2$	0.8390	1.0000	1.0000	0.9703	1.0000	1.0000	0.5566[-1]	0.2483	0.1338	0.1377	
$i$	$\beta_{i,1}$	$\beta_{i,2}$	$\beta_{i,3}$	$\beta_{i,4}$	$\beta_{i,5}$	$\beta_{i,6}$	$\beta_{i,7}$	$\beta_{i,8}$	$\beta_{i,9}$	$\beta_{i,10}$	$\sum_j (\beta_{i,j})^2$
8	-0.5676[-8]	-0.8817[-10]	-0.4877[-9]	-0.6810[-12]	-0.4417[-13]	-0.2539[-12]	1.0000	0.9747[-8]	-0.3296[-8]	0.1058[-7]	1.0000
9	0.3854[-1]	0.3486[-1]	0.4328[-1]	0.5524[-6]	0.3486[-6]	0.4329[-6]	0.9948	-0.6141[-1]	0.1331[-1]	-0.4308[-1]	1.0000
10	0.6945[-1]	-0.1077[-1]	0.2127[-1]	0.9955[-6]	-0.1077[-6]	0.2127[-6]	0.9878	-0.1106	0.2392[-1]	-0.7757[-1]	1.0000
11	0.7639[-1]	0.2475[-1]	-0.2465[-1]	0.1095[-4]	0.2474[-6]	-0.2466[-6]	0.9849	-0.1218	0.2639[-1]	-0.8541[-1]	1.0000
12	0.4248[-1]	0.1529[-1]	-0.1523[-1]	0.6089[-6]	0.1529[-6]	-0.1524[-6]	0.9806	0.1835	0.1468[-1]	-0.4750[-1]	1.0000
13	0.2660[-1]	0.4739[-2]	-0.4890[-2]	0.4214[-6]	0.5314[-6]	-0.3594[-6]	0.9578	0.2853	-0.2026[-1]	0.4760[-2]	1.0000
14	0.9475[-1]	0.2162[-1]	0.1480[-1]	-0.1069[-3]	-0.1759[-4]	-0.1882[-4]	0.9772	0.1584	-0.1543[-1]	-0.1007	1.0000
15	0.3111	0.7388[-1]	0.7419[-1]	-0.4452[-3]	-0.7367[-4]	-0.7439[-4]	0.7199	-0.4940	0.1102	-0.3432	1.0000
16	0.2879	0.1508	-0.3635	-0.4121[-3]	-0.1506[-3]	0.3634[-3]	0.6643	-0.4579	0.1022	-0.3176	1.0000
17	0.2538	0.5207	-0.2652	-0.3631[-3]	-0.5205[-3]	0.2651[-3]	0.5879	-0.4026	0.8984[-1]	-0.2799	1.0000



mogeneity of space (invariance with respect to space translation and momentum conservation), and  $\mathbf{e}_7$  to  $\mathbf{e}_{10}$  are a consequence of the invariance with respect to individual angular shifts. One notices that the vectors  $\mathbf{e}_2$  to  $\mathbf{e}_{10}$  are pairwise orthonormal, but  $\mathbf{e}'_1$  is not. In order to generate an orthonormal basis of the central manifold, it is enough to consider a GS orthonormalization only for  $\mathbf{e}'_1$  (since the other vectors are already orthonormal),

$$\mathbf{e}_1 = \frac{\mathbf{e}'_1 - \sum_{j=7}^{10} (\mathbf{e}'_1 \cdot \mathbf{e}_j) \mathbf{e}_j}{\|\mathbf{e}'_1 - \sum_{j=7}^{10} (\mathbf{e}'_1 \cdot \mathbf{e}_j) \mathbf{e}_j\|} ,$$

which yields

$$\mathbf{e}_1 = \frac{1}{\sqrt{\sum_{k=1}^4 (\vec{p}^k)^2}} (p_x^1, p_y^1, \dots, p_x^4, p_y^4; 0, 0, \dots, 0, 0; 0, 0, 0, 0; 0, 0, 0, 0) .$$

$\mathbf{e}_1$  replaces  $\mathbf{e}'_1$  in the equations above. The angle cosines of the projection of all Gram-Schmidt vectors onto this basis is shown in the upper part of Table 8.3, the corresponding projection matrix for the covariant vectors is shown in the lower part of this table. These data were obtained in a completely analogous way as the results in the Tables 8.1 and 8.2. A comparison of Table 8.3 with Tables 8.1 and 8.2 for the case without orientation angles shows that all the conclusions previously obtained are confirmed. In particular, it is shown below that the null subspace spanned by the orthonormal vector set  $\{\mathbf{e}_1, \dots, \mathbf{e}_{10}\}$  is not perpendicular to the stable and unstable subspaces of the system.

## 8.6 Transversality versus order violation in the local Lyapunov spectrum

The dynamics of the tangent bundle is characterized by a complete set of dissociated sub-bundles, which are defined by the Oseledec splitting,

$$\mathbf{TX}_\Gamma = \mathbf{E}^u \oplus \mathcal{N} \oplus \mathbf{E}^s ,$$

at any point  $\Gamma$  in phase space. Here,  $\mathbf{E}^u = \mathbf{v}_1 \oplus \dots \oplus \mathbf{v}_{D/2-3}$  and  $\mathbf{E}^s = \mathbf{v}_{D/2+4} \oplus \dots \oplus \mathbf{v}_D$  are the covariant unstable and stable subspaces, respectively, and  $\mathcal{N}$  is the covariant null subspace (the dimension  $D$  of the phase space equals  $5N$  for RHDS and  $4N$  for SHDS). The multiplicative ergodic theorem provides us with the following inequalities for the global Lyapunov spectrum

$$\lambda_1 > \dots \geq \lambda_{D/2-3} > \left[ \lambda^{(0)} \right] > \lambda_{D/2+4} \geq \dots > \lambda_D , \quad (8.16)$$

where the equal sign relates to degenerate exponents, and  $[\lambda^0] = 0$  is sixfold degenerate (assuming energy conservation and momentum conservation in  $x$ - and  $y$ -directions). These inequalities, which guarantee a hierarchy of the instabilities, imply also a certain dynamical isolation in the tangent bundle.

The order in Eq. (8.16) may be different, if the local Lyapunov exponents are averaged over a finite time (instead of an infinite time for the global exponents) to which we refer as “loss of isolation”. It may be expressed in terms of the order violation probability for the (finite-time averaged) local Lyapunov spectrum, which is the probability that the (finite-time averaged) local Lyapunov exponent  $\bar{\Lambda}_j^\tau$  is smaller than the (finite-time averaged) local Lyapunov exponent  $\bar{\Lambda}_i^\tau$  for which the global exponents obey  $\lambda_j \geq \lambda_i$ . Therefore, a spectrum is not violated, if all probabilities  $P(\bar{\Lambda}_j^\tau < \bar{\Lambda}_i^\tau) = 0$  for all times  $\tau > \tau_c$ , where  $\tau_c > 0$ . It implies that the angles between the Oseledec subspaces are bounded away from zero [25], which indicates uniform transversality for the respective subspaces. These considerations may be applied to the angles between all possible covariant vector pairs.

In Fig. 8.8 we show contour plots of  $P(\text{cov}\bar{\Lambda}_j^\tau < \text{cov}\bar{\Lambda}_i^\tau)$ ,  $\tau = 0.01$ , for all Lyapunov indices  $j < i$  (provided  $\lambda_j \geq \lambda_i$ ), and compare results for rough hard disks (top) with parameters  $N = 80$ ,  $\kappa = 0.1$  and  $\rho = 0.7$ , with analogous results for smooth hard disks with parameters  $N = 100$  and  $\rho = 0.7$ . The averaging period  $\tau = 0.01$  is small enough such that time averaging does not affect the local exponents much, and they can also be considered as “instantaneous” measures:  $\text{cov}\bar{\Lambda}_i^{0.01} \approx \text{cov}\Lambda_i$ , for all  $i$ .  $10^5$  such intervals were used for the construction of each contour plot. The regime  $UU$ , for which  $i \in [2, 187]$  and  $j \in [1, i - 1]$ , refers to vector pairs from the unstable manifold and is located in a triangle in the upper right corner of these plots. The regime  $SS$ , for which  $i \in [205, 400]$  and  $j \in [204, i - 1]$ , refers to vector pairs from the stable manifold and is located in a triangle in the upper left corner of these plots. The regime  $SU$ , for which  $i \in [204, 400]$  and  $j \in [1, 187]$ , refers to the case where  $\mathbf{v}_i$  is a covariant vector from the stable manifold and  $\mathbf{v}_j$  from the unstable manifold. This regime is located in a square in the center of the plot, which separates  $SS$  from  $UU$ . Vector pairs involving at least one vector from the central manifold are located in narrow stripes in between these domains. A fundamental difference between the rough and smooth disk case may be observed.

For smooth disks (SHDS) in Fig. 8.8, the violation probability  $P$  vanishes for all vector pairs from  $SU$ , which conforms our previous results that the minimum angle between the stable and unstable subspaces is well bounded away from zero, at least for finite  $N$  (see Chap. 3 and Ref. [18]). An entanglement of covariant vectors and, hence, a loss of isolation of covariant subspaces due to an order violation of local exponents only occurs within the stable and unstable manifolds. This causes the finite numbers for violation probability  $P$  in  $UU$  and  $SS$ . Our results

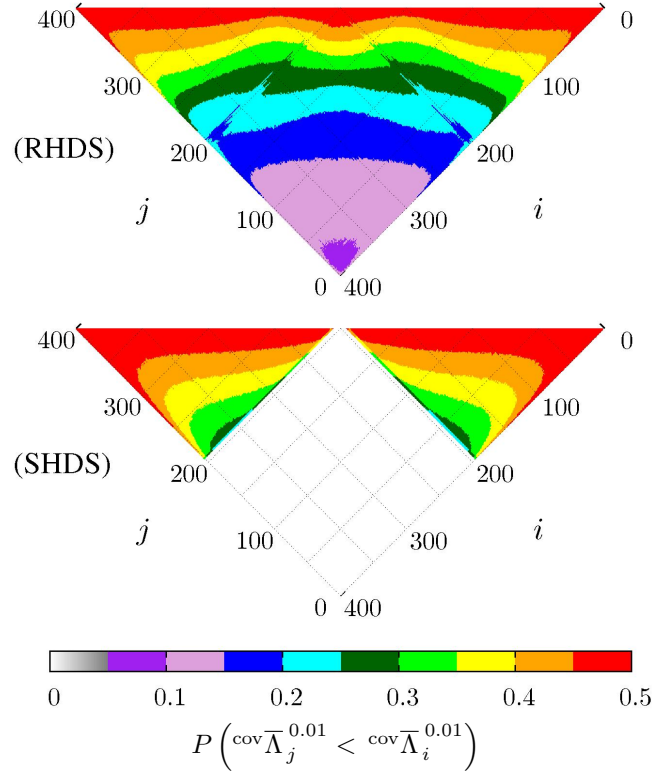


**Figure 8.8 :** Violation probability contour plot for covariant local exponents for averaging times  $\tau = 0.01$ . Top panel: rough-hard-disk system ( $\kappa = 0.1$ ). Bottom panel: smooth-hard-disk system. The order violation probability  $P(\text{cov}\bar{\Lambda}_j^{0.01} < \text{cov}\bar{\Lambda}_i^{0.01})$  is shown for all Lyapunov index pairs  $(i, j)$  for which the global exponents obey  $\lambda_j \geq \lambda_i$  (such that  $j < i$ ).

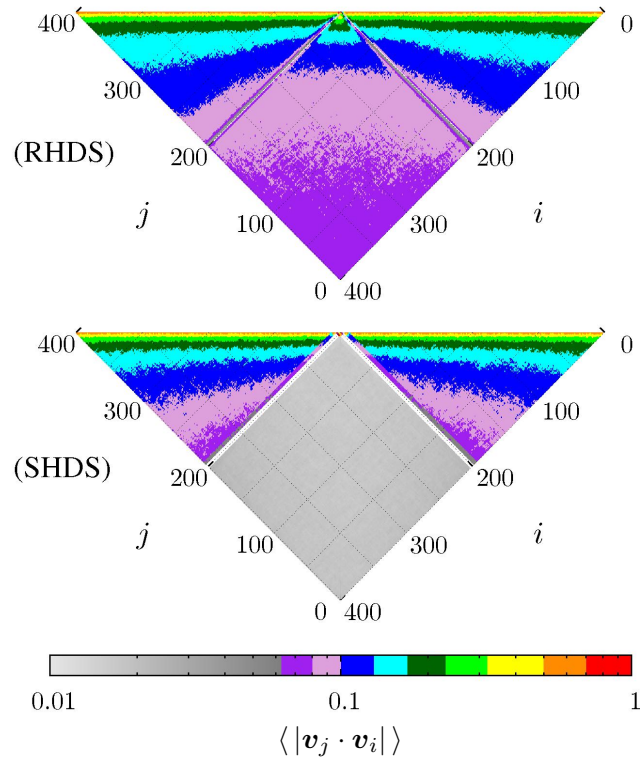


**Figure 8.9 :** Contour plot of  $\langle |\mathbf{v}_j \cdot \mathbf{v}_i| \rangle$  for all Lyapunov index pairs  $(i, j)$  such that  $j < i$ . Top panel: rough-hard-disk system ( $\kappa = 0.1$ ). Bottom panel: smooth-hard-disk system.

also imply that the stable and unstable manifolds have the same dimension at all points in phase space.

For rough disks (RHDS), however, the violation probability varies rather smoothly in Fig. 8.8 and does not vanish for vector pairs from  $SU$ . This means that stable covariant vectors are entangled with unstable covariant vectors and that the respective subspaces are not transversal to each other. Tangencies occur for pairs from the domains  $UU$ ,  $SS$  and  $SU$ . This is a new result. It has been argued that the appearance of these tangencies is responsible for the disappearance of Lyapunov modes in particle systems [25]. Our results confirm this conjecture (see Fig. 8.2).

Related and complementary information may be gained by considering the scalar products between covariant vector pairs. In Fig. 8.9 we show – for the same systems as before – contour plots of  $\langle |\mathbf{v}_j \cdot \mathbf{v}_i| \rangle$  for all  $j < i$ . The same domains  $UU$ ,  $SS$  and  $SU$  may be distinguished.

Let us again consider the SHDS first (bottom panel in Fig. 8.9). Most remarkably, vector pairs from  $SU$ , which correspond to the uniformly shaded square, are not orthogonal to each other. This confirms our results from Chap. 3, where we found that the stable and unstable manifolds are transversal but not orthogonal. The central manifold, however, is orthogonal to both the stable and unstable manifolds.

As expected, the situation is different for the RHDS (top panel in Fig. 8.9). One observes a very smooth variation of  $\langle |\mathbf{v}_j \cdot \mathbf{v}_i| \rangle$  for all three regimes and deviations from orthogonality everywhere. Most notably, these deviations persist also between a vector from the central manifold and another vector from the stable or unstable manifolds (the narrow stripes between  $SU$  and  $UU$  respective  $SS$ ). Thus, the central manifold is not orthogonal to the stable and unstable manifolds.

## 8.7 The RHDS is not symplectic

We have established in the previous sections that for the SHDS the central manifold is orthogonal to the stable and unstable manifolds, that for RHDS is not. Next we show that the SHDS is symplectic and RHDS is not.

Let us denote the energy associated with two colliding particles,  $k$  and  $\ell$ , by

$$\mathcal{H}_{k\ell} = \frac{1}{2} \left[ (\vec{p}_k)^2 + I(\omega_k)^2 + (\vec{p}_\ell)^2 + I(\omega_\ell)^2 \right] .$$

Then the energy difference between the satellite and the reference trajectory is

$$\delta\mathcal{H}_{k\ell} = \frac{\partial\mathcal{H}_{k\ell}}{\partial\mathbf{\Gamma}_k} \delta\mathbf{\Gamma}_k + \frac{\partial\mathcal{H}_{k\ell}}{\partial\mathbf{\Gamma}_\ell} \delta\mathbf{\Gamma}_\ell ,$$

where both trajectories are separated by a small perturbation vector  $\delta\mathbf{\Gamma} = (\delta\mathbf{\Gamma}_k, \delta\mathbf{\Gamma}_\ell)$ . Using the equations of motion, we verified analytically that both  $\mathcal{H}_{k\ell}$  and  $\delta\mathcal{H}_{k\ell}$  are exactly preserved by the collision for the SHDS and for RHDS. Also the free flight between two successive collisions does not change the total energy. However, the conservation of energy is not sufficient to ensure that the transformation is symplectic. Experimentally, it is easily proved that the sum of all local Gram-Schmidt exponents vanishes exactly at any point in phase space.

$$\sum_{i=1}^D \Lambda_i^{GS}(\mathbf{\Gamma}) = 0 \quad (8.17)$$

for both the SHDS and the RHDS. It follows that the phase volume is conserved for both systems.

It was shown by Ershov and Potapov [4] that the orthonormal Gram-Schmidt vectors are intimately connected to another set of spanning vectors of the tangent space already introduced by Oseledec [1], namely the eigenvectors of the matrix

$$[D\phi_{\mathbf{\Gamma}}^t]^\dagger D\phi_{\mathbf{\Gamma}}^t .$$

As before,  $\dagger$  means transpose. Let  $\mathcal{J}$  denote the even-dimensional skew-symmetric matrix,

$$\mathcal{J} = \begin{pmatrix} 0 & \mathbf{I} \\ -\mathbf{I} & 0 \end{pmatrix} .$$

For Hamiltonian systems it was shown by Meyer [26] that for any Gram-Schmidt vector  $\mathbf{g}_i$  also the vector  $\mathcal{J}\mathbf{g}_i$  belongs to the set of Gram-Schmidt vectors such that

$$\Lambda_{D+1-i}^{GS}(\mathbf{\Gamma}) = -\Lambda_i^{GS}(\mathbf{\Gamma}) , \quad (8.18)$$

$$\mathbf{g}_{D+1-i}(\mathbf{\Gamma}) = \pm\mathcal{J}\mathbf{g}_i(\mathbf{\Gamma}) , \quad (8.19)$$

for  $i \in \{1, \dots, D/2\}$ . In Chap. 5 and in Ref. [19] we have referred to Eq. (8.18) as symplectic local pairing symmetry.

Here, we test both expression for the SHDS and RHDS. In Fig. 8.10 the maximum and minimum local GS exponents are shown for a SHDS (left panel) and a RHDS (right panel). One observes

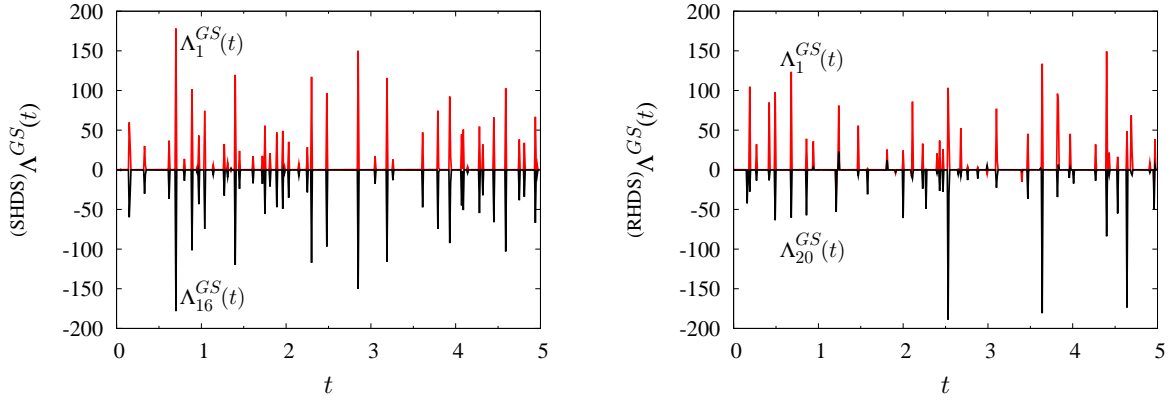


**Figure 8.10 :** Test of the symplectic symmetry of Eq. (8.18) for a SHDS with  $N = 4$  (left panel) and for a RHDS with  $N = 4$  (right panel).

that Eq. (8.18) is obeyed for the smooth case,

$$^{(\text{SHDS})} \Lambda_{\mathbf{D}+1-i}^{GS}(t) + ^{(\text{SHDS})} \Lambda_i^{GS}(t) = 0 ,$$

but not for the rough case,

$$^{(\text{RHDS})} \Lambda_{\mathbf{D}+1-i}^{GS}(t) + ^{(\text{RHDS})} \Lambda_i^{GS}(t) \neq 0 .$$

To test Eq. (8.19), we list in Table 8.4 the perturbation vectors for the largest and the most negative exponents of a four-particle system, where the conjugate perturbation components are indicates in the top block and where  $n$  enumerates the particles. For RHDS we have not included the perturbation components associated with the rotational degree of freedom. This comparison shows that Eq. (8.19) is obeyed for the SHDS (left column in Table 8.4) but not for the RHDS (right column in Table 8.4).

In summary, with this comparison we prove that the RHDS is not a Hamiltonian system, and we confirm here more thoroughly what we have already foreseen in Sec. 8.4.

Next, we demonstrate the non-Hamiltonian character of RHDS considering the transformation rules in the tangent bundle. Let us recall some notions of differential geometry linked to classical mechanics, e.g. [27, 28, 29]:

- i) A symplectic structure on a vector space is given by a bilinear skew-symmetric 2-form,  $\Delta^2$ . This form is called the “skew-scalar product”. The Euclidean space  $\mathbb{R}^{2F}$  together with the symplectic structure  $\Delta^2$  constitute the symplectic vector space.  $F$  corresponds to

**Table 8.4 :** Test of the symplectic symmetry of Eq. (8.19) for a SHDS with  $N = 4$  (left panel) and for a RHDS with  $N = 4$  (right panel). For RHDS we have omitted the perturbation components associated with the rotational degree of freedom.  $n$  enumerates the particles.

	SHDS		RHDS	
	$\begin{pmatrix} (\delta q_x)_{16}^n \\ (\delta q_y)_{16}^n \\ (\delta p_x)_{16}^n \\ (\delta p_y)_{16}^n \end{pmatrix}$	$\begin{pmatrix} -(\delta p_x)_{16}^n \\ -(\delta p_y)_{16}^n \\ (\delta q_x)_{16}^n \\ (\delta q_y)_{16}^n \end{pmatrix}$	$\begin{pmatrix} (\delta q_x)_{20}^n \\ (\delta q_y)_{20}^n \\ (\delta p_x)_{20}^n \\ (\delta p_y)_{20}^n \end{pmatrix}$	$\begin{pmatrix} -(\delta p_x)_{20}^n \\ -(\delta p_y)_{20}^n \\ (\delta q_x)_{20}^n \\ (\delta q_y)_{20}^n \end{pmatrix}$
$n = 1$	$\begin{pmatrix} -0.129760 \\ -0.422082 \\ -0.189845 \\ -0.584252 \end{pmatrix}$	$\begin{pmatrix} 0.129760 \\ 0.422082 \\ 0.189845 \\ 0.584252 \end{pmatrix}$	$\begin{pmatrix} -0.122329[-1] \\ -0.322550[-1] \\ -0.863835[-1] \\ -0.149908 \end{pmatrix}$	$\begin{pmatrix} -0.115517 \\ -0.136373 \\ -0.342865 \\ -0.588225 \end{pmatrix}$
$n = 2$	$\begin{pmatrix} 0.187058 \\ 0.287147 \\ 0.238637 \\ 0.454717 \end{pmatrix}$	$\begin{pmatrix} -0.187058 \\ -0.287147 \\ -0.238637 \\ -0.454717 \end{pmatrix}$	$\begin{pmatrix} 0.564003[-1] \\ 0.859799[-1] \\ 0.154315 \\ 0.243975 \end{pmatrix}$	$\begin{pmatrix} 0.287485[-1] \\ 0.170368 \\ 0.212333 \\ 0.643007 \end{pmatrix}$
$n = 3$	$\begin{pmatrix} -0.723013[-1] \\ 0.140295 \\ -0.576590 \\ 0.133684 \end{pmatrix}$	$\begin{pmatrix} 0.723013[-1] \\ -0.140295 \\ 0.576590[-1] \\ -0.133684 \end{pmatrix}$	$\begin{pmatrix} -0.477307[-1] \\ 0.483709[-1] \\ -0.745171[-1] \\ 0.411408[-1] \end{pmatrix}$	$\begin{pmatrix} 0.398695[-1] \\ -0.319941[-1] \\ 0.628463[-1] \\ -0.476581[-1] \end{pmatrix}$
$n = 4$	$\begin{pmatrix} 0.150037[-1] \\ -0.535970[-2] \\ 0.886748[-2] \\ -0.414995[-2] \end{pmatrix}$	$\begin{pmatrix} -0.150037[-1] \\ 0.535970[-2] \\ -0.886748[-2] \\ 0.414995[-2] \end{pmatrix}$	$\begin{pmatrix} 0.356330[-2] \\ -0.102095 \\ 0.658561[-2] \\ -0.135208 \end{pmatrix}$	$\begin{pmatrix} 0.468989[-1] \\ -0.200067[-2] \\ 0.676849[-1] \\ -0.712407[-2] \end{pmatrix}$

the number of degrees of freedom. Let us consider the standard symplectic space  $X^{2F} = (\mathcal{Q}^1, \mathcal{P}^1, \dots, \mathcal{Q}^F, \mathcal{P}^F)$ , where  $\mathcal{Q}^i$  and  $\mathcal{P}^i$  are conjugate variables consisting either of  $(q_x^i, p_x^i)$ ,  $(q_y^i, p_y^i)$  or  $(\theta_i, \omega_i)$ . The last degree of freedom applies only to rough disks. The differential 2-form can be expressed as

$$\Delta^2 = \delta \mathcal{Q}^1 \wedge \delta \mathcal{P}^1 + \dots + \delta \mathcal{Q}^F \wedge \delta \mathcal{P}^F .$$

- ii) The skew-scalar product of two vectors  $\varphi$  and  $\psi$  is the sum of the areas of the projections onto the  $F$  coordinate planes of the oriented parallelogram  $(\varphi, \psi)$ . The skew-scalar product consists of a Lie algebra. The binary operator in this algebra is known as a Poisson bracket  $\{ , \}$ .

- iii) A linear transformation  $\mathcal{S}$  of the symplectic space  $X^{2F}$  into itself is said to be “symplectic”

or “canonical” if, and only if,  $\mathcal{S}$  preserves the differential 2-form  $\Delta^2$ , i.e. preserves the skew-scalar product:

$$\{\mathcal{S}\varphi, \mathcal{S}\psi\} = \{\varphi, \psi\} \ , \quad \varphi, \psi \in X^{2F} \ . \quad (8.20)$$

Each of the differential forms  $(\Delta^2)^2, (\Delta^2)^3 \dots (\Delta^2)^F$  is invariant of the Hamiltonian phase flow. The preservation of

$$(\Delta^2)^F \equiv \delta\mathcal{Q}^1 \wedge \delta\mathcal{P}^1 \wedge \dots \wedge \delta\mathcal{Q}^F \wedge \delta\mathcal{P}^F \ ,$$

constitutes Liouville’s theorem.

- iv) Eq. (8.20) can be written in terms of the scalar product, since  $\{\varphi, \psi\} = \mathcal{J}\varphi \cdot \psi$ . Hence, the linear transformation  $\mathcal{S}$  is symplectic if, and only if, it satisfies

$$\mathcal{S}^\dagger \mathcal{J} \mathcal{S} = \mathcal{J} \ .$$

Applying this identity to the collision map onto the matrix transformations for the smooth- and rough-hard-disk models, Eqs. (8.22), (8.10) and (8.12), we proved analytically – after some tedious calculations (not shown here) – that the SHDS is Hamiltonian whereas the RHDS is not. In particular, this computation for the RHDS was carried out for both cases, with the orientation of the particles included and excluded.



## 8.8 Appendix: Matrix formulation of the phase-space and tangent-space dynamics, for the SHDS

In this Appendix we give the matrix formulation for the dynamical events – free streaming and collision between particles  $k$  and  $\ell$  – for the smooth-hard-disk model (SHDS), where we follow the notation of de Wijn and van Beijeren in Ref. [16]. It may be obtained from corresponding expressions (8.9) and (8.10) for the rough-hard-disk model (RHDS) treated in Sec. 8.3.2 by taking  $\kappa = 0$  and discarding all angular velocities,

The state and perturbation vectors for a particle  $n$  are denoted by  $\mathbf{\Gamma}_n^\dagger(\vec{q}_n^\dagger, \vec{p}_n^\dagger)$  and  $\delta\mathbf{\Gamma}_n^\dagger(\delta\vec{q}_n^\dagger, \delta\vec{p}_n^\dagger)$ . The matrix  $\mathcal{Z}(\tau)$  for the free flight between two successive collisions separated by a time  $\tau$  of the  $N$  particles corresponds to a  $N$ -block diagonal matrix, where each block is a  $4 \times 4$  - dimensional matrix defined as

$$\mathcal{Z}_n(\tau) = \begin{pmatrix} 1 & 0 & \tau & 0 \\ 0 & 1 & 0 & \tau \\ 0 & 0 & 1 & 0 \\ 0 & 0 & 0 & 1 \end{pmatrix}.$$

The collision map in the phase space is given by

$$\mathcal{M}_{k\ell} = \begin{pmatrix} \mathcal{I} & \mathbf{O} & \mathbf{O} & \mathbf{O} \\ \mathbf{O} & \mathcal{I} - \vec{n}\vec{n}^\dagger & \mathbf{O} & \vec{n}\vec{n}^\dagger \\ \mathbf{O} & \mathbf{O} & \mathcal{I} & \mathbf{O} \\ \mathbf{O} & \vec{n}\vec{n}^\dagger & \mathbf{O} & \mathcal{I} - \vec{n}\vec{n}^\dagger \end{pmatrix}, \quad (8.21)$$

where  $\mathcal{I}$  and  $\mathbf{O}$  are the respective  $2 \times 2$  identity and null matrices, and  $\vec{n} = (\vec{q}_k - \vec{q}_\ell)/\sigma$  is the unit vector at the impact point connecting the particles  $k$  and  $\ell$ . The collision map in tangent space follows,

$$\mathcal{S}_{k\ell} = \begin{pmatrix} \mathcal{I} - \vec{n}\vec{n}^\dagger & \mathbf{O} & \vec{n}\vec{n}^\dagger & \mathbf{O} \\ -\mathcal{C} & \mathcal{I} - \vec{n}\vec{n}^\dagger & \mathcal{C} & \vec{n}\vec{n}^\dagger \\ \vec{n}\vec{n}^\dagger & \mathbf{O} & \mathcal{I} - \vec{n}\vec{n}^\dagger & \mathbf{O} \\ \mathcal{C} & \vec{n}\vec{n}^\dagger & -\mathcal{C} & \mathcal{I} - \vec{n}\vec{n}^\dagger \end{pmatrix}, \quad (8.22)$$

where  $\mathcal{C}$  is a  $2 \times 2$  matrix

$$\mathcal{C} = \frac{\vec{n} \cdot \vec{p}}{\sigma} \left( \mathcal{I} + \frac{\vec{n}\vec{p}^\dagger}{\vec{n} \cdot \vec{p}} \right) \left( \mathcal{I} - \frac{\vec{p}\vec{n}^\dagger}{\vec{n} \cdot \vec{p}} \right),$$

and  $\vec{p} = \vec{p}_k - \vec{p}_\ell$ . The determinants for the maps  $\mathcal{M}$  and  $\mathcal{S}$  are also equal to unity,

$$\det(\mathcal{M}) \equiv \det(\mathcal{M}_{k\ell}) = 1 \quad \text{and} \quad \det(\mathcal{S}) \equiv \det(\mathcal{S}_{k\ell}) = 1,$$

due to the fact that SHDS is a Hamiltonian system.

## References

- [1] V.I. Oseledec, Trudy Moskov. Mat. Obsc. **19**, 179, (1968). English transl. Trans. Moscow Math. Soc. **19**, 197 (1968).
- [2] F. Ginelli, P. Poggi, A. Turchi, H. Chaté, R. Livi, and A. Politi, Phys. Rev. Lett. **99**, 130601 (2007).
- [3] D. Ruelle, Publ. Math. de l'IHÉS **50**, 27 (1979).
- [4] S.V. Ershov and A.B. Potapov, Physica D **118**, 167 (1998).
- [5] Ch. Dellago, H.A. Posch, and Wm.G.Hoover, Phys. Rev. E **53**, 1485 (1996).
- [6] H.A. Posch and R. Hirschl, in *Hard Ball Systems and the Lorentz Gas*, Encyclopaedia of Mathematical Sciences **vol. 101**, edited by D. Szász (Springer-Verlag, Berlin, 2000) p. 269.
- [7] Ch. Forster, R. Hirschl, H.A. Posch, and Wm.G. Hoover, Physica D **187**, 294 (2004).
- [8] T. Taniguchi and G.P. Morriss, Phys. Rev E **68**, 026218 (2003).
- [9] T. Taniguchi and G.P. Morriss, Phys. Rev E **68**, 046203 (2003).
- [10] J.A. van Meel and H.A. Posch, Phys. Rev. E **80**, 016206 (2009).
- [11] G.H. Bryan, in *Report on the Present State of our Knowledge of Thermodynamics*, Reports of the British Association for the Advancement of Science **vol. 64** (1894) p. 64.
- [12] S. Chapman and T.G. Cowling, *The Mathematical Theory of Non-Uniform Gases* (Cambridge University Press, New York, 3rd ed., 1990).
- [13] J. O'Dell and B.J. Berne, J. Chem. Phys. **63**, 2376 (1975).
- [14] B.J. Berne, J. Chem. Phys. **66**, 2821 (1977).
- [15] C.S. Pangali and B.J. Berne, J. Chem. Phys. **67**, 4571 (1977).
- [16] A.S. de Wijn and H. van Beijeren, Phys. Rev. E **70**, 016207 (2004).
- [17] T. Chung, D. Truant, and G.P. Morriss, Phys. Rev. E **81**, 066208 (2010).
- [18] H. Bosetti and H.A. Posch, Chemical Physics **375**, 296308 (2010).
- [19] H. Bosetti, H.A. Posch, Ch. Dellago, and Wm. Hoover, Phys. Rev. E **82**, 046218 (2010).
- [20] J.P. Eckmann, Ch. Forster, H.A. Posch, and E. Zabey, J. Stat. Phys. **118**, 813 (2005).

- [21] R. Ramaswamy, Eur. Phys. J. B **29**, 339 (2002).
- [22] H. Goldstein, *Classical Mechanics*, (Addison-Wesley, Toronto, 2nd ed., 1980).
- [23] P. Gaspard, *Chaos, Scattering, and Statistical Mechanics* (Cambridge University Press, 1998).
- [24] Ch. Dellago and H.A. Posch, Physica A, **240**, 68 (1997).
- [25] H.L. Yang and G. Radons, Phys. Rev. Lett. **100**, 024101 (2008).
- [26] H.D. Meyer, J. Chem. Phys. **84**, 3147 (1986).
- [27] V.I. Arnol'd and A.B. Givental', *Symplectic Geometry, Dynamical Systems IV* (Springer-Verlag, Berlin Heidelberg New York, 1990), pp. 1-136.
- [28] V.I. Arnol'd *Mathematical Methods of Classical Mechanics* (Springer-Verlag, Berlin Heidelberg New York, 1978).
- [29] Th. Frankel, *The Geometry of Physics* (Cambridge University Press, 2nd ed., 2004).



# Outlook

As is rather common with a scientific program, the work on a topic for a number of years – as is the case for this thesis – does not solve all of the problems, and some of the open problems have to be deferred to future work. More often than not, the answer to a particular question opens up new and refined questions.

For example, a problem not touched in this thesis is the existence, or lack of existence, of Fourier’s law in two-dimensional hard disk systems. As is well known from kinetic theory [1, 2], correlation functions in two dimensions tend to have a slow decay due to long-time tails caused by the famous Alder vortices [3, 4, 5]. This effect is responsible for a logarithmic divergence of the diffusion coefficient. A similar behavior is expected for heat diffusion. No computational problem arises for finite systems. Still, the problem of the existence of regular transport coefficients for systems with lower than three dimensions poses a vexing problem.

Another interesting question concerns the dependence of the local Lyapunov exponents on the metric and the coordinate system used. Whereas the local exponents depend on the metric, there is some evidence that the covariant vectors obtained with a particular coordinate system may be converted to the respective covariant vectors for another coordinate system [6] of the same state. This observation is very interesting and will be investigated further in the future.

Here, we have devoted much effort to clarify the properties of covariant Lyapunov vectors and of the associated local Lyapunov exponents. We have also clarified the non-symplectic nature of the rough-hard-disk system. An application of the covariant vectors to more practical systems is still a complicated and time consuming task, but in our opinion a promise for the future. It will require new ideas and improved computational facilities to apply this concept, say, to the dynamics of complex molecules such as polymer chains or biomolecules. But one may be confident that this method will eventually become a standard tool. It is hoped that the present thesis provides some guidance for the next moves in that direction.

## References

- [1] J.R. Dorfman and E.G.D. Cohen, Phys. Rev. A **6**, 776 (1972).
- [2] J.R. Dorfman and E.G.D. Cohen, Phys. Rev. A **12**, 292 (1974).
- [3] B. Alder and T.E. Wainwright Phys. Rev. A **1**, 18 (1970).
- [4] W.W. Wood, in *Fundamental Problems in Statistical Mechanics III*, edited by E.G.D. Cohen (North Holland, New York, 1975) p. 331.
- [5] D. Levesque and W.T. Ashurst, Phys. Rev. Lett **33**, 277 (1974).
- [6] H.A. Posch, arXiv:1107.4032.

**Ao. Prof. Dr. Harald A. Posch,**  
Faculty of Physics, University of Vienna,  
Boltzmanngasse 5  
A-1090 Wien, Austria

Remarks on the thesis

*On the microscopic dynamics of particle systems in and out of thermal equilibrium*

by M.Sc. Hadrien Bosetti under my supervision

The thesis is formally organized in part as a cumulative dissertation (where the Chapters 3, 5, and 6 have appeared in print [1, 2, 3]), whereas the remaining chapters contain new and as yet unpublished results. For all chapters the overwhelming part of the research and of the writing was carried out by Mr. Bosetti himself, where my contribution as a supervisor was restricted to the formulation of the original topic of research, to the discussion of possible interpretations of his work, to a few complementary simulations for checking the validity of some surprising and unexpected results, and to a thorough reading of the thesis.

Vienna, July 2011.

## References

- [1] H. Bosetti and H.A. Posch, *Covariant Lyapunov vectors for rigid disk systems*, Chem. Phys. **375**, 296 (2010).
- [2] H. Bosetti, H.A. Posch, Ch. Dellago, and Wm.G. Hoover, *Time-reversal symmetry and covariant Lyapunov vectors for simple particle models in and out of thermal equilibrium*, Phys. Rev. E **82**, 046218 (2010).
- [3] H.A. Posch and H. Bosetti, *Covariant Lyapunov vectors and local exponents*, in *Non-equilibrium Statistical Physics Today*, Proc. of the 11th Granada Seminar on Computational and Theoretical Physics, edited by P.L. Garrido, J. Marro, and F. de los Santos, American Institute of Physics, Conf. Proc. **vol. 1332**, p. 230 (2011).





# Curriculum Vitae

## Personal Information

---

Name: Hadrien Julien BOSETTI

Date and place of birth: December 27th, 1977, Fontenay-Aux-Roses, France

Nationality: French

## Education

---

Since 2005 Doctoral studies of Physics at the *University of Vienna*,  
supervised by Harald A. Posch.

2002–2003 DEA de Physique des Liquides [Second year Master’s degree, Liquid-state Physics],  
from “Ecole Doctorale de Physique de la Région Parisienne” [*ENS Paris*],  
at *Pierre and Marie Curie University (Paris VI)*.  
– Diploma Thesis, supervised by Maurice Courbage,  
at “Laboratoire de Physique Théorique de la Matière Condensée”,  
*Paris Diderot University (Paris VII)*,  
title: Kinetics and Chaotic Transport in Hamiltonian Systems.

2001–2002 Maîtrise de Physique [First year Master’s degree in Physics],  
at *Pierre and Marie Curie University (Paris VI)*.

1999–2001 Licence de Physique [Bachelor’s degree in Physics],  
at *Orsay University (Paris XI)*.

1997–1999 DEUG MIAS [Two-years First Diploma in Mathematics],  
at *Paris Descartes University (Paris V)*.

1996–1997 Baccalauréat Scientifique [Grammar school, General section, Science syllabus],  
at *Lycée Lavoisier (Paris)*.

## Professional History

---

- 2005–2008      Research Assistant at the Faculty of Physics, *University of Vienna*, funded by the FWF-projects P 15348 and P 18798-N20.
- 2003–2004      Research Assistant for Bioinformatics, supervised by Harald Strelec, at the *University of Natural Resources and Life Sciences, Vienna*.
- Summer 2000      Summer work term, supervised by Aurélien Perera (*CNRS*), at “Laboratoire de Physique Théorique des Liquides”, *Pierre and Marie Curie University (Paris VI)*.

## Journal Articles

---

- H. Bosetti, H.A. Posch, Ch. Dellago, and Wm.G. Hoover, Time-reversal symmetry and covariant Lyapunov vectors for simple particle models in and out of thermal equilibrium, [Phys. Rev. E \*\*82\*\*, 046218 \(2010\)](#).
- H. Bosetti and H.A. Posch, Covariant Lyapunov vectors for rigid disk systems, [Chem. Phys. \*\*375\*\*, p. 296 \(2010\)](#).
- H. Bosetti and A. Perera, Entropy-driven demixing in spherocylinder binary mixtures, [Phys. Rev. E \*\*63\*\*, 021206 \(2001\)](#).

## Proceedings

---

- H.A. Posch and H. Bosetti, Covariant Lyapunov vectors and local exponents, in *Non-equilibrium Statistical Physics Today*, Proc. of the 11th Granada Seminar on Computational Physics, edited by P.L. Garrido, J. Marro, and F. de los Santos, American Institute of Physics, [Conf. Proc. vol. \*\*1332\*\*, p. 230 \(2011\)](#).